NATIONAL INSTITUTE FOR FUSION SCIENCE

NIFS-SWJTU JOINT PROJECT FOR CFQS
-PHYSICS AND ENGINEERING DESIGN-
VER. 2.1

CFQS TEAM

National Institute for Fusion Science, National Institutes of Natural Sciences
Institute of Fusion Science, School of Physical Science and Technology,
Southwest Jiaotong University
Hefei Keye Electro Physical Equipment Manufacturing Co. Ltd

NIFS-SWJTU JOINT PROJECT FOR CFQS

~PHYSICS AND ENGINEERING DESIGN~

VER. 2.1
2019. SEP

CFQS Team

National Institute for Fusion Science, National Institutes of Natural Sciences

Institute of Fusion Science, School of Physical Science and Technology, Southwest Jiaotong University

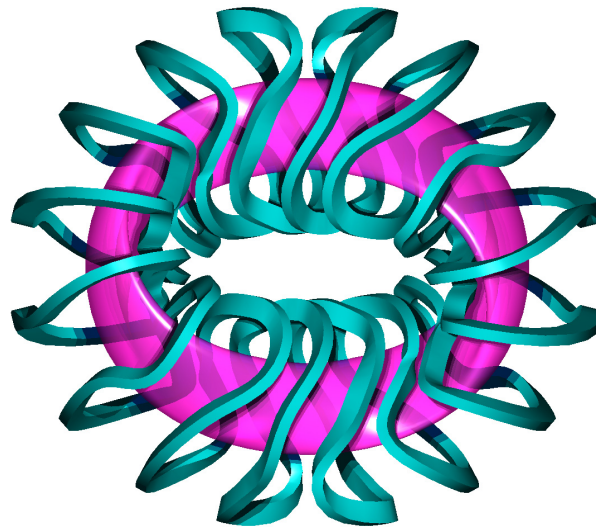Hefei Keye Electro Physical Equipment Manufacturing Co. Ltd

NIFS-SWJTU Joint project for CFQS: Physics and engineering design Ver 2.1

CFQS Team

National Institute for Fusion Science, National Institutes of Natural Sciences
Institute of Fusion Science, School of Physical Science and Technology, Southwest Jiaotong University
Hefei Keye Electro Physical Equipment Manufacturing Co. Ltd

Abstract

The National Institute for Fusion Science (NIFS) and Southwest Jiaotong University (SWJTU) concluded an agreement for international academic cooperation to promote cooperative research in helical fusion plasma research on July 3, 2017. Since then, NIFS and SWJTU have continued the design study of the quasi-axisymmetric stellarator CFQS as a joint project. NIFS and SWJTU have organized the steering committee to manage this joint project. This document summarizes achievements of physical and engineering design study of the CFQS up to the 2nd steering committee meeting, which was held on May 29, 2019 at SWJTU.

Principal parameters of the CFQS are as follows: the major radius is 1 m, the magnetic field strength is 1 T, the aspect ratio is 4, and the number of toroidal period is 2. Magnetic field configuration is designed based on that of CHS-qa. Good MHD stability is confirmed, and the effect of the neoclassical bootstrap current on the magnetic field configuration is estimated. Magnetic field coil system is designed for the CFQS, which consists of 16 modular coils. Supporting system is designed to withstand strong electro-magnetic force under 1 T operation. Analysis by using finite element method shows that the stress in the supporting structure is less than the allowable level. Layout of main components, e.g., CFQS itself, diagnostic system, heating system, and power supply in the torus hall is designed, which will be arranged in the building in Emei campus of SWJTU. For one of the modular coils, a mock up coil is designed and now is being constructed in the factory of Hefei Keye Electro Physical Equipment Manufacturing Co. Ltd. Details of physical and engineering design studies for the CFQS are reported in this document.

Documentation Contributors

(Alphabetical order of family name)

ISOBE	Mitsutaka	National Institute for Fusion Science (NIFS)
KINOSHITA	Shigeyoshi	National Institute for Fusion Science (NIFS)
LI	Yangbo	Southwest Jiaotong University (SWJTU)
LIU	Hai	Southwest Jiaotong University (SWJTU)
LIU	Haifeng	Southwest Jiaotong University (SWJTU)
MURASE	Takanori	National Institute for Fusion Science (NIFS)
NAGAOKA	Kenichi	National Institute for Fusion Science (NIFS)
NAKAGAWA	Sho	National Institute for Fusion Science (NIFS)
NAKATA	Motoki	National Institute for Fusion Science (NIFS)
OGAWA	Kunirhiro	National Institute for Fusion Science (NIFS)
OKAMURA	Shoichi	National Institute for Fusion Science (NIFS)
SHAO	Junren	Southwest Jiaotong University (SWJTU)
SHIMIZU	Akihiro	National Institute for Fusion Science (NIFS)
SUZUKI	Chihiro	National Institute for Fusion Science (NIFS)
WAN	Yi	Hefei Keye Electro Physical Equipment Manufacturing
WANG	Xianqu	Southwest Jiaotong University (SWJTU)
XIONG	Guozhen	Southwest Jiaotong University (SWJTU)
XU	Yuhong	Southwest Jiaotong University (SWJTU)
YANG	Lang	Southwest Jiaotong University (SWJTU)
YIN	Dapeng	Hefei Keye Electro Physical Equipment Manufacturing
YOSHIMURA	Yasuo	National Institute for Fusion Science (NIFS)

TABLE OF CONTENTS

1 Introduction

The controlled nuclear fusion research is one of the most important issues for human beings because it is necessary to secure stable energy resources in order to enrich human life in the future. Fusion energy does not produce hydrocarbons and hence does not contribute to the global warming, which is one of the most serious environmental problems for Earth. The source of energy are isotopes of hydrogen, which are a common resource for the world because the hydrogen isotopes are obtained from seawater.

The development of technologies so far for making controlled nuclear fusion is based on two methods, namely, magnetic confinement of high temperature plasmas and the strong compression of high density plasmas with ultra-high intensity laser. For the magnetic confinement, high technology devices with strong magnetic field produced by large currents are used. This research started from the 1950s and varieties of different designs of magnetic confinement devices were proposed. After intensive research all over the world for more than a half century, two major magnetic confinement schemes have been established as candidates for the future fusion reactor design, namely, tokamak and stellarator.

These two designs have different advantages and disadvantages. Tokamak devices have better confinement property for high temperature plasmas because of their axisymmetric configuration of the magnetic field. However, tokamaks have essential problems of suffering current disruptions, which is very hazardous for the devices, and the high cost of current drive system because a large plasma current flowing in the plasma is a necessary element for the tokamak concept. On the other hand, stellarator does not have current disruption problems and does not need high cost current drive system because it does not require plasma current as a necessary element of a magnetic confinement concept. However, because of the lack of axisymmetry of the magnetic configuration, the confinement is degraded when the plasma temperature approaches the necessary conditions for the fusion reaction.

At present, large effort toward magnetic confinement of high temperature plasmas is focused on tokamak researches. In France, ITER, the largest facility of magnetic fusion research is now under construction as an international joint project. This device is a tokamak type and it is planned to produce 10 times larger fusion reaction energy than the electric energy consumed for maintaining high temperature plasmas in the device. This program is the final goal of the long way in making good plasma confinement using tokamak type devices. As a next step of fusion research toward the power reactor, we must solve many engineering problems. One of those significant issues is technology problems related to the plasma current (disruptions and current drive). It is strongly pointed out that we should have a multi-line research strategy for the future reactor design, namely, that we should continue the stellarator research as a safe candidate for the fusion power plant free from the plasma current problems.

When the bright news of achieving high electron temperature in the tokamak device in Russia was distributed throughout the world fusion community in 1969, all plasma experimentalists began to work on tokamak experiments, thus giving up research with their own devices with different concepts from the tokamak. Since then, the main line of magnetic confinement fusion has been based on the tokamak concept. However, there were two continuous research activities for devices with the stellarator concept. In Kyoto University, in Japan, a series of devices with the names of Heliotron (A, B, C, D, DM, DR, E, J) were built and the plasma parameters were improved continuously. In Germany, a series of devices with the name Wendelstein (1, 2, 3, ..., 6) were producing very promising data with stellarator configuration. In the final phase of these series, Wendelstein 7a was built in Germany and started experiments in 1975. In Japan, Heliotron E was built and started experiments in 1980. Because the impact of experimental results from these devices were very large for the world fusion community, various types of stellarator programs were initiated in many countries in the 1980s.

In Japan, the designing work for Large Helical Device (LHD) started in 1985, and the construction of the device began in 1989. In Germany, the first design workshop for Wendelstein 7-X (W7-X) took place in 1987 and the first modular coil was ordered in 1998. These two world leading stellarator devices with super-conducting magnets are now in operation for experimental research in various topics of magnetic confinement with stellarator concept. In addition to these large devices, there were two medium size stellarators in operation from the 1980s to the 2000s both in Japan and in Germany. The roles of these devices were to conduct supporting experimental research in advance of the completion of construction and starting the experiments in larger-size major devices. Compact Helical System (CHS) was in operation from 1988 to 2006 and Wendelstein 7-AS was in operation from 1988 to 2002. The experimental results obtained in these devices before starting experiments in LHD and W7-X were very useful for planning experimental program in large devices. They also produced unique scientific results available only in the smaller size devices. In addition to these two experiments, many different types of stellarators were designed and built in other countries: in the United States, Advanced Toroidal Facility (ATF) with heliotron configuration and Helically Symmetric Experiment (HSX) with quasi-helical symmetric configuration started experiments in the 1980s. TJ-II in Spain and H-1 in Australia, both having the heliac configurations, started experiments in the 1980s. Among these devices, experiments in four devices are active at present, namely, LHD, W7-X, HSX, and TJ-II. Four other devices stopped experiments (ATF, W7-AS, CHS, and H-1).

The 1980s was an exciting period for stellarator research as many devices were designed and constructed. Fortunately, four devices continue in operation. However, we notice that it is too long for scientists in active research fields to keep running experiments in old devices designed and built more than 30 years ago even though the devices are in healthy condition for the experiments. In fact, there were two research activities for the advanced design of stellarator concept in 1990s. In Japan, when CHS completed its initial phase of experimental program, the discussion for the next device after CHS

was initiated in 1995. After making surveys for the possible candidates of the next devices, a plan for building a quasi-axisymmetric (QA) stellarator CHS-qa was chosen. Based on the physics and engineering design, a proposal of CHS-qa was completed in 2000 and submitted to the National Institute for Fusion Science (NIFS). Unfortunately, the proposal was not accepted because 2000 was just after the beginning of the LHD experiments and NIFS did not have financial and personnel capability to share in two large programs.

In Princeton Plasma Physics Laboratory (PPPL), a stellarator experiment program started in 1995 for building a medium size stellarator National Compact Stellarator Experiment (NCSX) in parallel to the existing spherical torus experiment, National Spherical Torus Experiment (NSTX). The design concept was a QA stellarator similar to CHS-qa. It had N=3 toroidal period number different from N=2 for CHS-qa. The proposal of the device construction was approved and PPPL started to build NCSX in 2000. Unfortunately, this program was cancelled in 2008 because of the rapid increase of the construction cost, which the United States government did not accept.

The advanced concept of QA stellarator is very attractive as it is a new scheme of stellarator configuration that had not been imagined by any scientists before 1994. A toroidal device of magnetic confinement must have rotating structures of magnetic field lines in a plasma toroid which can be produced either by a plasma current or by twisting of the plasma surface. Because a twisting shape is not axisymmetric, it is not naturally possible to make a twisting system as axisymmetric. A QA stellarator is not a hybrid device of tokamak and stellarator, either. When we design a hybrid system of two different concepts, all advantageous points and disadvantageous points are mixed together in general. However, the QA stellarator combines only advantageous points from both tokamak and stellarator, thus producing a new advantageous concept. Because such a new invention of the stellarator concept was not realized in the real experimental program in 2000, we now need to recover the lost 15 years by starting a new QA stellarator experiment with the Chinese First Quasi-axisymmetric Stellarator (CFQS).

The present design of the CFQS device incorporates numerous experiences we have learned in CHS-qa design work. In addition, we are adding many new design points that have been learned in theoretical and computational works during the past 15 years. The divertor configuration design, which is supposed be one of the most important research issues in advanced stellarator concept, was renewed from the CHS-qa design with a new concept of the island bundle divertor configuration. For the engineering design of the device and manufacturing, we will make use of new numerical technologies of mechanical design and of new engineering facilities in order to obtain very high accuracy of the three dimensional shape of the device.

This program is a joint project conducted by NIFS in Japan and Southwest Jiaotong University (SWJTU) in China. We concluded the MoU in 2017 on NIFS and SWJTU Joint Project (NSJP) for CFQS experiment. In addition, we are working together with Keye Electro Physical Equipment

Manufacturing Co., Ltd. in Hefei with their contribution in engineering design and manufacture of the device. Thus, in fact, the program is a joint project by three organizations in Japan and China. We have been working together for the physics and engineering design of CFQS device. SWJTU and the Keye company are primarily responsible for the engineering design and for manufacturing the device. NIFS is primarily responsible to contribute in preparing plasma heating system and diagnostic system. The experiment in the device will be conducted as international collaborations by NIFS, SWJTU and other researchers in foreign countries who will be interested in the challenging advanced stellarator program in Chengdu, China.

In the following sections, important items in the physics and engineering designs of CFQS will be described. We hope this report will provide give sufficient information to all researchers in the world about our CFQS program and motivate them to participate in the joint program of NSJP.

2   Research target

The CFQS is an internationally joint project between SWJTU (China) and NIFS (Japan). It is the first stellarator to be manufactured and assembled by the Hefei Keye Electro Physical Equipment Manufacturing Co. Ltd. in China. Whereas in China there have been several tokamaks built by national institutions there is no stellarator up to now. As the stellarator is technically much more complicated than the tokamak, our first target is to successfully construct the CFQS device and make it in good operation status in SWJTU. Secondly, we want to scientifically prove the major advantage of a QA stellarator in confining plasmas with reduced ripple, and hence, neoclassical transport in comparison with previous conventional stellarators. Thirdly, for complementing the 2D tokamak physics, we will thoroughly study the intrinsic 3D physics in the CFQS stellarator to improve our understanding on related 3D issues appeared in the tokamak, which has primarily 2D magnetic configuration.

The main focus of the CFQS research activities is on basic physics studies under the advanced QA configuration. The scientific subjects include neoclassical transport, macro-scale magnetohydrodynamics (MHD) instabilities (*interchange, ballooning, kink and tearing modes, etc.*), micro instabilities (*electron drift wave, ITG, TEM and ETG modes, etc.*) and turbulence-induced transport, nonlinear interaction and energy cascading of multi-scale turbulence and zonal flows, confinement scaling and isotopic effects, plasma rotations, and edge and divertor physics. Special attention will also be paid on MHD activities arising from the bootstrap current and the maximum J issue in the QA configuration.

3   The physics design

3.1   Equilibrium

The characteristics of three dimensional magnetic field configuration is uniquely determined, if the geometry of outermost magnetic surface, the radial profile of pressure and the toroidal current as a function of flux are given [3.1-1]. The equilibrium of the magnetic field configuration is obtained by the VMEC code [3.1-2]. This code calculates the equilibrium from the given outermost magnetic surface, the pressure and the toroidal current profile. The geometry of the torus outermost magnetic surface can be parameterized by the Fourier series as follows,

$$R(\theta, \phi, s) = \sum R_{mn}(s)\cos(m\theta - N_p n\phi),$$
$$Z(\theta, \phi, s) = \sum Z_{mn}(s)\sin(m\theta - N_p n\phi).$$

Here, θ and, ϕ, s are the poloidal angle, toroidal angle, and the radial flux coordinate, m, n, are the poloidal and toroidal mode, and N_p is the toroidal periodic number of the magnetic field configuration. In other words, the geometry of the outermost magnetic surface (namely, the characteristics of the magnetic field configuration equilibrium) is expressed numerically by the dataset of R_{mn}, Z_{mn}. In stellarator optimization, we consider these parameters (R_{mn}, Z_{mn}) as control parameters, and some

specific characters of magnetic field configuration are optimized. For numerical optimization, characters of magnetic field configuration are expressed numerically. For example, the sum of non-axisymmetric components of magnetic field in the Boozer coordinates [3.1-3], the Mercier criteria of D_I, and the effective helical ripple ε_{eff} etc. are used for the numerical evaluation of the magnetic configuration. These values that characterize the magnetic field configuration are optimized by changing the control parameters, *i.e.*, (R_{mn}, Z_{mn}) by using a non-linear optimization method. The guiding center orbits of charged particles in stellarators are determined by the absolute value of the magnetic field in the Boozer coordinates [3.1-3,4], therefore the spectrum of magnetic field strength B_{mn} in the Boozer coordinates are important. If the magnetic field strength in this coordinate system, B, is axisymmetric, *e.g.* it depends on only the θ, the guiding center orbits in this coordinates also become axisymmetric. This configuration is called as a QA system, because the geometry of plasma boundary is three dimensional, however, in the boozer coordinates the particle orbit becomes axisymmetric and the good particle confinement property like tokamaks can be achieved.

As the post CHS project, the QA device, CHS-qa, was designed in NIFS [3.1-5]. The parameters of this device were as follows: Toroidal periodic number N_p is 2, the toroidal magnetic field strength B_t is 1.5 T, the major radius R is 1.5 m, and the aspect ratio A_p is 3.2, which is called as the 2b32 configuration. This configuration was designed to have a good QA property with good magnetic well and ballooning mode stability. Based on this configuration, new QA configuration is designed for the CFQS. Toroidal periodic number N_p of 2, the toroidal magnetic field strength B_t of 1.0 T, the major radius R is 1.0 m are chosen for the CFQS. From the engineering point, the same low aspect ratio of the CHS-qa is not easy to realize, so the plasma size is shrunk and A_p of 4 is selected. In Fig. 3.1-1, the equilibrium of vacuum magnetic surface calculated by VMEC code. The R_{mn}, Z_{mn} for the CFQS are shown in Table 3.1-1. The radial profile of the rotational transform and the magnetic well are shown in Fig. 3.1-2. The profile of rotational transform is characterized by low shear, and the magnetic well property is realized in the all radial region.
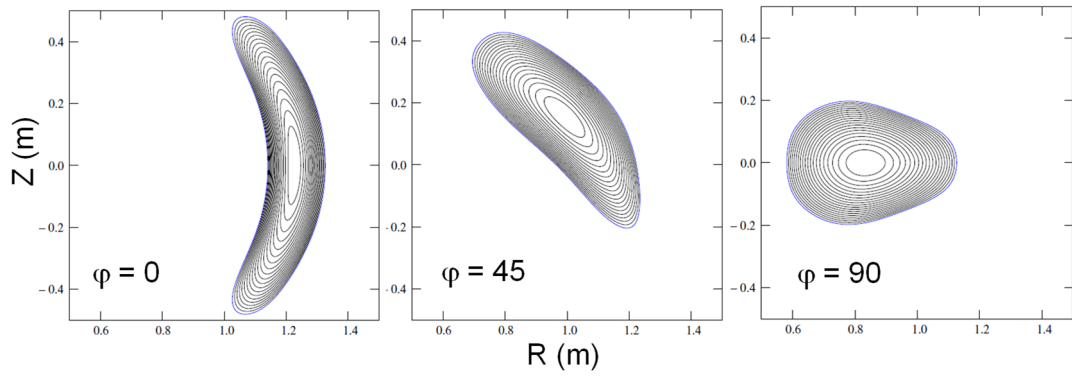
Fig. 3.1-1   CFQS vacuum magnetic surface calculated by VMEC code. Cross sections at toroidal angle of 0, 45, 90 degrees are shown.
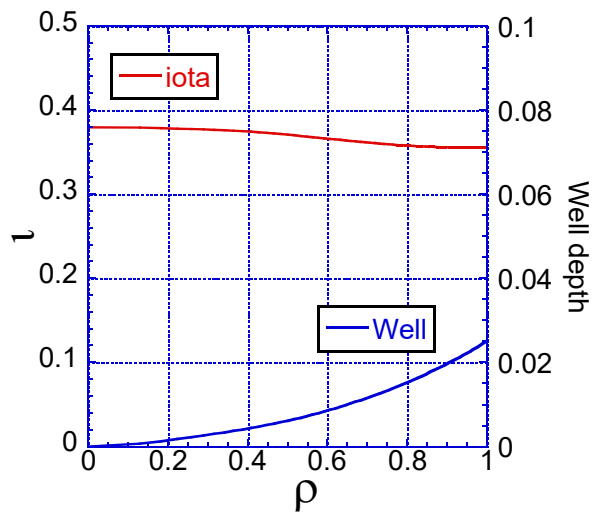

Fig. 3.1-2 Radial profiles of the rotational transform and magnetic well.

Table 3.1-1   Fourier components of R_{mn}, Z_{mn} for the CFQS boundary surface

m	n	Rmn	Zmn
0	0	1.000000E+00	0.000000E+00
0	1	1.391875E-01	-1.041401E-01
0	2	3.510066E-03	-2.047598E-03
0	3	-1.013876E-04	1.642899E-03
0	4	-9.175025E-05	1.845669E-05
1	-4	2.798909E-05	6.083008E-05
1	-3	-8.309604E-04	-1.061025E-03
1	-2	5.350281E-04	-1.240619E-03
1	-1	3.272968E-02	3.765426E-02
1	0	1.980512E-01	3.153157E-01
1	1	-1.190292E-01	1.059881E-01
1	2	-9.839016E-03	1.600162E-02
1	3	-1.036865E-04	-1.235699E-03
1	4	-1.774901E-04	-1.233294E-05
2	-4	-1.276662E-05	1.619552E-05
2	-3	-2.212222E-04	-1.655420E-04
2	-2	2.659139E-03	9.708512E-04
2	-1	5.392748E-03	3.943360E-03
2	0	2.368458E-02	5.220414E-03
2	1	4.800571E-02	1.879457E-02
2	2	1.418504E-02	-1.281654E-02
2	3	6.331471E-04	3.229137E-03
2	4	3.216150E-04	-3.067359E-05
3	-4	-2.244352E-05	-2.337868E-05
3	-3	2.247393E-06	7.071358E-05
3	-2	1.535243E-04	-7.055294E-05
3	-1	2.756543E-03	8.833038E-04
3	0	-3.334046E-03	3.224783E-03
3	1	-7.588701E-03	-6.650261E-03
3	2	-5.415940E-03	-2.327107E-03
3	3	-1.395157E-03	2.106916E-03
3	4	3.497018E-04	-6.340033E-04
4	-4	-1.132392E-05	4.601234E-06
4	-3	2.972533E-05	2.318047E-05
4	-2	-5.763365E-06	-6.467228E-05
4	-1	-8.356260E-05	-6.036524E-05
4	0	2.323114E-05	7.077580E-04
4	1	1.594329E-03	-9.755319E-04
4	2	-1.043988E-03	-2.935019E-03
4	3	-3.632249E-05	1.253345E-03
4	4	8.926982E-05	-2.034287E-04

5	-4	-1.660390E-06	-3.428524E-06
5	-3	2.634658E-06	4.226553E-06
5	-2	2.735705E-06	-5.476804E-07
5	-1	2.253818E-05	-1.345821E-05
5	0	-6.240069E-05	9.560246E-05
5	1	2.985376E-04	3.224349E-04
5	2	2.590860E-04	-7.446490E-05
5	3	2.474033E-04	2.527979E-04
5	4	9.280067E-05	-1.552233E-04
6	-4	1.525797E-05	-1.628272E-05
6	-3	-3.190926E-06	8.024808E-06
6	-2	7.765667E-06	-1.349779E-06
6	-1	-6.667636E-06	3.234683E-05
6	0	-4.959176E-05	-2.079634E-04
6	1	2.254973E-04	4.967132E-04
6	2	-1.654727E-04	-2.109075E-04
6	3	4.065117E-06	1.641132E-04
6	4	-1.144226E-05	-2.856708E-05
7	-4	-1.117052E-05	4.973842E-06
7	-3	-2.019870E-06	2.080768E-06
7	-2	1.753082E-06	9.119779E-07
7	-1	8.999813E-06	7.420079E-06
7	0	-2.983144E-05	-4.351131E-05
7	1	7.571942E-06	1.951069E-05
7	2	1.239090E-04	1.100027E-04
7	3	-4.699164E-05	-6.161755E-05
7	4	3.831545E-05	5.227709E-05

References

[3.1-1] J. Nuhrenberg, R. Zille, physics Letters **A 129** (1988) 113.

[3.1-2] S. P. Hirshman, J. C. Whitson, Physics of Fluids **26** (1983) 3553.

[3.1-3] A. H. Boozer, Physics of Fluids **23** (1980) 904.

[3.1-4] A. H. Boozer, Physics of Fluids **24** (1981) 1999.

[3.1-5] S. Okamura *et al*., Nuclear Fusion **41** (2001) 1865.

3.2 QA-ness

As stated above, the guiding center drift orbit is determined by the absolute value of B in the Boozer coordinates, because in the guiding orbit equation only the absolute value of B appears and the vector components of B do not appear. The Fourier components of the CFQS magnetic field in the Boozer coordinates are shown in Fig. 3.2-1. The toroidal ripple component, B_{10} is dominant for the good QA property. The contour map of magnetic field strength in the toroidal and poloidal angle plane is shown in Fig. 3.2-2.

Due to the QA property, the bootstrap current is driven by the neoclassical effect. The bootsj code can give us the neoclassical bootstrap current in the collision less limit [3.2-1]. With the bootsj code, the neoclassical bootstrap current is estimated for the CFQS. Fig. 3.2-3 shows the dependency of the neoclassical bootstrap current on the volume-averaged plasma beta $<\beta>$. Here, low-density case (n_{e0} =1.0 × 10^{19} m^{-3}, T_e = 10 T_i), and high-density case (n_{e0} =2.0 × 10^{19} m^{-3}, T_e = T_i) are considered. Radial profiles for density and temperature are assumed to be parabolic, $n_e \propto (1-\rho^2)$ and T_e, $T_i \propto (1-\rho^2)$. For the beta scan, n_e is fixed, and T_e, and T_i are changed. When $<\beta>$ reaches 1 %, the neoclassical bootstrap current of 30 kA is expected. For low-density case, the change of the rotational transform profile is shown in Fig. 3.2-4. The MHD instability, such as kink mode, will be studied in the future.

The neoclassical transport in the $1/\nu$ regime can be estimated by the NEO [3.2-2] code. By this code, so called the effective helical ripple ε_{eff}, is estimated and the neoclassical diffusion coefficient D is proportional to $v_d \varepsilon_{\text{eff}}^{3/2}/\nu$. Here, v_d and ν are the drift velocity and the collision frequency, respectively. The radial profile of $\varepsilon_{eff}^{3/2}$ are shown in Fig.3.2-5. The magnetic configurations of the CFQS in this figure are calculated with VMEC, on fixed boundary and free boundary condition. The $\varepsilon_{eff}^{3/2}$ of the CFQS are two or three order less than that of the CHS. Up to β of 1.5%, the good neoclassical confinement property is kept.
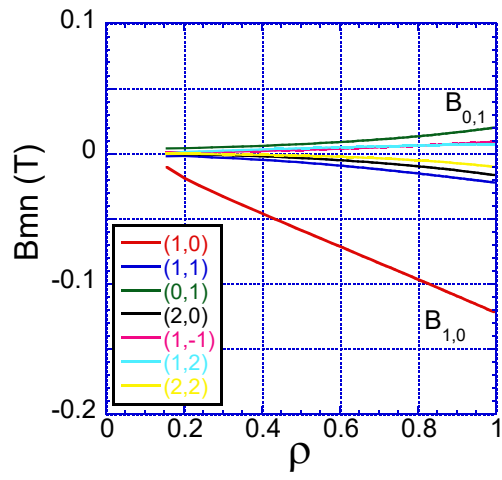
Fig. 3.2-1 Fourier spectrum of B in the Boozer coordinates.
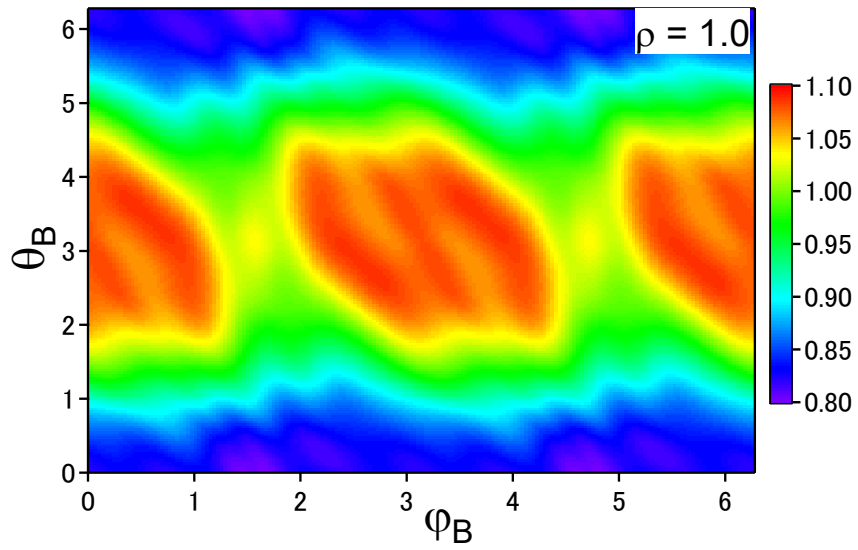

Fig. 3.2-2   The contour map of the magnetic field B in the Boozer coordinates on the outer most magnetic surface of the CFQS.
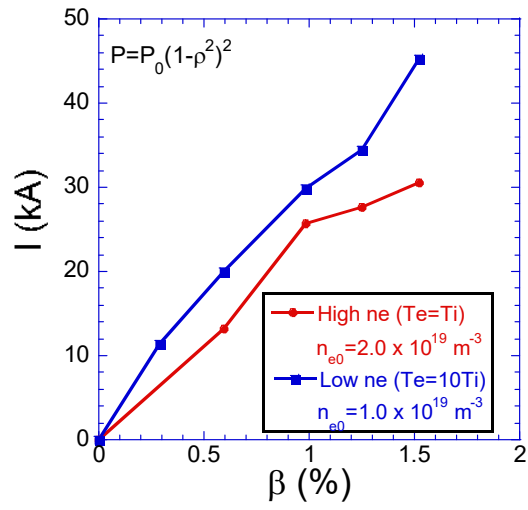
Fig. 3.2-3 Dependency of the neoclassical bootstrap current on the volume-averaged plasma beta.
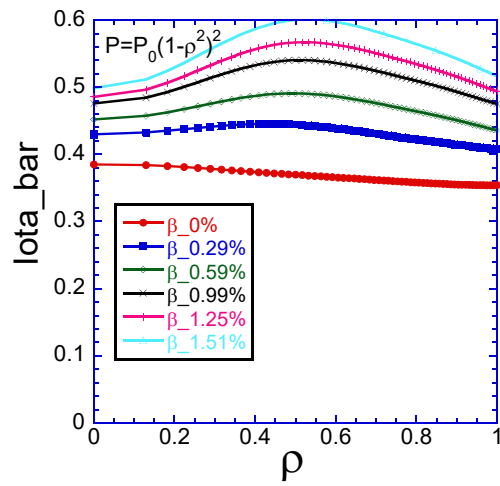

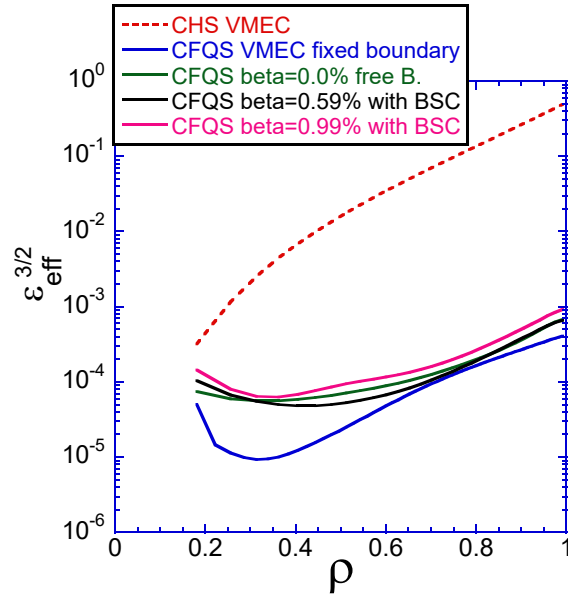Fig. 3.2-4 Radial profile of the rotational transform considering the neoclassical bootstrap current.

Fig. 3.2-5   Radial profiles of the effective helical ripple, $\varepsilon_{\text{eff}}^{3/2}$. In the latter three cases, i.e., green, black, and pink, the free-boundary calculation result of the VMEC are used to estimate $\varepsilon_{\text{eff}}^{3/2}$.

References

[3.2-1] K. C. Shaing *et al*., Phys. Fluids **B 1** (1989) 148.

[3.2-2] V. V. Nemov *et al*., Phys. of Plasmas **6** (1999) 4622.

3.3   MHD stability

Key MHD stabilities in the design of a finite-β QA stellarator configuration are discussed in this section. Mercier stability, ballooning mode, kink mode and tear mode are investigated to determination of β limit. These four issues are not independent. The VMEC, COBRAVMEC, BOOTSJ, and TERPSICHOR codes are executed to estimate them [3.3-1~5].

References

[3.3-1] S.P. Hirshman, and J.C. Whitson, Phys. Fluids **26** (1983) 3353.

[3.3-2] A. H. Boozer, Phys. Fluids **24** (1981) 1999.

[3.3-3] K.C. Shaing *et al*., Phys. Fluids **B1** (1989) 1663.

[3.3-4] R. Sanchez *et al*., J. Comp. Physics **161** (2000) 576.

[3.3-5] C. Mercier, Nucl. Fusion **1** (1960) 47.

3.3.1   Mercier stalibity

The Mercier criterion is a necessary condition for the stability of localized interchange modes in a toroidal plasma, according to the ideal MHD model [3.3.1-1]. These modes are localized around mode-

rational surfaces, where the parallel wave vector vanishes, so as to minimize the magnetic field line bending energy. The driving force for these modes is the pressure gradient across surfaces with average unfavorable curvature. The Mercier stability criterion involves competition between the driving force and the stabilizing effect of magnetic shear. The Mercier criterion can be written as summation of four terms, corresponding to the contributions coming from the shear, magnetic well, net currents, and geodesic curvature, respectively.

Once the magnetic field coils have been designed it needs to be established that these coils actually reproduce the desired MHD equilibrium and its relevant properties. For this purpose, free boundary equilibria were computed for volume averaged $\langle\beta\rangle=0$ and $\langle\beta\rangle = 2$ %. The cross sections of the plasma boundary obtained from free boundary equilibrium calculations (*i.e.* using the external magnetic field generated by the modular coils described in Sec. 4.2) are obtained. A comparison of the flux surfaces of the vacuum field and the $\langle\beta\rangle = 2$ % solution (both VMEC) is presented in Fig. 3.3.1-1. It is observed that the Shafranov shift of the axis exists. The variation of Shafranov shift with $\langle\beta\rangle$ is displayed in the Fig. 3.3.1-2. When $<\beta>$ equals to 1.7%, the Shafranov shift is about the half of the minor radius.
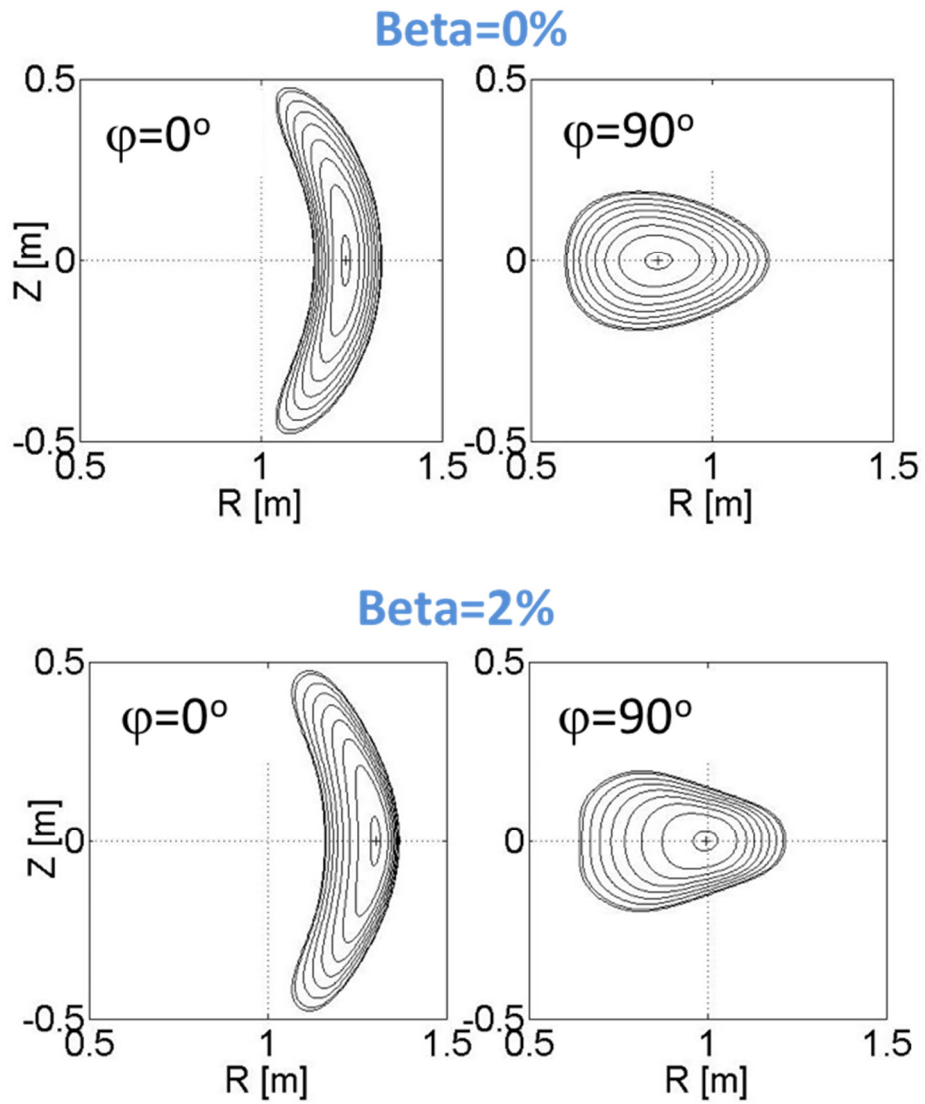
Fig.3.3.1-1 Poloidal cross sections of the free-boundary equilibrium calculated by VMEC code with the plasma pressure free (top panel) and volume averaged $\beta = 2$ % (bottom panel).
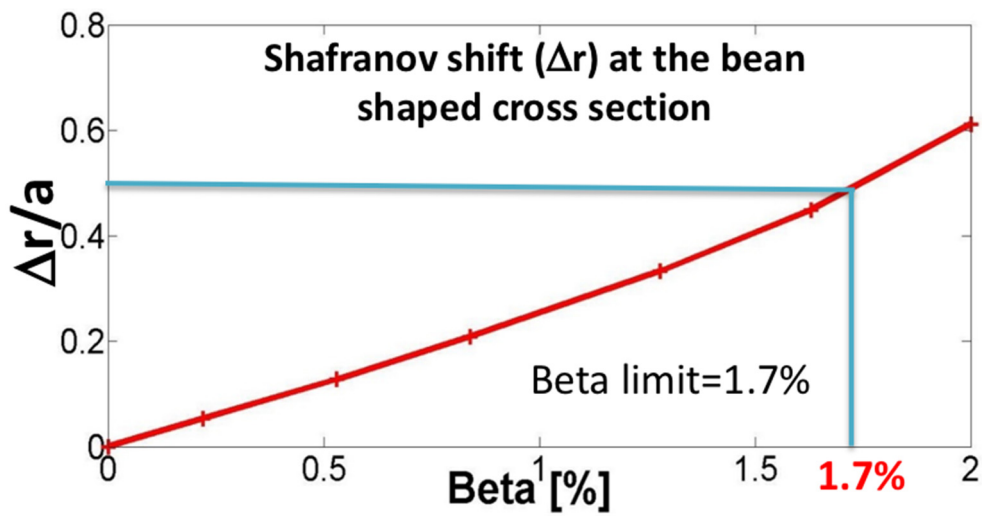
Fig.3.3.1-2   Shafranov shift vs the volume averaged β at the bean shaped cross section.

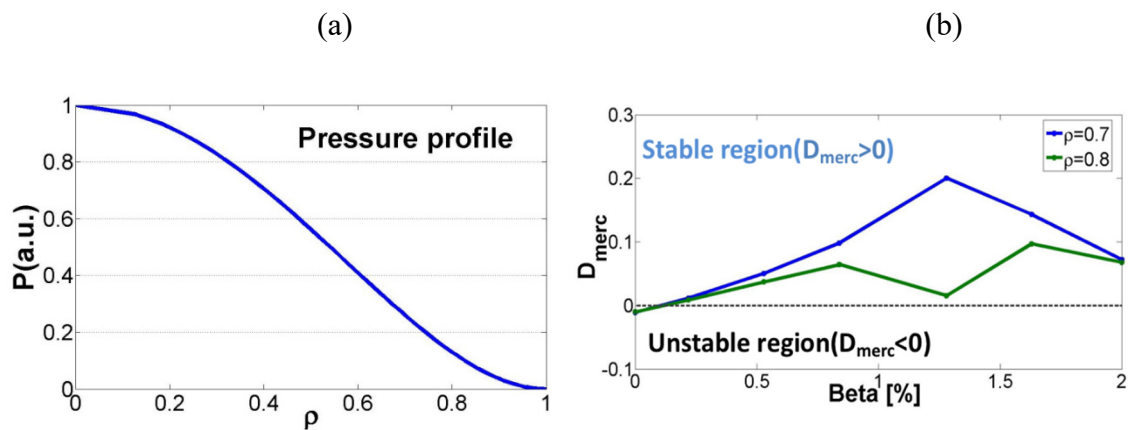(a)   (b)

Fig.3.3.1-3   (a)Assumed radial profile of plasma pressure (quadratic form) and (b) the variation of Mercier stability with the volume-averaged β at two different radial position, i.e., ρ=0.7 and 0.8.
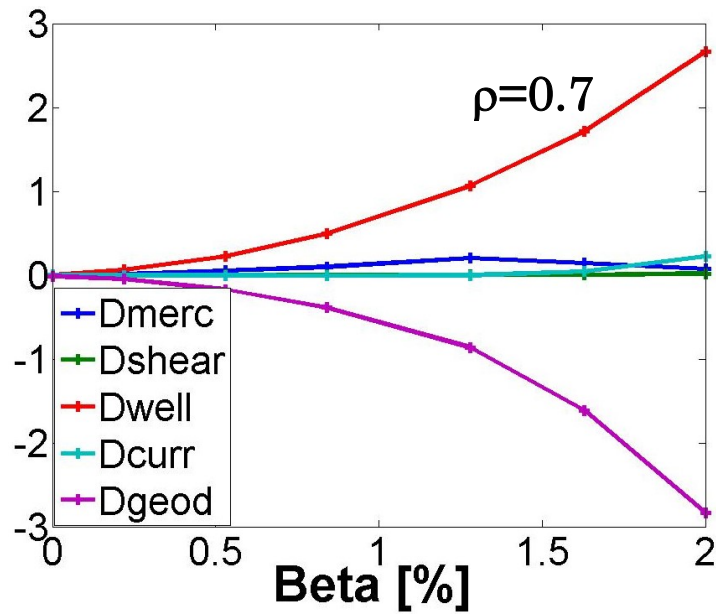
Fig.3.3.1-4   Shear term, well term, current term and geodesic curvature term versus the volume-averaged

beta at radial position $\rho = 0.7$, showing stabilization from the contribution of magnetic well.

The Fig.3.3.1-3. (a) gives the input profile of plasma pressure $P(\rho)=P_0(1+\rho^2)^2$ for the VMEC calculation with the unfixed plasma boundary and Fig.3.3.1-3 (b) displays the variation of Mercier stability with the volume-averaged beta at two different radial positions, i.e., $\rho=0.7$ and 0.8. It shows that up to $<\beta>=2$ %, the interchange mode is stable. The Mercier criterion can be expressed as $D_{merc}=D_{shear}+D_{well}+D_{curr}+D_{geod}$, where these terms correspond to the contributions coming from the shear, magnetic well, net currents, and geodesic curvature, respectively. In the Fig.3.3.1-4, the variation of these four terms versus the volume-averaged beta at radial position $\rho=0.7$ is shown, which depicts the stabilizing effect from the magnetic well ($D_{well}>0$) is stronger than the destabilizing effect from the geodesic curvature term ($D_{geod}<0$).

References

[3.3.1-1] C. Mercier, Nucl. Fusion **1** (1960) 47.

3.3.2   Ballooning mode

A principle aim of stellarator research is to understand the physical mechanisms that limit the plasma stored energy. The expectation is that pressure driven instabilities will be excited as the plasma energy increases relative to the magnetic energy. Since one of the advantages of stellarators is the avoidance of current limiting instabilities, pressure driven instabilities may be critical in limiting stellarator operation. In theoretical studies of particular configurations, local criterion deduced from ideal MHD ballooning theory is often used to predict the plasma pressure limits of stellarators.

A feature related to second stability, which we call 'self-stabilization' for large pressure gradients after Ref. [3.3.2-1] has been observed in various stellarator experiments [3.3.2-2,3]. In these results, geometrical deformations associated with the Shafranov shift result in configurations which are stable with respect to Mercier modes as the plasma pressure increases. In this section, the COBRAVMEC code is utilized to calculate ideal ballooning stability for VMEC equilibria.
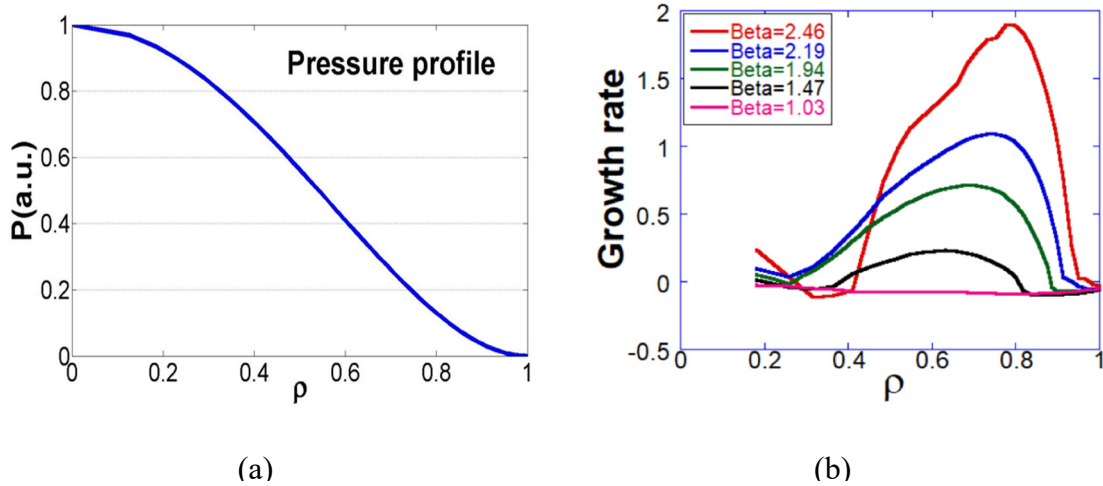

(a)   (b)

Fig.3.3.2-1   (a)Assumed radial profile of plasma pressure (quadratic form), (b) Ballooning growth rates from COBRAVMEC as a function of the normalized flux for various volume-averaged beta, indicating the first stability boundary.

For the reference configuration, a quadratic pressure profile, $P(\rho)=P_0(1+\rho^2)^2$ was chosen. Ballooning growth rates as a function of the normalized flux label, ρ, are shown in Fig.3.3.2-1(a). As the plasma pressure increases, the plasma first becomes ballooning unstable at 1.03%, displayed in Fig.3.3.2-1(b). The region of instability grows until 3%, where a region of second stability appears as shown in Fig.3.3.2-2.
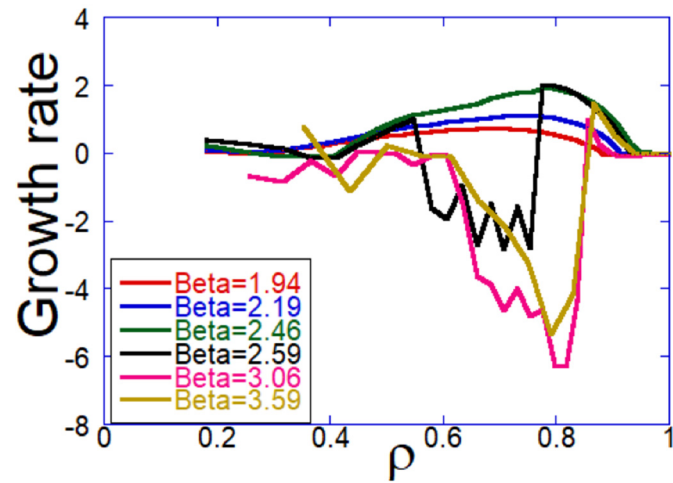
Fig.3.3.2-2　Ballooning growth rates from COBRAVMEC as a function of the normalized flux for various volume-averaged beta, indicating the onset of second stability.

References

[3.3.2-1] R. D. Hazeltine and J. D. Meiss, Plasma Confinement (Addision Wesley, Redwood City, 1992), pp. 309–312.

[3.3.2-2] C. C. Hegna and S. R. Hudson, Phys. Plasmas **9** (2002) 2014.

[3.3.2-3] R. Hudson and C. C. Hegna, Phys. Plasmas **10** (2003) 4716.

3.3.3 Kink mode

In a QA configuration, larger amount of neoclassical bootstrap current (BSC) flows and increases rotational transform due to its tokamak-like magnetic field structure. Therefore, the onset of an external kink mode should be carefully assessed in the ideal MHD stability analysis including plasma current. If a BSC profile is given, global low-n ideal MHD stability can be calculated with the TERPSICHORE code [3.3.3-1]. Since such a calculation for the CFQS configuration has not been performed yet, a typical example for the CHS-qa configuration [3.3.3-2] is described below.

A self-consistent BSC profile for a CHS-qa reference configuration has been calculated with SPBSC code [3.3.3-3]. We have solved finite beta equilibria including BSC assuming the fixed density and temperature profiles for three representative cases; (A) $n_e = 1.0 \times 10^{20}$ m^{-3}, $T_e = 1.04$ keV, (B) $n_e = 0.2 \times 10^{20}$ m^{-3}, $T_e = 5.2$ keV, (C) $n_e = 1.5 \times 10^{20}$ m^3, $T_e = 1.04$ keV [3.3.3-4]. The resulting rotational transform is shown in Fig. 3.3.3-1 as a function of the normalized toroidal flux. Then the ideal global MHD stability has been analyzed with artificially changing the total parallel current while keeping its profile. The dependences of the most unstable eigenvalues on the total current are shown in Fig. 3.3.3-2 for the three representative cases. The onset of destabilization above 150 kA in the cases A and B clearly corresponds to the crossing of the edge rotational transform beyond 0.5 and 0.6. The associated amplitude of the dominant perturbation mode increases toward the edge, which clearly indicates the characteristics of an external kink instability. On the other hand, the global mode is kept stable up to 250 kA for the case C which has a different current profile. It indicates the possibility of stabilization of the external kink mode by controlling the current profile in a QA configuration.
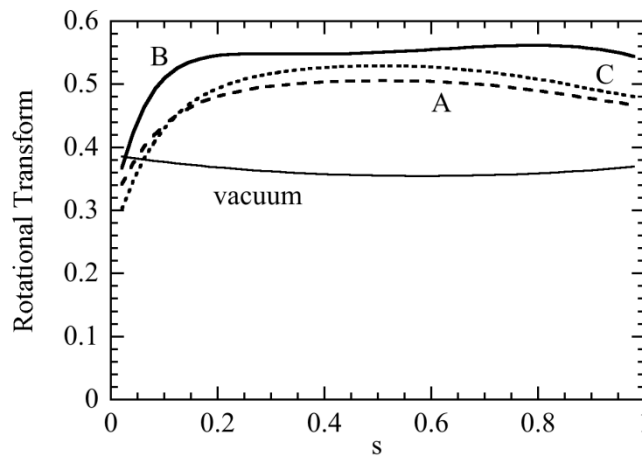

Fig. 3.3.3-1   Radial profiles of rotational transform for the three representative cases.
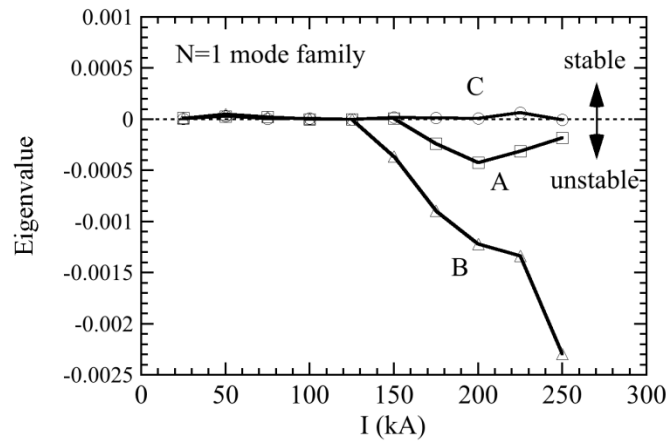
Fig. 3.3.3-2   Most unstable eigenvalues as functions of total current for the three representative cases.

References

[3.3.3-1] D.V. Anderson *et al*., Int. J. Supercompt. Appl. **4** (1990) 34.

[3.3.3-2] C. Suzuki *et al*., J. Plasma Fusion Res. SERIES **6** (2004) 519.

[3.3.3-3] K.Y. Watanabe *et al*., Nucl. Fusion **35** (1995) 335.

[3.3.3-4] M. Isobe *et al*., J. Plasma Fusion Res. SERIES **5** (2002) 360.

3.3.4　Tearing mode

The tearing mode stability, which is determined by Δ', is analyzed for existing singular point in the plasma region with the same code described in Ref. 3.3.4-1 for the CHS-qa configuration [3.3.4-2]. Here, we consider a pressure less plasma in the cylindrical system with parabolic net toroidal current density J_z and check whether the tearing mode is stable or not at the rational surface of interest with increasing J_z. The tearing mode is stable for rational surfaces n/m=2/5, 3/7, 4/9, and 1/2 in the core domain (see Fig. 3.3.4-1) but the analyses indicate that it becomes unstable when singular point is in outer region (r/a>0.6) for n/m=1/2.
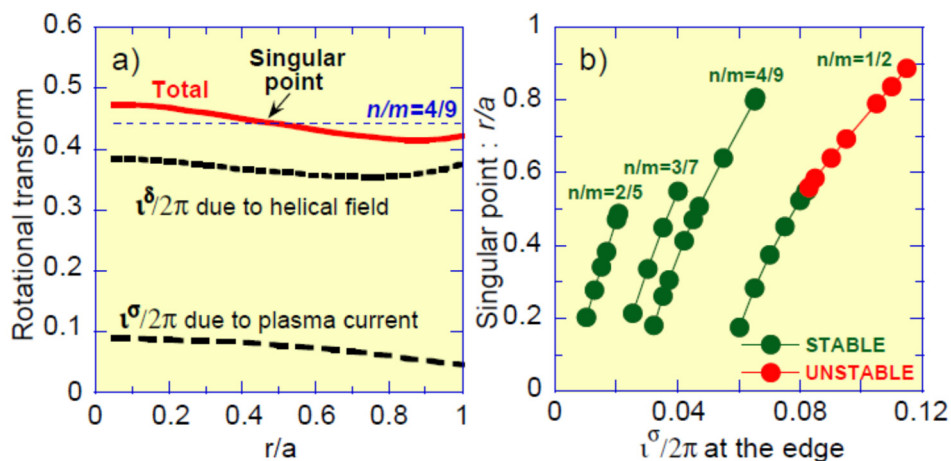

Fig. 3.3.4-1　(a) An example of rotational transform profile for tearing mode analysis for $n/m = 4/9$, and (b) Δ' analysis results are shown.

References

[3.3.4-1] K. Matsuoka *et al*., Nuclear Fusion **17** (1977) 1123.

[3.3.4-2] M. Isobe *et al*., 28th EPS Conference on Controlled Fusion and Plasma Physics., Funchal, Portugal, 18-22. June 2001, ECA Vol. **25A** (2001) 761.

3.3.5   Alfven mode

To further study the MHD stability in CFQS configuration, we perform the MHD simulation by MEGA code without energetic particles. The module and equations of this code are same as that of reference [3.3.5-1,2]. The plasma pressure profile is calculated by HINT2 code in Fig. 3.3.5-1 (b) with the core averaged pressure value being 3.7×10^{-3}[3.3.5-3]. The random initial perturbation and small normalized dissipation coefficients (=1×10^{-8}) are adopted. From the Fig. 3.3.5-2, we can find that in this configuration the MHD mode is stable with the negative growth rate defined by $\gamma = d(\ln E_k)/dt$.
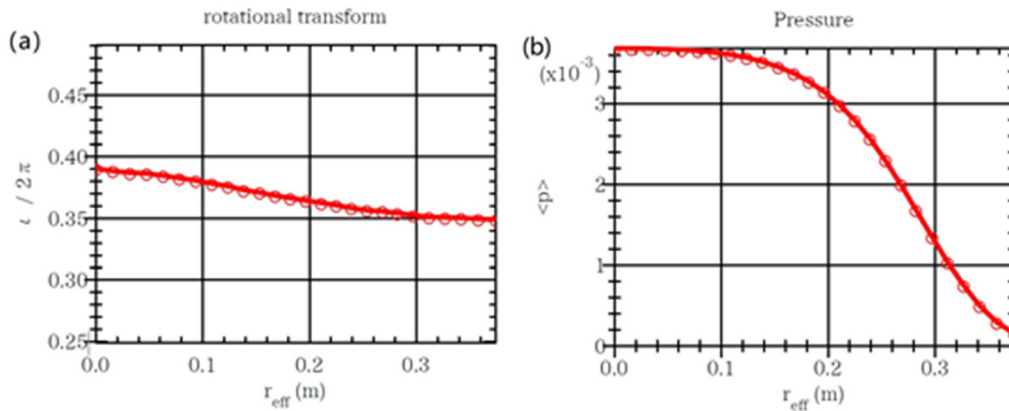

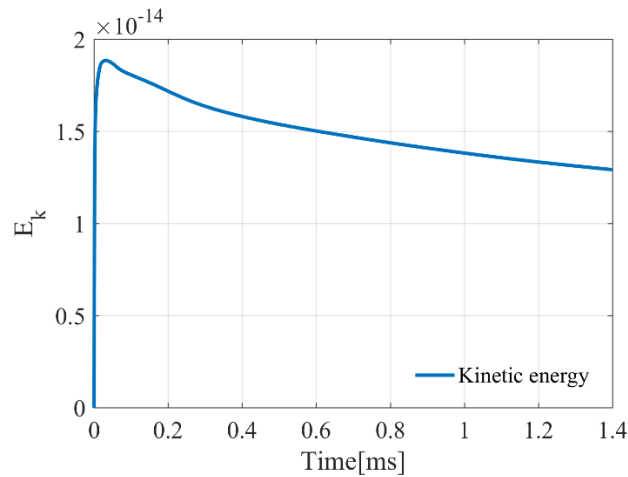Fig. 3.3.5-1   Equilibrium profiles for (a) iota and (b) plasmas pressure

Fig. 3.3.5-2 Time evolution of kinetic energy

[3.3.5-1] Y. Todo, Nakajima N., Sato M., and Miura H. 2010 Plasma Fusion Res.**5** S2062.

[3.3.5-2] Y. Todo, *et al*, Phys. Plasmas **24** (2017) 081203.

[3.3.5-3] Y. Suzuki, *et al*, Nucl. Fusion **46** (2006) L19–L24.

3.4 Micro instability and anomalous transport

3.4.1 Maximum-J

The turbulent fluctuation suppression in the CFQS has got emphasized considerably. The suppression of the turbulent transport due to the sheared flow induced fluctuation decorrelation has been widely investigated, theoretically, leading to the significant progress in the understanding of the improved confinement regime. The other possible mechanism for turbulent suppression has been proposed based on the stabilization of microinstabilities. Several kinds of microinstabilities appear when directions of the diamagnetic drift and ∇B drift (B is the magnetic field strength) are in the same direction for trapped particles [3.4.1-1, 2]. In an axisymmetric configuration, the relevant drift is in the toroidal direction (toroidal precession). The velocity of the toroidal precession can be expressed in terms of the second adiabatic invariance J [3.4.1-3]. Also, the stability condition for microinstabilities is derived [3.4.1-4] with a scalar plasma pressure P as

$$\nabla P \cdot \nabla J > 0,$$

which is frequently called the Maximum-J condition; it reduces to $dJ/dr < 0$ for a usual pressure gradient with $dP/dr < 0$. This indicates that microinstabilities can be stabilized or suppressed if the toroidal precession of trapped particles is in a favorable ($dJ/dr < 0$) direction.

Orbits of blocked or helically trapped particles: These particles are located in the region of phase space near the locally trapped- passing boundary. These particles may be regarded as locally trapped for a few bounces but they are able to de-trap collisionlessly. A blocked particle's trajectory is not restricted to a single toroidal segment but extends to neighbouring sections. Such particles are also called transitioning [3.4.1-5]. An illustration of these three types of orbits and a comparison with particle orbits in an axisymmetric plasma is given in Fig. 3.4.1-1.

The contour plot of J is shown as a function of the minor radius and the toroidal angle in the Fig. 3.4.1-2. The calculation of J is made by following the particle orbits starting from the outboard side of the torus with different toroidal angles. $\zeta_N = 0$ corresponds to the vertically elongated cross section and $\zeta_N = 0.5$ to the horizontally elongated cross section. When B_{ref} equals 0.95 T, there is no Maximum-J region. Whereas B_{ref} equals 0.97T, the Maximum-J region comes up at the core area.

References

[3.4.1-1] H. P. Furth and M. N. Rosenbluth 1969 Proc. Conf. 3rd Int. on Plasma Physics and Controlled Nuclear Fusion Research (Novosibirsk, 1968) vol. **1** (Vienna: IAEA) p 821.

[3.4.1-2] B. B. Kadomtsev and O. P. Pogutse 1970 Reviews of Plasma Physics vol. **5** (New York, London: Consultants Bureau) p 249.

[3.4.1-3] B. B. Kadomtsev and O. P. Pogutse Nucl. Fusion **11** (1971) 67.

[3.4.1-4] R. J. Hastie *et al.*, Ann. of Phys. **41** (1967) 302.

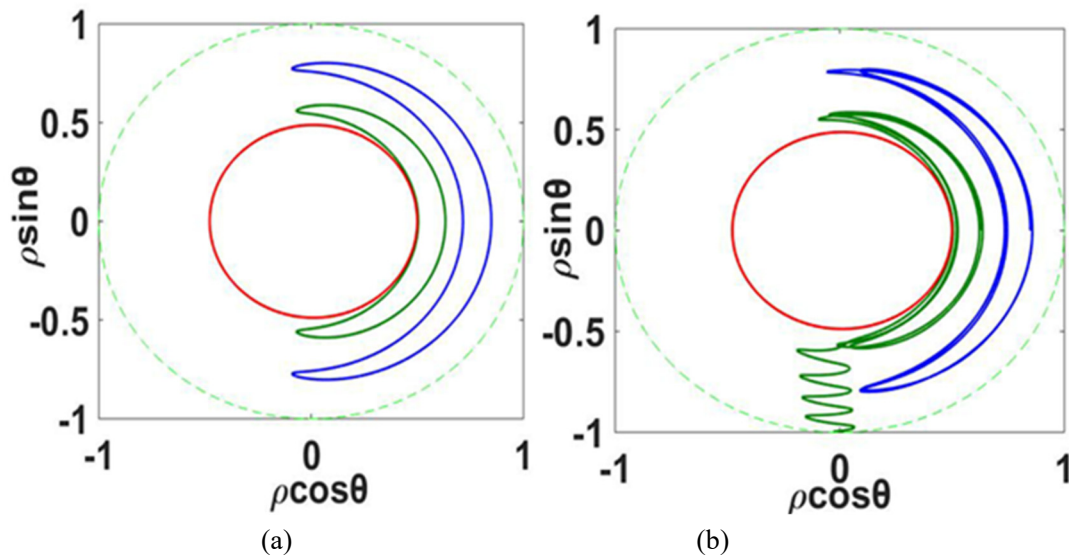[3.4.1-5] C. D. Beidler *et al.*, Phys. Plasmas **8** (2001) 2731.

Fig. 3.4.1-1   Examples of the main orbit topologies in an axisymmetric versus a CFQS equilibrium. The dashed line represents the last closed flux surface in each case. (a) E=1 Mev, passing particles (red, B_{ref}=1.5) and trapped particles (green, B_{ref}=0.94 and blue, B_{ref}=0.98) orbit in axisymmetric equilibrium. (b) E=1 Mev, passing particles (red, B_{ref}=1.5), drifted particles (green, B_{ref}=0.94) and trapped particles (blue, B_{ref}=0.98) orbit in the CFQS equilibrium.

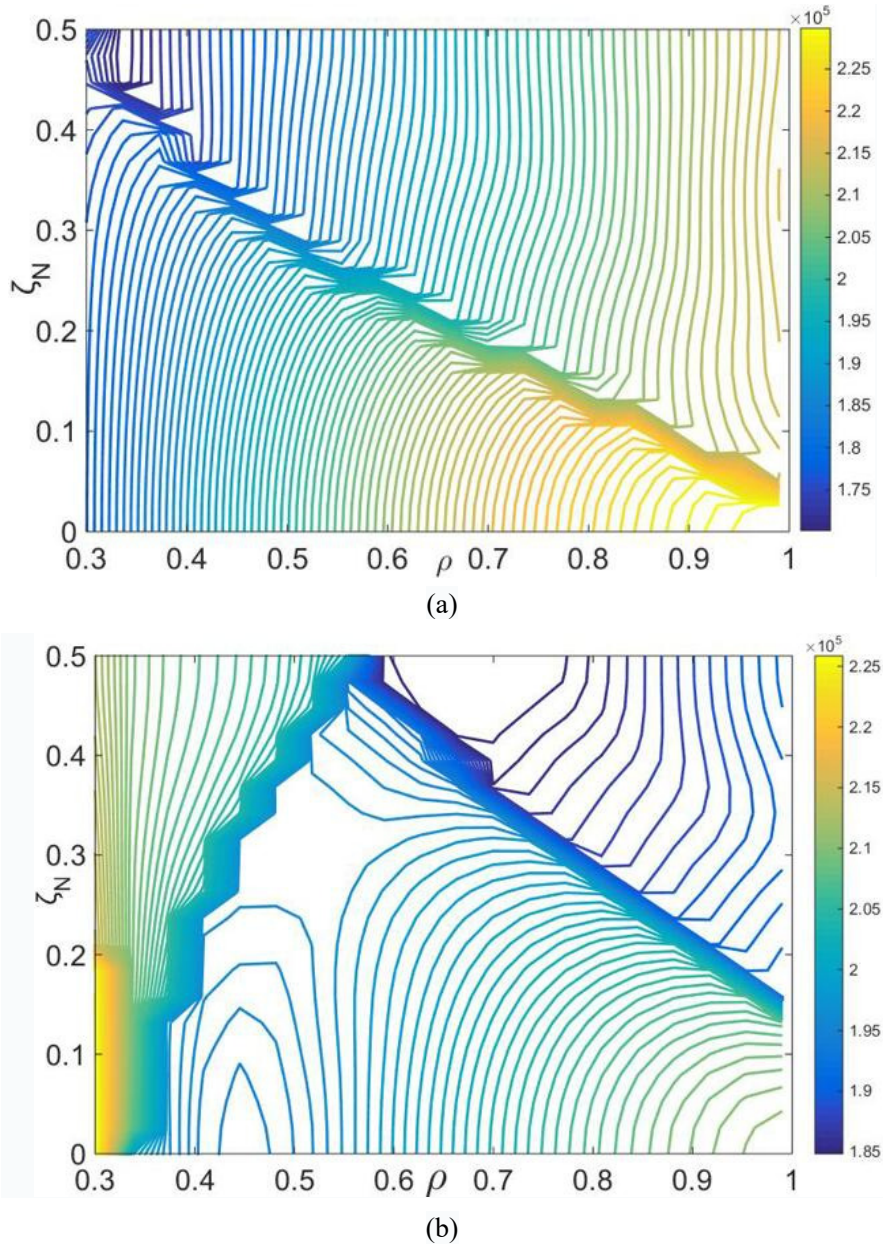Fig. 3.4.1-2   Contour J on the (ρ, ζ_N) plane (a) B_{ref} equal to 0.95 T, without Maximum-J region (b) B_{ref} equal to 0.97 T, with Maximum-J region.

3.4.2   Ion temperature gradient mode

The linear ion temperature gradient(ITG) driven instability is examined by means of the electromagnetic gyrokinetic Vlasov simulations with GKV[3.4.2-1], where a local flux-tube at the mid-minor radius of $\rho=0.5$ in the vacuum equilibrium is considered. An axisymmetric limit with the same rotational transform, the magnetic shear, and the aspect ratio is compared to identify the impact of non-axisymmetric geometry on the microinstability properties, where the circular poloidal cross section is assumed for the simplicity. The linear growth rate spectra of the ITG mode is shown in Fig. 3.4.2-1, where the electrons are assumed to be adiabatic here. It is found that the CFQS has more unstable ITG modes with higher growth rate $\gamma R_{ax}/v_{ti}$ in a wider range of the wavenumber space $k_\theta \rho_{ti}$, compared with that in the axisymmetric limit[3.4.2-2]. The difference is mainly associated with the geometric structures appearing in the squared perpendicular wavenumber $(k_\perp \rho_i)^2$, which provides the finite Larmor radius(FLR) stabilization of the ITG modes. The nonlinear ITG turbulence simulation has also been carried out. As shown in Fig. 3.4.2-2(a), we observe that the saturated turbulent transport level Q_i/Q_{GB} in the CFQS is comparable or less than that in the axisymmetric limit. It is also found from Fig. 3.4.2-2(b) that the CFQS indicates a relatively stronger zonal-flow generation W_{ZF}/W_{total}, in comparison to the axisymmetric limit. The magnetic fluctuations effects in the finite β cases, which can destabilize the kinetic ballooning modes(KBM) and microtearing modes(MTM), will be investigated in the future works.
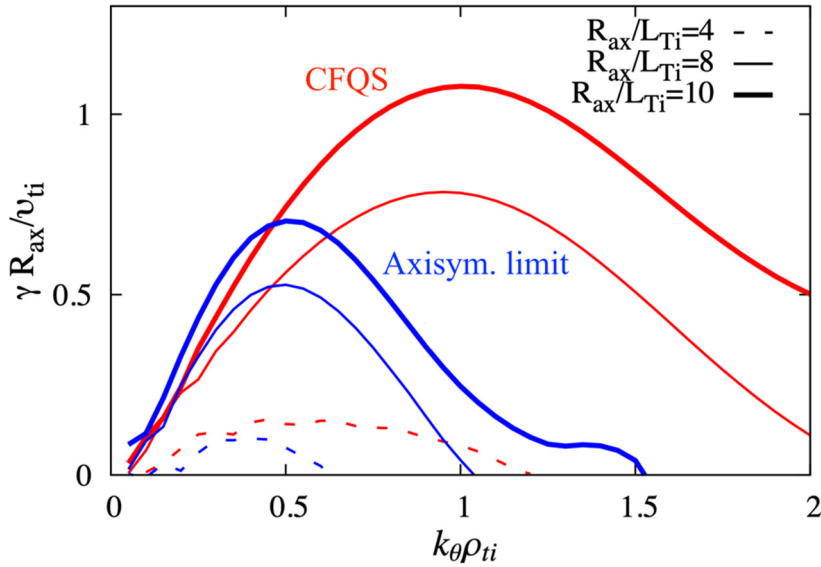

Fig. 3.4.2-1   Linear growth rate spectra for the ITG mode in CFQS and the axisymmetric limit (Axisym. limit) for several cases of the normalized ion temperature gradient parameters R_{ax}/L_{ti} = - $R_{ax}d(\ln T_i)/dr$.
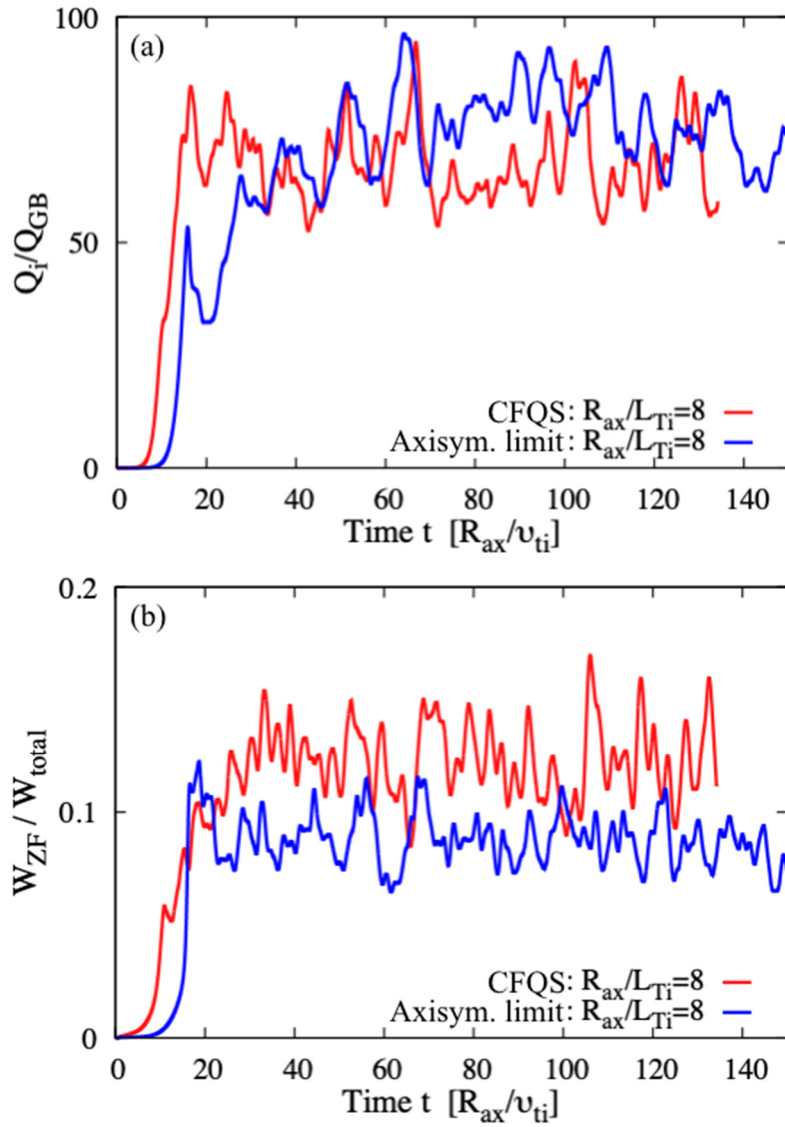
Fig. 3.4.2-2　Nonlienar GKV simulation results of (a)the ion turbulent heat flux Q_i/Q_{GB} and (b)the zonal flow energy normalized by the total energy W_{ZF}/W_{total} in the ITG-driven turbulence in the CFQS and the axisymmetric limit(Axisym. limit).

References

[3.4.2-1] T. –H. Watanabe and H. Sugama, Nucl. Fusion **46** (2006) 24.

[3.4.2-2] M. Nakata *et al*., "Turbulent transport and zonal flow generation in quasi-axisymmetric stellarator", The 27th International Toki Conference and the 13th Asia Pacific Plasma Theory Conference (2018).

3.5   Plasma rotation

In conventional helical devices, an impact of radial electric field on plasma confinement has extensively been investigated so far. It is one of the major issues also in a QA device because plasma rotation, which is closely related to radial electric field, can be driven more easily, and because anomalous transport can be possibly reduced by controlling plasma rotation/flow. Since the discovery of H-mode in tokamaks, the roles of shear flow on an improved confinement have been widely understood also in helical systems; e.g., high ion/electron temperature modes [3.5-1,2]. Consequently, the reduction of anomalous transport by shear flow has become a general issue in toroidal plasmas.

Unlike tokamaks, radial electric field or plasma rotation in helical devices are determined by a solution of an ambipolar condition according to the neoclassical theory. Also, toroidal plasma rotation tends to be dissipated in conventional helical systems because of larger toroidal viscosity which originates from larger toroidal ripple of magnetic field strength [3.5-3]. According to theoretical studies on tokamaks, transport barriers are established by a positive feedback mechanism that reduces the transport coefficients through the increase in local pressure gradient. Radial electric field (or plasma flow), which is strongly correlated with the local pressure gradient, is a key parameter for the mechanism mentioned above. In order to promote such spontaneous growths of shear flow and pressure gradient, plasma flow should be free from any constraints.

In conventional helical devices such as CHS, plasma mainly rotates poloidally because of larger toroidal viscosity. In this situation, Pfirsch-Schlüter-type return flow should exist so as to satisfy incompressibility, which can possibly be dissipated by helical ripple [3.5-4]. Therefore, it is quite difficult to drive high speed plasma rotation in conventional helical systems due to large parallel viscosity both in toroidal and poloidal directions. Indeed, the radial electric field strengths observed in CHS and Heliotron-E are around 100 V/cm at most. Furthermore, the scale length of the radial electric field tends to be longer, which leads to weaker shear. Consequently, tokamak-like transition phenomena relevant to edge transport barrier have never been observed so far in helical systems.

In order to establish transport barriers, a magnetic configuration should be free from any constraints of plasma flow due to parallel viscosity. This expended parameter range of plasma rotation is one of the reasons why we adopt the QA configuration, which is ideal for reducing toroidal viscosity as well as achieving low aspect ratio and incompressible flow at the same time.

In QA configuration, ripple trapped particles can be suppressed by reducing residual ripple. In such a situation, according to the neoclassical theory, confinement property is similar to that in an axisymmetric system. That is to say, values of radial electric field are never restricted by the ambipolar condition, which is a characteristic feature not found in the other optimized stellarators. As described below, the residual ripple in a QA configuration is drastically reduced in comparison with CHS.

In the earlier experiments in tokamaks and helical devices, it has been found that the plasma current, plasma rotation (or radial electric field) are well explained by the neoclassical theory, while

particle/heat transport is dominated by anomalous transport [3.5-5]. The plasma rotation interpreted by the neoclassical theory gives a good hint to study the anomalous transport. Also, it is important to study the neoclassical theory itself as it is still incomplete for non-axisymmetric systems. In addition, it would be also important to investigate whether the neoclassical theory can predict bootstrap current, toroidal viscosity and radial electric field in a QA configuration with non-axisymmetric perturbation.

Neoclassical parallel viscosity is roughly proportional to the square of the magnetic field ripple strength defined by $\gamma^2 = <(\delta B/\delta s)^2 / B^2>$, where $\delta/\delta s$ is differential with respect to the flow direction and $<>$ denotes averaging on a magnetic surface. This parameter should be quantitatively evaluated from the calculations including all of the Fourier components of the field strength B because higher order mode may largely contribute to the value of γ. Since the calculation of γ for the CFQS configuration has not been carried out yet, the results for the CHS-qa configuration [3.5-6] are shown hereafter. In principle, similar results are expected in the CFQS.
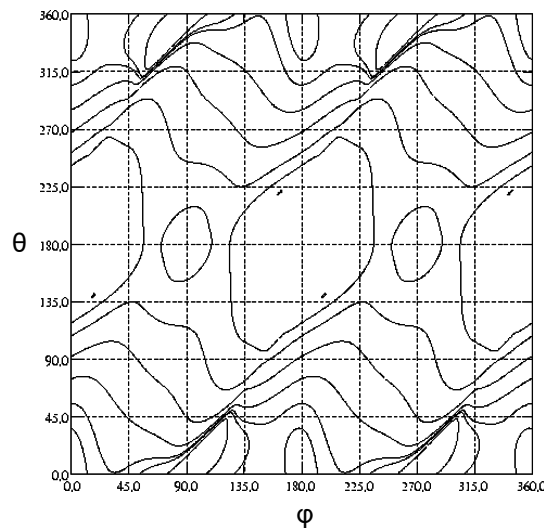

Fig. 3.5-1 Contour plot of B for the LCFS of CHS-qa (2w39) configuration.
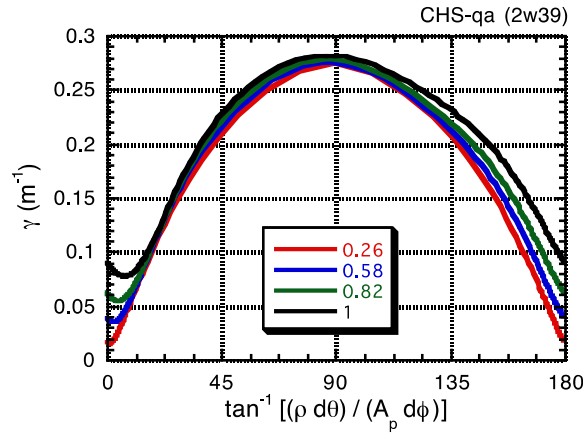
Fig. 3.5-2 Angle dependence of γ for CHS-qa (2w39) configuration.

Fig. 3.5-1 shows a contour plot of B on the last-closed flux surface (LCFS) of a reference configuration of CHS-qa (2w39). The grid data for B in cylindrical coordinates (R, Z, Φ) are constructed from the result of VMEC code calculation. Toroidal (ϕ) and poloidal (θ) angles are expressed in real coordinates, and $\theta = \tan^{-1}[(R-R_{ax})/(Z-Z_{ax})]$, where R_{ax} and Z_{ax} are R and Z values at the magnetic axis in an equal ϕ plane, respectively. This means that the effect of the excursion of the magnetic axis is ignored in the calculation. We assumed a flow direction expressed by a straight line in this ϕ-θ plane. When averaging, we fixed the angle of $\delta/\delta s$ direction with respect to the toroidal direction ($=\tan^{-1}(r\,\theta/R\,\phi)$).

Fig. 3.5-2 shows the calculated dependence of γ on the flow direction at the four different flux surfaces (normalized minor radii of 0.26, 0.58, 0.82 and 1.0). As shown, the values of γ have peaks around 90 degrees in the QA configuration, which indicates larger parallel viscosity in the poloidal direction. In the toroidal direction, γ is less than 0.1 even in the LCFS, which implies that perpendicular/anomalous viscosity plays an important role for determining toroidal rotation speed in a similar way to tokamaks. Though the effect of coil ripples is not included in the present calculation, the angle minimizing γ is not zero but 1.1~6.8 degrees unlike tokamaks, which is considered to be the effect of residual non-axisymmetric components.
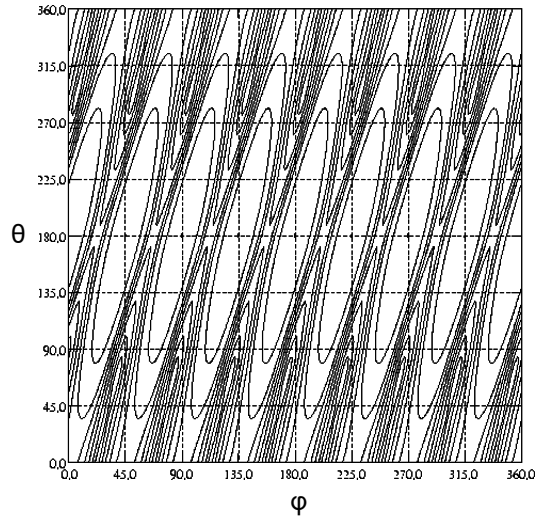
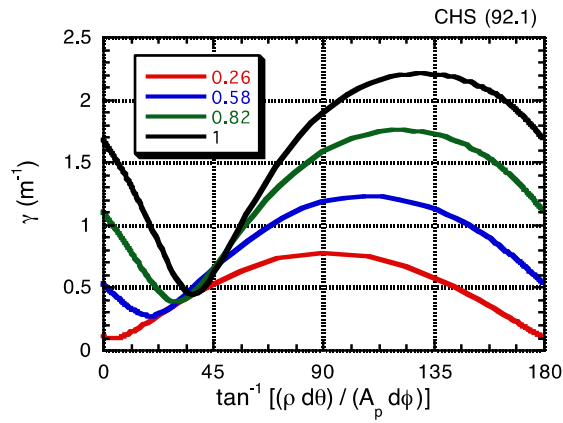Fig. 3.5-3 Contour plot of B for the LCFS of CHS (R_{ax}=92.1 cm) configuration.

Fig. 3.5-4 Angle dependence of γ for CHS (R_{ax}=92.1 cm) configuration.

For the comparison with a conventional helical device, the calculation of γ has been performed for a representative configuration of CHS. The contour of B on the LCFS and the results of the γ calculation are shown in Fig. 3.5-3 and 3.5-4, respectively, in a similar way to the CHS-qa. The angle minimizing γ is around 40 degrees, which indicates the flow tends to be driven along the helical structure (m=2, n=1) of the CHS configuration. Nevertheless, this minimum value of γ in CHS is still larger than the maximum value of γ along the poloidal direction in CHS-qa. Therefore, high speed toroidal rotation cannot be driven in CHS because of strong toroidal viscosity, as demonstrated in the previous CHS experiment.
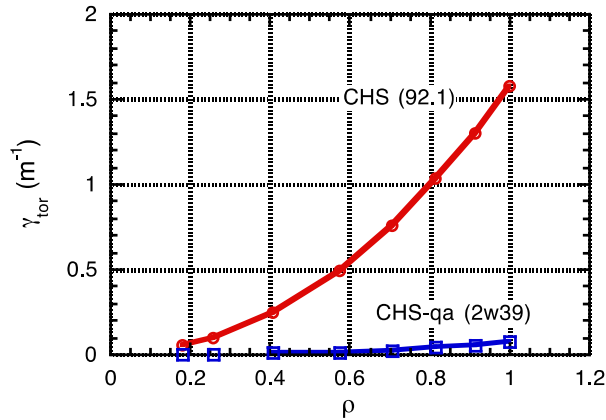
Fig. 3.5-5 Dependence of toroidal γ on minor radius for CHS-qa and CHS.

In reality, the direction of plasma flow cannot be expressed simply by a straight line in real coordinates. Experimental results in CHS suggests that the spontaneous rotation, which is driven without external momentum input (with NBI), tends to be driven along the direction minimizing parallel viscosity. In a QA configuration, this direction is the toroidal direction in the Boozer coordinates. Therefore, we have also calculated γ with the angle of $\delta/\delta s$ direction fixed in the Boozer coordinates. Fig. 3.5-5 shows γ in the toroidal direction as a function of normalized minor radius for CHS and CHS-qa. As shown, γ_{tor} in CHS-qa is much smaller than that in CHS, which implies tokamak-like nature of a QA configuration with respect to plasma rotation.

References

[3.5-1] K. Ida et al., Phys. Rev. Lett. **76** (1996) 1268.

[3.5-2] A. Fujisawa et al., Phys. Rev. Lett. **79** (1997) 1054.

[3.5-3] K. Ida et al., Phys. Rev. Lett. **67** (1991) 58.

[3.5-4] S. Nishimura et al., Phys. Plasmas **7** (2000) 437.

[3.5-5] O. Okamoto, NIFS-PROC-25 (1995).

[3.5-6] C. Suzuki et al., Plasma Phys. Control. Fusion **44** (2002) A225.

3.6   Energetic particle and NBI deposition analysis

Energetic alpha particles produced by the d-t reaction will play an essential role in sustaining a self-ignition condition in burning plasma in the future. When alpha particles are substantially lost from the plasma, the self-ignited state is easily terminated. Moreover, the localized heat load on the first wall due to the impact of the escaping alphas may seriously damage the device. Because of the reason above, a great deal of attention has to be paid to physics issues related to energetic ions such as the magnetic field ripple transport, anomalous transport and/or loss caused by MHD instabilities. Note that although neoclassical transport in CFQS is outstandingly reduced, it does not always guarantee good energetic-ion confinement. Since QAS is quite similar to tokamak in magnetic field structure, EP orbits in QAS is also quite similar to those in tokamak [3.6-1 ~ 5].

To obtain high plasma parameter and to study the beam ion confinement in QA configuration, the installation of neutral beam (NB) injector is planned with CFQS. Feasibility study of NB injection on CFQS is performed using the beam deposition calculation code and the guiding center orbit following code [3.6-6]. Fig. 3.6-1 shows the schematic drawing of the CFQS with NB injector. According to the CAD modeling including the coil case, the vacuum vessel, and the coil supporting structure, the possible injection angle of NBI is from 44 degrees to 52 degrees [3.6-7]. Here, we considered to use an NB injector operated in the Compact Helical System [3.6-8] with injection energy and power of 30 keV and 0.9 MW.
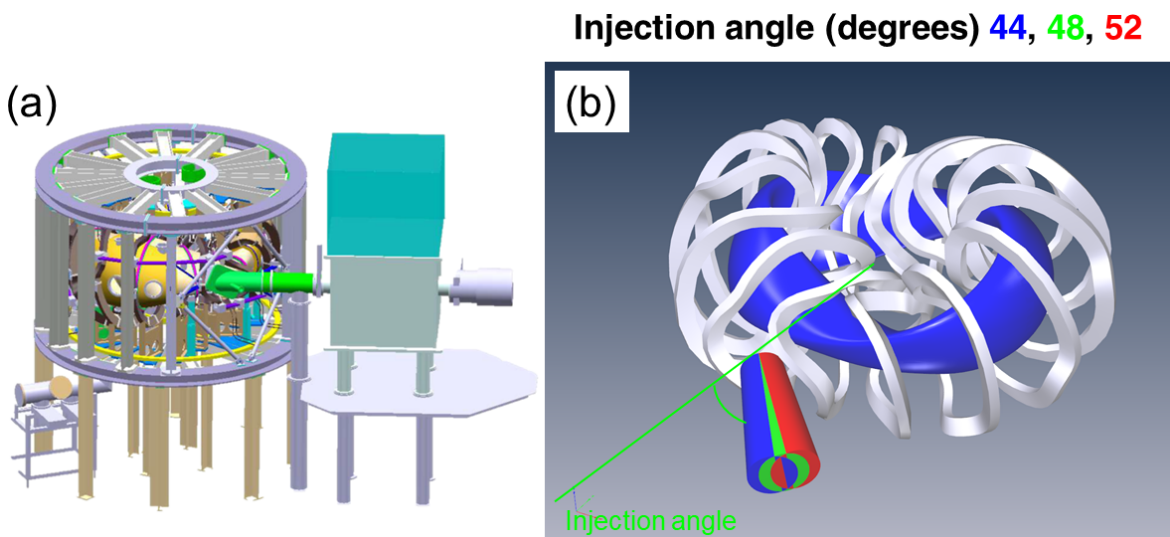

Fig. 3.6-1 (a) Schematic drawing of CFQS with NB injector (b) Possible NB injection lines

Deposition fraction on NB injection angle was surveyed by means of HFREYA code which is deposition calculation code using the Monte Carlo methods [3.6-9]. Here, the plasma parameter is assumed to be parabolic profile, i.e., $\sim(1-(r/a)^2)^2$. The central electron temperature T_{e0} is given using

central electron density n_{e0} with $T_{e0} = 2.0/n_{e0}$ (10^{19} m^{-3}) in order to maintain the plasma stored energy. We changed NB injection angle from 44 to 52 degrees with 2 degrees steps. Fig. 3.6-2 shows the deposition fraction of NB injection as a function of line-averaged electron density (n_{e_avg}). The deposition fraction rapidly increase with n_{e_avg} at n_{e_avg} of less than 4×10^{19} m^{-3}. The maximum deposition fraction is obtained with NB injection angle of from 44 to 48 degrees.
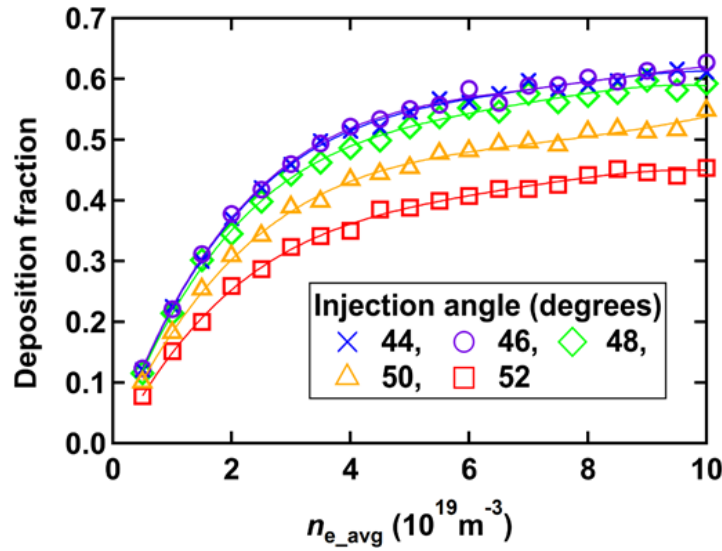
Fig. 3.6-2 Dependence of deposition fraction of NB on line-averaged electron density

The beam ion orbit calculation is performed by the guiding center orbit following code in the Boozer coordinates DELTA5D [3.6-5] in order to evaluate the beam ion confinement. Fig. 3.6-3 shows the Poincaré plots of typical collisionless orbit of co-going transit ion (H$^+$) at B_t of 1 T in toroidal angles of 90 and 180 degrees. Here, beam ion energy and pitch angle are 30 keV and 22 degrees, respectively. The deviation of orbit from the magnetic flux surfaces is relatively large due to the relatively low magnetic field strength and the relatively low rotational transform. Beam ion confinement is evaluated using DELTA5D code including beam-plasma collision. Here, we randomly choose 1000 beam ions injected by co-inject NB and followed in thermalization time of beam ions (~50 ms). Time evolution of loss energy of beam ions as a function of time is plotted in Fig. 3.6-4 (a). Here, calculation is performed with n_{e_avg} of 2×10^{19} m^{-3}. Loss energy gradially increases with time until t of 25 ms, and then is almost saturated. We obtained ralatively low loss energy at the injection angle of 48 to 52 degrees. Fig. 3.6-4 (b) shows the loss energy at t of 50 ms as a function of n_{e_avg}. The loss energy slightly increase with the n_{e_avg}. The loss energy at 50 ms is relatively lower at the injection angle of 48 to 52 degrees when $n_{e\_avg} < 4 \times 10^{19}$ m^{-3}. This is because the fraction of beam ions deposited in smaller R region, where the confinement of co-passing beam ion seems to be worse due to the large outward deviation of orbit becomes larger with the decrease of the injection angle. It seems that the injection angle of 48 degrees is more favorable regarding deposition and beam ion confinement.

Energy: 30 keV,
Pitch angle: 22 degrees

(a) φ of 90 degrees
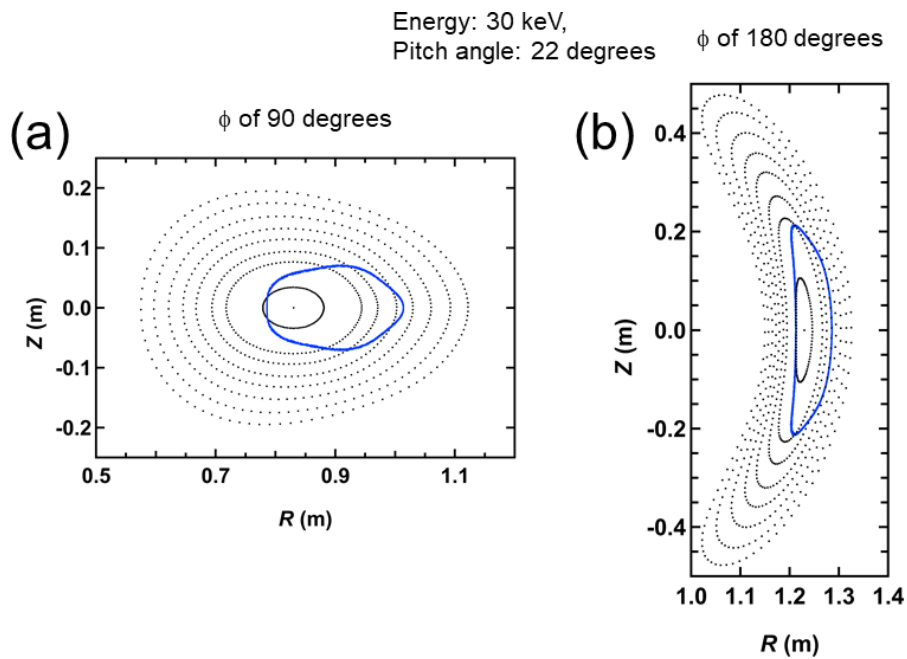
(b) φ of 180 degrees

Fig. 3.6-3 Poincaré plots of typical co-going transit beam ion orbit at two different toroidal angles
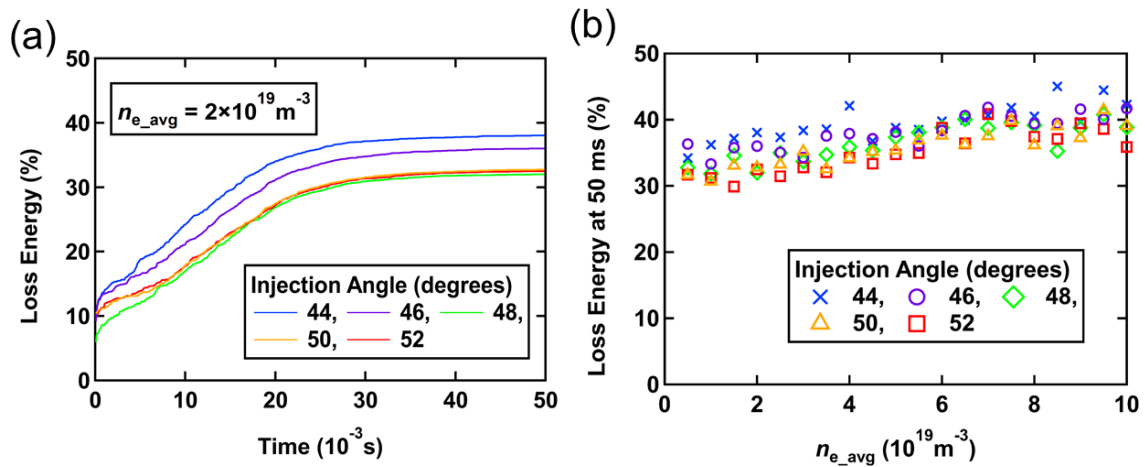

Fig. 3.6-4   (a) Time evolution of loss energy of beam ions. (b) Loss energy at 50 ms as a function of line-averaged electron density.

References

[3.6-1] M.H. Redi *et al.*, Phys. Plasmas **6** (1999) 3509.

[3.6-2] M. Isobe *et al.*, J. Plasma Fusion Res. SERIES **6** (2004) 622.

[3.6-3] H.W. Kugel *et al.*, Fusion Sci. Technol. **51** (2007) 203.

[3.6-4] S. Murakami *et al.*, Proceedings of 1997 International Symposium on Plasma Dynamics in Complex Electromagnetic Fields ~ for Comprehension of Physics in Advanced Toroidal Plasma Confinement ~, 8-11 December, 1997. **IAE-RR-98 054**, March 1998, pp. 137-140.

[3.6-5] D. A. Spong *et al*., Phys. Plasmas **18** (2011) 056109.

[3.6-6] K. Ogawa *et al*., Plasma Fusion Res. **14** (2019) 3402067.

[3.6-7] S. Kinoshita *et al*., "Engineering Design for the Chinese First Quasi-axisymmetric Stellarator (CFQS)", The 27th International Toki Conference and the 13th Asia Pacific Plasma Theory Conference (2018) and accepted for publication in Plasma and Fusion Research.

[3.6-8] K. Matsuoka *et al*., Plasma Phys. Control. Fusion **42** (2000) 1145.

[3.6-9] S. Murakami *et al*., Trans. Fusion Technol. **27** (1995) 256.

3.7　ECRH deposition analysis

ECRH power deposition and electron cyclotron current drive (ECCD) are analyzed using the ray-tracing code, TRAVIS [3.7-1]. For the analysis, a CFQS equilibrium file "wout.2b40R1mB01" was applied for the TRAVIS code. The frequency and the injected power of EC-wave in X-mode polarization are 54.5 GHz and 1 MW, respectively. As a test case, peaked electron temperature profile with T_{e0} of 3.5 keV and flat electron density profile with n_{e0} of 1.0×10^{19} m^{-3} were assumed. The T_e and n_e profiles are plotted in Fig. 3.7-1.
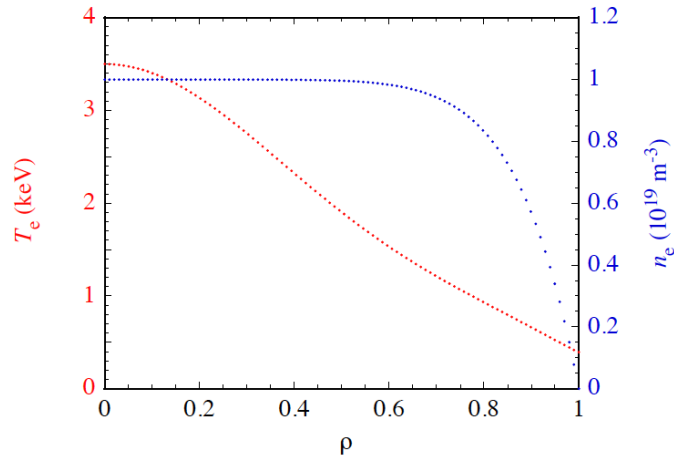
Fig. 3.7-1　Assumed electron temperature and density profiles for ECRH power deposition and ECCD analysis using the TRAVIS code.

Considering the dimension of the ECH power injection port (CFQS O-8.5 port, ICF406), the size of 2-D steerable final plane mirror is determined as H134×W96 mm, the position of the center of the plane mirror is (R: major radial position = 1.55 m, T: toroidal position = 0 m, and Z: vertical position = −0.104 m) and the focused beam waist radius (1/e radius of electric field amplitude) is 25 mm at the position (R = 1.185 m, T = 0 m, and Z = 0 m), in this analysis. Positive directions of T and Z are right side looking from outside of the torus and upper side, respectively. Using the 2-D steerable mirror, EC-wave power deposition control and ECCD can be realized.

Fig. 3.7-2 shows the controllability of power deposition position by scanning beam aiming position (R_f, T_f, Z_f). Here, R_f, T_f, and the magnetic field on axis at the bean-shape poroidal cross section, B, were fixed at 1.2 m, 0 m, and 0.975 T, respectively. Z_f was varied vertically as 0, −0.1, −0.2, and −0.25 m. The vertical axis of Fig. 3.7-2 is absorbed power density per volume, dP/dV (MW m^{-3}). By the variation of Z_f, the peak position of power deposition shifts toward outside as ρ = 0, ~0.2, ~0.4, and ~0.6, respectively. Though the heating efficiency degrades with the outward shift of the power deposition position, high heating efficiency over 80% can be expected in the wide range.
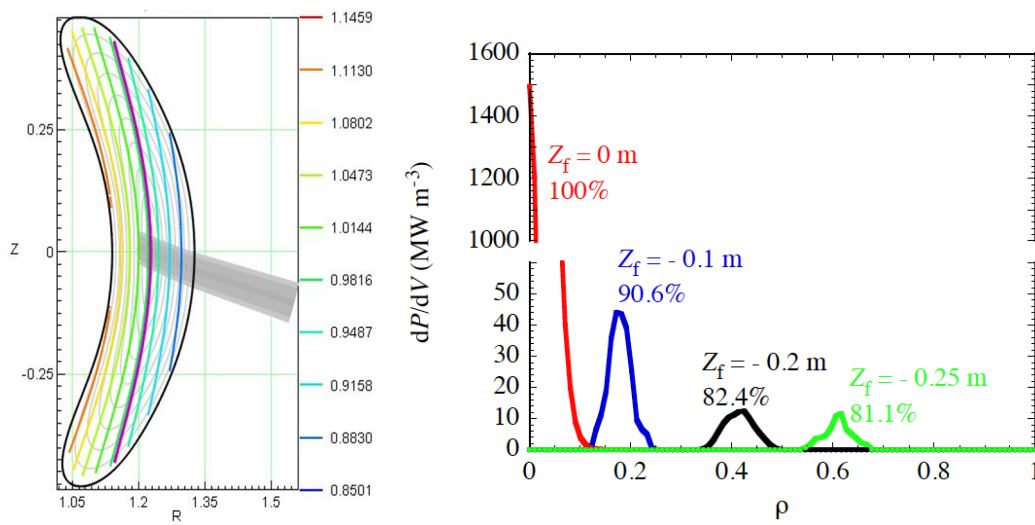
Fig. 3.7-2   Left: an example of a poloidal cross section plotted with an EC-wave beam path (here, Z_f = 0 m) and right: power deposition profiles with Z_f settings at 0, −0.1, −0.2, and −0.25 m.

Scanning EC-wave beam direction toroidally, dependence of EC-driven current I_{ECCD} against the parameter T_f is obtained as seen in Fig. 3.7-3. Here, R_f was fixed at 1.2 m. Z_f and B were slightly adjusted at each T_f, to keep on-axis heating and center-peaked current profile.
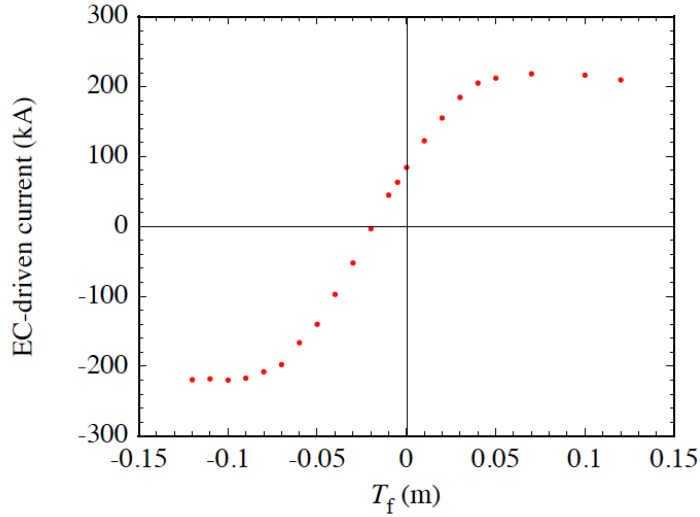

Fig. 3.7-3   EC-driven current as a function of T_f. Positive direction of current is clockwise looking from top side of the torus.

The magnitude of I_{ECCD} increases up to ~200 kA and then saturates with the magnitude of T_f. The asymmetry of I_{ECCD} about $T_f = 0$ m comes from the downward shift of the start position of the EC-wave beams (that is, center of the final plane mirror).

Thus, the 2-D steerable EC-wave beam injection system is expected to be available for a wealth of physical experiments in CFQS which require power deposition, current, and current profile controls.

References
[3.7-1] N.B. Marushchenko *et al.*, Phys. Plasmas **18**, 032501 (2011).

3.8 Modular coil design and optimization by NESCOIL

Vacuum equilibrium properties of a toroidal configuration are determined by the shape of the LCFS (plasma boundary). Generally, considering the nested magnetic flux surfaces, the VMEC code enables to solve the three dimensional MHD equilibrium accurately and efficiently. In order to achieve the target magnetic configuration, a modular coil system is necessary to be designed to reproduce the plasma boundary. Due to the Neumann boundary condition, the accuracy of the magnetic configuration induced by the coil system is dependent on the normal component of the magnetic field on the plasma boundary, which is expressed as where B is the vacuum magnetic field generated from the coil system on the plasma boundary and n is the normal unit vector of this surface. Via the minimization of on the plasma boundary, the modular coil geometry is optimized. Meanwhile, the engineering constraints are taken into account which are the minimum interval between adjacent coils and maximum curvature. They are under consideration to avoid the coil-coil overlap and reduce complexity of the coil shape. This optimization process is accomplished by the NESCOIL code [3.8-1]. In the design of the coil system for the CFQS, the coil numbers, major radials and aspect ratio have been scanned to achieve an optimum modular coil system. The corresponding parameters of coil systems are listed in the Table 3.8-1. We have designed 10 magnetic configurations and 17 coil systems in total. The N_p of all configurations is the same, 2.0. Making a comparison among them, the configuration with the major radius R_0=1.0m, aspect ratio Ap=4.0, magnetic field strength Bt=1.0 T and minor radius a=0.25 m is advantageous. In our work, the 20-coil, 16-coil and 12-coil systems are designed. The results of filament-coil optimization are listed in the table 3.8-2. In comparison of the physics and engineering constraints among them, the table indicates that the 16-coils system is preferable, which shows that the minimum interval between adjacent filament coils is the widest; the minimum radius of curvature is the largest and the magnetic flux surface generated is the closest to the target surface.

Table 3.8-1 Parameters for 10 magnetic configurations designed, showing the configuration with the major radius R_0=1.0m, aspect ratio A_p=4.0, magnetic field strength B_t=1.0 T and minor radius a=0.25 m.

R_0(m)	Ap	a (m)	B_t(T)	Num of modular coils
1.5	3.2	0.47	1.0	20
1.5	3.9(2w39)	0.38	1.0	20
1.5	4.0	0.38	1.0	20
1.5	5.0	0.30	1.0	20
1.2	3.8	0.32	1.0	Ongoing
1.2	4.0	0.30	1.0	24, 20,16,12
1.2	5.0	0.24	1.0	Ongoing
1.0	3.2	0.31	1.0	20,16,12
1.0	3.6	0.28	1.0	20,16,12
1.0	4.0	0.25	1.0	20,16,12
Total	Number of configurations:10		Number of coil systems:17	

Table 3.8-2 Parameters of three different types of coil systems for CFQS-2b40.

A_p	R_0(m)	a (m)	Number of coils	Minimum distance between coils (cm)	Minimum radius of curvature (cm)	$B \cdot n/|B|$	Current per coil (MA)	Cross section of coils (cm^2)
4.0	1	0.25	20	17.0	18.2	1.11%	0.2500	17×9
4.0	1	0.25	16	18.5	21.5	0.97%	0.3125	18×10
4.0	1	0.25	12	14.2	14.7	1.21%	0.4167	19×13

Fig. 3.8-1 gives the of 16-modular coil system. Due to $N_p = 2$ and stellarator symmetry, the whole torus consists of four symmetric sections. Therefore, the coils system possesses four different shaped modular coils. The centerline of each finite sized coil is assigned by the corresponding filament coil. The all 16 filament coils are from the results of the NESCOIL code. The coil cross section is rectangular and the area is 18×10 cm^2 which includes copper conductor, insulation and coil casing.
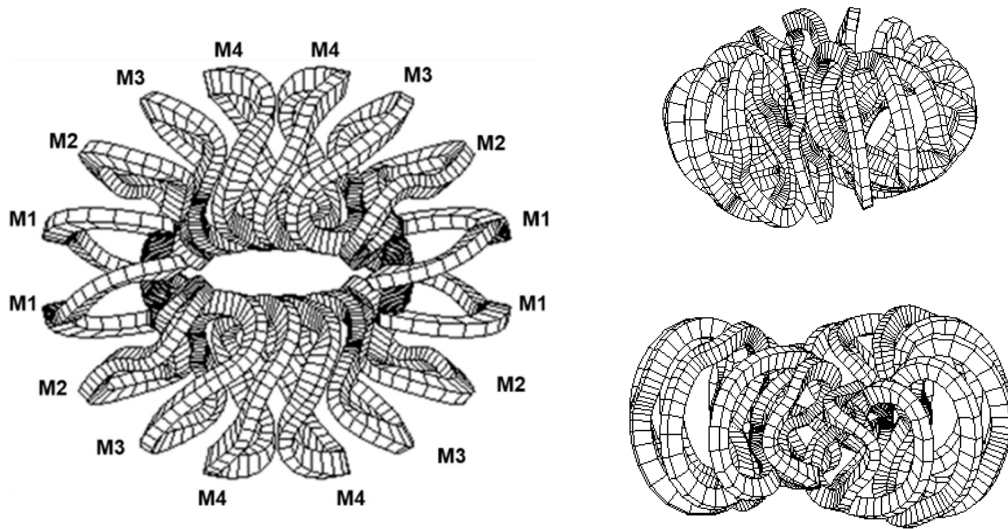
Fig. 3.8-1   Modular coils of the CFQS, the top view and side views at toroidal angle=0º (vertical elongation), and 90º (horizontal elongation). The serial number of coils represents the various shapes of coils. The coil system comprises of four different shape coils.

In order to estimate the accuracy of the magnetic configuration induced by the 16-coil system, the coils generated magnetic flux surfaces, rotational transform and Fourier spectrum of the magnetic field strength are calculated. In the Fig. 3.8-2, Poincaré plots of magnetic flux surfaces and rotational transform induced by the modular coils are analyzed, assuming the coils are filament ones. At the toroidal angle= 0º, 45º and 90º, cross sections are displayed. The angle = 0º and 90º correspond to the vertically and horizontally elongated cross sections, respectively. The average of $\boldsymbol{B} \cdot \boldsymbol{n}$ / $|\boldsymbol{B}|$ on the plasma boundary is below 1%, which cannot be reduced from the viewpoint of the engineering. The rotational transform profile and magnetic well induced by coils and target profile are compared in the Fig. 3.8-2 (d). Horizontal axis ρ in this figure represents the normalized average minor radius. The figure shows a good agreement between coils induced rotational transform profile and depth of

magnetic well and target ones. From the Fig. 3.8-2 (a)-(c), they depict a good coincidence in the shapes of a magnetic flux surface and that of target plasma boundary. It should be noted that the width of outmost flux surface produced by modular coils is larger than that of target plasma boundary, which is beneficial to raise the plasma volume by movable limiters. In order to precisely estimate the QA property of the configuration, the magnetic field strength is decomposed into a Fourier spectrum in the Boozer coordinates. The Fig. 3.8-3 (a) depicts the spectrum of the magnetic field strength based on the target magnetic configuration. To extinguish the small-amplitude components, the largest component B_{00} is omitted. In the Fig. 3.8-3 (a), the magnetic field strength is 1.0 T. B_{10} is the dominant component resulting from the toroidicity. Others components, such as mirror ripple (B_{01}) and helical ripples (B_{11}, B_{12}), are much less than B_{01}, which indicates a tokamak-like/QA configuration. In the Fig. 3.8-3 (b), coil induced spectrum of magnetic field strength is given. On the basis of synthetical analyzation, the designed 16-coil system is well workable.
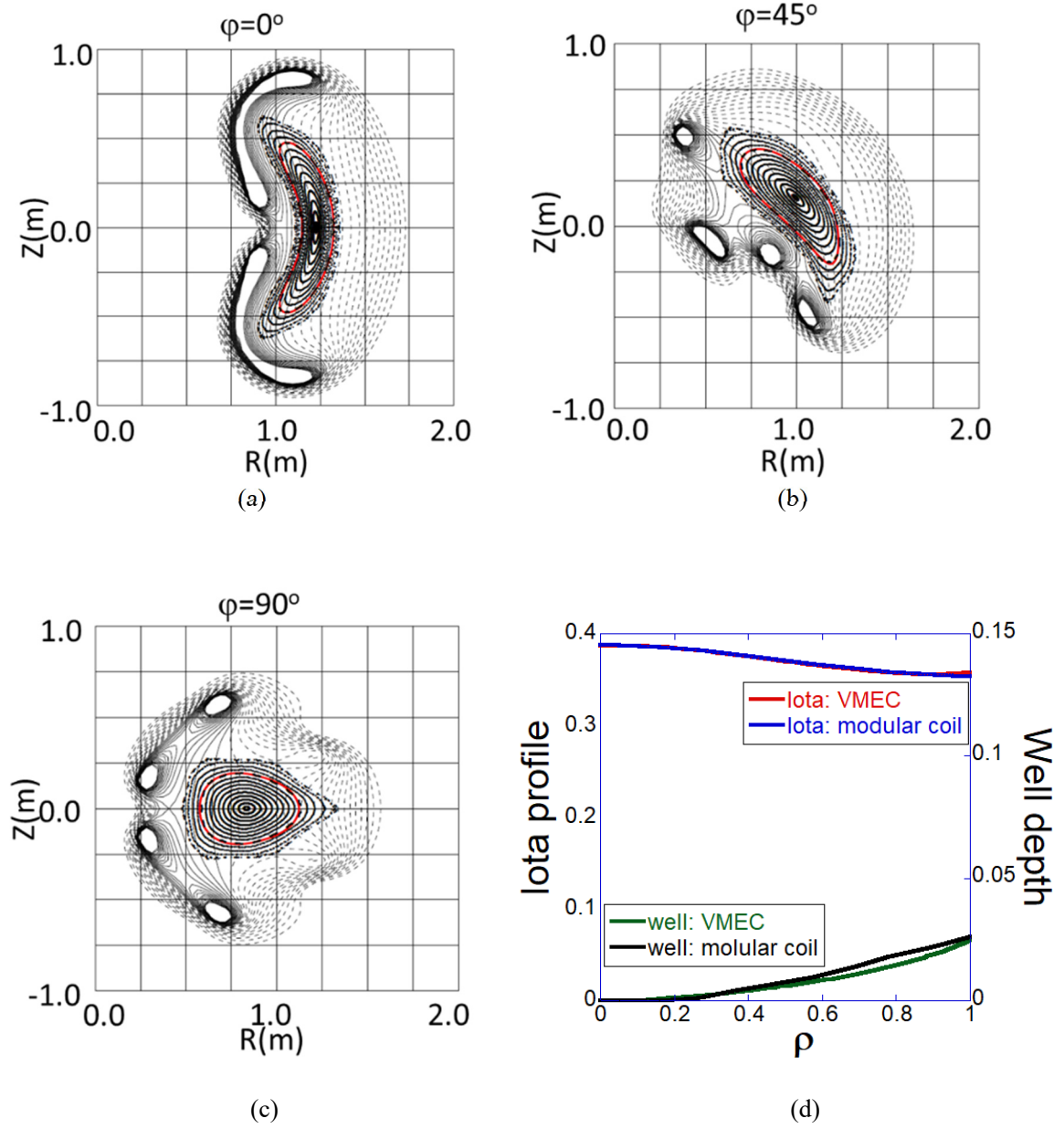
Fig. 3.8-2   Poincaré plots of magnetic flux surfaces at the toroidal angle =0º, 45º, and 90º for (a)-(c) respectively. The red curve represents the target plasma boundary. (d) shows the comparison of the rotational transform and magnetic well between the configuration produced by modular coils and target one.

(a)   (b)
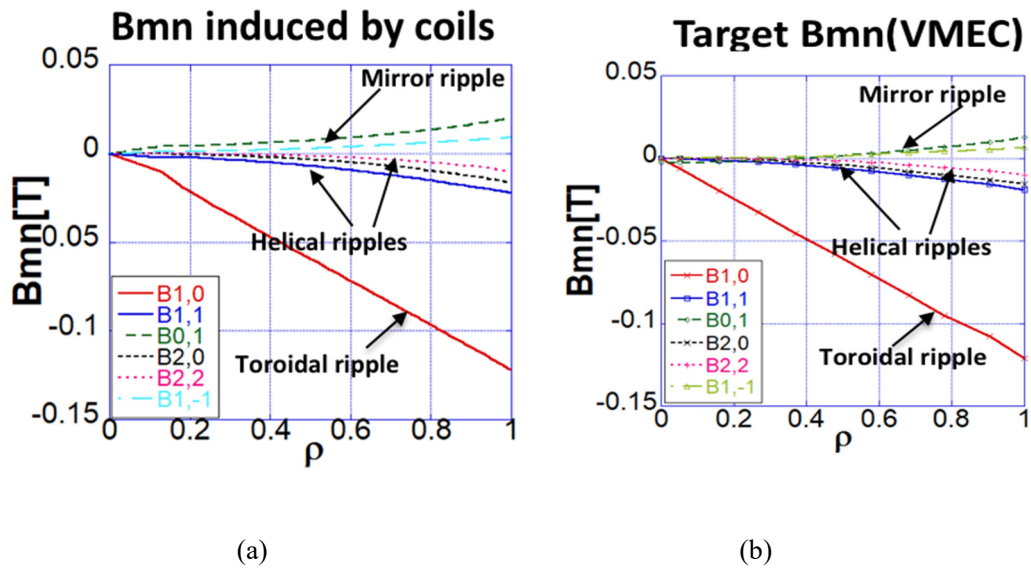
Fig. 3.8-3   Fourier spectrum of the magnetic field strength for the CFQS configuration in the Boozer coordinates. (a) B_{mn} from VMEC results (target spectrum), (b) B_{mn} generated by modular coils.

References

[3.8-1] M. Drevlak, Fusion Technology **33** (1998) 106.

3.9 The design of modular coils without torsions

In the fabrication of coils, the coil's torsion has a great influence on the difficulty of manufacture. The greater the torsion, the coil is more complex. So, we have optimized the coil system by reducing the torsion.

We compute the torsion by these equations as follows:

For arbitrary point r_c in the modular coil cross section,

$$r_c(l,\xi,\eta) = r_G(l) + \xi u(l) + \eta v(l) \tag{3.9.1}$$

Tangential vector is as follows,

$$t_c \equiv \frac{dr_c}{dl_c} = \left(\frac{dr_G(l)}{dl} + \xi\frac{du(l)}{dl} + \eta\frac{dv(l)}{dl}\right)\Big/\frac{dl_c}{dl} \tag{3.9.2}$$

$$-x_w \leq \xi \leq x_w \qquad -y_w \leq \eta \leq y_w$$

We define vector, $\quad \mathbf{b} = t_c \times u \ \ \mathbf{n} = \mathbf{b} \times t_c$ (3.9.3)

Torsion,

$$\tau(l) = -\mathbf{n} \cdot \frac{d\mathbf{b}}{dl_c} \tag{3.9.4}$$

We rotate the cross section of coils and calculate the torsion after each rotation. Next, we can find the minimum torsion in our calculated result. When we get the minimum in all cross section, we finish the optimization of the coil.

The following figures (Fig.3.9-1~8) show the torsion of the coil without optimization and with optimization, respectively.

<div align="center">(a)   (b)</div>
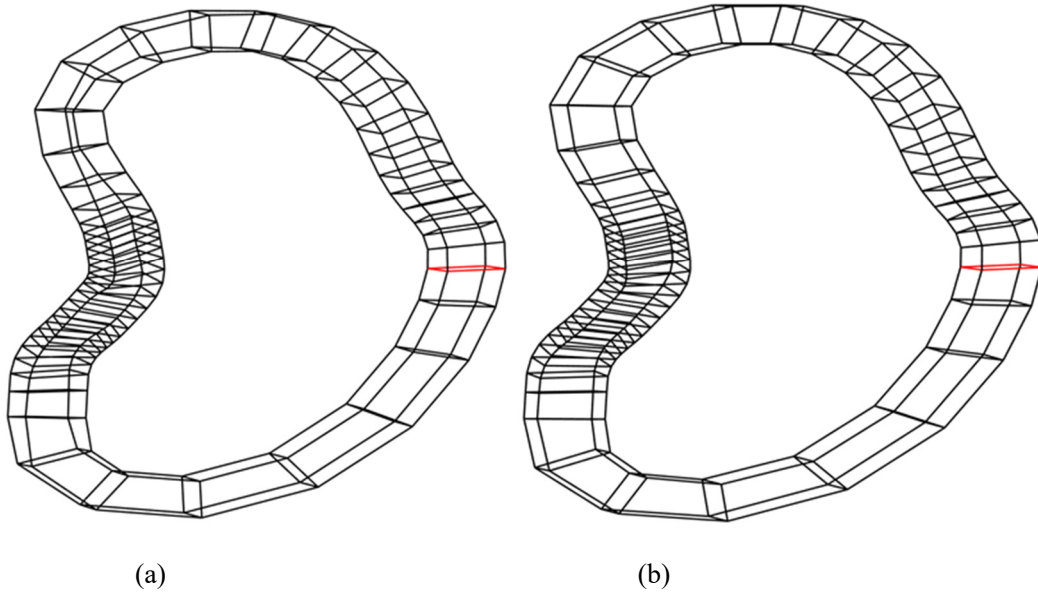
Fig.3.9-1   M1 coil without optimization and with optimization ((a) and (b), respectively, the red line is the first cross section)

<div align="center">(a)   (b)</div>
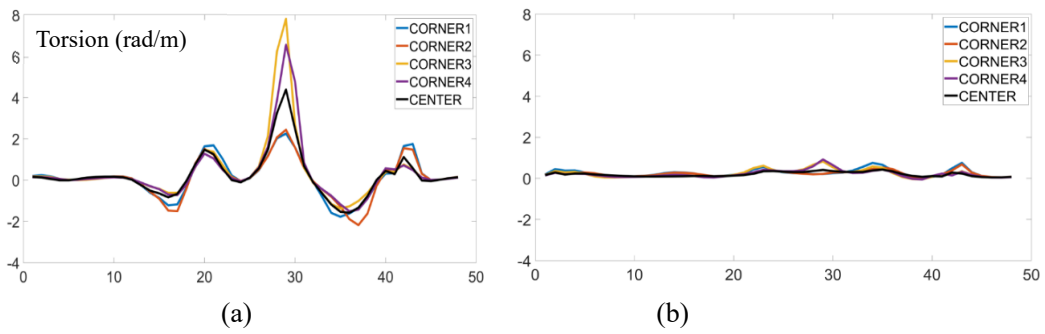
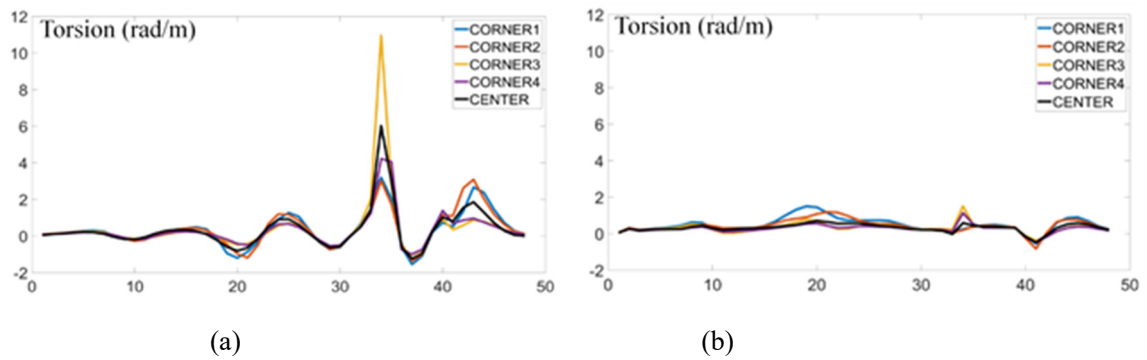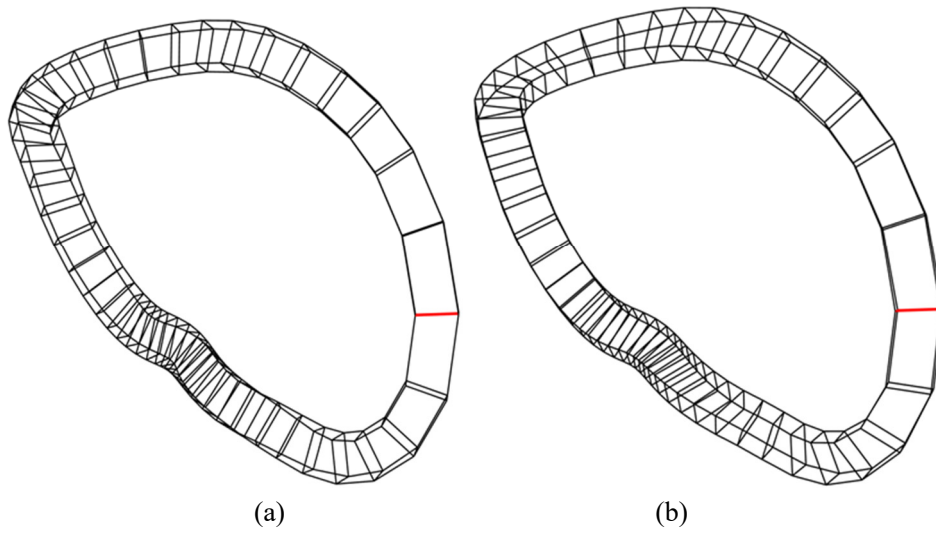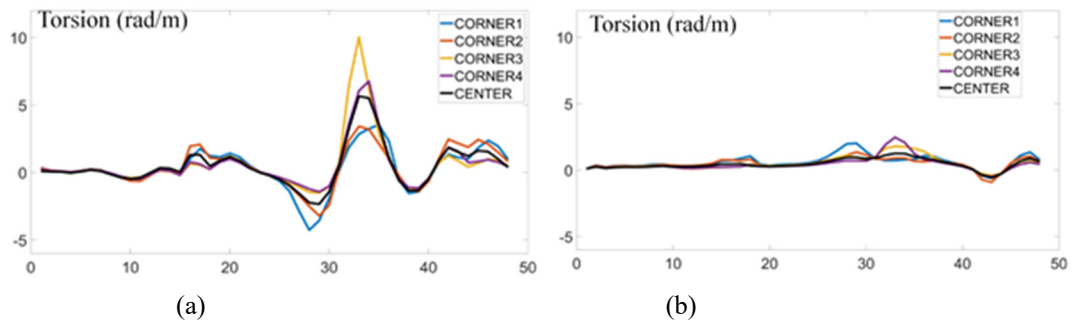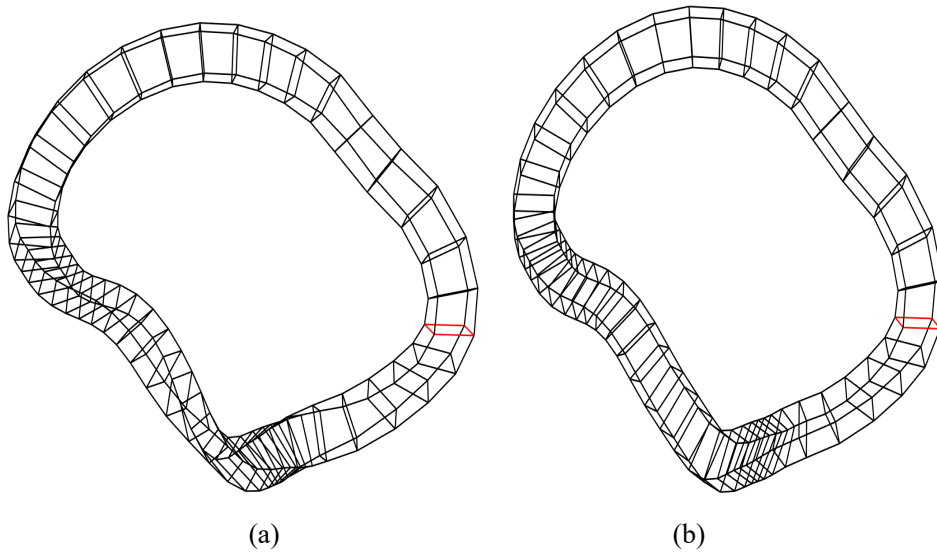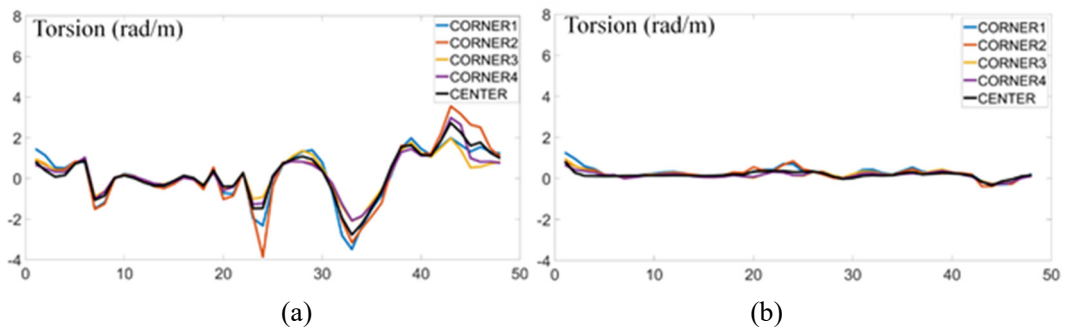Fig. 3.9-2   Torsion of M1 coil without optimization and with optimization ((a) and (b), respectively)

<center>(a)   (b)</center>
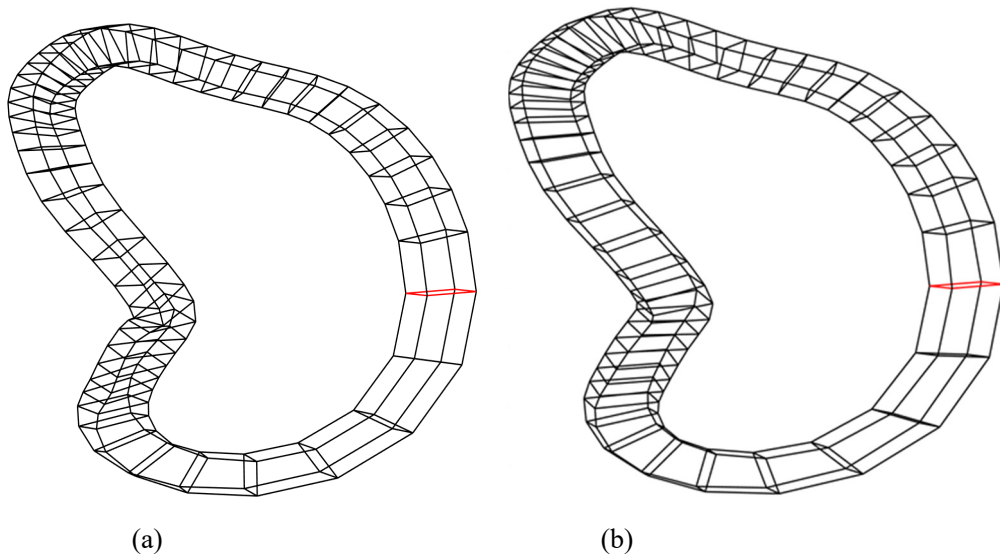
Fig.3.9-3   M2 coil without optimization and with optimization ((a) and (b), respectively)

<center>(a)   (b)</center>

Fig.3.9-4   Torsion of M2 coil without optimization and with optimization ((a) and (b), respectively)

<center>54</center>

<center>(a)   (b)</center>

Fig.3.9-5 M3 coil without optimization and with optimization ((a) and (b), respectively)
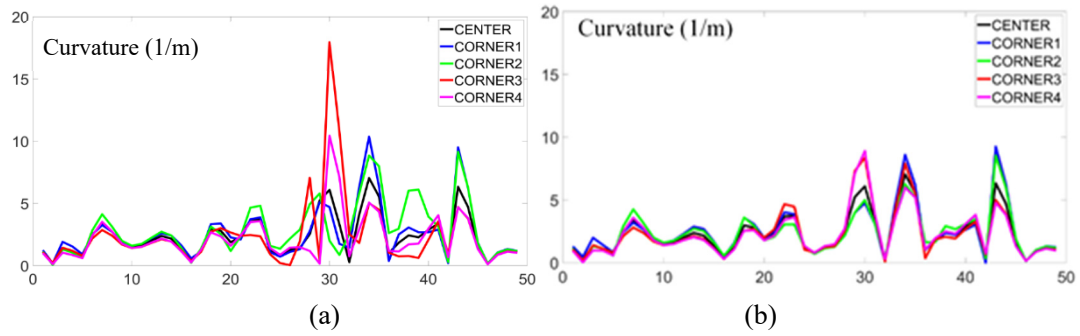

<center>(a)   (b)</center>

Fig.3.9-6 Torsion of M3 coil without optimization and with optimization ((a) and (b), respectively)

Fig.3.9-7 M4 coil without optimization and with optimization ((a) and (b), respectively)
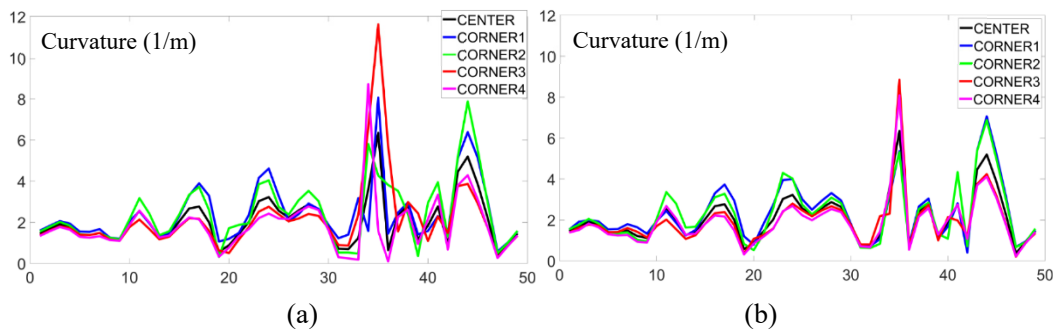

Fig.3.9-8   Torsion of M4 coil without optimization and with optimization ((a) and (b), respectively)

Through the figures above, it's clearly shown that the torsion has been well optimized.

In addition, curvature is also an important parameter for the coil system, of course, it is not a good parameter for the coil, the equations of curvature as follows:

$$\text{k} = \left|\frac{d\boldsymbol{t_c}}{dl_c}\right| = \left|\frac{d^2\boldsymbol{r_c}}{dl_c^2}\right|.$$

$\boldsymbol{t_c}$ is calculated in equation (3.9.2) and $\boldsymbol{r_c}$ is calculated in equation (3.9.1).

Then, we compare the curvature of coils without optimization and with optimization, respectively.

Fig.3.9-9   Curvature of M1 coil without optimization and with optimization ((a) and (b), respectively)

Fig.3.9-10   Curvature of M2 coil without optimization and with optimization ((a) and (b), respectively)
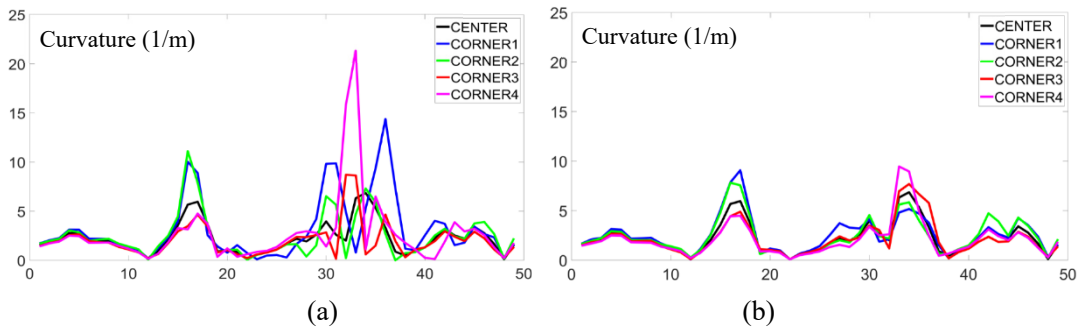

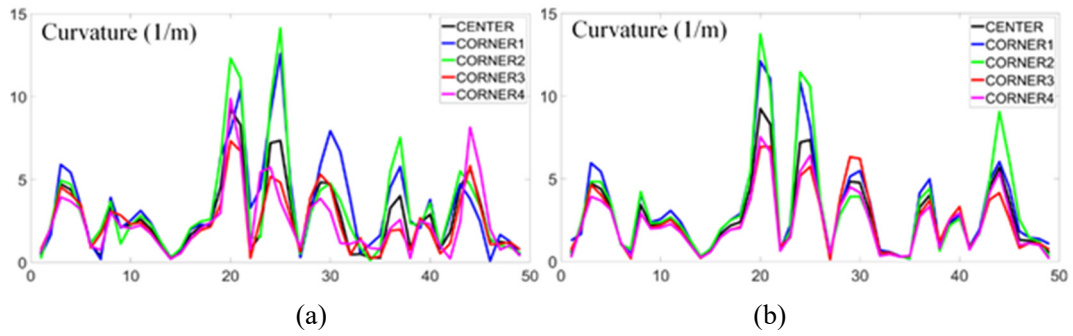Fig.3.9-11   Curvature of M3 coil without optimization and with optimization ((a) and (b), respectively)

Fig.3.9-12 Curvature of M4 coil without optimization and with optimization ((a) and (b), respectively)

The above figures (Fig.3.9-9~12) show that the coil optimized for torsion is also have a good improvement in curvature.
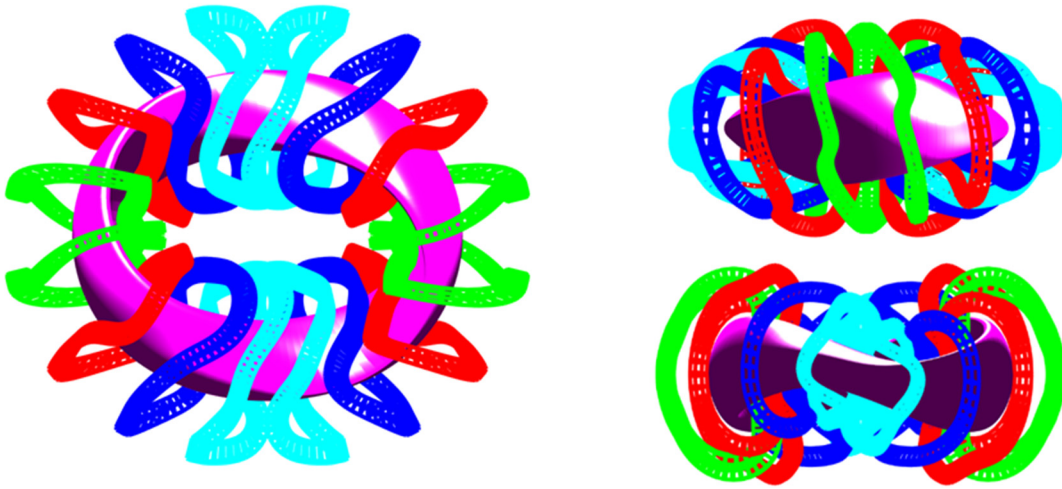
Fig.3.9-13 Modular coils and plasma boundary of CFQS

3.10 Divertor configuration

In designing the magnetic configuration of an experimental device, the first priority is placed on designing the configuration of the core confinement region. However, it is well known that without a proper design of magnetic configuration of the peripheral region the concept is not useful for the fusion reactor. This is called 'divertor design' because the most important physics issue related to the peripheral magnetic configuration is particle and heat removal.

In tokamak research, the concept of divertor is almost established and all existing tokamak devices in the world have similar divertor configuration (single null divertor) with the direct extension to the tokamak demo design. There are still discussions for the new ideas of advanced configurations (double null divertor and snow flake divertor) but they have not been adopted in real experimental devices. In stellarator research, we do not have one established concept of divertor partly because we have varieties of stellarator configurations and divertor concept strongly depends on the magnetic configuration of core confinement region. In fact, for the two largest stellarator experiments, LHD and W7-X, these devices have different divertor structures. In LHD, the intrinsic helical divertor has divertor magnetic field lines connecting the ergodic boundary layer of the core confinement region and the divertor plates on the wall [3.10-1]. In W7-X, the island divertor provides a sophisticated divertor structure combined with small islands created near the boundary of the core confinement region [3.10-2]. For the new stellarator CFQS in China, we are designing a new divertor configuration which provides a sufficiently long connection length of magnetic field lines between the plasma boundary and the wall.

Three poloidal cross sections of the LCFS of CFQS are shown in Fig.3.10-1. Modular coils were designed to realize such a magnetic configuration with a choice of the number of coils around the torus as 16 [3.10-3,4]. The success of this coil design was the most important contribution to the finding of a new divertor concept for CFQS. Fig. 3.10-2 shows the punctual plots of the vacuum magnetic field lines (magnetic surfaces) produced with these modular coils (for the third cross section in Fig.3.10-1). Red line shows the LCFS of the target configuration in the modular coil design. The magnetic field produced by the modular coils has many closed magnetic surfaces with a larger area beyond the target LCFS. In usual cases of designing modular coils for the advanced stellarator, it is very difficult to make larger closed magnetic surfaces beyond the target LCFS because the boundary area usually becomes stochastic.

Fig. 3.10-3(a) shows the profile of the rotational transform of the magnetic configuration produced by the modular coils. A very flat profile for the outer region is also very important for the new divertor concept. Red mark shows the averaged radius of the LCFS of the target configuration. Although we decided upon an aspect ratio of 4 for the CFQS device, it is technically possible to create a larger confinement region if we design the vacuum chamber with a sufficiently large size to provide space

for such larger magnetic surfaces. A control of plasma boundary with movable limiter might be a possible choice for the plasma operation control.

When we introduce the auxiliary toroidal coils to provide additional toroidal field to the stellarator field produced with modular coils, the magnetic configuration is changed to include large islands at the boundary of the core confinement region shown in Fig. 3.10-4. The QA propety is conserved with the additional toroidal field. The strength of the additional toroidal field is -0.055 times averaged toroidal field produced by modular coils. The rotational transform is increased to change the boundary value to 0.4 (shown in Fig. 3.10-3(b)). This is a typical magnetic configuration for any type of stellarator that has a rational value of the rotational transform near the boundary. However, essential differences between the configuration shown in Fig. 3.10-3 from many other cases are 1) large size of islands and 2) the completeness of the island magnetic surfaces. It is shown in Fig. 3.10-3 that clearly formed island bundle flux surrounds the core confinement region with a clearly defined interface of the magnetic field separatrix. This is the reason why we call such a configuration as 'island bundle divertor (IBD)'. The entire magnetic confinement area is clearly separated into two regions: hot plasma region in the core and cold plasma region in the periphery.

Fig. 3.10-5 shows the divertor field line tracing, which is created in the following calculation procedures. We found first the LCFS of the core confinement region. Then we distributed many field line tracing starting points with a small deviation (5 mm for R=1 m torus) from the LCFS. Because the island magnetic surfaces are complete, there is no escaping field line in such a calculation. Fig. 3.10-5 shows blue line for one of the possible shapes of the vacuum chamber wall. If we install divertor plates at this wall position, the cold plasma in the island bundle flux can be absorbed at the divertor plates. Fig. 3.10-6 shows the divertor tracing with the wall target where the field line tracing is stopped. The pattern of the magnetic field line punctual plots is very similar to the tokamak divertor structure. In fact, the transport of the magnetic field lines is exactly the same as tokamak divertor, where the peripheral regions of the divertor are connected to the core confinement region with a clear magnetic separatrix, and divertor magnetic field lines in divertor region have long connection length between the null point and the wall. Because the magnetic field lines go around through all five island bundle fluxes with very small incident angles to the wall, the distribution of the heat load on the divertor plates is determined by the precise geometric design of the shapes and the locations of divertor plates.

The length of the followed field lines between start points near LCFS and the divertor plate position is more than 150 m in this calculation and there is no exceptional field line with shorter length. This is because the island magnetic surfaces are very clear and there is no ergodic region between the core confinement region and the divertor bundle flux. This is a very clear difference from the LHD-type divertor structure where there are some field lines with shorter length between the core region and the divertor plate because of the ergodicity of the boundary layer of the core confinement region. In the discussions of connection length, the island bundle divertor is similar to the tokamak divertor situation

in the sense that the divertor field lines do not have strong poloidal magnetic field component, which makes the connection length shorter.

Because the rotational transform of IBD region is 0.4, island bundles shown in Fig. 3.10-4 are connected together. In other words, this bundle flux is a single flux. Thus particles and heat flux transferred from the core confinement region to the IBD can be removed at any position in the torus. Because the space between the plasma and the wall is very narrow in the toroidal position of the crescent shape of plasma (the leftmost LCFS in Fig. 3.10-1), we can avoid installing divertor structure at this region and take advantage of installing it where the space is larger. As shown in Fig. 3.10-6, the number of divertor feet is as many as ten. Thus it is possible to reduce the maximum heat load at the divertor compared with the tokamak case, where the number of feet is two (in the case of a single null). On the other hand, because the divertor fields are all connected into a single structure, it is not necessary to install as many as ten divertor plates.

Since the island structure is in general very sensitive to the control of the rotational transform, the control of bootstrap current in the stellarator operation will be essential to keep the IBD concept stable. However, we know that any plasma parameters and engineering parameters must be controlled extremely accurately in the future fusion reactor. The control of bootstrap current would be within available control knobs in the fusion reactors. Furthermore, the increase of the rotational transform necessary for IBD formation is in the range of possible bootstrap current effect of the QA stellarator.

References

[3.10-1] Y. Takeiri *et al*., Nucl. Fusion **57** (2017) 102023.

[3.10-2] R. C. Wolf *et al*., Nucl. Fusion **47** (2017) 102020.

[3.10-3] H. Liu *et al*., Plasma and Fusion Research Series **13** (2018) 3405067.

[3.10-4] A. Shimizu *et al*., Plasma and Fusion Research Series **13** (2018) 3403123.
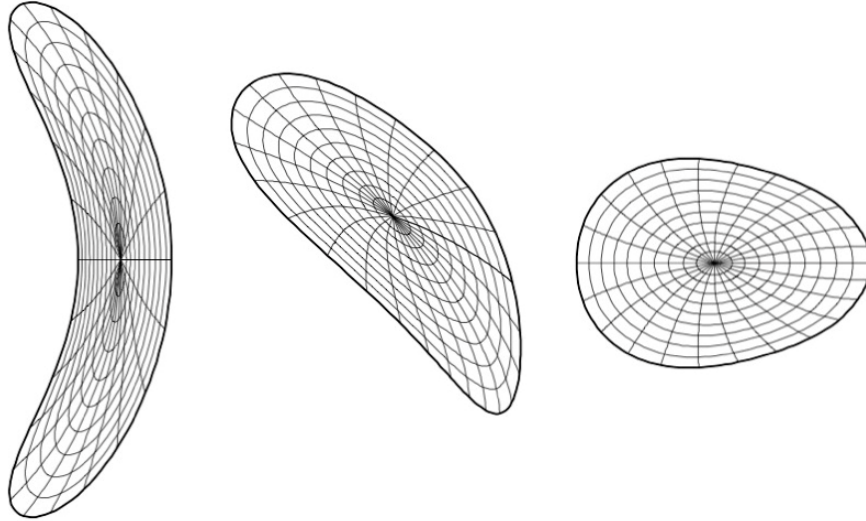
Fig. 3.10-1   Last closed magnetic surfaces for CFQS advanced stellarator design. Cross sections for three toroidal positions are shown.
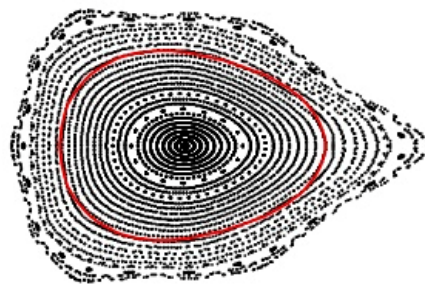

Fig. 3.10-2   Punctual plots of magnetic surfaces for CFQS configuration produced by 16 modular coils. Red line corresponds to the LCFS of the 3rd plot in Fig. 3.9-1
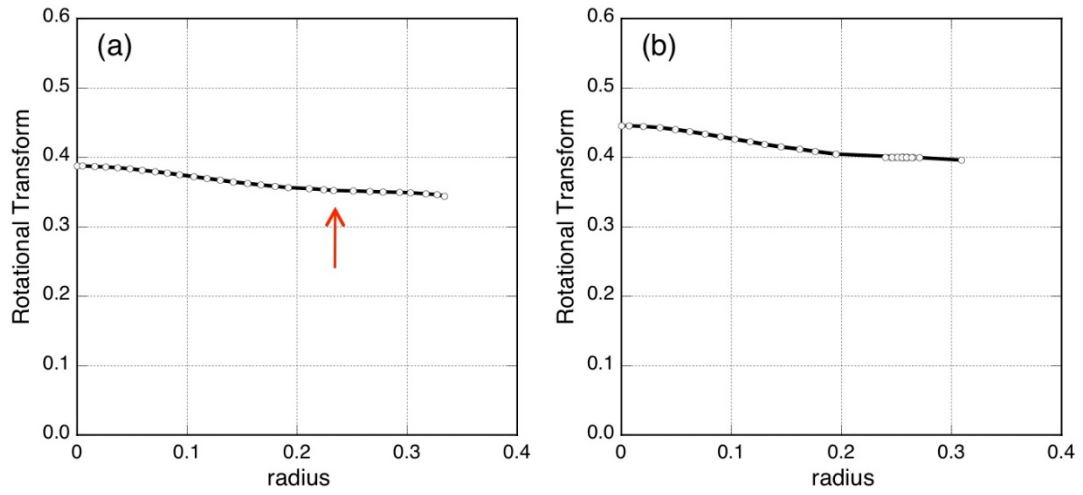
Fig. 3.10-3 (a) Rotational transform profile of vacuum field of CFQS. Red arrow indicates the position of LCFS of target configuration. (b) Rotational transform profile of island bundle divertor configuration with additional toroidal field.
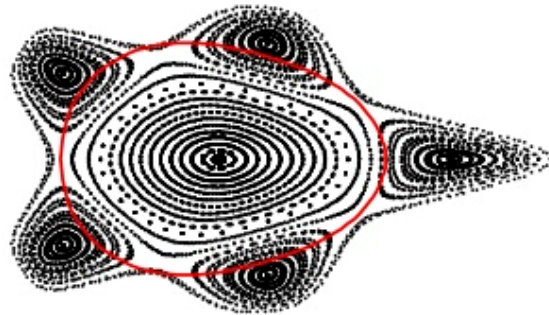
Fig. 3.10-4 Magnetic configuration of island bundle divertor.
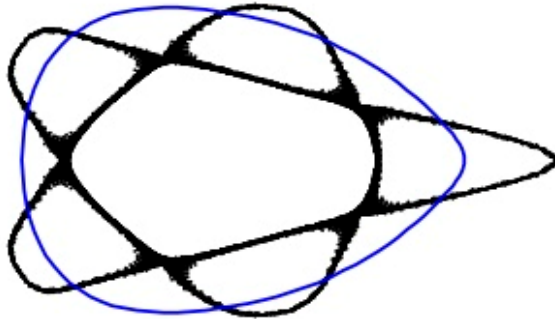
Fig. 3.10-5   Divertor field line tracing for island bundle divertor. Blue line shows one example of vacuum chamber wall position for locating divertor plates.
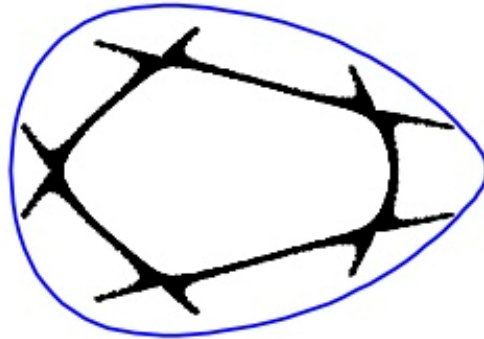
Fig. 3.10-6   Divertor field line tracing with assumed existence of divertor targets.

4　Engineering design

4.1　Overall Structure

The CFQS design reduces the major radius, increases the aspect ratio, and reduces the magnetic field slightly in order to reduce costs and make it easier to manufacture by using the 2b32 CHS-qa configuration. Table 4.1-1 shows physical main parameters of CFQS. We are able to achieve low magnetic shear and a shallow well structure throughout the entire region as mentioned in the chapter for the equilibrium. The dominant ripple is the toroidal mode $B_{1,0}$, which indicates a tokamak-like or QA configuration. The CFQS project aims to confirm the effectiveness of this equilibrium.

Because aspect ratio of the CFQS is small, an engineering design is expected relatively harder than other devices. For example, the work area in the central region is very narrow and special structural idea is necessary for assembling the CFQS. The electromagnetic force will be large although the magnetic field is not so large. They are engineering disadvantages caused by cost reduction.

Table 4.1-1　　Comparison of physical specifications for stellarators

No	Parameters	CFQS	W7-X	NCSX	HSX
1	Major Radius (m)	1.0	5.5	1.4	1.2
2	Minor radius (m)	0.25	0.5	0.33	0.15
3	Aspect ratio	4	11	4.2	8
4	Magnetic Field (T)	1	3	2.1	1
5	Toroidal Periodic Number	2	5	3	4
6	Rotational Transform	0.35～0.38	0.85～1	0.4 ～ 0.65	1～1.1
7	Magnetic Well Depth	0～0.025			

Fig. 4.1-1 to Fig. 4.1-3 show schematics of the CFQS, which is approximately 2800 mm high between a top frame and a bottom frame and has an outer diameter of 4300 mm. The electromagnetic force applied to the modular coils is supported by a cage-type support structure, with diagonal beams to absorb the overturning force and two central pillars to absorb the centripetal force. These devices will be installed in a torus hall with power supplies for plasma heating, as shown in Fig. 4.1-4. The plasma heating apparatus is intended to provide for tangential neutral beam injection (NBI) of 40 kV and 1 MW and electron cyclotron resonance heating of 54.5 GHz and 450 kW. For plasma diagnostics, we will use a Thomson scattering system, a microwave interferometer, a charge exchange system, a heavy ion beam probe, and magnetic measurements, among others.

Table 4.1-2 gives technical data. A basic QA configuration can be produced by four types of modular coils (for total of 16). However, in order to allow flexible configuration, we have installed

four poloidal field coils (to move the magnetic axis horizontally) and twelve toroidal field coils (to change the rotational transform). The coil currents are driven by eight or nine SCR power supplies in the rated operation conditions.

The power supplies, the diagnostics and the heating apparatus are different in the experimental phase, but the main body of the CFQS is common. It will be constructed under the rated operation conditions.
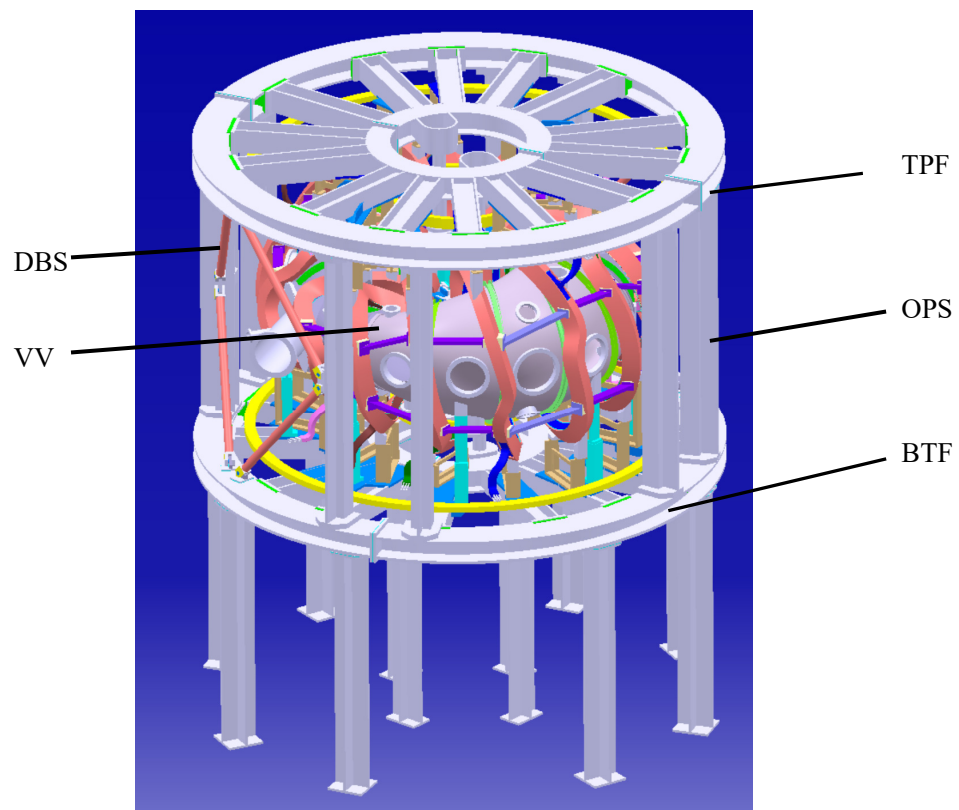

Fig. 4.1-1　　Schematic of the CFQS. DBS: Diagonal beams, VV: Vacuum vessel, TPF: Top frame, OPS; Outer pillars, BTF Bottom frame.
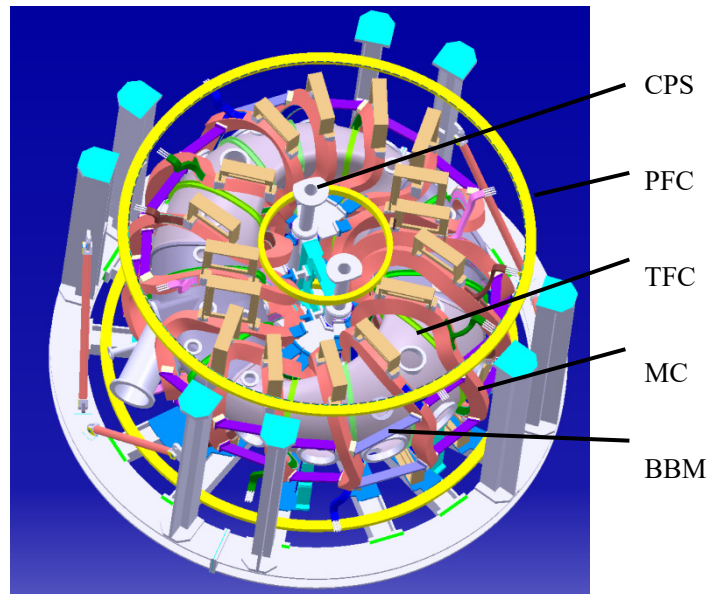
Fig. 4.1-2   Schematic inside the cage type support structure consist of CPS,OPS,TPF,BTF and DBS. CPS; Center pillars, PFC; Poloidal field coils, TFC; Auxiliary toroidal field coils, MC, Modular coils, BBM; Beams between modular coils.
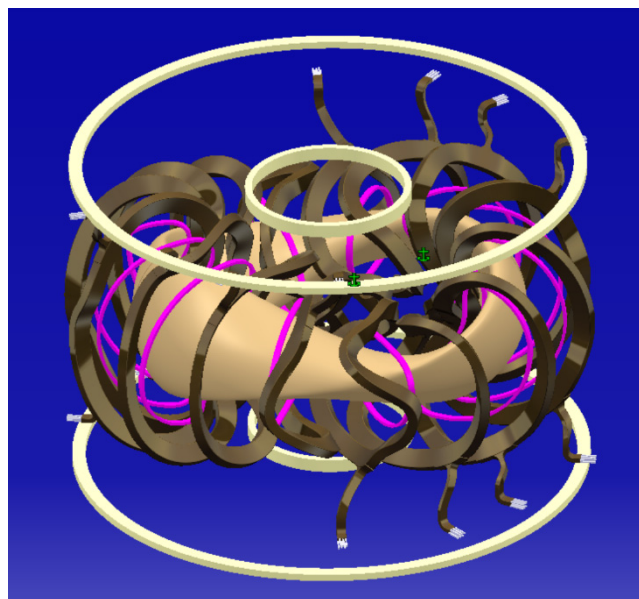
Fig. 4.1-3   Schematic of the coil system. Showing 16 modular coils (brown), 4 poloidal field coils (yellow) and 12 auxiliary toroidal field coils (pink). The outermost magnetic flux surface is shown in beige.
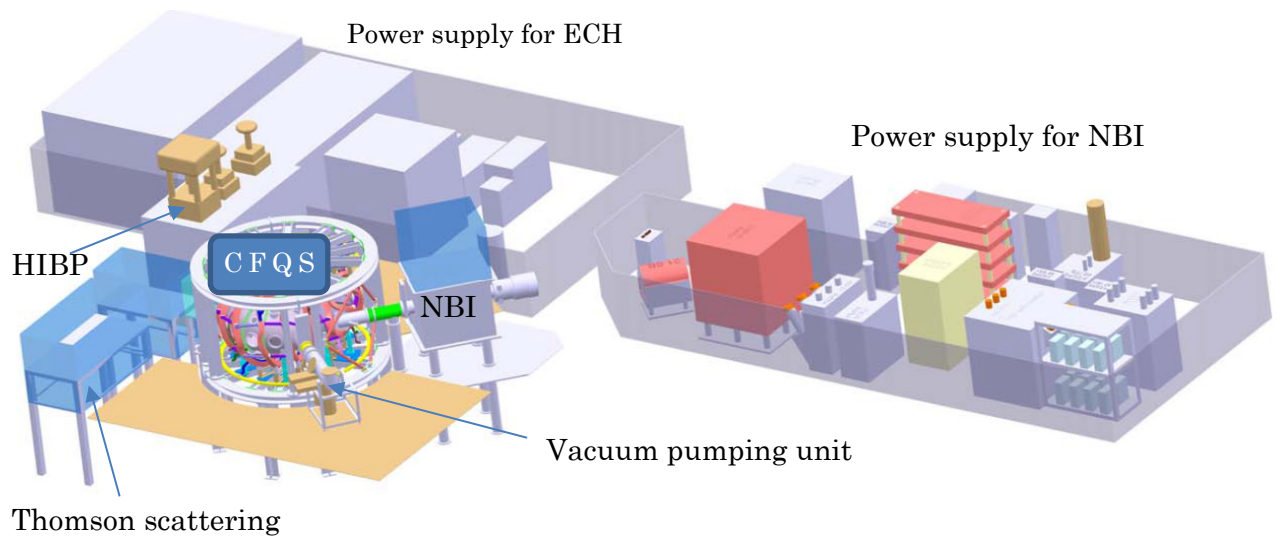
Fig. 4.1-4 Layout in the torus hall

Table 4.1-2   Technical data for the CFQS

No	Device	Technical data			
		Initial experiment	Rated operation		
1	Magnetic Field	0.09T	1T		
2	Plasma production	2.45GHz 20kW ECH	54.5GHz 450KW ECH and 40kV 1MW NBI		
3	Coil design	MC	MC	PFC	TFC
	Characteristics	Cover in SUS case	Cover in SUS case	Simple cylinder	Winding on the VV
	Number of coils	16	16	4	12
	Number of types	4	4	2	3
	Turns for a coil	72	72	32	8
	Conductor current(A)	390	4,340		
	Current density (A/mm^2)	6.7	74		
	Overall cross section (mm^2)	132×69	132×69	90×48	40×20
	Total current (kAT)	450	5,000	556	420
	Conductor	Water-cooled hollow copper conductor			
	Operation	Continuous	0.6s pulse with interval 5 minutes		
	Power capacities(kVA)	120	12,000	8,000	4,500
	Power source	Commercial source	A motor generator		
	Number of Power supplies	2	4	2	2 or 3
	Voltage(V)	300	2,400	1,500	430
4	Vacuum vessel design				
	Cross Section	0.45m $\times$ 1.2m at vertical elongated section			
	Material	SUS316L with thickness 6mm			
	One turn resistance	0.3mΩ without one turn break			
	Baking	130°C by inductive heating			
	Vacuum pumping	1500 ℓ/s TMP $\times$ 2			
5	Diagnostics	Magnetic Probe Electrostatic probe visible spectrometer Microwave interferometer	Thomson scattering FIR interferometer VUV spectrometer HIBP , CXRS etc.		

4.2　Coil system

4.2.1　Engineering design of modular coils

Shapes of the modular coils are shown in Fig. 4.2.1-1 and their cross section in Fig. 4.2.1-2. Since the current density is very high, the conductor temperature rises about 20 degrees per second of operation. In order to absorb this heat before next shot, the coils are cooled by pure water.

Very large magnetic forces are applied to the modular coils. The forces' magnitude and direction may be very complicated, and their characteristics are not easy to describe. They are similar to those of a tokamak's toroidal field coil, but the modular coils are more difficult to analyze and operated under more severe conditions because even the components that are negligible for tokamaks cannot be ignored. The strength of the coil conductor and insulation alone is not expected to be sufficient for large forces, it is reinforced with a SUS case like the tokamak's toroidal field coil.

The structure of the coil and the case is shown in Fig. 4.2.1-3. In order to reduce costs, the case is planned to consist of two parts, L shape plate and lid. The L shape plate has a barrier on the outside to interfere the coil when it is covered in the case. In order to solve this assembly concern, the modular coil shape is devised. Its design method is shown below.

- The center trajectory is calculated with the NESCOIL code, but only adjusted locally and manually to eliminate extremely large curvatures (small radius of curvature).
- The cross sectional area is defined in consideration of the limit of current density.
- The tilting angle of the normal vector for the current carrying surface (CCS) is selected so that production or assembly is easy as shown in Fig. 4.2.1-4.

We had checked first a design that a longer axis (the normal vector) was perpendicular to the CCS, and found a problem in the assembly process. We have optimized the angle to eliminate the interference problem. They are 20 degrees for the M1, M2 and M3, and 30 degrees for the M4.

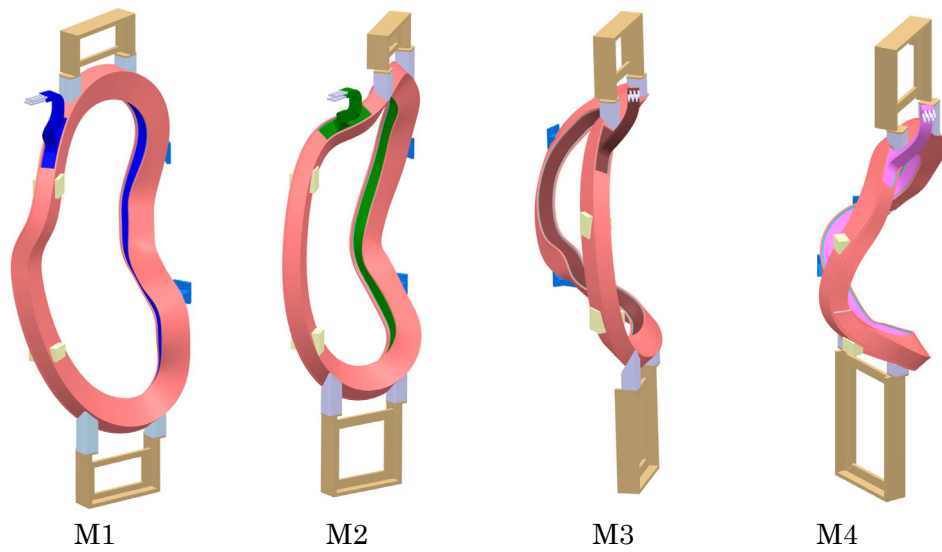M1   M2   M3   M4

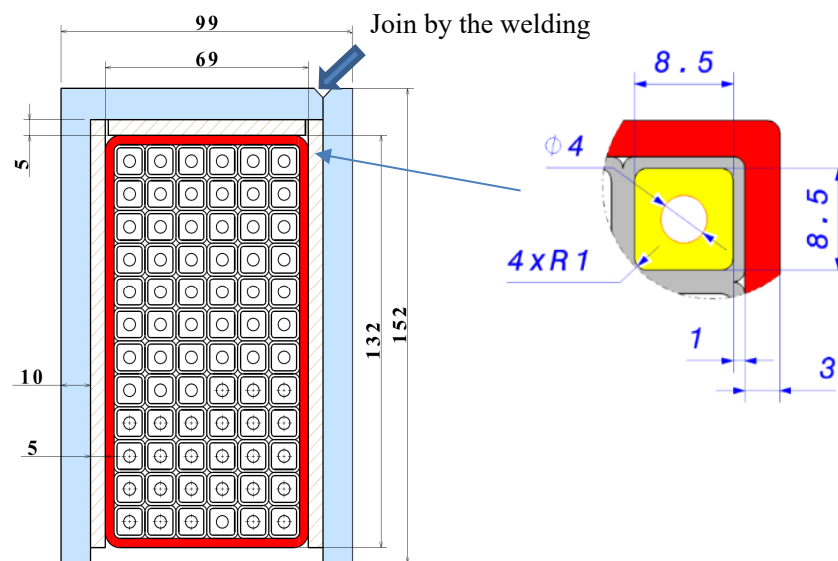Fig. 4.2.1-1   Modular coils, showing the legs, supports and SUS cases.

Fig. 4.2.1-2   Cross section of a modular coil, composed of 72 hollow conductors. The coil is covered in two plates (blue, L shape plate and lid) of SUS case, some FRP spacers (hatting) are inserted for adjusting gap and the two plates of SUS case are joined by the welding.
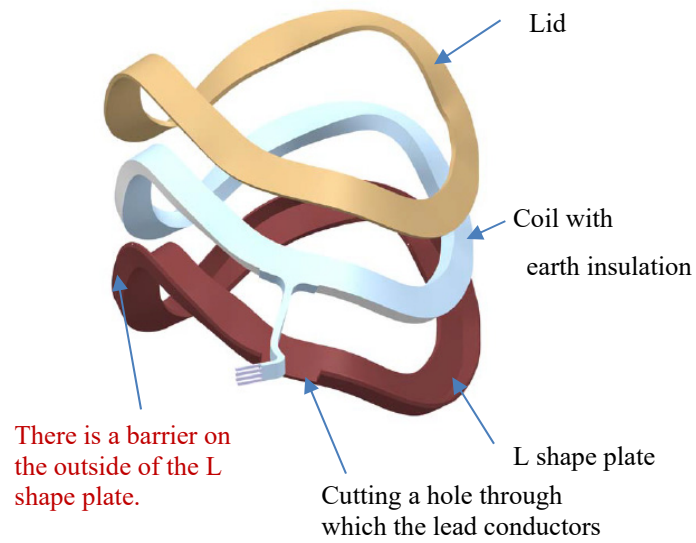
Fig. 4.2.1-3 Coil case and coil with insulation. There is a barrier on the outside of the L shape plate, that may interfere with the case when it is put in the case. A similar interference problem may occur in the process of the coil removing from winding frame.

u_n is a normal vector of the Current Carrying Surface

$\theta=20°$ for M1,M2,M3
$\theta=30°$ for M4
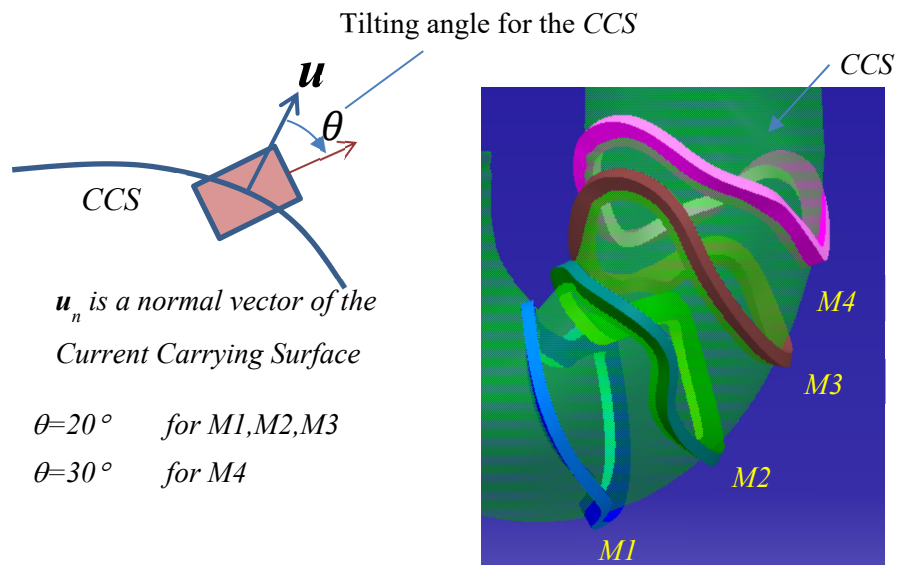
Fig. 4.2.1-4 Normal direction of the rectangular cross section, determined from the engineering view point. If the tilting angle θ were 0 degrees, the coil interfered with the case when the coil is put in the case.

4.2.2   Engineering design of poloidal field coils

Two pairs of PFCs will be installed to the CFQS. Main purpose of poloidal field coils is to apply vertical field to change the position of magnetic axis. Parameters of poloidal field coils are as follows.

Table 4.2.2-1   Parameters of PFCs

Parameters	unit	OV	IV	remarks
R	m	1.695	0.536	
Z	m	1.100	0.900	
DR	m	0.048	0.09	
DZ	m	0.09	0.048	
Conductor Current	A/turn	4.34E+03	4.34E+03	
pulse length	s	1	1	
Number of coils		2	2	
Cross-sectional area	m^2/turn	5.880.E-05	5.880.E-05	
turns		32(8×4)	32(8×4)	1 coil
Current	AT	2.78E+05	2.78E+05	2 coils
Length of conductors	m/turn	10.6	3.4	
	m/coil	340.8	107.8	
Resistivity	Ωm (75℃）	1.90E-08	1.90E-08	
Resistance	Ω/turn	3.43E-03	1.09E-03	
	Ω/coil	1.10E-01	3.47E-02	
Resistance component of Voltage RI	V	953.3	301.5	2 coils
Nagaoka coefficient		2.00E-01	2.00E-01	
Inductance	H	2.58E-02	4.80E-03	1 coil
Time constant	s	2.35E-01	1.38E-01	
Stored magnetic energy	J	4.86E+05	9.04E+04	2 coils
Heating energy	J	4.14E+06	1.31E+06	2 coils
Current change rate	A/s	2.17E+04	2.17E+04	
Inductive component of Voltage	V	5.60E+02	1.04E+02	2 coils
Maximum PS voltage	V	1.51E+03	4.06E+02	

4.2.3 Engineering design of auxiliary toroidal field coils

Auxiliary TFCs will be installed to CFQS to control the rotational transform. At present design, we have designed total of 8 TFCs with two types. As the option, the total of 12 TFCs with three types are being designed. TFC3 is now under design. Parameters of TFCs are shown as follows.

Table 4.2.3-1   Parameters of TFCs

Parameters	unit	No.3	No.1	No.2	Remarks
Name		TFC10	TFC32	TFC70	
location	degrees	10	32	70	
turns	/coil	8	8	8	
current	A/turn	4,340	4,340	4,340	
Rise time	s	0.2	0.2	0.2	
Current change rate	A/s	2.17E+04	2.17E+04	2.17E+04	
number of coils		4	4	4	
Cross-section	m^2/turn	5.88E-05	5.88E-05	5.88E-05	
Resistivity	Ωm	1.90.E-08	1.90E-08	1.90.E-08	at 70°C
Perimeter	m	3.39	3.12	2.58	
Equivalent radius (Perimeter/2π)	m	0.540	0.497	0.411	
Length of conductors	m/coil	27.12	24.96	20.64	
Resistance R	Ω/coil	8.76E-03	8.07E-03	6.67E-03	
Inductance L (by FEM)	H/coil	1.50E-04	1.37E-04	1.13E-04	
Resistance component of Voltage	V/coil	38.03	35.00	28.95	RI
Inductive component of Voltage	V/coil	3.26	2.97	2.45	LdI/dt
Maximum PS voltage	V/PS	165	152	126	
Time Constant	s	0.0171	0.0170	0.0169	L/R
Stored magnetic energy LI**2/2	J/coil	1.41 kJ	1.29 kJ	1.06 kJ	sum= 15.1 kJ
Heating energy RI**2	J/coil	165 kJ	152 kJ	126 kJ	sum= 1.77 MJ

4.2.4 Design of supporting structure

The cage type support structure is shown in Fig. 4.2.4-1. A cage type structure with diagonal beams (DBS) and the modular coil cases (CCS) that prevents deformation by the overturning moments or vertical forces and handle the entire load. It also has, among other components, a vacuum vessel, other coils, and a diagnostic system attached to it. For use in future NBI experiments, we adopted a design that does not have pillars (OPS) around the large rectangular ports. Instead surrounding it with the diagonal beams.

Large tokamaks are typically designed with TFC wedges to support the centripetal forces. Since the CFQS cannot take this approach due to shape of constraints, it instead absorbs such a large force with the central connection board (CCB). There is a big rectangular hole in it to access the inside port on the vacuum vessel. The attractive forces between adjacent modular coils are canceled out by beams (BBM) sandwiched. Since this type of D-shaped coils are easily deformed by their own expansion force, they are reinforced by coil cases (CCS).
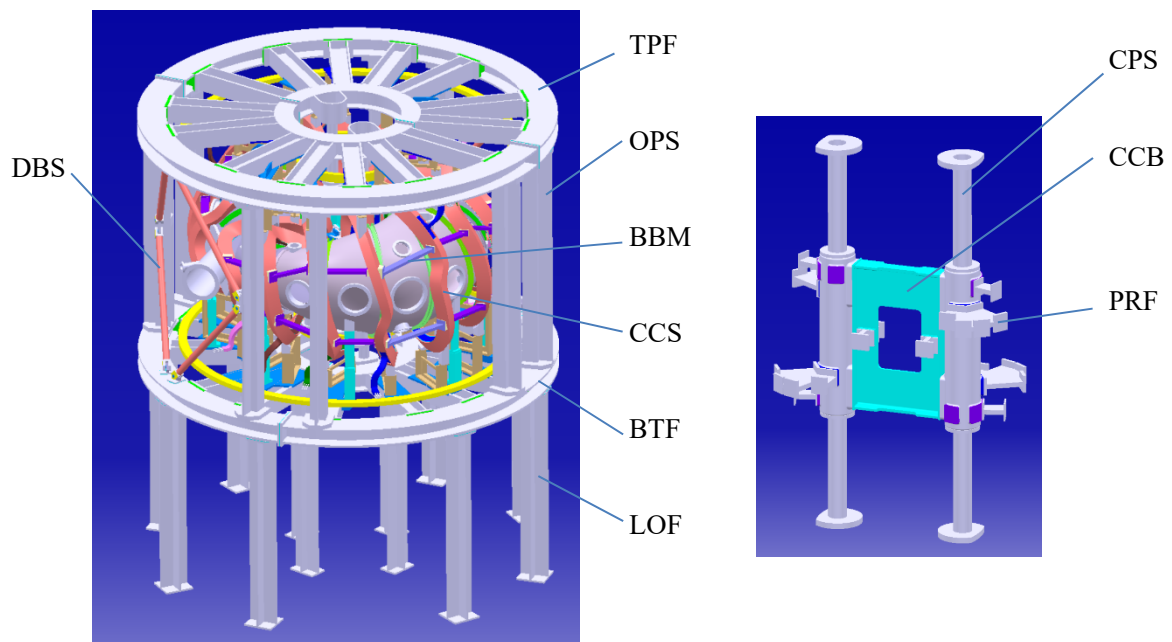
Fig. 4.2.4-1 Cage type support structure. Coil cases (CCS) absorb the modular coils' expansion forces. Outer pillars (OPS) and diagonal beams (DBS) prevent the overturning forces rolling the coils over. Beams between the modular coils (BBM) are used to cancel out the toroidal force imbalance. Two central pillars (CPS), one central connection board (CCB) and some pedestals receiving force (PRF) absorb the large centripetal forces. The vertical force and gravity are received by a top frame (TPF), a bottom frame (BTF) and legs of frame (LOF).

4.2.5   Electromagnetic force analysis of supporting structure

A strong support structure is necessary for keeping device in a safety state when operating it. As for magnetic confinement fusion device, the electromagnetic force is the main load on the coil system, which is the key component of whole device. Therefore, we need to understand the electromagnetic force on coil system and then design a reliable support structure.

4.2.5.1   Electromagnetic force on modular coils

There are total 16 modular coils, poloidal(vertical) field coils and toroidal field coils in this device. The following table shows the total current in each type of coils, Fig. 4.2.5.1-1 shows the coil system of CFQS.

<div align="center">Table 4.2.5.1-1   Currents in different coils</div>

Coil type	Current in one conductor	Total current in one coil
Modular Coil		4.34×72=312.5 kA Turn
Poloidal Field Coil	4.34 kA	4.34×32=138.8 kA Turn
Auxiliary Toroidal Field Coil		4.34×12=52.08 kA Turn
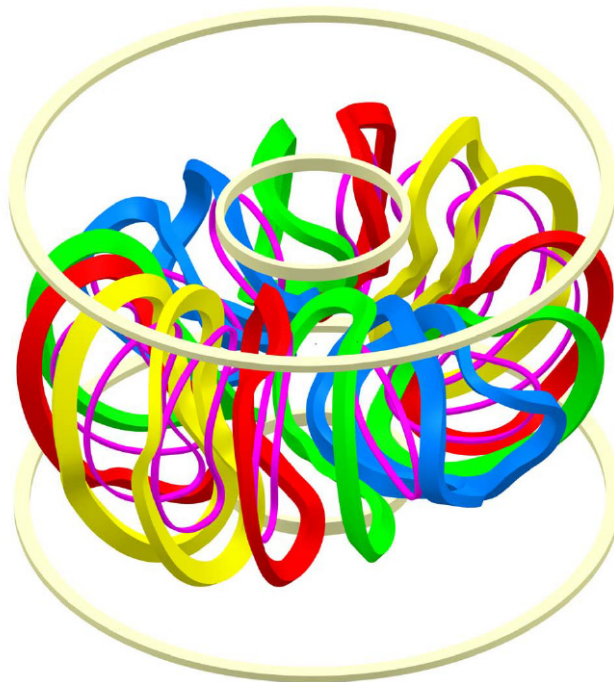
<div align="center">Fig. 4.2.5.1-1   CFQS coil system</div>

The modular coils are the major part of coil system, they have the most complicate shape and largest total current, so our analysis mainly focus on them. In our analysis, the FEA method is used, the results are calculated by ANSYS Maxwell and ANSYS Workbench. In Fig. 4.2.5.1-2, each coil name of modular coils is shown. Table 4.2.5.1-2 shows three major electromagnetic force components on modular coils. These three force component are defined in cylindrical coordinate system, the centripetal force is a R-axis component, vertical force is a θ-axis component, and vertical force is a Z-axis component.
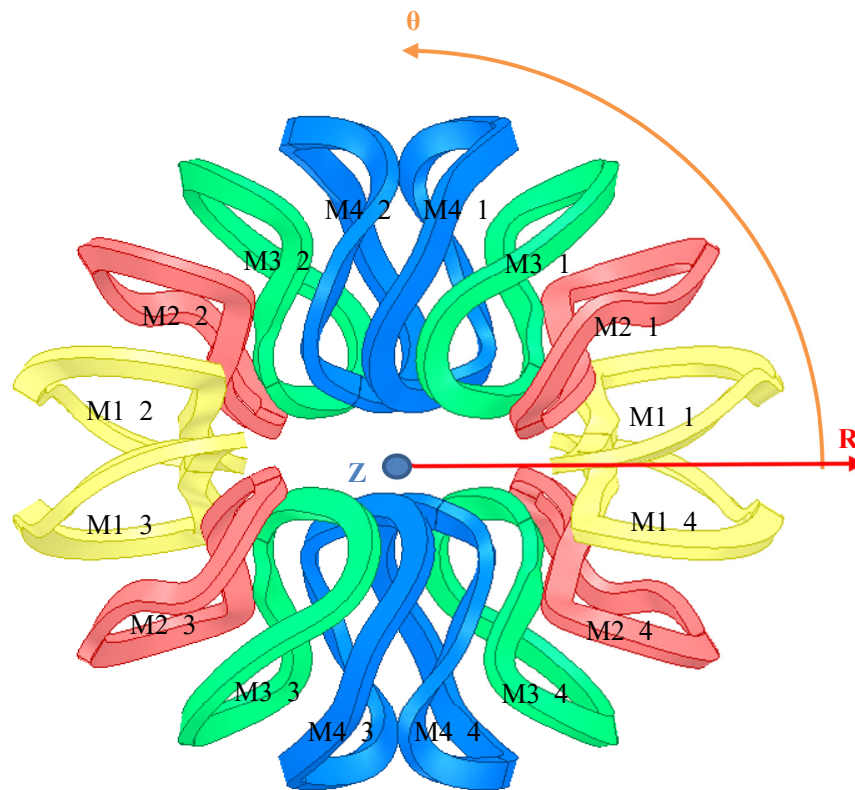
Fig. 4.2.5.1-2 Top view of modular coils

Table 4.2.5.1-2 Three major components of Electromagnetic force on modular coils

Coil Name	Centripetal Force (N)	Vertical Force (N)	Toroidal Force (N)	Total Force
M1_1	-167050	-19396	-13066	168680
M1_2	-167050	19393	13068	168680
M1_3	-167050	-19408	-13070	168680
M1_4	-167030	19401	13046	168660
M2_1	-142390	-60467	-37651	159210
M2_2	-142390	60463	37657	159210
M2_3	-142390	-60469	-37687	159230
M2_4	-142370	60470	37674	159200
M3_1	-94524	-92567	-37910	137620
M3_2	-94517	92568	37944	137630
M3_3	-94495	-92588	-37915	137620
M3_4	-94490	92559	37925	137600
M4_1	-39344	-38238	-45916	71542
M4_2	-39327	38242	45912	71532
M4_3	-39333	-38232	-45893	71518
M4_4	-39361	38243	45900	71544

Table 4.2.5.1-3 Differences of EM force components between tokamak and modular coils

Force Component	Tokamak TFC	CFQS Modular Coils
Centripetal Force	Very Large	Very Large
Vertical Force	Negligibly small	Large on some coils
Toroidal Force	Negligibly small	Small

Table 4.2.5.1-4　　　Differences of EM force between different type of modular coils

Coil Type	Centripetal force	Toroidal force	Vertical force	Overturning force
M1	Very Large	Small	Large	Small (Need further evaluate)
M2	Very Large	Small	Large	Small (Need further evaluate)
M3	Large	Small	Very Large	Large (Need further evaluate)
M4	Large	Small	Very Large	Large (Need further evaluate)

As we all known, CFQS is a tokamak-like device, so we refer the force component in tokamak toroidal field coils and get the result in Table 4.2.5.1-3 and Table 4.2.5.1-4, but we need further observation because these results are force components applied on gravity center of each coil. For designing support structure, we need to know the force distribution on coils. Fig. 4.2.5.1-3 - Fig. 4.2.5.1-14 show the distribution of different force components on different type of coils. For different type of coils, the magnitude of each force component is different due to the coil shape and position. From previous results, we can easily understand the force distribution on modular coils, it will be helpful for us to design and improve our support structure.
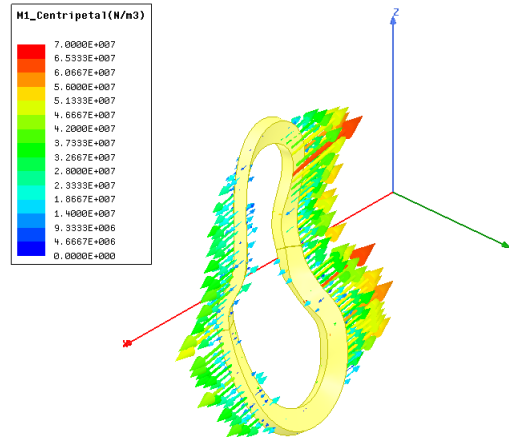
Fig. 4.2.5.1-3　Centripetal force on M1 coil
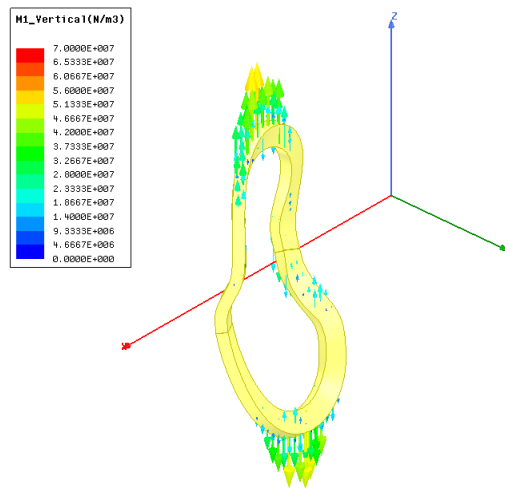
Fig. 4.2.5.1-4　Vertical force on M1 coil
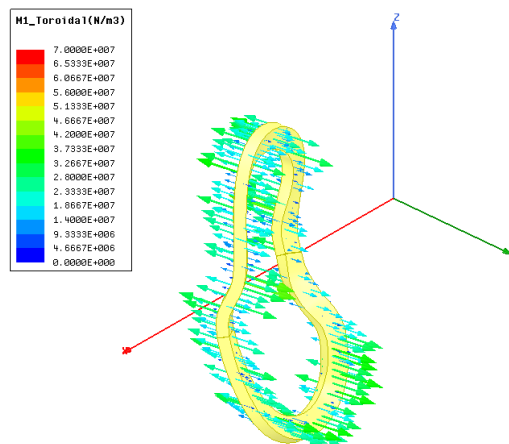
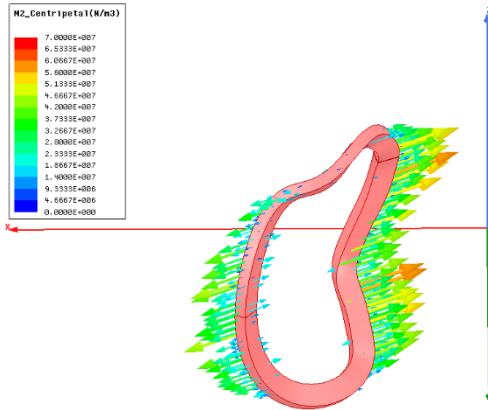Fig. 4.2.5.1-5　Toroidal force on M1 coil

Fig. 4.2.5.1-6   Centripetal force on M2 coil
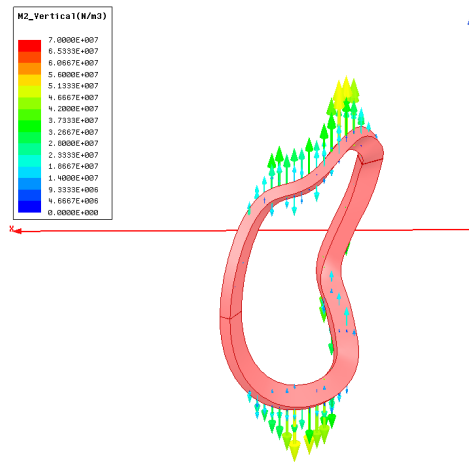

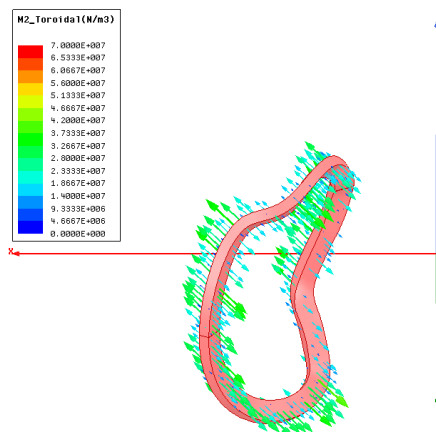Fig. 4.2.5.1-7 Vertical force on M2 coil

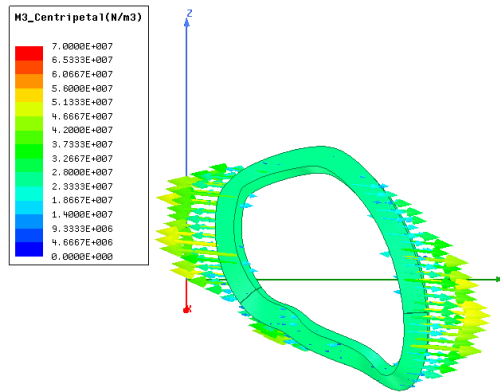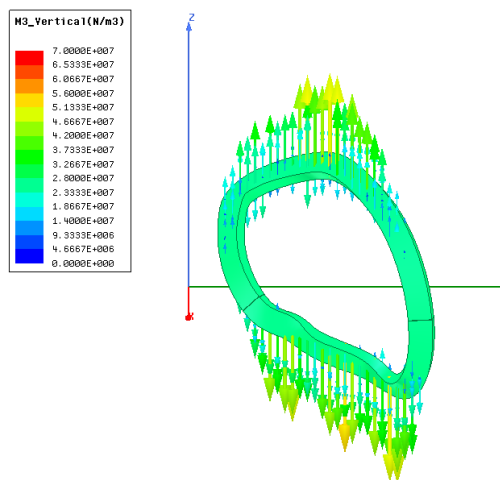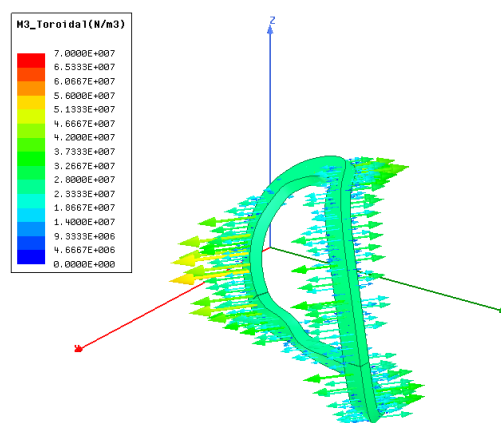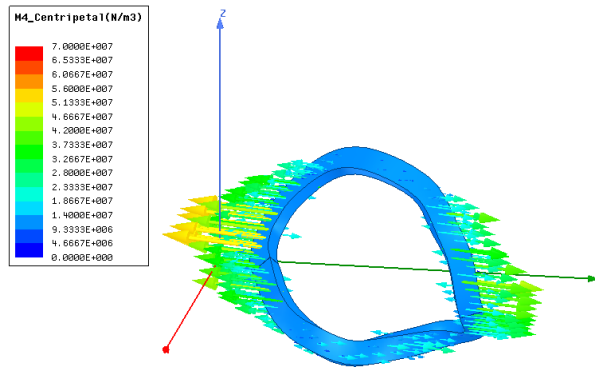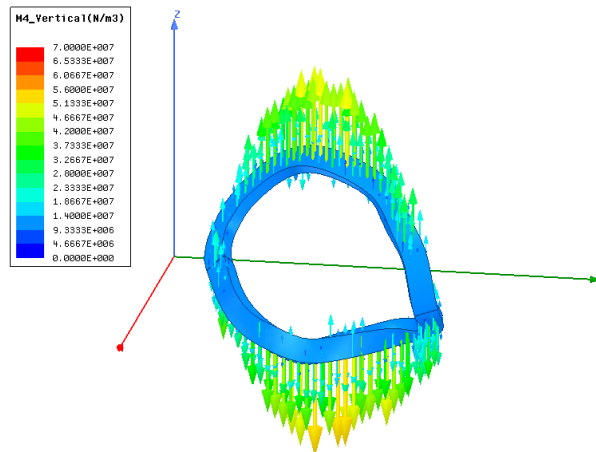Fig. 4.2.5.1-8   Toroidal Force on M2 coil

Fig. 4.2.5.1-9   Centripetal force on M3 coil
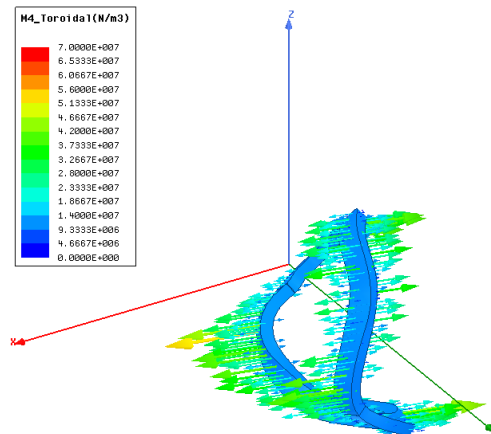

Fig. 4.2.5.1-10 Vertical force on M3 coil

Fig. 4.2.5.1-11 Toroidal force on M3 coil

Fig. 4.2.5.1-12 Centripetal force on M4 coil

Fig. 4.2.5.1-13 Vertical force on M4 coil

Fig. 4.2.5.1-14 Toroidal force on M4 coil

4.2.5.2 FEA of support structure

In our design, lots of small parts are used in supporting coil system. To make analysis easier, we divide whole structure into three major parts, 1) support frame, 2) center support, and 3) coil support. Fig. 4.2.5.2-1 shows the support structure, and Fig. 4.2.5.2-2(a)-(c) show the three major parts.
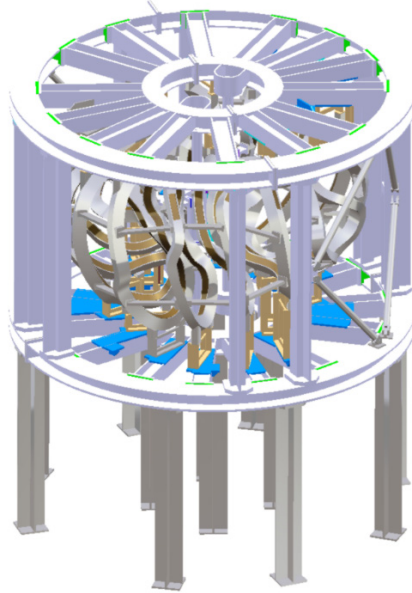
Fig. 4.2.5.2-1   3D model of support structure

According to previous result of electromagnetic force analysis, these three parts are used to support different force component. Support frame is mainly used for supporting vertical force and whole device, center support resists the large centripetal force, coil supports resist toroidal force , overturning force and coil's bending, moreover, they resist the centripetal force also.

To make sure the support structure is reliable, we need to check the stress, strain and deformation of the device. Refer to the allowable guideline (refer appendix in this booklet), the stress should be less than 140 MPa on main body of support structures (which are made by stainless steel), and less than 30 MPa on coils (which are made by copper alloy with resin). In addition, the total deformation and elastic strain should be less than 1mm and 0.1%.
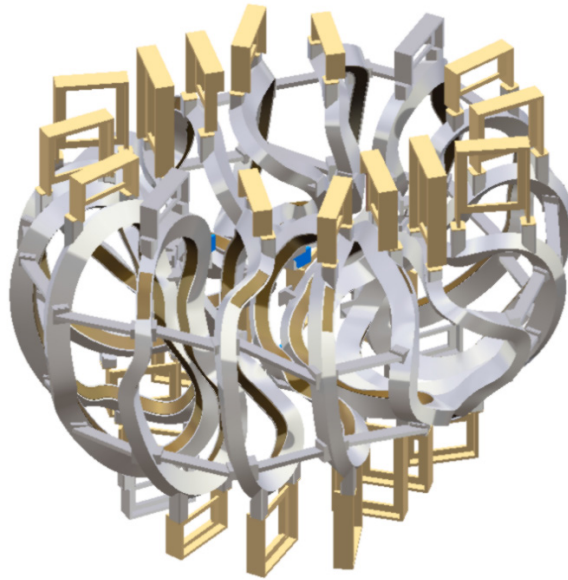
Here, previous result of electromagnetic force analysis is coupled into mechanical analysis by ANSYS workbench, bottom pillars of support frame are fix as the boundary condition. Fig. 4.2.5.2-3(a)-(i) show the mechanical analysis result.
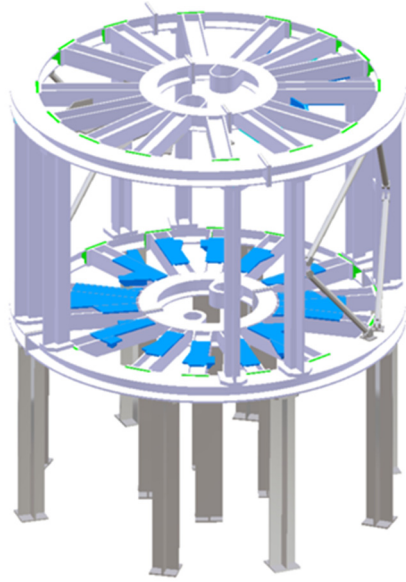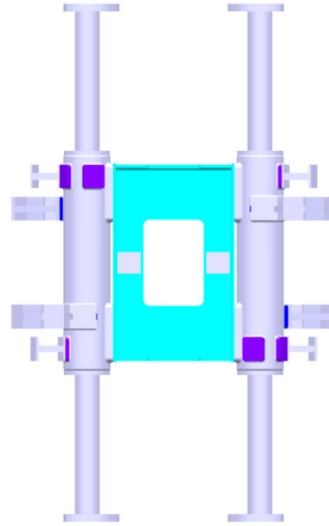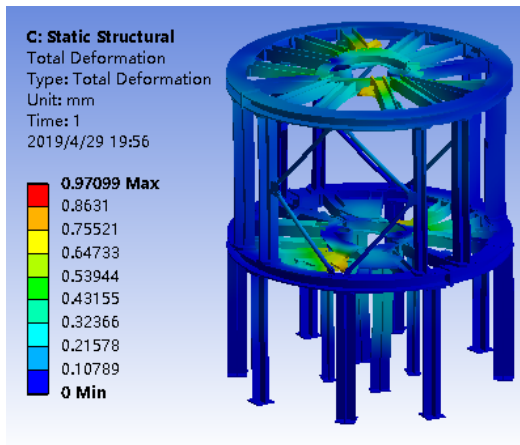
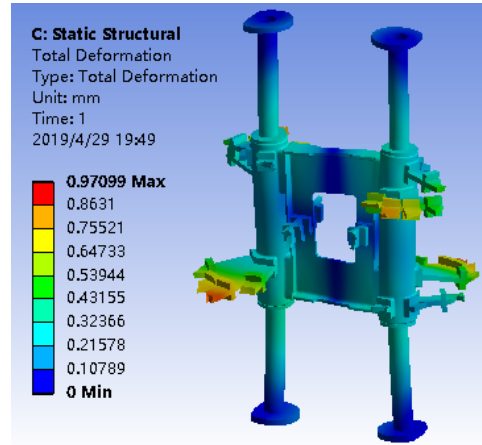(a) Support frame   (b) Center support
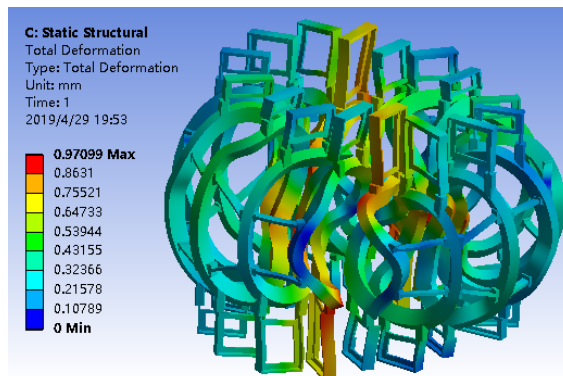

(c) Coil supports

Fig. 4.2.5.2-2   Three major parts of support structure
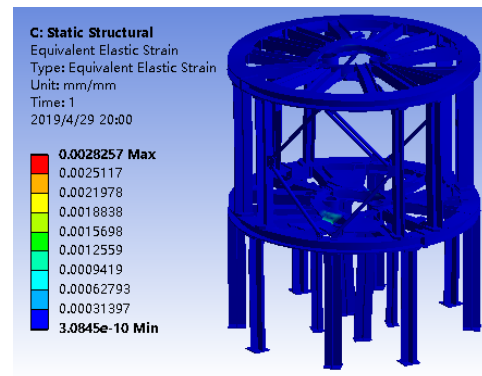
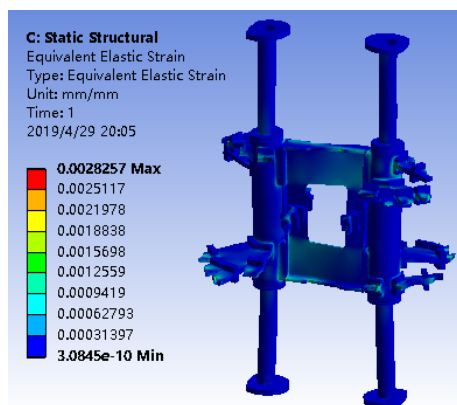(a) Deformation of support Frame

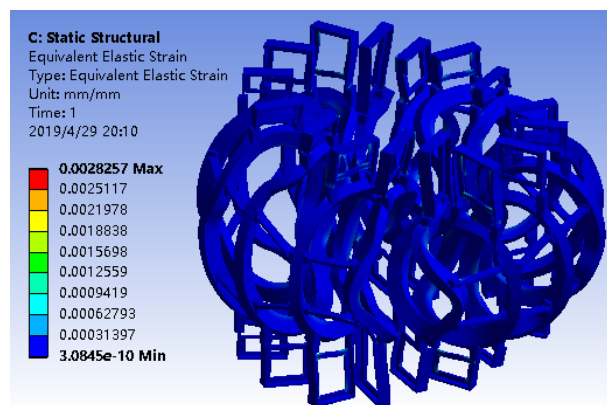

(b) Deformation of center support

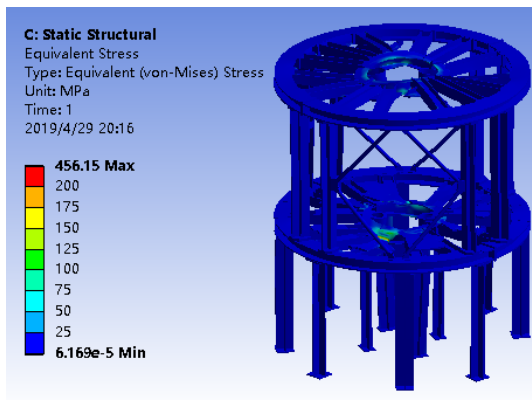(c) Deformation of coil support

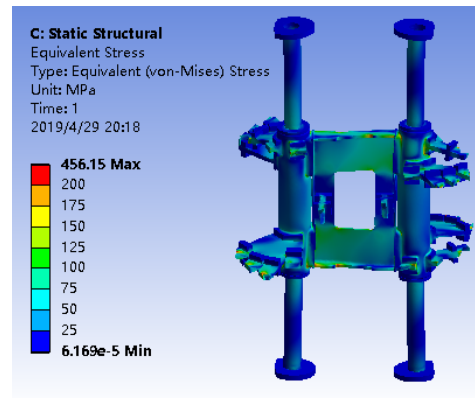(d) Elastic Strain on support frame

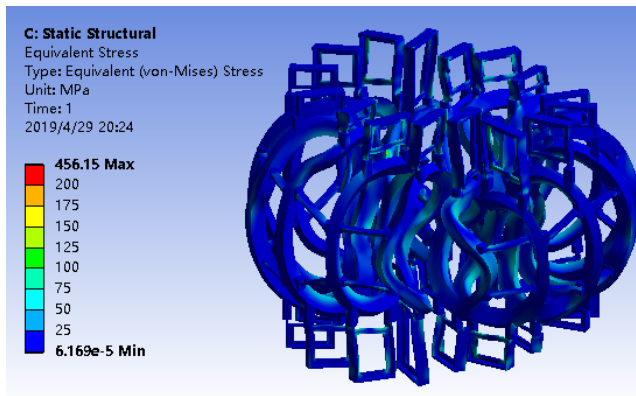(e) Elastic strain of center support

(f) Elastic strain of coil support

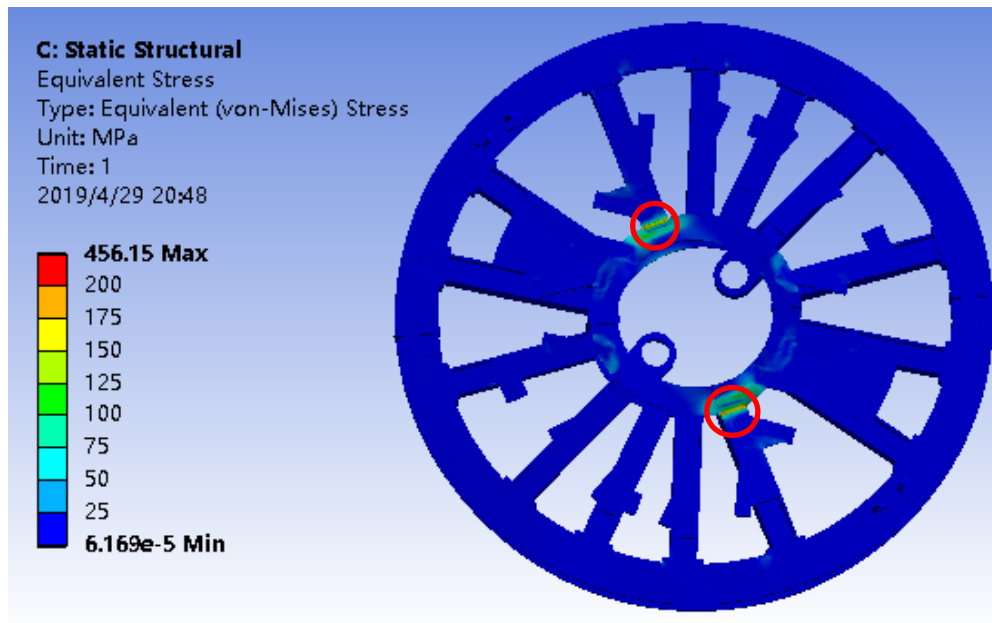(g) Stress on support frame   (h) Stress on center support
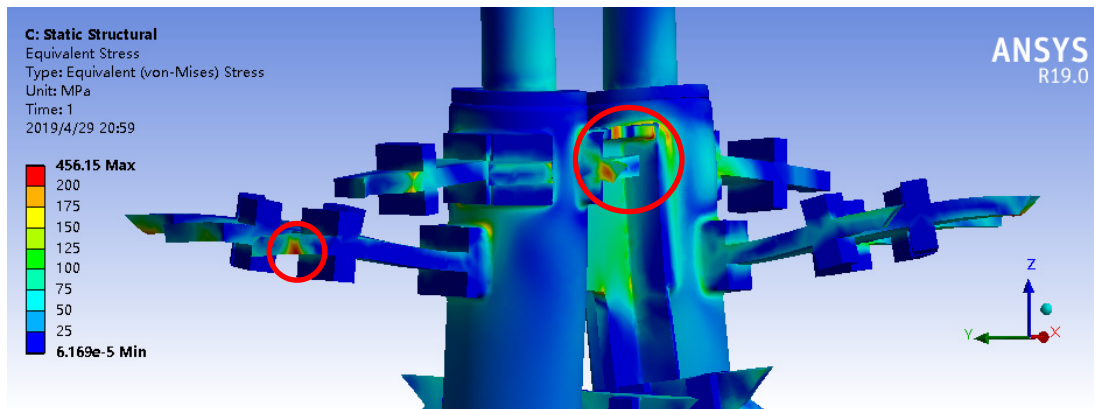

(i) stress on coil support

Fig. 4.2.5.2-3   Mechanical analysis result on support structure

It is obvious that the support structure satisfies the allowance deformation, stress and strain on main part, although there are some small areas still have high stain and stress, these large stress/strain areas are shown in Fig. 4.2.5.2-4(a)-(b). The appearance of these areas may be caused by calculation error (the element quality is not very good on these area) or large loads. These large stress/strain areas appear on bottom base, center support and coil cases. On these areas, the stresses are larger than 200Mpa, much larger than allowed stress (140Mpa) on stainless steel.

In Fig. 4.2.5.2-4 (a), the stress is larger than 140Mpa because the nearby bottom support beam must support vertical force of two coils (M3 and M4), which vertical force components are large. In Fig. 4.2.5.2-4 (b), due to the large centripetal force of M1, M2, M3 coils and bad element quality, the stress become large on some small area at contact region of coil case and center support.

(a) Large stress on bottom base (in the red circle)

(b) Large stress on center support (in the red circle)

Fig. 4.2.5.2-4 The largest stress area on support structure

For coils, the stresses are lower than 30 MPa on whole body (except some small area influenced by large stress applied on coil case), and deformation is smaller than 1mm. That means the coil case can successfully prevent the coils from deformation and large stress. Fig. 4.2.5.2-5(a)-(b), show the deformation and stress distribution on modular coils.

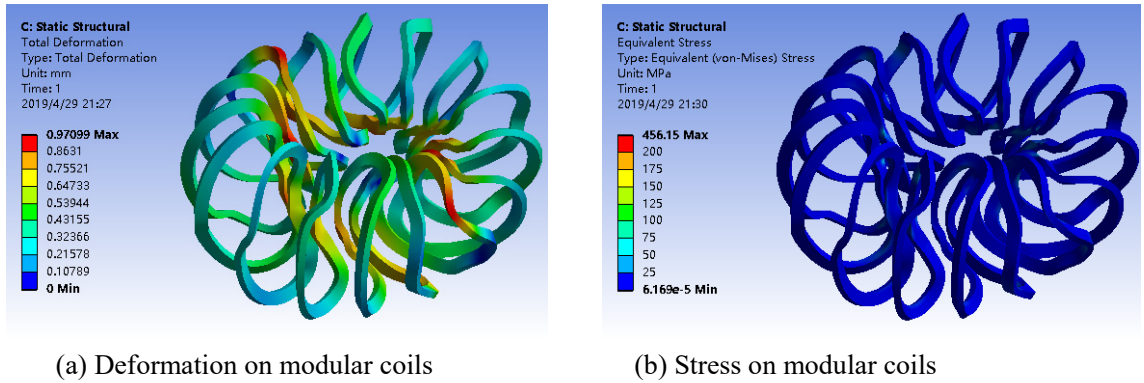(a) Deformation on modular coils   (b) Stress on modular coils

Fig. 4.2.5.2-5   . The deformation and stress on modular coils

According to our analysis result, this support structure can satisfy main design requirements, but it still need further improvement. Of course, a better result of electromagnetic force and mechanical analysis should be carried out, such as transient analysis with time varying current and add effects of poloidal or auxiliary toroidal coils would be much more closed to the real system.

4.2.6   Mockup coil of a modular coil

The total number of the CFQS modular coil is 16. The number of M4 coil is 4, and the M4 is the most complex coil. So the M4 mock up coil will be manufactured firstly.

4.2.6.1   Engineering design of the mock-up coil.

4.2.6.1.1   Conductor and insulation design of M4 mock up coil

The coil cross section is shown in the Fig. 4.2.6.1.1-1, the total turns of M4 mock up coil is 72. The conductor dimension used for the mock up coil is 8.5*8.5*Φ4mm, the layer insulation thickness is 1mm, and the ground insulation is 3mm.
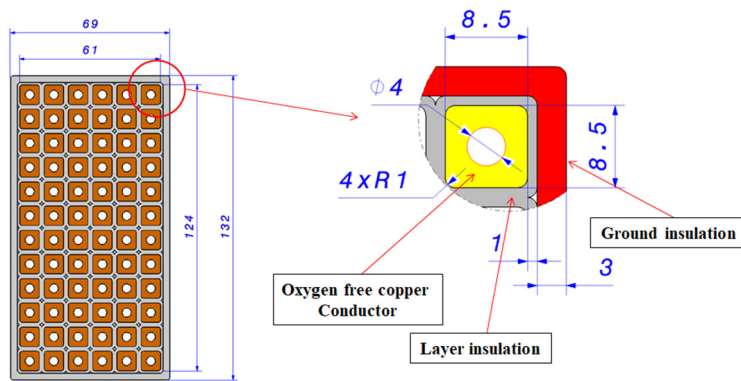

Fig. 4.2.6.1.1-1   Conductor and insulation of M4 mock up coil

Eight units Cu conductors have been purchased in Keye company, each unit length is about 100m. The material of the conductor for the mock up coil is oxygen-free copper and the chemical composition is shown in the   Table 4.2.6.1.1-1. The Cu content is 99.97% and oxygen content is 0.0008%. The mechanical performance of the conductor is shown in Table 4.2.6.1.1-2. The tensile strength is 239Mpa, and elongation is 45%. The dimension tolerance of the conductor is 8.5*8.5*Φ4 $\pm$0.08mm.

Table 4.2.6.1.1-1   The chemical composition of the Cu conductor

化学成分（%）Chemical Composition	Cu	O						
标准值 Standard Requirement 实测值 Test	≥99.97	≤0.002						
180829	99.97	0.0008						

Table 4.2.6.1.1-2   The mechanical performance of the Cu conductor

试验项目 Test 标准值 Standard Requirement 实测值 Test	外观·尺寸 Visual & Dimension	抗拉强度 Rm(Mpa) Tensile Strength	延伸率 A(%) Elongation	导电率(%) Electrical	气压 Pneumatic Pressure	耐击穿电压	钢珠通试
		≥205	≥35	≥100	合格		通过
180829	合格	239	45	100	合格		通过
检验员签章 Inspector:	技术条件 Technical Conditions:		备注 Remark :	上 海 上 大 众 鑫 科 技 发 展 有 限 公 司 SHANGHAI STARKING SCIENCE AND TECHNOLOGY CO., LTD 质保部 Quality Department			

The main material for the insulation is fiber glass tape and polyimide (Kapton) as shown in Fig. 4.2.6.1.1-2. The width and thickness of the fiber glass tape and the Kapton are 16 mm × 0.2 mm and 10 mm × 0.05 mm respectively for the mock up coil.
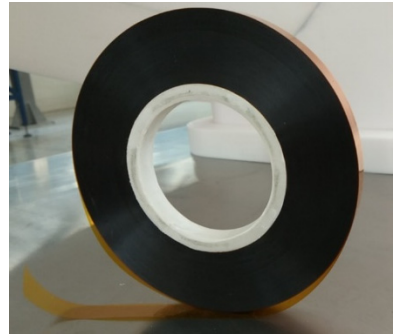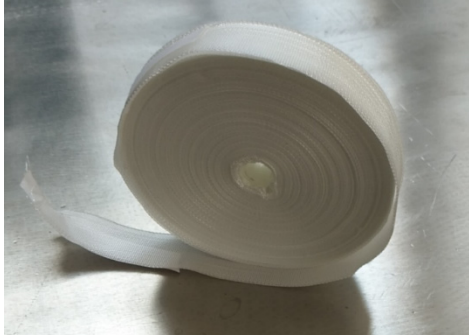
(a) Fiber glass tape

16 mm × 0.2 mm × 50 m

Tensile strength 1920 N/25 mm

(b) Polyimide (Kapton)

10 mm × 0.05 mm × 2000 m

Tensile strength 115 MPa

Fig. 4.2.6.1.1-2 Insulation materials

4.2.6.1.2   M4 mock up coil design

The structure design of the M4 mock up coil is shown in Fig. 4.2.6.1.2-1. It mainly consists of coil main body, layer to layer S-bending, turn to turn S-bending, coil joints and joint filler blocks.
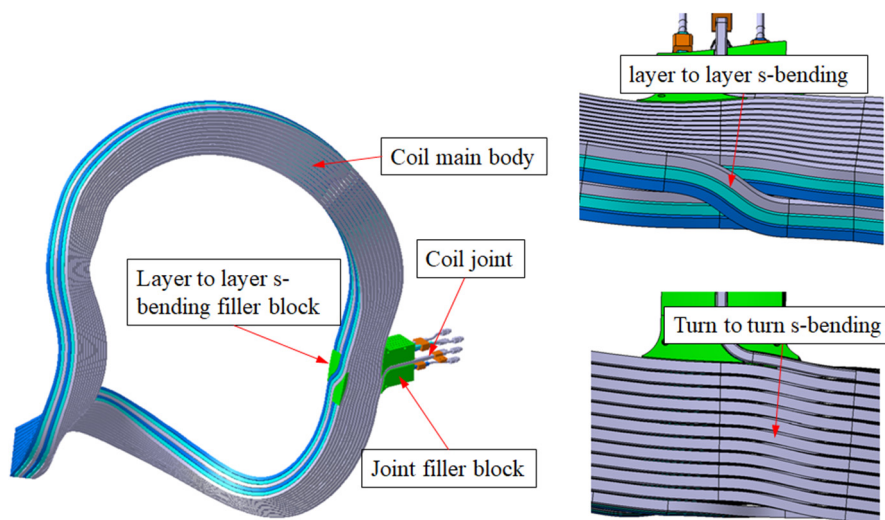

Fig. 4.2.6.1.2-1 M4 mock up coil design

4.2.6.1.3   M4 mock up coil joint design

In order to reduce the power supply, two joints are designed, as shown in Fig. 4.2.6.1.3-1. The joint_1 is used to connect layer 2 and layer 4; The joint_2 is used to connect layer 3 and layer5.The current for each coil is 4.34KA.
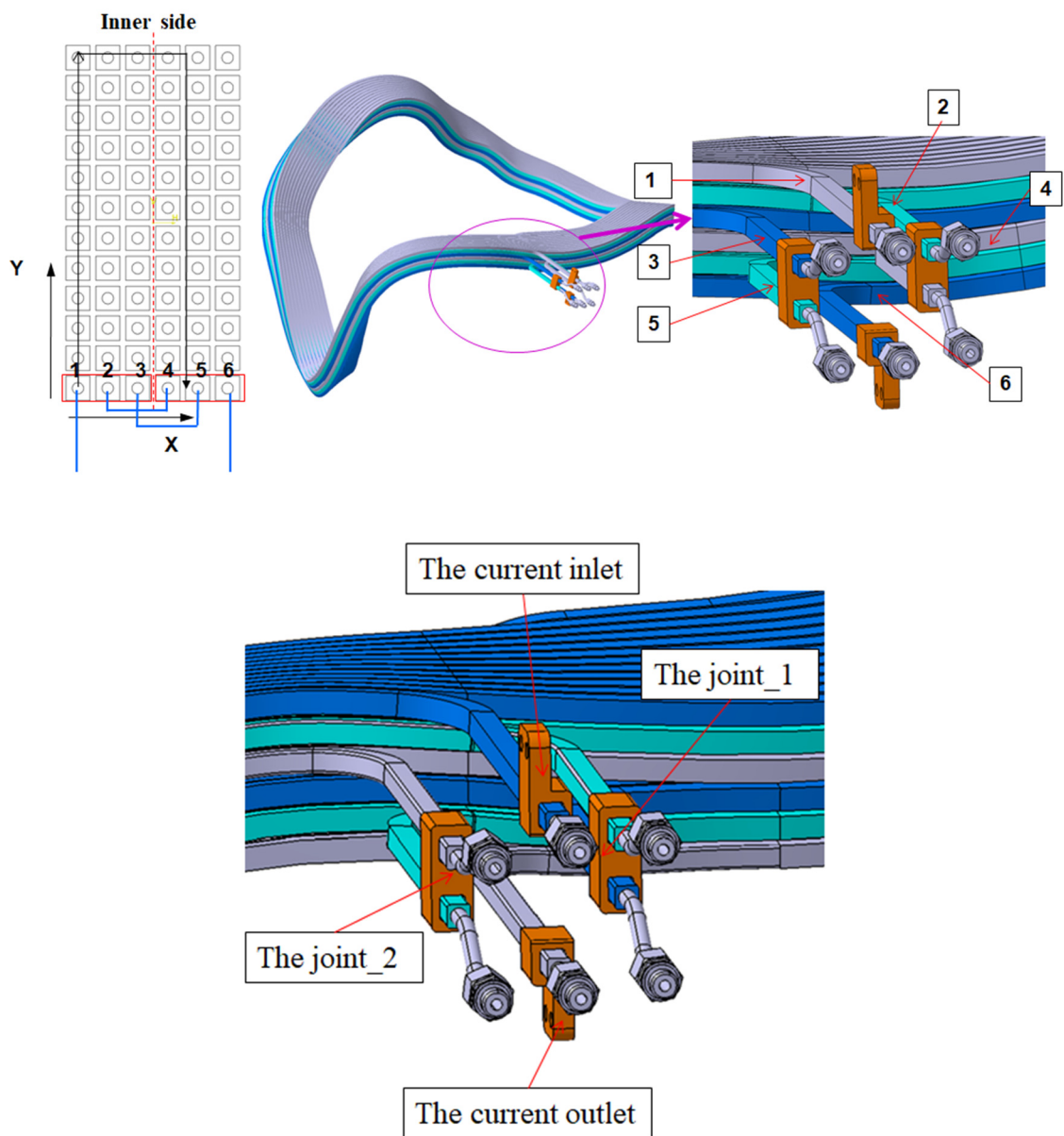

Fig. 4.2.6.1.3-1 M4 mock up coil joint design

A copper block is designed to connect the conductors, as shown in Fig. 4.2.6.1.3-2.

- Two square holes are designed on the copper block, the two conductors can be inserted from one side.
- After inserting of the conductors, the copper block will be welded with the conductors by silver brazing.
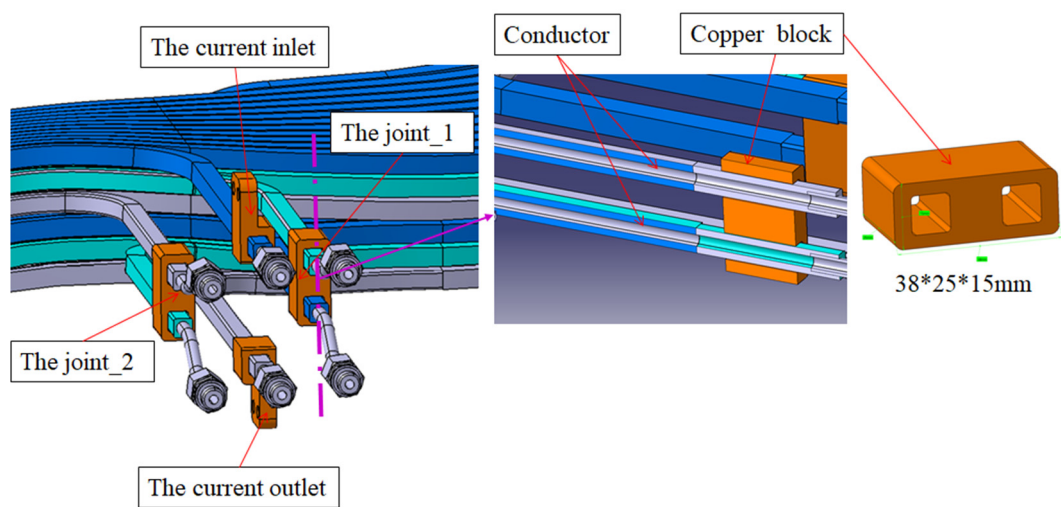

Fig. 4.2.6.1.3-2 M4 mock up coil joint detail design

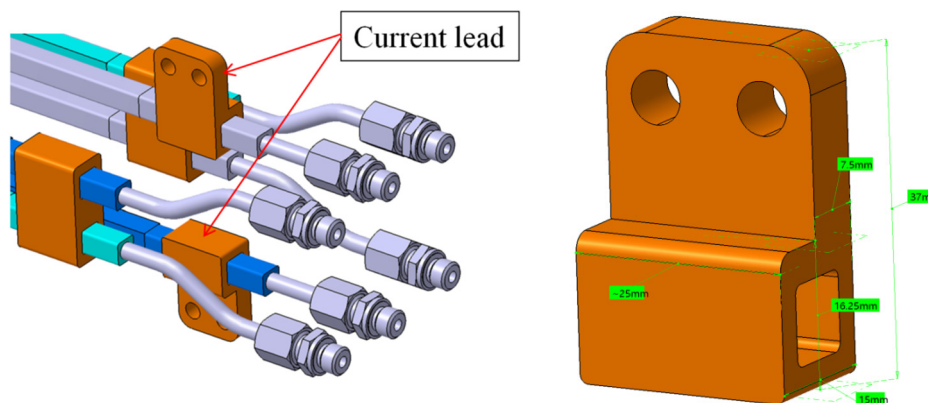### 4.2.6.1.4   M4 mock up Current lead design

Fig. 4.2.6.1.4-1 M4 mock up coil current lead design

A copper block is designed for current inlet and outlet, as shown in Fig. 4.2.6.1.4-1.

- A square hole is designed on the copper block, the conductor can be inserted from one side.
- After inserting of the conductor, the copper block will also be welded with the conductors by silver brazing.

4.2.6.1.5 Dimension of the joints

The joint position and dimension are shown in Fig. 4.2.6.1.5-1.

- The distance between the copper joint and coil main body is about 100-140 mm.
- After finish the coil winding, the coil main body has been wrapped with layer insulation. But for the joint area, there is no insulation.
- As the copper block and the water cooling pipes will be brazed with the conductors,   in order to avoid damage the insulation by the high temperature of the brazing, the cooper block should keep large than 100 mm distance with the coil insulation.
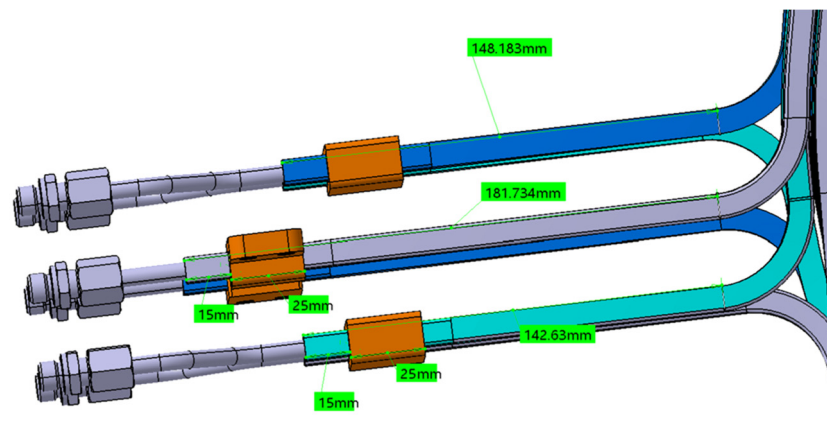- After brazing, the joint area conductors will be also wrapped with insulation.

Fig. 4.2.6.1.5-1 M4 mock up coil joint dimension

4.2.6.1.6 Cooling water joint design

A Φ6* Φ4 pipe is designed for the water cooling pipes as shown in Fig. 4.2.6.1.6-1. The material of the pipes is stainless steel. The terminal of the conductors will be drilled a Φ6mm hole for inserting of the pipe.

A standard water pipe joint is selected for the cooling water and the material is also stainless steel. The pipes will also be welded with the conductors by silver brazing.
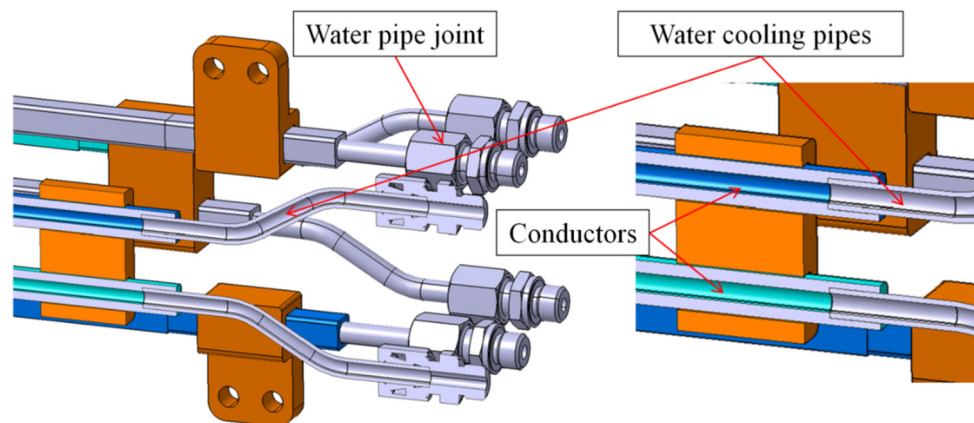
Fig. 4.2.6.1.6-1 M4 mock up coil cooling water joint design

4.2.6.1.7 Filler block design

The function of the s-bending filler block is to fill the gap of the s-bending area to provide a smooth surface for wrapping the 3mm ground insulation. The function of the joint filler block are:

- To fix all the joint conductors together to resist electromagnetic force.
- To fill the gap of the joint area for wrapping the 3mm ground insulation.

The detail design of the filler blocks is shown in Fig. 4.2.6.1.7-1.
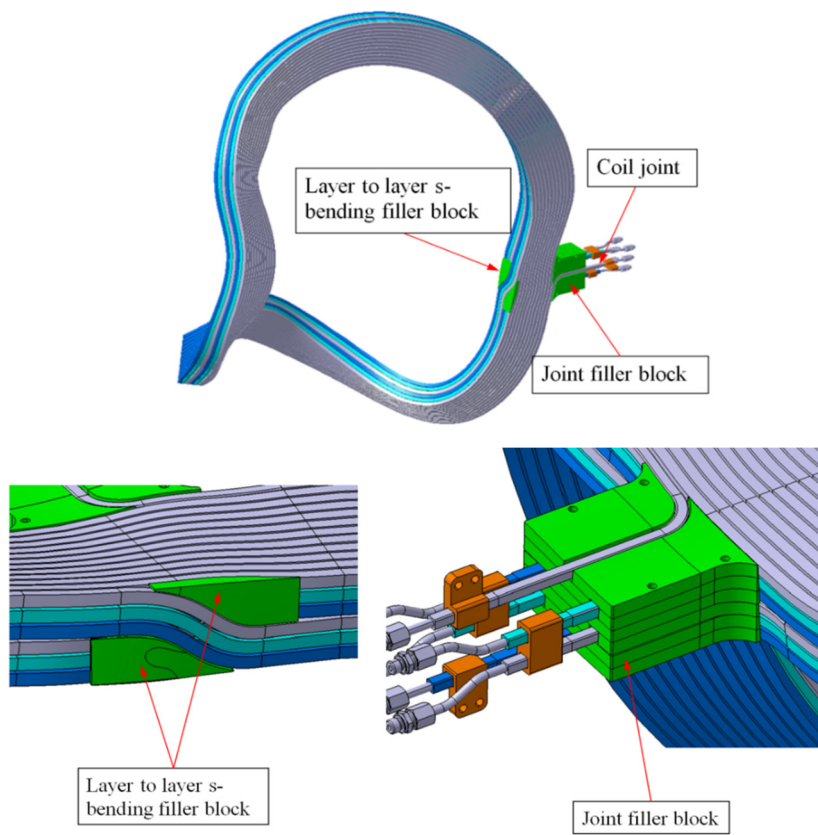
Fig. 4.2.6.1.7-1 M4 mock up coil filler block design

4.2.6.2   The winding mould design for the M4 mock up coil

The conceptual design of the coil winding manufacture line for the mock up coil is shown in Fig. 4.2.6.2-1. It mainly includes rotating platform, winding mould and clamping, copper conductors, insulation wrapping and conductor straightening.

Fig. 4.2.6.2-1   Conceptual design of the coil winding manufacture line

The winding mould has been designed base on the M4 coil profile shape, it consists of inner mould and bottom mould as shown in Fig. 4.2.6.2-2. The inner mould contains 12 types blocks.
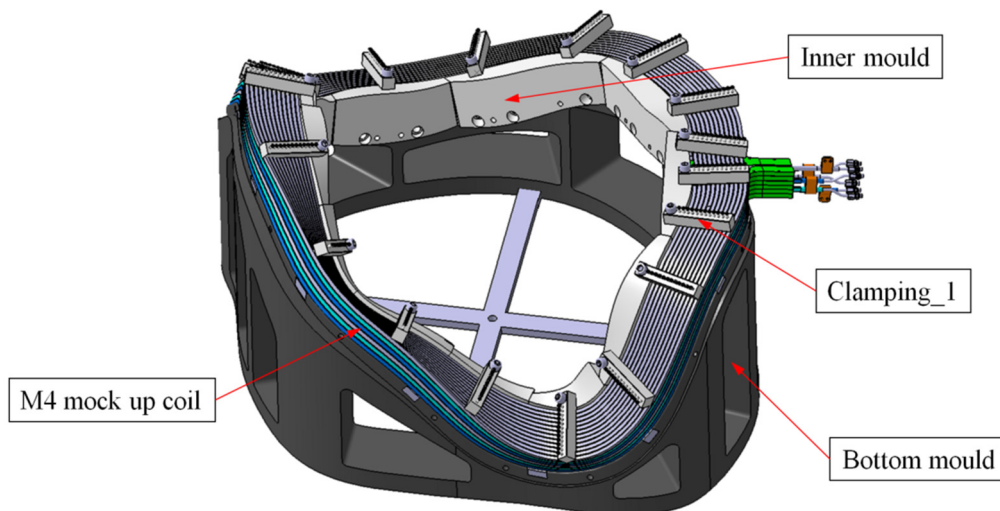
Fig. 4.2.6.2-2   The winding mould for M4 mock up coil

Fourteen grooves are designed on the bottom mould, as shown in Fig. 4.2.6.2-3. The function of grooves is for installation of the bottom plate of the clamping_2. The clamping_2 will be used to fix the coil after finish the coil winding.
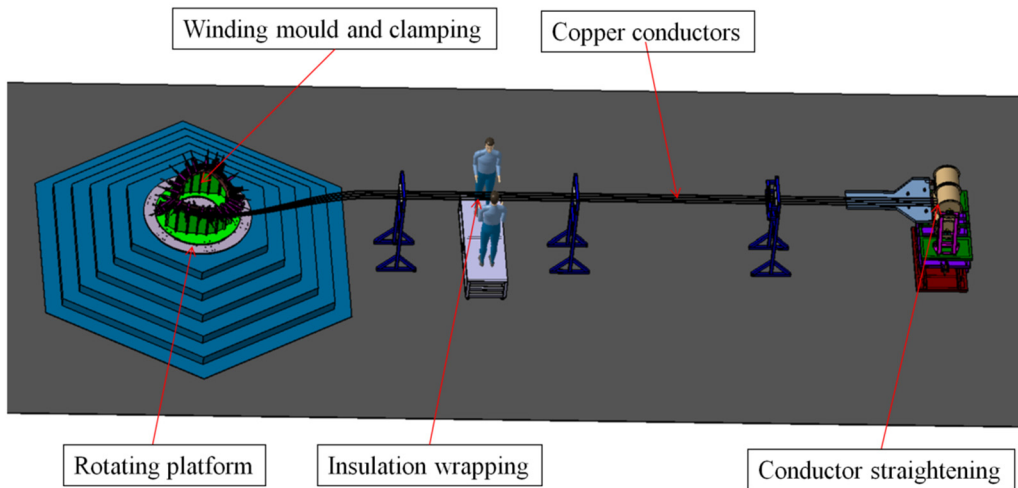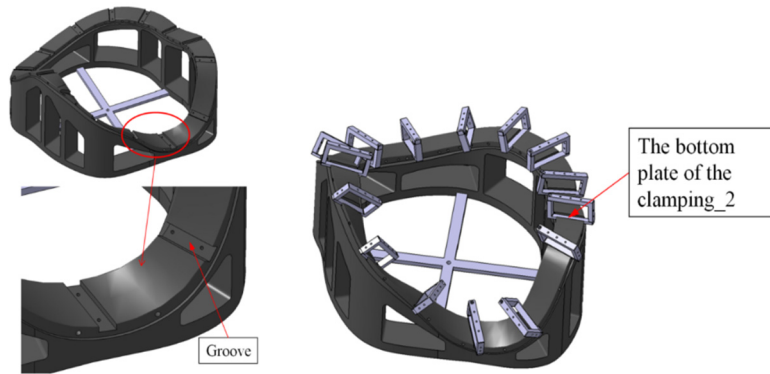

Fig. 4.2.6.2-3　The bottom mould design

The usage of the winding mould is divided into 2 stage as shown in Fig. 4.2.6.2-4:

- 1st stage: It will be used for the coil winding
- 2nd stage: It will be used for coil VPI

After finish the coil winding, the mock up coil will be fixed by the clamping_2 and removed from the winding mould. And then the mock up coil will be wrapped with the 3 mm ground insulation without winding mould. And the winding mould "L" surface will be machined 3 mm (ground insulation thickness) for the VPI. Before VPI, the mock up coil will be wrapped with 3 mm ground insulation and will be put on the winding mould again and adjust the shape of the coil by clamping.

Fig. 4.2.6.2-4　The usage of the winding mould

4.3 Vacuum vessel

4.3.1 Main vessel

✓ **Overall structure and port arrangement of main vessel**

Fig.4.3.1-1 shows a schematic of the main vessel, which will be manufactured by welding together four sections in the toroidal direction. The flanges used for welding are also shown in the figure. Since the electromagnetic forces on the vessel are expected to be small, it will be fabricated from SUS316L with relatively thin walls of 6 mm. As a result, th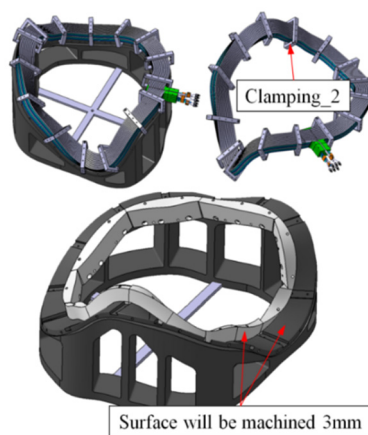e one-turn resistance is roughly 0.3 m which we believe to be sufficiently large while not producing significant joule heating. The walls will be conditioned by baking them at 130‑150 ℃ via induction heating at about 500 Hz.

The main vessel is fixed to the cage-type support structure by eight leaf-type legs, added to allow for the vessel's thermal expansion during baking. Winding frames have also been included on the vessel in order to wind the TFCs. The toroidal angle of splitting main vessel and placing the TFC's are show in Fig. 4.3.1-2.

More than 42 large ports with a diameter of at least 114 mm, will be provided for heating and measurement. Two of them are large rectangular ports both for a worker to enter and for use in NBI and Thomson scattering. As small ports of 70 mm or less in diameter are unexamined, there is a possibility that they can be added in the future if necessary for the experiment. Please refer to the appendix in this booklet for the structure and arrangement of ports and legs.

✓ **Procedure manufacturing each section of main vessel**

Fig. 4.3.1-3 shows the procedure to product one section of the main vessel. Each section is manufactured with 6 plates bent with mold, two large flanges to prevent welding deformation and several ports as shown in Fig. 4.3.1-4 and Fig. 4.3.1-5.

✓ **Assembly procedure and cross sectional shape of main vessel**

The main vessel will be assembled as shown in Fig. 4.3.1-6. We drew up a design plan in order to carry out this process and conduct various equilibrium experiments. The important points are as follows.

1) Minimizing field work for cost saving and reducing lead-time on site

2) Providing inspection process in the middle of the production and reducing the risk of backtracking work (all over again)

3) Thinking about how to respond to problems and designing a structure that can be repaired or modified.

4) Making it possible to utilize the space inside the vacuum vessel. It is difficult to access the vacuum vessel from the outside because a large number of parts, mainly coils, are installed nearby.

5) Providing a large port for entering the inside of the vacuum vessel, and ensuring a workable cross-

sectional area.

The shape of inner surface is shown in Fig. 4.3.1-7. The cross-sectional area is much larger than that of the 2b32 reference surface that is defined for the island bundle divertor experiment, and minimum space required from a physical point of view. The outermost magnetic surface of standard 2b40 equilibrium is narrower than the 2b32 surface. The minimum gap between the 2b32 plane and the inner surface of main vessel is about 30 mm. Please refer to the appendix of this booklet for the specific shape of main vessel at different toroidal angles.

The width and height of the inner surface are both at least 450 mm, which is sufficient for people to work inside. Using such a large vessel also helps to make the experiment more flexible. Two large rectangular ports with an opening diameter of 340 mm × 580 mm are also included, both for workers to enter and for use in NBI and Thomson scattering.
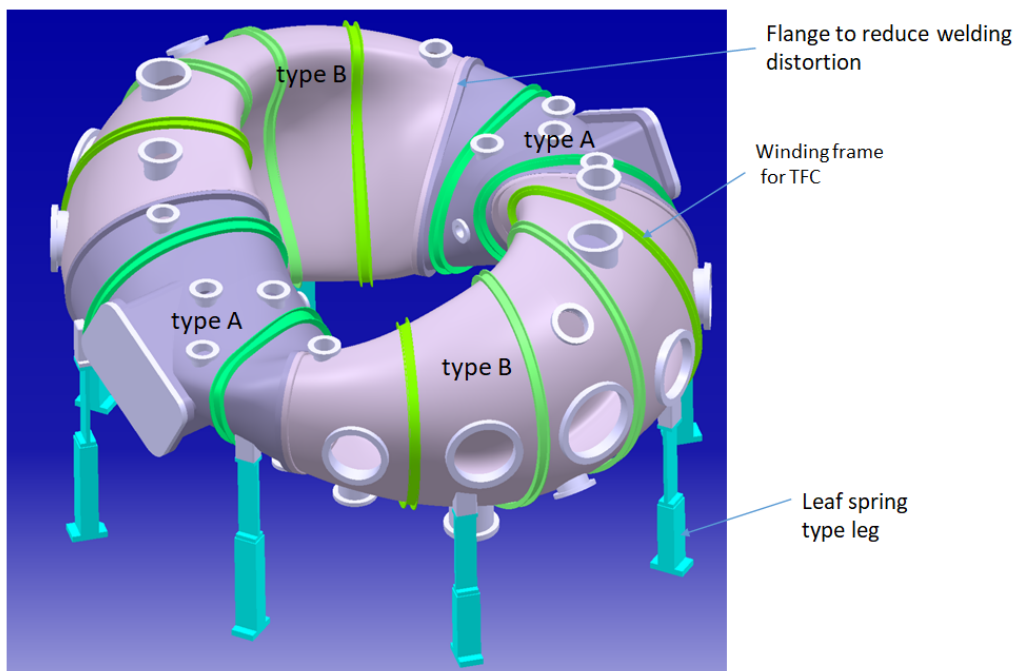

Fig. 4.3.1-1   Schematic of the vacuum vessel, which will be manufactured by welding together four sections of two types in the toroidal direction and supported by eight leaf-type legs. The flanges to prevent welding deformation are also shown. The vessel has twelve winding frames for the TFC (shown in green).

(a)

20 degrees

22 degrees

38 degrees

40 degrees

67.5 degree

(b)
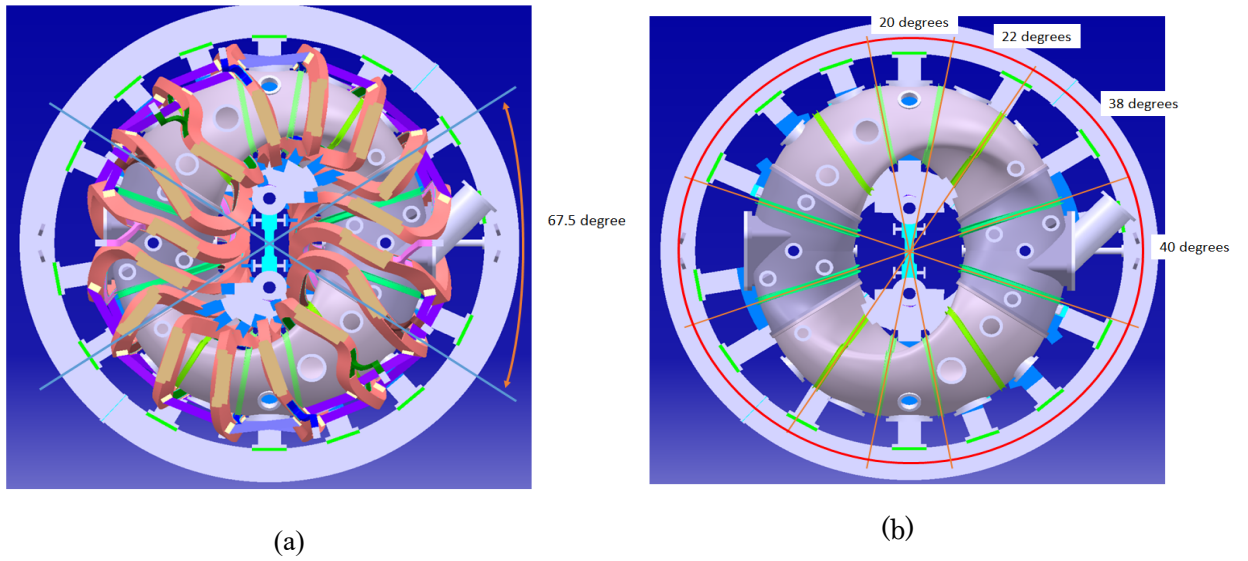
Fig. 4.3.1-2   (a) shows toroidal angle of spliting and (b) shows tha to place TFC's

Bending plates by the press forming

Attaching the welding deformation prevention jig

Machining the periphery of the plates

Welding bent plates together

Adding flange at split places with some extra

Correcting weld deformation

Making port holes on vacuum vessel

Welding port flanges and leg bases

adding TFC guides

Removing the welding deformation prevention jig

Machining flange surfaces at split places

Fig. 4.3.1-3   Procedure to product a section of main vessel.
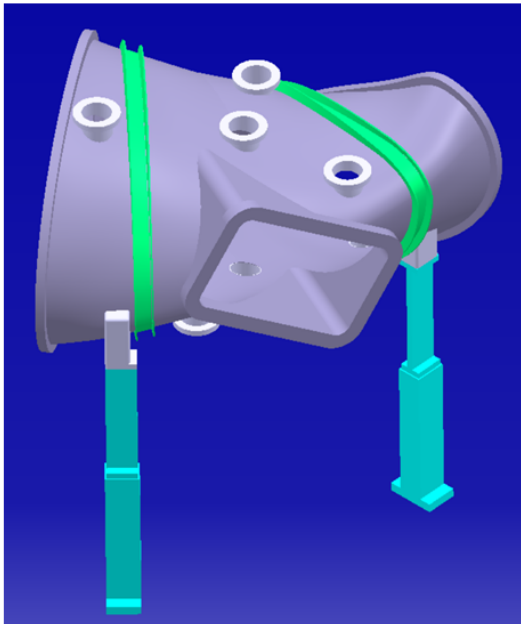
- Toroidal angle ; 67.5 degree
- 3 types of 6 plates bent with mold
- One rectangular port
- Nine circular ports
- Two leaf spring type legs
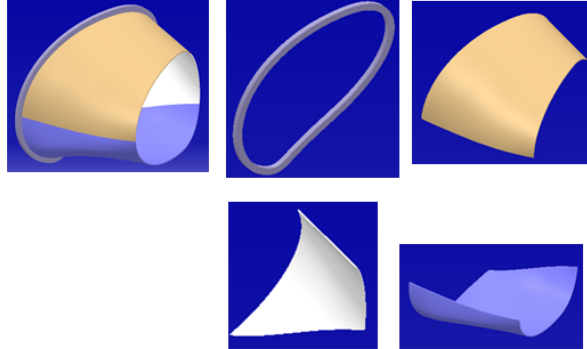
Fig. 4.3.1-4   Type A section of main vessel, that is manufactured with 6 plates bent with mold, 2 large flanges to prevent welding deformation and 9 ports
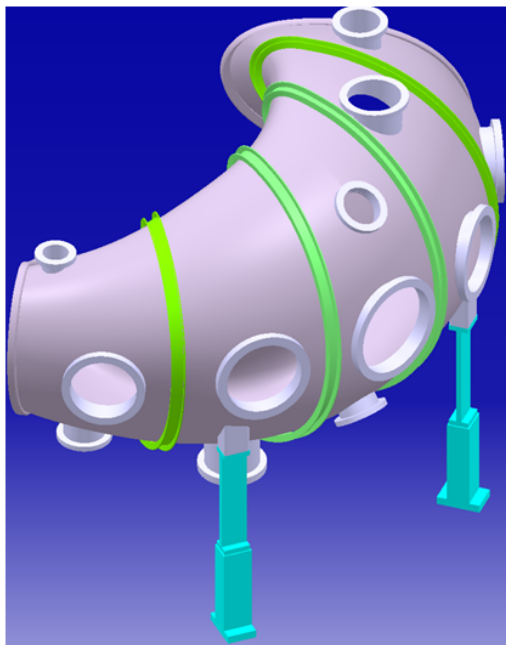
- Toroidal angle ; 112.5 degree
- Three types of 6 plates bent with mold
- Thirteen circular ports
- Two leaf spring type legs
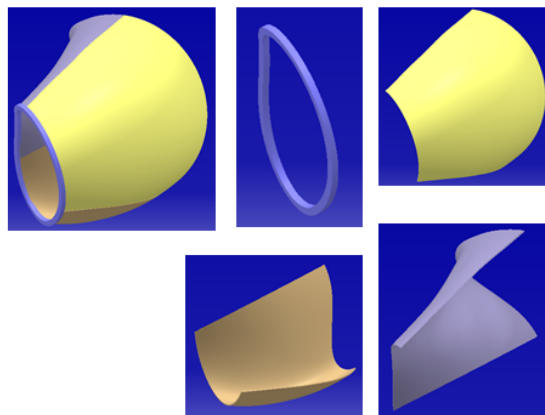
Fig. 4.3.1-5   Type B section of main vessel, that is manufactured with 6 plates bent with old, 2 large flanges to prevent welding deformation and 13 ports
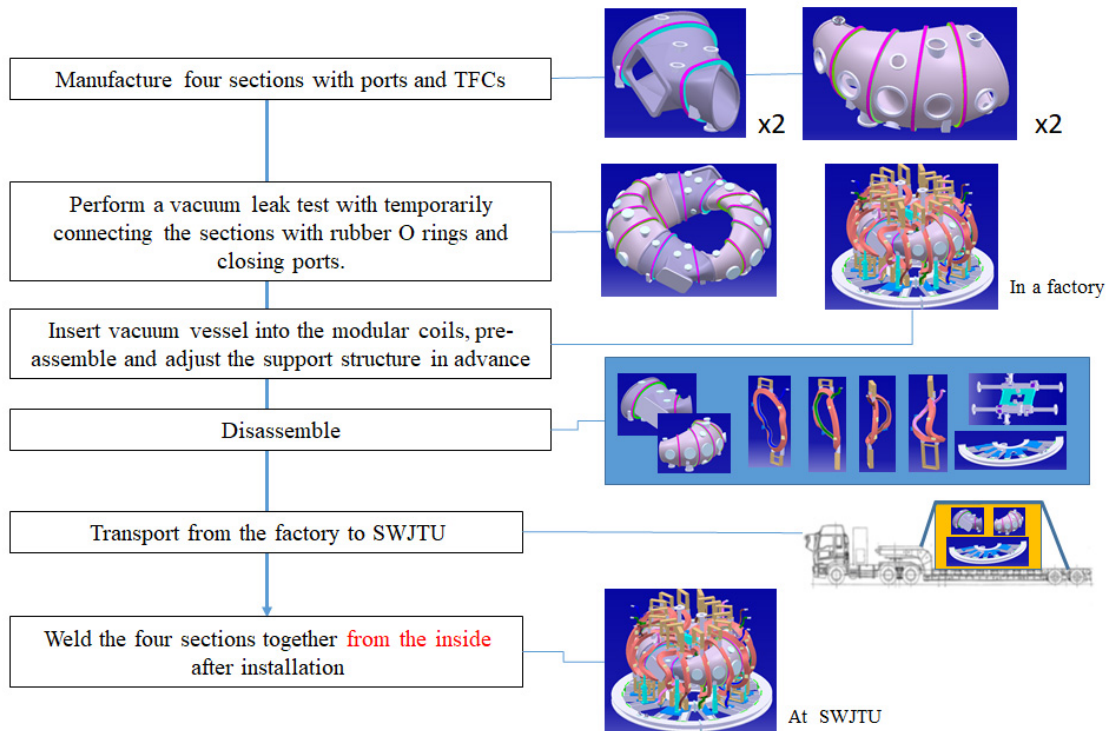
Fig. 4.3.1-6   Procedure to assemble a vacuum vessel and 16 modular coils.
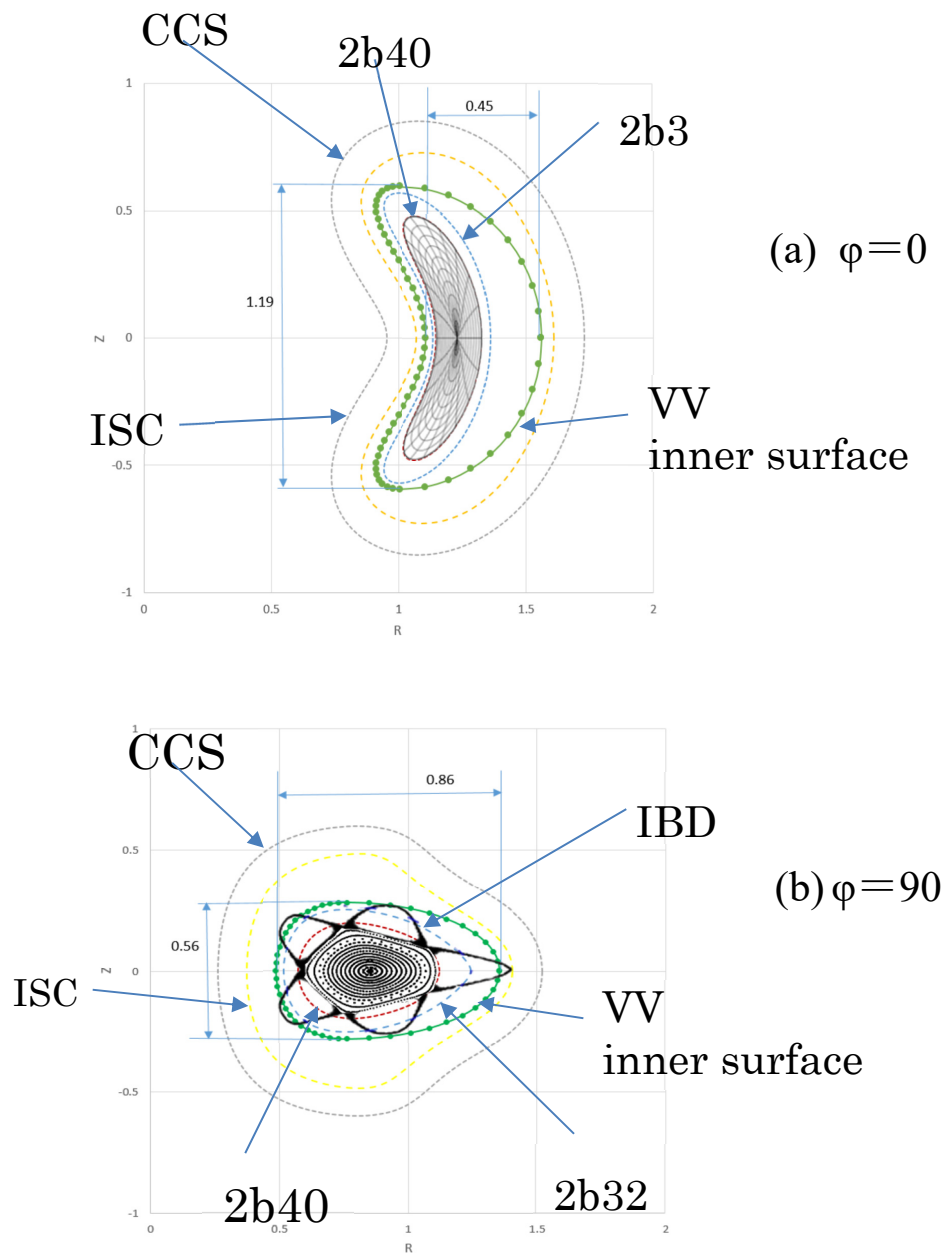
Fig. 4.3.1-7   Cross section of inner surface of main vessel. 2b40 shows an outermost magnetic surface of standard equilibrium confirmation (aspect ratio; 4.0), 2b32 a reference surface of IBD configuration (aspect ratio;3.2), CCS Current Carrying Surface on which the center of modular coil is placed, ISC Innermost peripheral Surface of modular Coil and IBD Island Bundle Divertor.

4.3.2   Finite element analysis for vacuum vessel

On plasma operation, the vacuum vessel is exposed to atmospheric pressure while keeping the inside in a vacuum. In addition, the thermal stress occurs due to thermal deformation during baking. To ensure that all stresses are within an allowable range on these conditions, FEM analysis for vacuum vessel have been done.

In this analysis, we have chosen 3 load cases as shown in Table 4.3.2-1.

Table 4.3.2-1   Condition of FEM analysis

|	Atmospheric pressure during vacuum evacuation	Thermal load during baking	Self-weight
Case 1	0.1 MPa	Nothing-	Ignored
Case 2	0	Temperature rise 100 °C	Ignored
Case 3	0.1 MPa	Temperature rise 100 °C	Included

The temperature distribution required as a thermal load is obtained by heat transfer analysis in advance, which is shown in Fig. 4.3.2-1(a). For simplicity, the vacuum vessel and bottom surfaces of legs have been fixed to 122 °C and 22 °C, respectively. Fig. 4.3.2-1(b) shows boundary conditions and load conditions for structural analysis. Atmospheric pressure (0.1 MPa) is applied on the outer surface as shown in red and the bottom surfaces of eight legs are fixed for constraint condition. Furthermore, gravitational acceleration is applied on the entire vacuum vessel considering a self-weight.

(a)   (b)
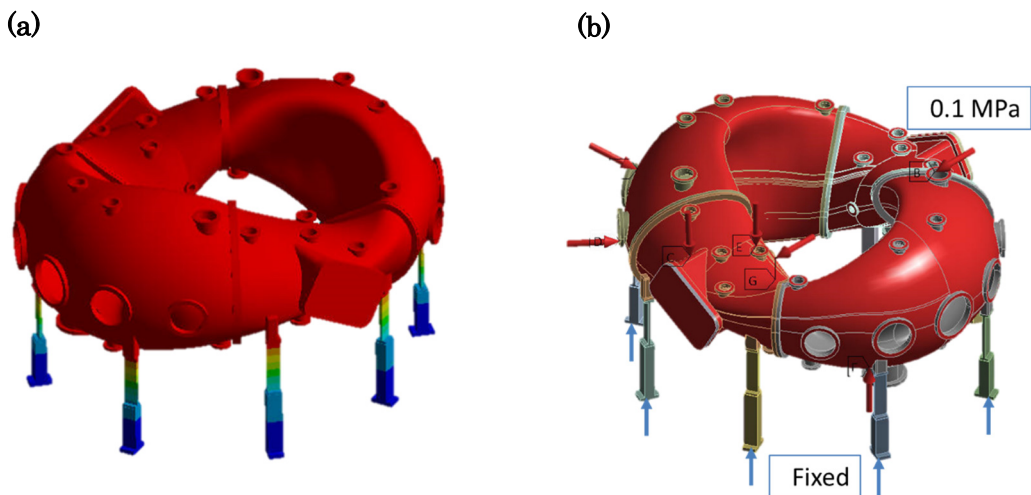
Fig. 4.3.2-1   (a) Temperature distribution during baking   (b) Boundary conditions and load conditions for structural analysis

Fig. 4.3.2-2 to Fig. 4.3.2-4 show the results of each cases, and (a) and (b) show equivalent (Mises) stress and deformation, respectively. In case 1, the maximum stress is 87.4 MPa which is less than design stress and the maximum deformation is 1.03 mm. In case 2, the maximum stress is 128 MPa near the leaf spring type legs, which is acceptable. In case 3, significant stress does not appear. Therefore, it is confirmed that there is no problem for structural integrity on these conditions.
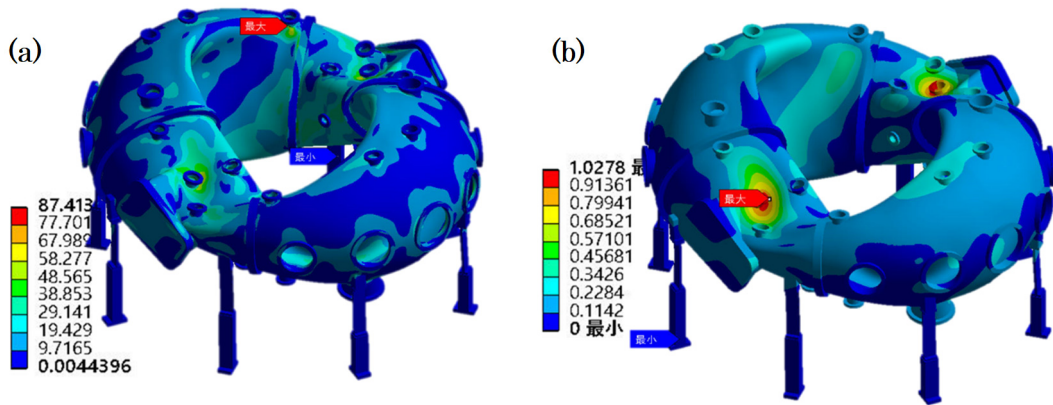
Fig. 4.3.2-2   Result of case 1   (a) Equivalent (Mises) stress [MPa]   (b) Deformation [mm]

Fig. 4.3.2-3   Result of case 2   (a) Equivalent (Mises) stress [MPa]   (b) Deformation [mm]

Fig. 4.3.2-4   Result of case 3 (a) equivalent (Mises) stress [MPa]   (b) Deformation [mm]

4.3.3   Eddy current on vacuum vessel

During the ramp up of the current in poloidal field coil (PFC), and toroidal field coil (TFC), the eddy current is produced in the vacuum vessel. The eddy current in the vacuum chamber is mainly characterized by the time constant, because it determines the life time of eddy current after finishing the ramp up phase. The FEM calculation model to estimate the eddy 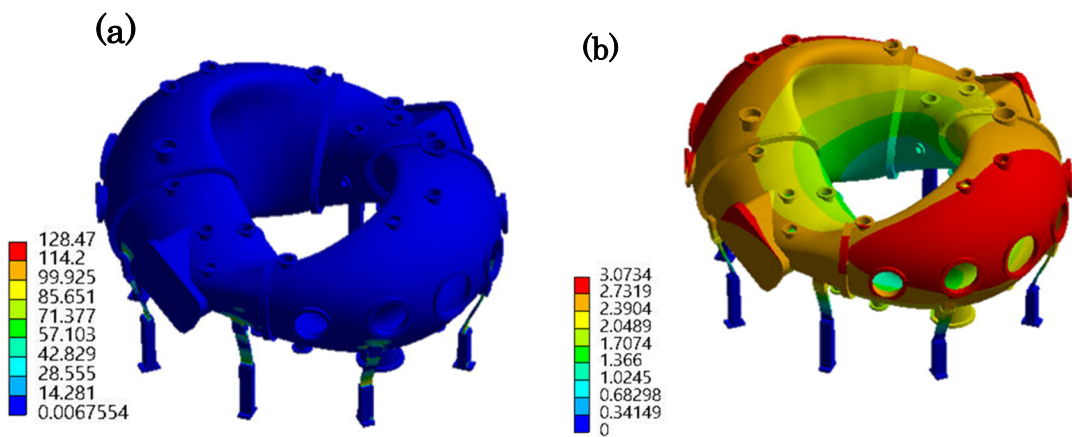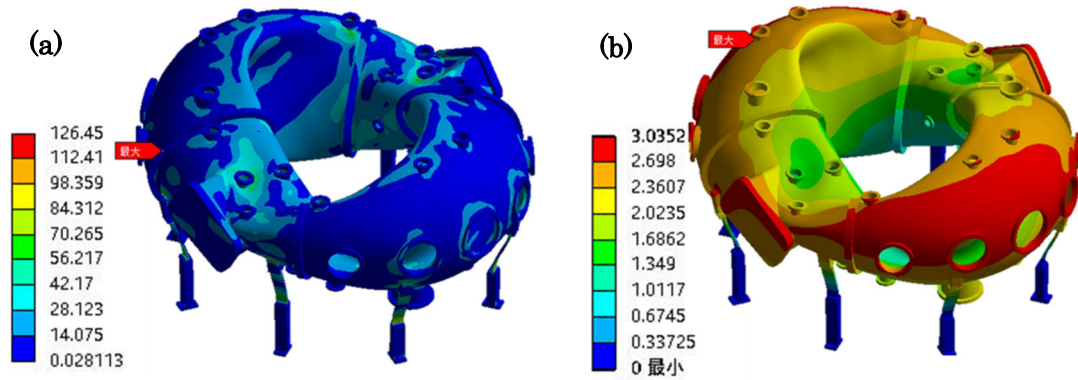current caused by PFC is shown in Fig. 4.3.3-1. Total of 265,000 elements is made for vacuum vessel and PFC to calculate the eddy current.

The eddy current density on vacuum vessel is shown in Fig.4.3.3-2, when the ramp down of the current in PFC is considered as shown in Fig.4.3.3-3 (a). The current density tends to be high near the opening, *i.e.* near the port. The time evolution of integrated eddy current is shown in Fig. 4.3.3-3 (b). Here, the eddy current is integrated over the poloidal cross section of vacuum chamber to calculate the total current of toroidal direction. Time constant of the eddy current caused by the change in PFC current is 4.4 ms, which is less than the flat top duration of modular coil current and plasma discharge time (~100 ms). Therefore, the effect of the eddy current caused by the PFC current change on the magnetic field configuration is not significant during the plasma discharge in CFQS.
Similarly, the time constant of eddy current caused by the change in toroidal field coil (TFC) current is estimated. The estimated time constant is 2.4 ms, which is also less than the flat top duration of modular coil current and plasma discharge time.
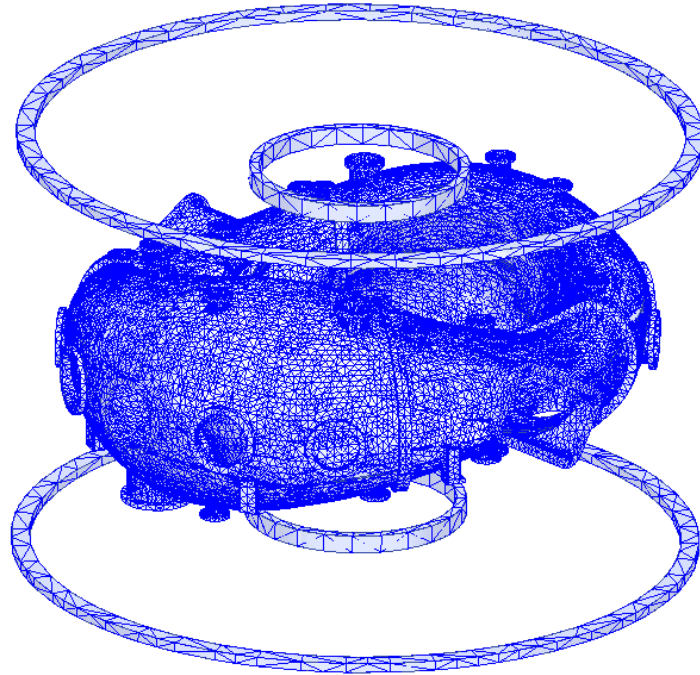
Fig.4.3.3-1　　　FEM model of PFC and vacuum chamber
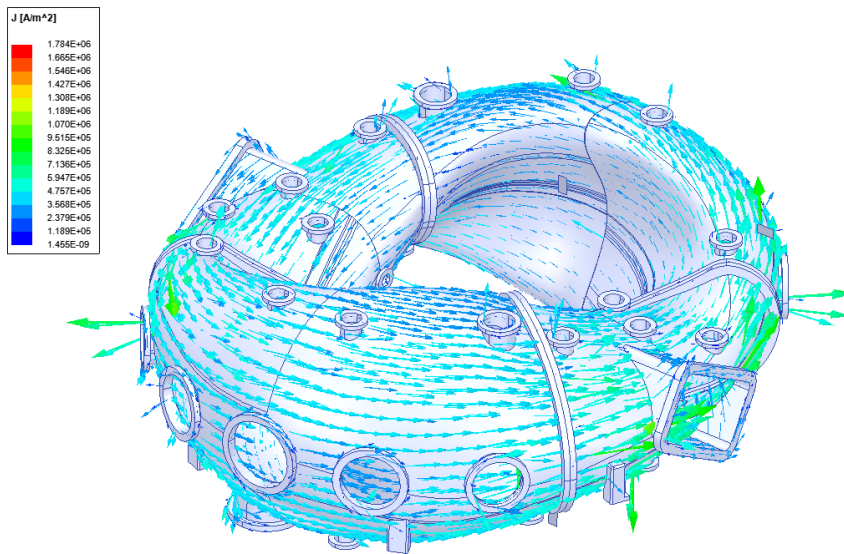
Fig.4.3.3-2　　　Current density on vacuum vessel
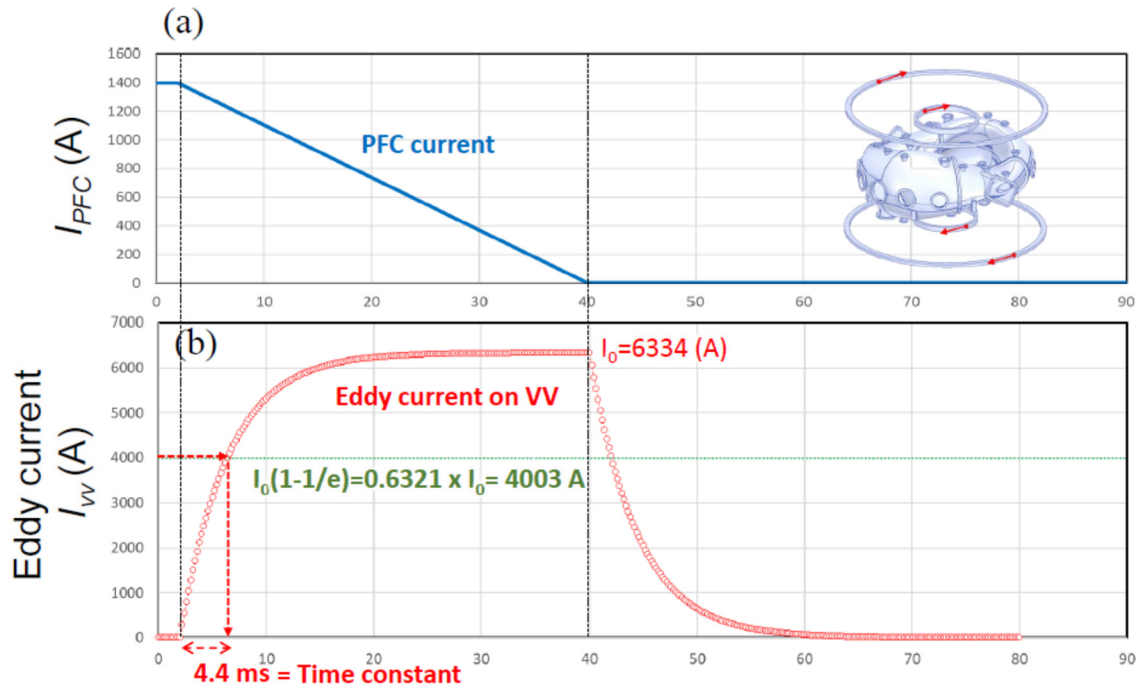
Fig.4.3.3-3 (a) Time evolution of assumed PFC current and (b) Time evolution of estimated eddy current, that is integrated to estimate total toroidal current in vacuum chamber.

4.3.4 Real scale vacuum vessel model

Real scale model of vacuum chamber type A (Fig. 4.3.1-4) has been manufactured by 3D printer. Since the size of the vacuum vessel is large, a real scale model cannot be made by 3D printer all at once. Therefore, the type A vacuum vessel has been cut into 16 pieces to print by 3D printer.

Each of 16 pieces has been made by 3D printer in Keye company. These 16 pieces has been assembled. In Fig. 4.3.4-1, how to Type A vacuum chamber is cut into 16 pieces.
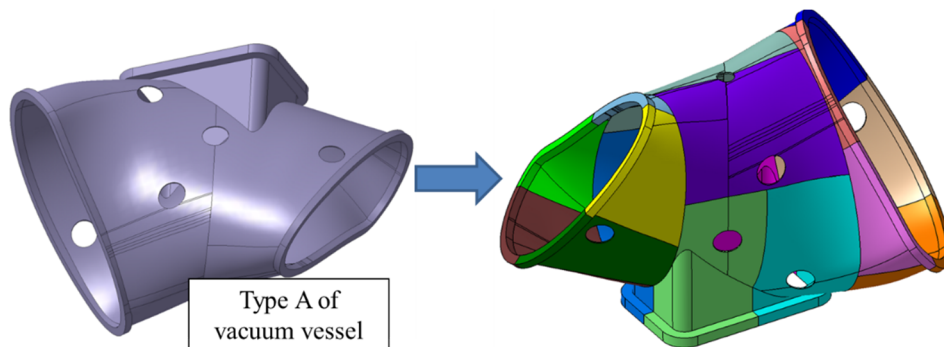
Fig. 4.3.4-1 Type A of vacuum chamber is cut into 16 pieces to print by 3D printer.
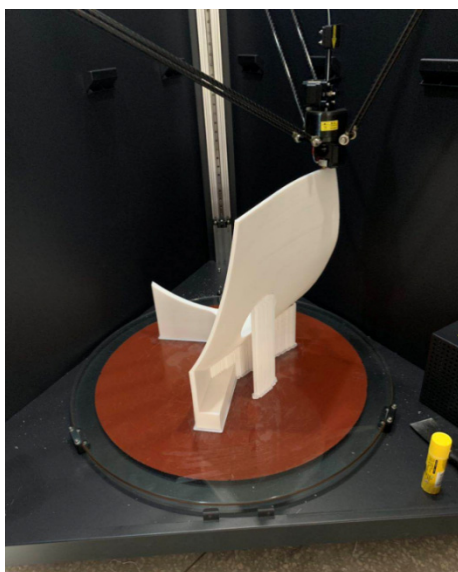
Fig. 4.3.4-2   3D printer to fabricate real scale vacuum chamber model

Fig. 4.3.4-3   Pictures of assembled real scale 3D vacuum chamber model made by 3D printer.

As shown in Fig. 4.3.4-2, each parts of vacuum chamber model were fabricated by 3D Printer. Each parts were stuck each other with an adhesive as shown in Fig. 4.3.4-3.

4.3.5   Limiter system

As in other magnetically confined fusion devices, the plasma in the CFQS is confined within closed magnetic flux surfaces and a boundary exists between plasmas and the machine-wall components. This boundary is generally called the scrape-off layer (SOL), which is determined by a solid surface (limiter) or topologically by magnetic field perturbations (divertor) [4.3.5-1]. In the SOL the impurities originated from plasma-facing components (PFCs) may cause a lot of problems, such as huge radiative power loss and dilution of fuel particles, it is therefore a crucial task to reduce impurities released from the PFC and prevent them from entering the plasma core region.

For the divertor configuration, plasma particles and energy leaving the confinement region are guided to the divertor target plate by open field lines. In stellarators, this divertor configuration can be intrinsically developed on the base of special edge magnetic structures arising from the small radial magnetic field resonant with rational surfaces [4.3.5-2]. Nevertheless, the stellarator divertor geometries may differ from each other, depending on the global magnetic shear. In the case of low-shear there exist chains of the island divertor, while in high-shear case the overlapping of island chains may form a stochastic layer [4.3.5-3]. In CFQS, the vacuum rational transform is designed between 2/6 and 2/5 from the core to the edge to avoid low-order rational surfaces, thus, the magnetic shear is quite low. It is expected from calculations that at the periphery of the CFQS, an island bundle divertor configuration will be formed under certain discharge conditions.

In different from the divertor, the limiter configuration is to use a solid surface to define the edge of the plasma. Depending on the shape and the positioning of the solid diaphragm, the limiters are generally divided into (i) poloidal limiter; (ii) rail limiter and (iii) toroidal limiter, as depicted in Fig. 4.3.5-1. The poloidal limiter is the simplest concept with a circular hole defined by a diaphragm normal to the toroidal magnetic field. The diameter of the hole is thus smaller than that of the vacuum chamber. Inside the hole the field lines are closed, while outside the hole the field lines are truncated by the diaphragm and the plasma density and temperature are radially decreasing due to parallel losses of particle and energy flux onto the limiter in the SOL. As a consequence, the limiter primarily serves to protect the wall from erosion by plasma heat loads. For withstanding heavy heat load, the limiter itself is usually made of a refractory material, such as carbon, tungsten, or molybdenum.

In the CFQS stellarator, although an innate divertor configuration exists in the plasma boundary, we intend to put two sets of the poloidal limiter inside the vacuum chamber for defining the plasma and also protecting the wall. These two limiters will be installed at two approximately opposite toroidal locations of the torus. One limiter has a fixed diameter with a minor radius $a = 27$ cm. For the other one, its diameter is adjustable and the minor radius can be varied within a range of $r = (20\text{-}27)$ cm. Because the CFQS is free of major plasma disruptions, there is little thermal shock occurred during

the operation. Thus, the sputtering and arcing rates from limiters are expected to be very low. The material for the limiters can be C, W or Mo.
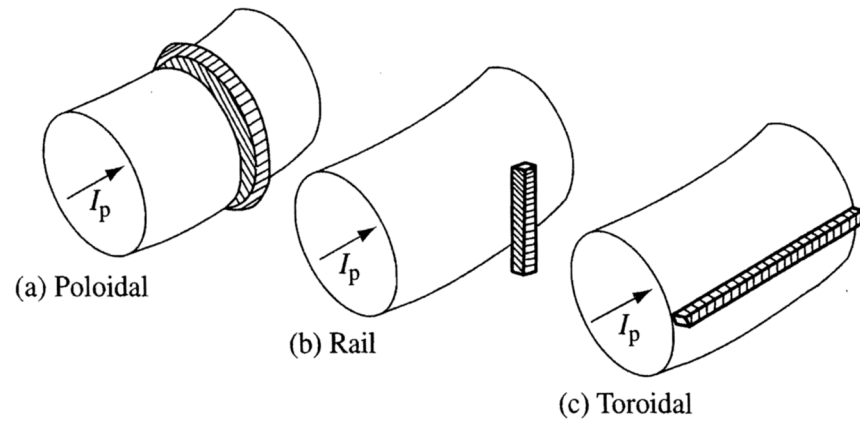

Fig. 4.3.5-1   Schematic of different types of the limiter

References

[4.3.5-1] J. Wesson, Tokamaks, fourth edition, Oxford University Press, 2011.

[4.3.5-2] Y. Xu, Matter and Radiation at Extremes **1** (2016) 192.

[4.3.5-3] Y. Feng, *et al*., Plasma Phys. Control. Fusion **53** (2011) 024009.

4.3.6   Baking system

For baking of vacuum vessel, we will use the inductive current in the vacuum vessel produced by coupling between modular coils and vacuum vessel. For the modular coils, the special power supply of AC 500 Hz is connected to produce the eddy current in the vacuum vessel for baking. This method is already used in a reverse field pinch of KTX. The eddy current obtained by this system in the vacuum vessel will be analyzed by ANSYS Maxwell.

4.3.7   Wall conditioning

Wall conditioning is important to produce plasma after the maintenance of vacuum vessel. Typical wall conditioning method is discharge cleaning by 2.45 GHz microwave heating system. The resonance magnetic field strength of this frequency is 0.0875 T, and steady state magnetic field is favorable for this purpose. Microwave is generated by magnetron and transferred by wave guide. For other wall conditioning, glow discharge by using helium is also employed.

4.3.8   Pumping system

Pumping system in CHS will be transferred to CFQS. As shown in the below figure, rotary pump is used for rough pumping, then the turbo pump gets involved.

Rotary pump is used for 20-30 Pa, then start the turbo molecular pump, to reduce the time reach the work pressure. Two turbo molecular pumps are used to achieve and sustain high degree of vacuum in vacuum vessel of CFQS.
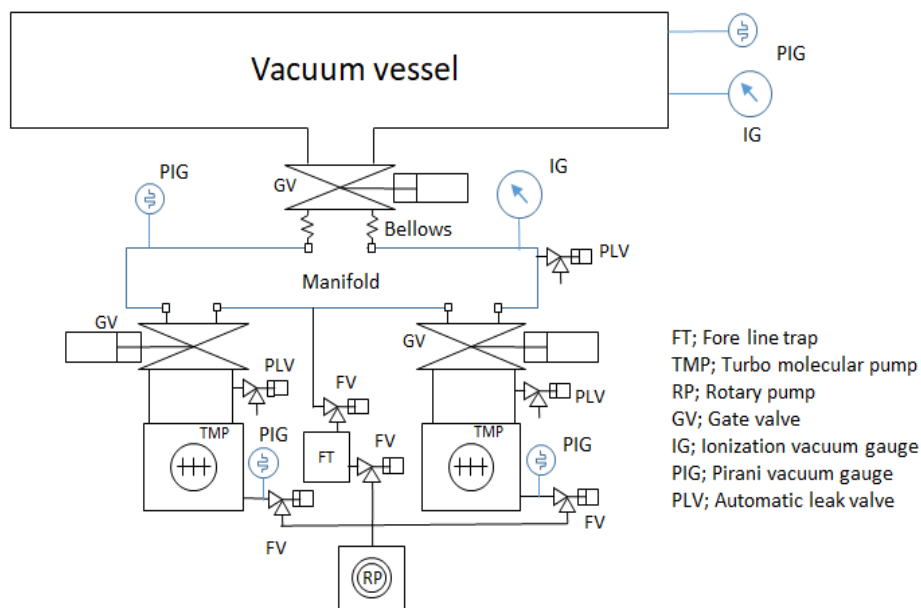

Fig. 4.3.8-1   Sketch of vacuum pumping system

4.4   Power supply system

4.4.1   Requirement to power supply system

Chinese power environment is different from Japan as shown in Table 4.4.1-1. In order to relocate some equipment's for the CHS and use them for CFQS experiments, it is reasonable to prepare converters, mainly transformers, for solving the difference in voltage. Although it is possible to install individual transformers for each used device, it is considered that cost reduction can be achieved by putting them together as there are many devices scheduled to used.

Table 4.4.1-2 shows summary of required power required to use several equipment's transferred from the CHS. Fig. 4.4.1-1 shows the preliminary one line diagram of power supply system for the CFQS. Where, the parts surrounded by the red broken line indicate the equipment's transferred from the CHS. Instead of a transformer of 10 kV/6.6 kV, there is also a proposal to replace transformers of TH and ITP.

Table 4.4.1-1   Comparison of power environment

	Frequency	HV	LV 1f	LV 3f
NIFS in Japan	60(West Japan)	6.6 kV	100 V	200 V
SWJTU in China	50	10 kV	220 V	380 V

HV ; High voltage   LV ; Low Voltage

Table 4.4.1-2   Total electric power to be required for using the equipment's of the CHS

No	Power board	Voltage	phase	Total capacity	use
1	LV 1Φ	100 V	1Φ	20 kVA	5kVA for control panel for NBI, 15 kVA for diagnostic etc.
2	LV 3Φ	200 V	3Φ	200 kVA	154 kVA for NBI, 46 kVA for vacuum pump etc.
3	HV	6,600 V	3Φ	4 MVA	power supply for NBI

In order to apply large currents to the CFQS coils, a short pulse large capacity power supply of about 60 MVA and 1s of a pulse length is required. Since it is difficult to supply this power from the commercial power source, a current source with energy storage function. The power supply system in Fig. 4.4.1-1 has a generator driven by a motor. Please refer to Appendix for examples of the motor generator system. As 2.5 MW of power is required to operate this level of the motor and 4 MVA of power is required to operate the NBI, a power of about 10 MVA is temporarily required including some margin.

A high power electron cyclotron heating (ECH) system is required to generate high temperature plasma with the CFQS. Since the ECH system will be able to use a capacitor bank power supply and the instantaneous power can be designed small, we believe that it will receive from a low voltage power board.

In the initial experiments where CFQS will be completed, we have a plan to carry out measurement experiments of plasma shape with low magnetic field and longtime discharge. At that stage, we think the power supply shown in Fig. 4.4.1-2 is enough.

Fig. 4.4.1-1   Power system for rated operation of 1T

The shaded part is unnecessary for the initial stage.

The power capacity (kVA) shows rating in a continuous operation.

Fig. 4.4.1-2   Power system for initial experiment of 0.09T. Some devices in shaded area will not be used
in the initial experiment with lower magnetic field of 0.09T.

4.5   Pure water cooling system

Pure water cooling system is required to cool magnetic coil system, heating system, diagnostic system, and pumping system. Detail will be designed in the future.

4.6   Compressed air supply system

Compressed air supply system is mainly used to control the gate valve. Detail will be designed in the future.

4.7 Plasma heating system

4.7.1 ECRH system

The main component of the electron cyclotron resonance heating (ECRH) system is gyrotron. The gyrotron which was used for CHS experiment and will be used in CFQS experiment has an oscillation frequency of 54.5 GHz and the maximum output power of up to 450 kW. The maximum pulse length is 100ms. The gyrotron was produced by a Russian company, GYCOM.

The EC-waves generated by the gyrotron effectively and locally heat the electrons at a position on the EC-wave beam path where the resonance condition ($n \cdot \omega_{ce} = \omega - k_{//} \cdot v_{//}$ and $\omega_{ce} \equiv eB/m_e$) is satisfied.

Here, integer n denotes harmonic number, ω_{ce} is electron cyclotron angular frequency, e is a unit charge of an electron, B is the strength of magnetic field, m_e is the mass of an electron with relativistic effect, ω is angular frequency of EC-waves, and $k_{//}$ and $v_{//}$ are the components of wave number and electron velocity parallel to the magnetic field line, respectively.

Applying the frequency of 54.5 GHz with n = 1 (fundamental resonance) and $k_{//} = 0$ (pure ECRH without Doppler effect), in the non-relativistic case, the resonance condition is satisfied with $B = 1.95$ T. For n = 2 (second harmonic resonance), $B = 0.97$ T should be set.

In the case of the CHS experiment, the EC-wave power was transmitted from the gyrotron to the CHS vacuum vessel by a quasi-optical transmission line. The transmission line was furnished with focusing and plane mirrors, polarizer mirrors to control transmitted wave's polarization arbitrarily, and vacuum window to keep the vacuum condition in CHS. In the CHS vacuum vessel, an EC-wave beam injection antenna system consisted of a focusing mirror and a two-dimensionally steerable plane mirror was installed. By use of the power transmission and injection systems, effective and localized ECRH with power deposition control, electron cyclotron current drive (ECCD), and electron Bernstein wave heating (EBH) were realized [4.7.1-1 ~ 8].

For localized and controlled ECH power deposition and current drive, two dimensionally steerable power injection system with beam focusing is necessary. To realize the power injection system, at least, two mirror antenna system (one is plasma facing 2-D steerable plane mirror, and the other is beam focusing mirror) inside the vacuum vessel is required. The dimensions of the mirrors depend on the focused beam waist size at the plasma core region and the distance between the plasma and the mirrors. The antenna design should be optimized under the available circumstance of CFQS vacuum vessel design, to realize the beam waist size as small as possible in the plasmas.

For the power injection to the vacuum vessel, adequate vacuum window is needed. To minimize power reflection at the vacuum window, the thickness of the window d must satisfy a relation:

$$d = n\lambda_{in}/2.$$

Here, n is an integer and λ_{in} is wavelength of the heating wave in the window material.

✓ **Power supply for ECRH**

For the operation of the 54.5 GHz gyrotron, power supply (PS) systems such as precisely controlled high voltage direct current (DC) PS, DCPS of ~kV order output, and low voltage alternating current (AC) electric power up to 200 V. Here, the PS system used in the CHS experiment is described as an example.

The high voltage DCPS system consists of:

- Charger which generates DC high voltage up to 100 kV from 200 V AC,
- Condenser bank with 86 condensers of 1.5 micro Farad electrostatic capacitance each,
- Crowbar which works as fast high voltage switch in the case of failure detection, and
- Regulator tube (EIMAC X2062K tetrode tube) which supplies precisely controlled high voltage up to 70 kV DC to the gyrotron.
- Ion pumps to keep the vacuum conditions inside the gyrotron and the regulator tube require DCPSs of ~3.5 kV output.
- Heaters to generate thermal electron beams in the gyrotron and the regulator tube require ACPSs of up to 150 V output.
- High voltage PS used for crowbar-drive works at 8 kV DC.
- Super conducting magnet (SCM) which generates magnetic field around gyrotron cavity requires DCPS of ~2 V/33 A output.

✓ **Pure water cooling system for ECRH**

For safety operation of the 54.5 GHz gyrotron, required flow rates of cooling water to remove heat loads on the parts of the gyrotron are,

> Collector: 100 L/min.
>
> Body: 6 L/min.
>
> Vacuum window: 9 L/min.
>
> Oil tank: 6 L/min.

with the water pressure of < 2 kgf/cm^2 at inlet flow.

If a regulator tube is used in the high voltage power supply system for the gyrotron, flow rate of the cooling water of ~120 L/min for the regulator tube EIMAC X2062K, as an example in the case of CHS experiment, would be additionally required.

References

[4.7.1-1] Y. Yoshimura *et al*., J. Plasma and Fusion Research Series **6** (2004) 651.

[4.7.1-2] Y. Yoshimura *et al*., Plasma and Fusion Research **1** (2006) 029.

[4.7.1-3] Y. Yoshimura *et al*., J. Korean Physical Society **49** (2006) S197.

[4.7.1-4] Y. Yoshimura *et al*., J. Physical Society of Japan **75** (2006) 114501.

[4.7.1-5] Y. Yoshimura *et al*., Plasma and Fusion Research **1** (2006) 053.

[4.7.1-6] Y. Yoshimura *et al*., Fusion Science and Technology **52** (2007) 216.

[4.7.1-7] Y. Yoshimura *et al*., Fusion Science and Technology **53** (2008) 54.

[4.7.1-8] Y. Yoshimura *et al*., Plasma and Fusion Research **3** (2008) S1076.

4.7.2　NBI system

　Neutral beam injection (NBI) is a powerful tool for plasma heating and drive of the plasma current and flow. In order to study energetic particle physics, tangential NBI is an inevitable device. Tangential port with diameter of 300 mm is recommended to install NBI. The beamline is required to be arranged at the beam injection port with area of 10 m^2. The power supply system for filament arc discharge is also required to be arranged near the beamline. Fig. 4.7.2-1 shows CHS-NBI#2 that will be moved for the CFQS experiment in the future.
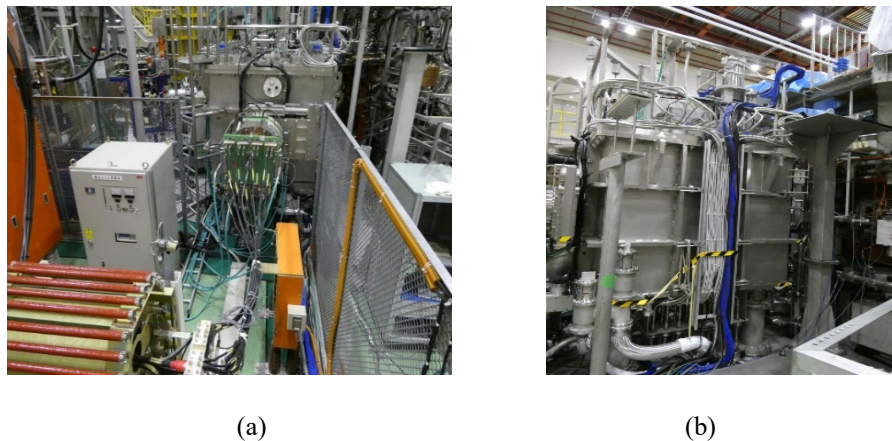

(a)　　　　　　　　　　　　　　　　(b)

Fig. 4.7.2-1　(a) Back side view of CHS-NBI#2 and positive ion source, (b) Side view of CHS-NBI#2

✓　**Technical specifications**

　Followings are specification of NBI planned in this project.

- Beam species: H/D
- Beam energy: 20-40 keV
- Port-through power: 1 MW
- Beam duration: ~1 sec
- Ion source: Filament-arc discharge with cusp magnets
- Beam acceleration area: ϕ 300 mm
- Aperture radius: ϕ 5 mm
- Current density: 250 mA/cm^2
- Beam optics: Conversing beam via offset aperture
- Focal length of the beam: ~3.0 m
- Beam divergence angle: ~1 degree
- Diameter of drift Tube: ϕ 250mm

- Neutralization: gas cell
- Main vacuum pump: cryosorption panel (326 m^3/s)
- Diagnostics: calorimetric beam profile measurement
- Access power to Electricity for NBI with port-: through power of 1 MW
- Beam duration; 1 s

✓ **Required area and electric power**

Typical area required for NBI system is summarized in Table 4.7.2-1 and summary of access power to electricity is summarize in Table 4.7.2-2.

Table 4.7.2-1 Summary of Access power to Electricity for NBI operation with port-though power of 1 MW and beam duration of 1 sec

Area	Main Device	N-S [m]	E-W [m]	Area [m^2]
Area1F-1	A/F PS	3.5	6.5	22.75
Area1F-2	TRF,ACSW,DCC,	4.2	5.3	22.26
Area1F-3	CRYO cntl. panel	1	2	2
Area2F-1	GTOSW(GSW), DCL, VD,GS	5.5	5.2	28.6
Area2F-2	VCB, LVD	5.5	2	11
AreaB1	CryoComp	5	1.5	7.5
Total				94.11
BL Area	Beamline, IS	4	2.5	10
Cntrl Area	CPx2 + CPDx1 + PC	3.5	1.5	5.25

Table 4.7.2-2 Summary of Access power to Electricity for NBI operation with port-though power of 1 MW and beam duration of 1 sec.

Acl PS	A/F PS	DclPS	BndMag PS	total
3.7MVA	250kVA	26kVA	20kVA	~4MVA

4.8 Diagnostics

4.8.1 Diagnostics system

Diagnostics are indispensable for studying high temperature plasma physics in modern fusion research. There are a lot of interesting topics to be studied; transitions to improved confinement modes, formation of transport barriers, and their impact on plasma turbulence, etc. Roles of diagnostics are increasing in the studies on high temperature plasma properties, not only for fusion but also for basic physics.

CFQS is an innovatively designed device so as to achieve tokamak-like confinement properties and helical-like stability at the same time. Plasmas produced in the CFQS will become a good target for researches which aim at achieving cost-effective stable burning plasmas. High-quality data based on detailed measurements should be obtained for comprehensive understanding of toroidal plasmas.

As mentioned above, anomalous transport and improved confinement modes are important issues for understanding toroidal plasmas. Based on the successful results of the advanced diagnostics in CHS and LHD, we will employ advanced diagnostic systems such as heavy ion beam probe (HIBP) and microwave reflectometry in CFQS to study the following topics:

      1) Spatio-temporal turbulence structure

      2) Structures of electric field and plasma flow

After the installation of NBI in the future, we will consider developing charge exchange spectroscopy (CXS) for the measurement of radial electric field and plasma flow velocity to study the relation between toroidal rotation and momentum input.

Also, physics of density limit is important in helical devices because confinement property of helical systems is improved as the density increases following the scaling law. Therefore, higher priorities are given for the diagnostics of edge plasma, MHD and radiation power, including magnetic probe, bolometer, etc.

For basic diagnostics, microwave interferometer should be firstly developed to measure the electron density. Thomson scattering is also important to study the physics of transport barriers. Multi-dimensional measurement is useful for studying internal structure of basic plasma parameters. Therefore, the development of two-dimensional or three-dimensional measurements will be performed as far as possible. So that the structure and non-linear development of plasmas can be observed in detail.

Diagnostics planned in the CFQS are listed in Table 4.8.1-1. Assignment of ports to these diagnostics will be planned in the future. Some of the ports should be specifically designed for HIBP and Thomson scattering because these diagnostics require special geometries.

Table 4.8.1-1 Diagnostics planned in the CFQS

Basic diagnostics

Parameters	diagnostics	Remarks
Electron density	Microwave interferometer	150 GHz
	Far infrared interferometer	
	Thomson scattering	Multichannel
Electron temperature	Thomson scattering	Multichannel
	Electron cyclotron emission	
Ion temperature	Charge exchange spectroscopy	After NBI installation
MHD	Magnetic probe	
Edge plasma	Langmuir probe	
	Hα detector	
Radiation power	Pyroelectric detector	
	Resistive bolometer	
	AXUV photodiode array	20 channel
Stored energy	Diamagnetic loop	
Plasma Current	Rogowski coil	
Impurities	Vacuum ultraviolet spectroscopy	

Advanced diagnostics

Parameters	diagnostics	Remarks
Electric potential/field	Heavy ion beam probe	
Plasma rotation	Charge exchange spectroscopy	After NBI installation
Lost ions	Lost ion probe	
Turbulence	Heavy ion beam probe	
	Microwave reflectometer	Multichannel

4.9   Building

4.9.1   Torus hall

Subsystems of CFQS, briefly, include vacuum chamber, coil system, supporting structure, power supply, diagnostics, heating system, fueling system, cooling system and so on. The torus hall of CFQS is reconstructed by a workshop with about 48 m in length, 35.5 m in width. And the torus hall is divided into three parts in the length direction. The heights/widths of three parts are 7.2 m/12 m, 11.2 m/11.5 m and 7.2 m/12 m, respectively. The detail sizes of the torus hall are shown in Fig. 4.9.1-1. According to the function, the hall is divided into 6 regions roughly. The locations and sizes of 6 regions are shown in Fig. 4.9.1-2. Brief descriptions of each region are given below:

1. **Device and diagnostic region**: the blue part in Fig. 4.9.1-2. With a major radius, R=1 m, it is estimated that the entire device should occupy an area of about 4 m in diameter (compact arrangement), in which the vacuum chamber, coil system, supporting structure, first wall, molecular pumps, partial diagnostics (i.e. internal magnetic coils, optical probes and other internal components) are including. The diagnostic region is around the device. In this region, there are electrostatic probes, optical diagnostics (CCD cameras, etc.), spectroscopic diagnostics (visible, VUV, H_α), microwave diagnostics, laser assisted diagnostics, Soft/Hard X-ray), etc. In order to facilitate operation of the diagnostics, a platform will be built, which occupies an area of 10×11 m^2. In addition, these should be a grounding system.

2. **Preassemble and repair region**: This region is for the preparation and debugging before the assembling of the device and other components. It also includes the repair, leakage testing, cleaning, etc. of each component. The area of this region is about 640 m^2.

3. **Unloading channel**: This channel is toward to the Gate for unloading, lifting and so on.

4. **Control and DAQ room**: Two rooms, one for data acquisition and another for operation control will be built in the hall. Detail information is given in the Fig. 4.9.1-3.

5. **ECRH region and NBI region**: the red part in Fig. 4.9.1-2. This region is for placing the ECRH wave source system and inducting into the device through the optical path / waveguide. At the same time, this region is also for placing the NBI system. The total area of this region is about 400 m^2.

6. **Power supply region:** The power supply cabinet and traction motor are placed in the hall. It includes power supply cabinet (connect the traction motor) of the coil system, power supply cabinet (connect the capacitor) of the heating system, power supply cabinet (connect campus electricity) of the discharge cleaning / wall treatment and so on. These power cabinets are for the device discharge. This region is in the southeast of the hall with about 25 m in length, 12 m in width and surrounded by protective netting. In this region, the energy storage power supply (traction motors, charge / discharge equipment), power debugging equipment (on-site commissioning equipment, fake load, etc.), power control equipment (monitoring, control,

protection, grounding, etc.), high-power switching system, etc., are accommodated. A grounding pile system is needed. The energy storage power source region is relatively far away from the weak electric system such as diagnostics, and is physically separated from the device region. The arrangement should be reasonable.

7. Others: Some underpass are needed, for example, water channel for the cooling water and cable channel for the high voltage wire. In Fig. 4.9.1-2, the water channel and cable channel have been denoted by black and blue lines.
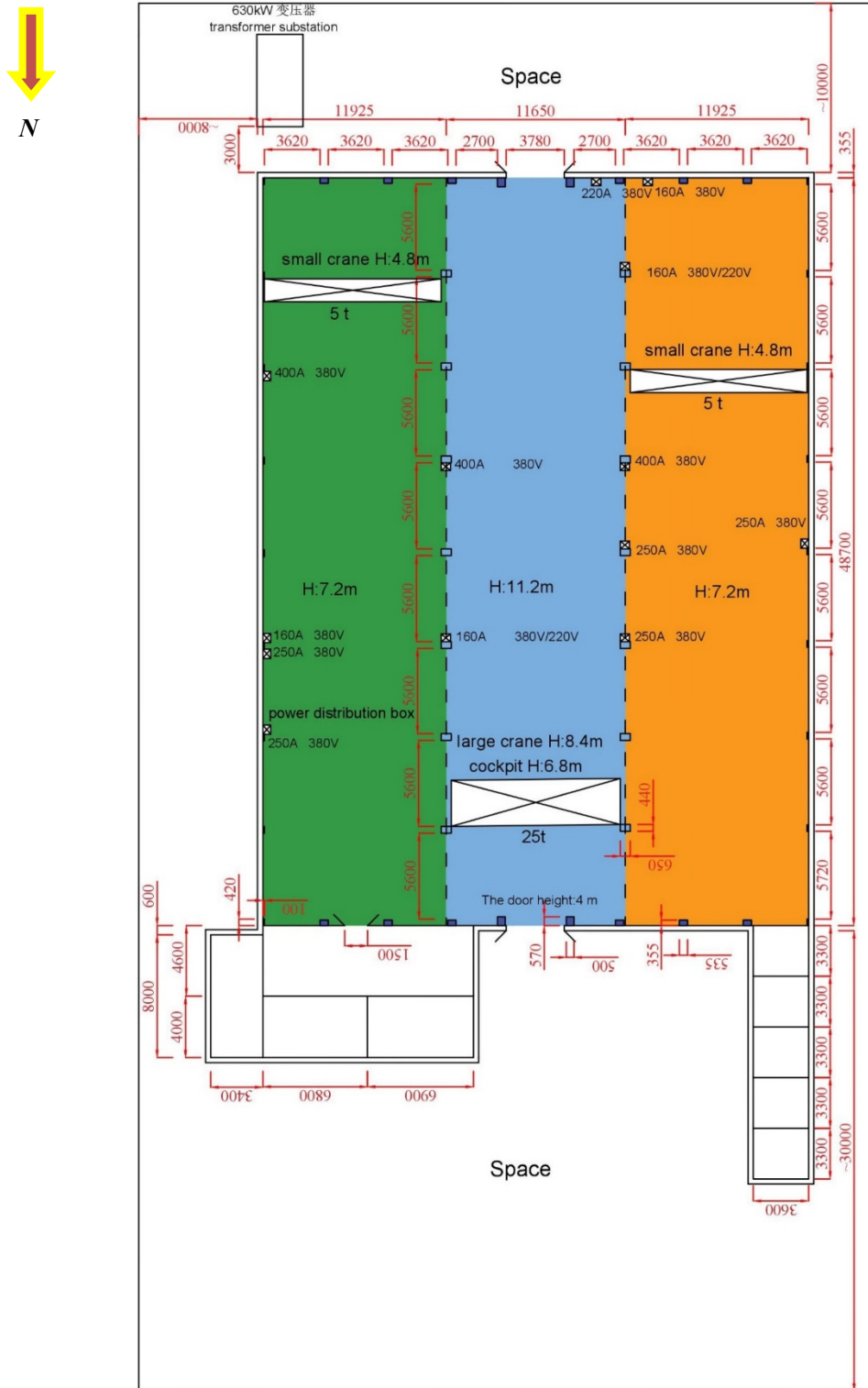
Fig. 4.9.1-1　Sizes of the CFQS hall (height between the small (large) crane bottom and ground is 4.8 (8.4) m and the gate is 3.9 m in width and 4.0 m in height)

N

630kW变压器
transformer substation

Space 空地

~0008

3000

11925

11650

11925

10000

310

8000

10000

310

6800

23900

Water-treament plant region
水处理区域

水管沟
Water channel

Unloading channel
卸货渠道
1000kg/m²

Device and diagnositic
装置及诊断区域
3000kg/m²

电缆沟
Cable channel

Power supply and control region
电源及控制区域
1000kg/m²

Pre-assambly and repair region
预装和修理区域
1000kg/m²

Heating(ECRH,NBI)
ECRH及NBI区域
2000kg/m²

33475

7612.5

7612.5

~30000

数据采集室
data acquisition room

运行控制室
operation control room

The door height:4 m

water tap
水龙头

Space 空地

Fig. 4.9.1-2   Layout of the CFQS hall
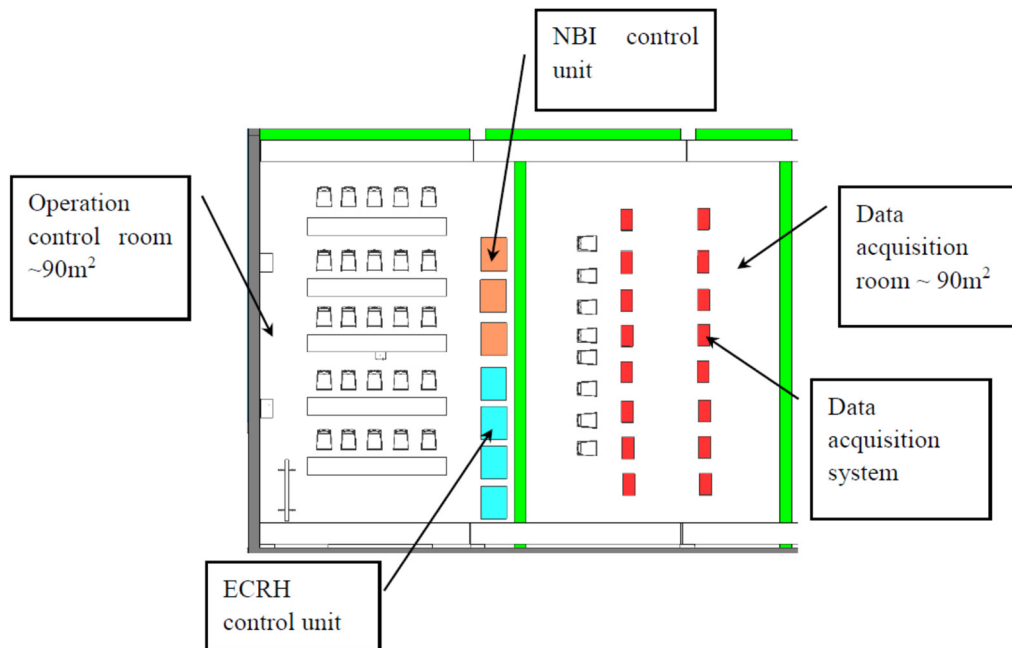
Fig. 4.9.1-3   One- floor arrangements of the experimental region

4.9.2   Room for peripherals

There are some rooms outside the hall, shown in Fig. 4.9.1-1. These rooms are applied as the **Office rooms**, **Conference room**, **Reception room**, **Experimental material room** (spare parts, cable, optical fiber, metal material, insulating material etc.), **Vacuum preparation room** (placing vacuum equipment: leak detector, leak gas, flanges, vacuum sealed devices, cleaning bench/equipment etc.), **Metalworking workshop** (drill, grind, tool, bench, spreader tooling, fastening pieces etc.) and **Central laboratory** (Room for experiment co-ordination arrangements and discussion).

The **water-treatment plant region** is the outside the hall and the region closes to the source of water. This arrangement can keep the danger (from the power supply and water-treatment systems) away and ensure the safety of experimenters. At the same time, it can keep the noise away from the control room. Detail descriptions are as following: This region is in the north of the hall with 48.7 m in length, 8 m in width. The high pressure water cooling system is located in this region. The cooling water uses the deionized water. The consumption of the water is plentiful, so the primary circuit and the secondary circuit should be designed reasonably. In addition, high pressure gas system, which is for the pneumatic vacuum valve, pneumatic probe system and vacuum chamber baking system, is also set in this region. And the region is covered by the canopy to avoid the cooling tower rusting.

4.9.3　Control room

The control room has been introduced briefly. The control room (including operation control room and DAQ room) is located at the northwest of the hall, as shown in Fig. 4.9.1-2. The **Operation control room** is the nerve center of the device. The discharge control component, heating control (NBI and ECRH) component, and some diagnostic control components are arranged in it. In the primary plan, the control room is about 90 m^2, if necessary, it can be expanded according to actual condition.

5 Research plan and schedule

The CFQS manages to offer available solutions to critical challenges for toroidal confinement fusion: it provides a steady-state, disruption-free reactor concept as well as neoclassically optimized magnetic configurations. With respect to the magnetic configurations, the CFQS is designed and operated to achieve three types of advanced configurations, i.e., quasi-axisymmetric, mirror linked and divertor configurations. To guarantee the safety of the facility operation and accuracy of each magnetic configuration two steps are scheduled to operate CFQS, which are the low magnetic field operation and standard magnetic field operation.

5.1 Physics research plan

5.1.1 Research plan for 0.1 T operation

The research plan for the 0.1 T operation is as follows,

    i.   Operate all the diagnostics and auxiliary systems, e.g., electron gun, CCD camera, interferometer, probes, visible light, etc.

   ii.   Achieve flexible magnetic configurations, i.e., quasi-axisymmetric configuration, mirror linked configuration as well as divertor configuration; check the accuracy of magnetic field configurations in vacuum by mapping experiment.

  iii.   Verify optimization of neoclassical transport and whether the tokamak-like fundamental transport properties are realized or not.

5.1.2 Research plan for 1.0 T operation

The research plan for the 1.0 T operation is as follows,

    i.   Neoclassically optimized magnetic configurations

   ii.   Turbulence and transport research

  iii.   Island bundle divertor

  iv.   Plasma-Materials Interactions in 3D systems

   v.   Fast particle confinement

  vi.   Equilibrium and Stability at High-β

 vii.   Impurity confinement and accumulation

viii.   Optimize the coil system, Optimize the coil system for the next generation stellarator.for the next generation stellarator.

5.2   Construction schedule

The schedule plan is shown in the Table 5.2-1.

- Phase I; Physics design and main machine design
    Configuration
    Neoclassical transport
    MHD
    Modular coils
    Vacuum vessel
    Supporting structure etc.

- Phase II; Fabrication of CFQS and transfer essential heating and diagnostic systems from NIFS to SWJTU
    NBI
    Gyrotron
    Interferometer
    X-ray diagnostic etc.

- Phase III; Commissioning, verify construction accuracy and obtain first plasma.
- Phase IV; Magnetic configuration studies and heating experiments in 0.1 T operation.
- Phase V; Magnetic configuration studies and heating experiments in 1.0 T operation

More detail plan is shown in the Table 5.2-2. Up to end of September in 2021, the first plasma of the CFQS will be achieved. Operation of 1.0 T will be started at the end of September in 2023.

Table 5.2-1   Schedule of the NSJP for the CFQS

JFY	4	5	6	7	8	9	10	11	12	1	2	3
H30(2018)	Phase I: Physics design and main machine design											
R1(2019)	Phase II: Fabrication of CFQS / Transfer heating systems and diagnostic systems from NIFS to SWJTU											
R2(2020)	Phase II: Fabrication of CFQS / Transfer heating systems and diagnostic systems from NIFS to SWJTU											
R3(2021)	Phase II: Fabrication of CFQS / Transfer heating systems and diagnostic systems from NIFS to SWJTU						Phase III: Fabrication of CFQS, Commissioning and First plasma		Phase IV: Operation			
R4(2022)	Phase IV: Operation											
R5(2023)	Phase V: Operation											

Table 5.2-2   Detailed schedule plan

APPENDIX

NIFS-SWJTU JOINT PROJECT FOR CFQS

~PHYSICS AND ENGINEERING DESIGN~

VER. 2.1
2019. SEP

TABLE OF CONTENTS

LIST OF TABLES

LIST OF FIGURES

[1]   ALLOWABLE LIMIT VALUE OF STRESS AND STRAIN FOR CFQS

Although there is no publicly determined standard for fusion research, it is convenient to define something as guidelines. The fusion research often follows the ASME III. Even in the CFQS project, we will be better to follow the same guideline. Table 1-1 may be used as a guidelines for CFQS, that is a just guideline, not a necessary and sufficient condition. If it cannot be satisfied, it may be sometimes used on condition that the integrity (健全性) is confirmed in the periodic inspections (定期点検).

The stress component of the fusion device is complicated and its analysis not sufficient. So it is not easy to step in detail on technical standards. We may only follow the basic idea, but we should think about the details flexibly.

Table 1-1   Design guideline of typical materials

Material			SUS316	C1020 -O	C1020 -1/2H	Resin	Composite (Coil)	FRP
Young's Modulus	(GPa)	E	197	100	100	1～3	100	100
Design Stress	(MPa)	S_m	137	50	90	-	30	50
Design Strain		ε					＜0.1%	
Tensile Strength	(MPa)	σ_u	520	230	270	10～100	200	2000
Yield Strength	(MPa)	σ_y	205	80	250	-	80	500
Elongation	(%)		40	50	25	1～2	1～2	5
Poisson's ratio		ν	0.3	0.34	0.34	-	0.3	0.3
Density	(kg/m^3)	ρ	8000	8960	8960	1100	8000	1500
Thermal expansion		α	1.73×10^{-5}	1.65×10^{-5}	1.65×10^{-5}	5×10^{-5}	1.65×10^{-5}	2.0×10^{-5}
Comments			300k	OFC	OFC	after curing	OFC + isolation	Varies

- **S_m = min (2/3 σy, 1/3 σu) -- ASME III criterion**
- **The S_m is changed according to operating temperature.**
- **If possible, it is desirable that strain ratio ε is less than 0.1% or 0.5% at worst for the coil**

1.1.   Guideline for coil design

Because the material properties of a coil (that is on copper and insulation composite) differ greatly from structural material, the ASME III should not be strictly applied for them.

The strength of the coil is affected by the working method and the heat treatment conditions in addition to the selection of the material. As these data are not released to the public, they need to be acquired by developers themselves through element prototyping and inspection.

It is difficult to decide the guidelines when it is not done, but it is inconvenient if it is not at all. So, we will temporarily extend the ASME III to the coil but also consider the unique properties. Those are

- The conductor is very flexible and cannot be cut in a short time even if it exceeds the yield strength.
- The insulation (especially cured resin close to glass) is easy to crack and should be restricted by strain.
- It is more reliable to minimize the deformation of the coil within the measurable range. The target of the deformation is 1mm or less.

[2]   EXPLANATION OF ASME III CRITERION AS A REFERENCE

ASME III defines the following criterion to get allowable limit value of stress. It may be evaluated by the following procedure because it is difficult to distinguish stress components by the FEM calculation.

- Pm + PL + Pb + Q < 3Sm, absolute requirement everywhere
- Pm < Sm, should be satisfied in major area
- Pm + Pb < 1.5Sm, local or thermal stress is permitted
- Pm + Pb > 1.5Sm, may be permitted in extremely limited area

Here, Sm is a Design Stress Strength (設計応力強度) obtained by the material properties and P_m, P_L, P_b, Q are stress components obtained by the s stress analysis as a von Mises stress. Where technical terms are defined below.

2.1.   Material property

Sm is a design stress strength that is a reference intensity allowed to load by setting is given as the efficient design. It is obtained from the following equation.

- Sm = min (2/3 σ_y, 1/3 σ_u)

where σ_y is a proof stress or offset yield strength that is a stress changing from elastic deformation to permanent deformation. σ_u is a tensile strength that is a maximum tensile stress appearing in the material before breaking.

2.2.   Design criteria

Pm is a primary general membrane stress that is an average value of stress in a cross section. Discontinuities and stress concentration are excluded.

PL is a primary local membrane stress that is an average value of stress by discontinuities.

Pb is a primary bending stress that is a stress component proportional to the distance from the centroid in a cross section. Discontinuities and stress concentration are excluded.

Q is a secondary stress (bending and membrane stress) that is a self-equilibrium stress generated in discontinuity of structure

[3]   O-RING FOR VACUUM AS A REFERENCE

Depending on the operating temperature, it is necessary to select the material of O ring properly. Operating temperature is as follows.

- Nitrile rubber (NBR)   -50 〜80℃

unusable at baking temperature 100〜150℃.

- Fluorine rubber (FKM, Viton)   -15〜200 ℃

may be usable, but worry about low temperature damage due to liquid nitrogen or cryogenic gas that is sometimes used for evacuation.

- Metal O-ring   -250 〜650 ℃

can be used at wide range of temperature. See attached URL and Table 3-1.

-
  - ▸ http://www.mitsubishi-cable.co.jp/en/products/group/seal/semicon_e.html
  - ▸ http://www.mitsubishi-cable.co.jp/ja/products/group/seal/pdf/61_metal_o-ring.pdf
  - ▸ http://www.seals.de/downloads/Metall_Ringe_GB.pdf
  - ▸ https://www.canon-anelva.co.jp/english/products/component/catalog/pdf/catalog_vol_2_en.pdf

Table 3-1   ConFlat Fixed flanges

Name	A	C	T	ΦH	N	PCD	bolt	pipe
ICF34	34	16	7.5	4.5	6	27	M4x20L	Φ19.1xΦ16.7
ICF70	70	38.5	12.7	6.7	6	58.9	M6x35L	Φ41xΦ38
ICF114	114	61	17.5	8.4	8	92.2	M8x45L	Φ63.5xΦ60.2
ICF152	152	97	20	8.4	16	130.3	M8x50L	Φ101.6XΦ95.6
ICF203	203	148.5	22	8.4	20	181.1	M8x55L	Φ153xΦ147
ICF253	253	198.5	25	8.4	24	231.9	M8x60L	Φ203xΦ197
ICF305	305	250	28	8.4	32	284	M8x70L	Φ250xΦ244
ICF356	356	295	28.5	10.5	30	325.4	M10x70L	Φ295xΦ289
ICF406	406	350	28.5	10.5	30	381	M10x70L	Φ350xΦ344

ConFlat is a registered trademark of Varian Co.

-
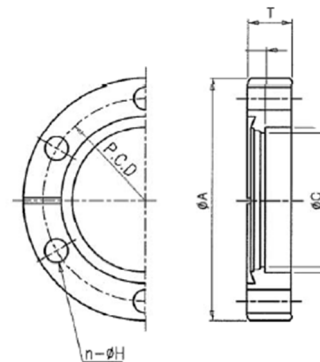
[4]　　PHYSICAL PROPERTY OF STAINLESS STEEL (SUS) AS A REFERENCE

There are slight differences in mechanical properties due to differences in composition. Please choose them according to your purpose.

SUS 304 is the most distributed and inexpensive. However, as the permeability may increase, caution is required for nuclear fusion. SUS316L is SUS316 with low carbon and has slightly better cold workability and corrosion resistance but it is a little expensive and a little weak.

- Material composition

SUS316　 = Cr16-18% + Ni10-14% + Mo2-3% + C (less than 0.08%)
SUS316L = Cr16-18% + Ni12-15% + Mo2-3% + C (less than 0.03%)

- Mechanical properties

SUS316　　　　　　　　σ y = 205　 σ u = 520
SUS316L　　　　　　　 σ y = 175　 σ u = 480 　 weak
SUS314　　　　　　　　σ y = 205　 σ u = 520

- Magnetic permeability

SUS304　　　　　　　　μ =1.004 　 $\rightarrow$ 　1.1 or more
SUS316,316L　　　　　 μ =1.004 　 $\rightarrow$ 　1.004

SUS304 turns into magnetic material by bending or rolling. It is better not to use it in a magnetic field. We are worried about distorting the magnetic field profile. SUS316,316L is more stable.

[5]　STANDARD SPECIFICATION FOR SUS PIPE AS A REFERENCE

Table 5-1　　　List of outside diameter and thickness of SUS pipe

ND		OD (mm)	Thickness (mm)							JIS
A	B		Sch5s	Sch10s	Sch20s	Sch40	Sch80	Sch120	Sch160	
6	1/8	10.5	1.0	1.2	1.5	1.7	2.4			G3459 TP
8	1/4	13.8	1.2	1.65	2.0	2.2	3			G3459 TP
10	3/8	17.3	1.2	1.65	2.0	2.3	3.2			G3459 TP
15	1/2	21.7	1.65	2.1	2.5	2.8	3.7		4.7	G3459 TP
20	3/4	27.2	1.65	2.1	2.5	2.9	3.9		5.5	G3459 TP
25	1	34.0	1.65	2.8	3.0	3.4	4.5		6.4	G3459 TP
32	1-1/4	42.7	1.65	2.8	3.0	3.6	4.9		6.4	G3459 TP
40	1-1/2	48.6	1.65	2.8	3.0	3.7	5.1		7.1	G3459 TP
50	2	60.5	1.65	2.8	3.5	3.9	5.5		8.7	G3459 TP
65	2-1/2	76.3	2.1	3.0	3.5	5.2	7.0		9.5	G3459 TP
80	3	89.1	2.1	3.0	4.0	5.5	7.6		11.0	G3459 TP
90	3-1/2	101.6	2.1	3.0	4.0	5.7	8.1		12.7	G3459 TP
100	4	114.3	2.1	3.0	4.0	6.0	8.6	11.1	13.5	G3459 TP
125	5	139.8	2.8	3.4	5.0	6.6	9.5	12.7	15.9	G3459 TP
150	6	165.2	2.8	3.4	5.0	7.1	11.0	14.3	18.2	G3459 TP
200	8	216.3	2.8	4.0	6.5	8.2	12.7	18.2	23.0	G3459 TP
250	10	267.4	3.4	4.0	6.5	9.3	15.1	21.4	28.6	G3459 TP
300	12	318.5	4.0	4.5	6.5	10.3	17.4	25.4	33.3	G3459 TP
350	14	355.6	4.0	5.0	8.0	11.1				G3468 TPY
400	16	406.4	4.5	5.0	8.0	12.7				G3468 TPY
450	18	457.2	4.5	5.0	8.0	14.3				G3468 TPY
500	20	508.0	5.0	5.5	9.5	15.1				G3468 TPY

ND; Nominal Diameter,　　OD; Outer Diameter

[6]   VACUUM PUMPING SYSTEM FOR CHS

We plan to transfer vacuum pumping system for CHS in NIFS to CFQS. Their main specification is shown below. In order to use this unit with CFQS, modification adding some parts will be required as shown in Fig. 6-5.

Table 6-1   Main parameters for the vacuum pumping system

No	Item	Contents
1	Input power supply	AC 220V , 50/60Hz , 1Φ/3Φ, 20A(at startup)
2	Cooling water	8kgf/cm^{2}G, 5ℓ/min or more, 27℃ or less
3	Compressed air	7kgf/cm^{2}G, 20Nm^3/h
4	Turbo molecular pump (TMP)	Number of units 2 Model; TH1502VW (Osaka Vacuum Ltd.) Exhaust speed; 1500ℓ/s Ultimate pressure; 1x10^{-7} Pa Cooling method; water cooling Allowable temperature; 120℃
5	Rotary pump (RP)	Number of units 1 Model; T2063A (Adixen/Alcatel) Exhaust speed; 1420ℓ/min(60Hz) 1180ℓ/min(50Hz)
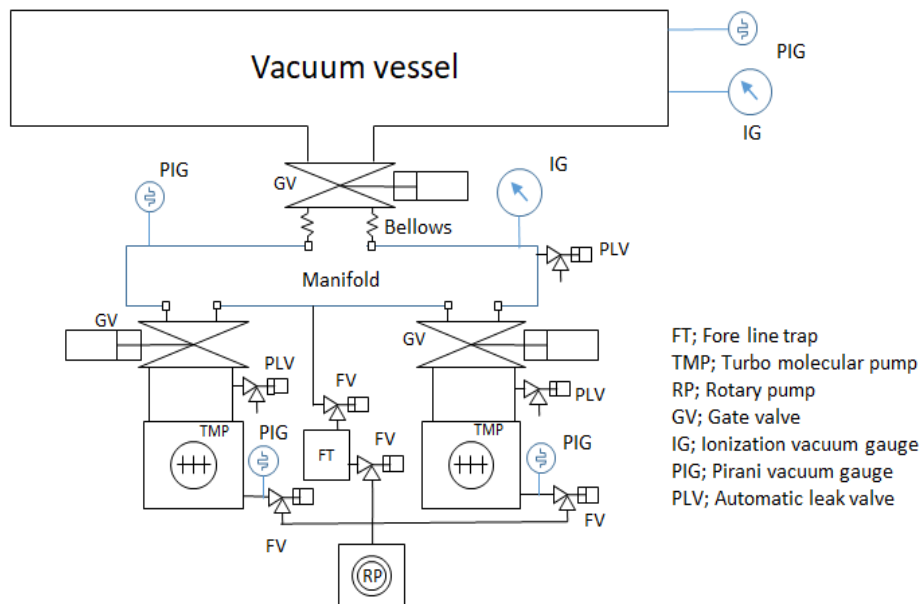
Fig. 6-1 System diagram of vacuum pumping unit
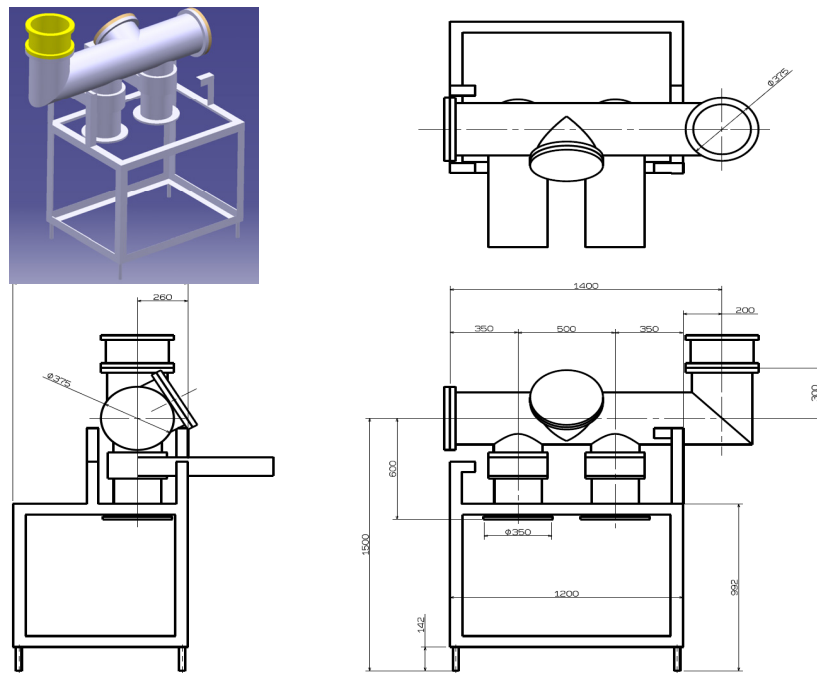
Fig. 6-2 Main dimension of vacuum pumping system for CHS
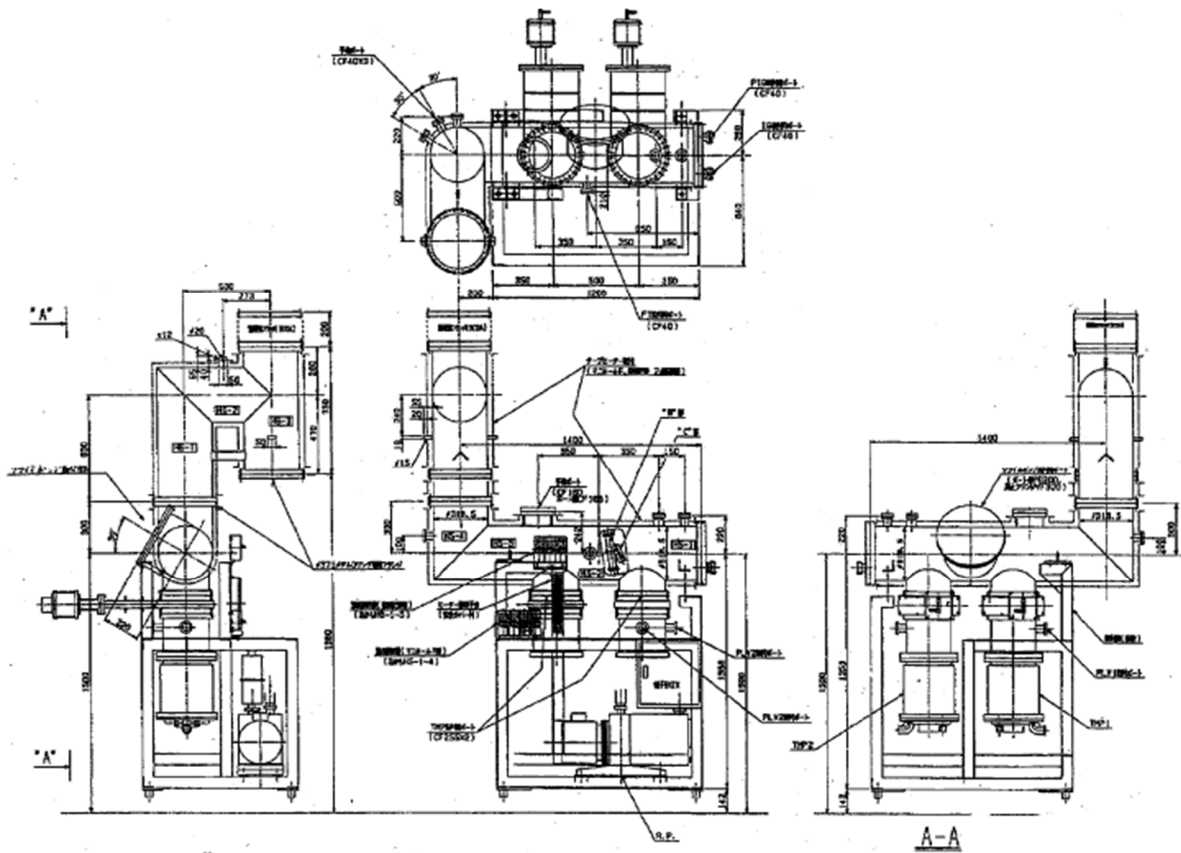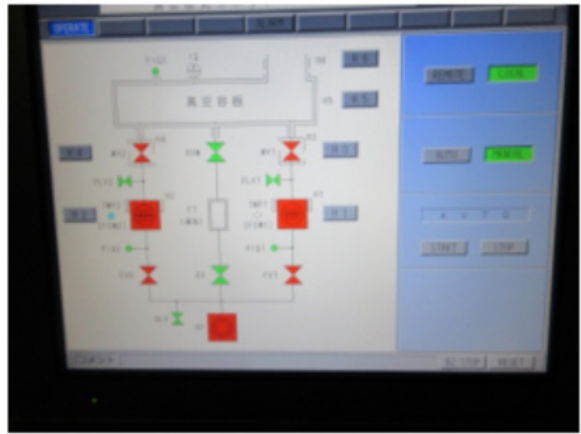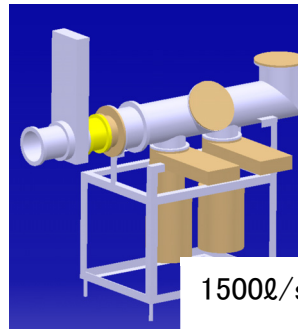

Fig. 6-3 Drawing of vacuum pumping system
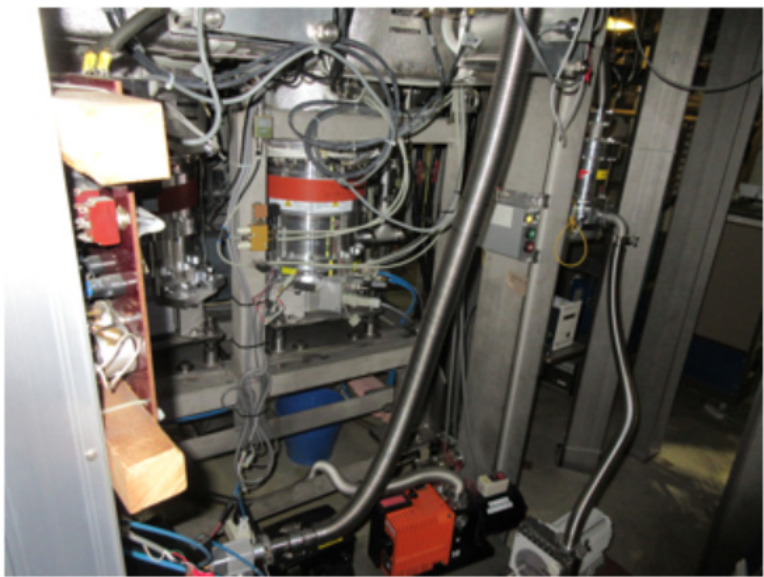
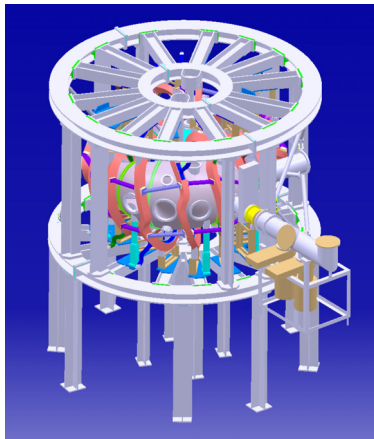Fig. 6-4 Picture of vacuum pumping system for CHS

1500ℓ/s TMP x 2

Gate valves

Additional parts

900
260
964
1400
φ305
φ318.5
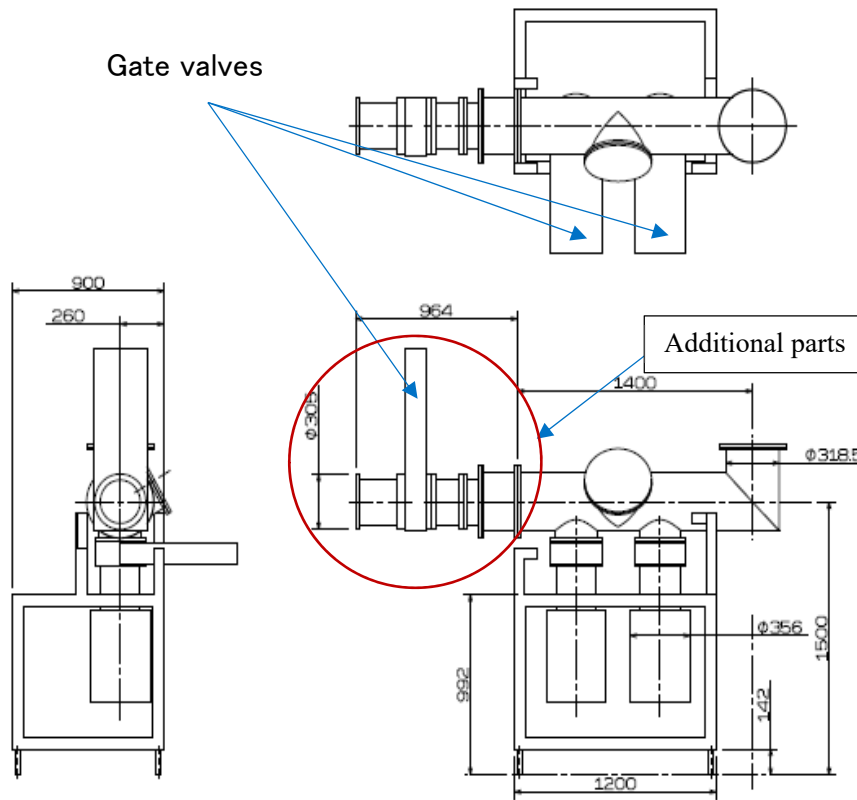φ356
992
142
1500
1200

Fig. 6-5 Vacuum pumping unit for CFQS
It will be transferred with some modifications from the CHS

[7]   DESIGN SPECIFICATIONS OF MODULAR COIL CONDUCTOR FOR CFQS

1)   Specification

Material   Hollow square tube with oxygen free copper(OFC-O)
Total current for one coil   IAT = 312.5 kAT
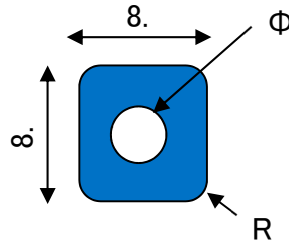Number of conductors in one coil N = 12 x 6 = 72
Pulse length $\Delta t = 2$

Fig. 7-1 Cross section of a conductor

2)   Cross-sectional area of cooling hole

$$S_{H2O} = \pi D^2/4 = 12.566 \ [mm^2]$$

3)   Cross-sectional area of conductive section (when the corner R is 1mm)

$$S_{CU} = W^2 - S_{H2O} - \text{Lack of corners}$$
$$=8.5 \times 8.5 - 12.566 - (2 \times 2 - \pi \times 1 \times 1) = 58.825 \quad mm^2$$

4)   Current in a conductor

$$I = I_{AT}/N = 312.5/72 = 4.34 kA$$

5)   Current density

$$j = I/S_{CU} = 4340 / 58.825 = 73.78 \ A/mm^2$$

6)   Adiabatic rise of temperature in a pulse

$$dT/dt = j^2 \times 5.9 \times 10^{-3} = 32 \ k/s$$

$$\Delta t \ dT/dt = 32 x 2 = 64 \ k \quad \text{(may be reasonable)}$$

7)   Cooling time

It may be typically 5 to 10 minutes, which depends on flow rate of the water.

[8] FORMULA OF ADIABATIC TEMPERATURE RISE

The temperature without cooling during pulse operation of the copper coil can be easily evaluated by the following equation. It almost matches the temperature change in a short time, because the standard thermal time constant is much longer than the pulse length.

The temperature change of the conductor is obtained from the thermal equation.

$$C\frac{dT}{dt} = Q_h - Q_c$$

$$Q_h = I^2 R = (jS_{cu})^2 \times \rho_e L/S_{CU} = j^2 S_{cu}\rho_e L \qquad [W = J/s]$$

$$Q_c = 0$$

where C is a heat capacity, Q_h is a heating power and Q_c is a cooling power.

Heat capacity of conductor;	$C = mC_p$	$[J/K]$
Mass of conductor;	$m = LS_{cu}\rho$	[kg]
Density of conductor;	$\rho = 8,888 kg/m^3$	[kg/m3]
Specific heat of conductor;	$C_p = 361$	$[J/kgK]$
Resistivity of conductor;	$\rho_e = 1.895 \times 10^{-8}$	$[\Omega m]$

It is as follows when the physical property value of copper at 75 ℃ is inputted.

$$\frac{dT}{dt} = \frac{Q_h}{C} = \frac{j^2 S_{cu}\rho_e L}{LS_{cu}\rho C_p} = j^2 \frac{\rho_e}{\rho C_p} = j^2 [A/mm^2] \times 5.9 \times 10^{-3}$$
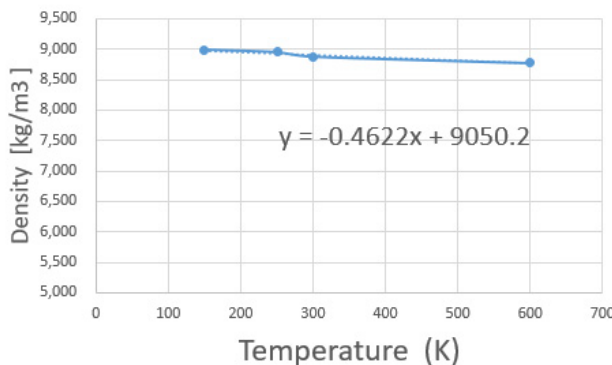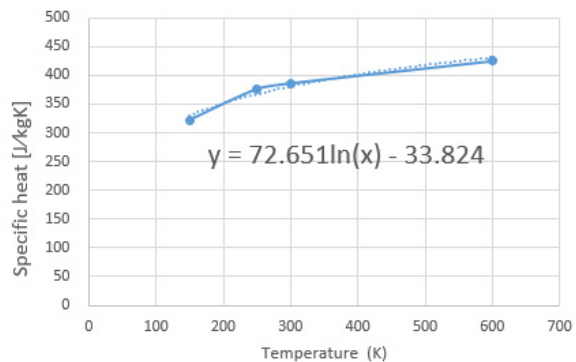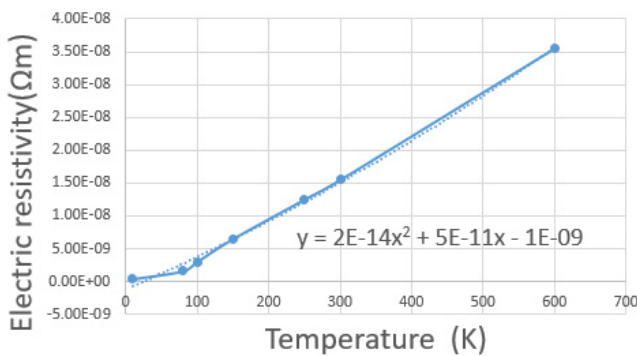
Ref.
JSME Data Book : Heat Transfer 4th Edition
I Hirata : Journal of the Cryogenic Society of Japan (1970)

[9]　　INDUCTANCE MATRIX OF MODULAR COILS FOR CFQS

Table 9-1 and Table 9-2 were obtained by NIFS at May 2019 after the design change of reducing the maximum curvature and tilting the normal direction to the current carrying surface. They were obtained by ANSYS/Maxwell.

Table 9-1　　　　Inductance matrix of modular coil

	M1-1	M1-2	M1-3	M1-4	M2-1	M2-2	M2-3	M2-4	M3-1	M3-2	M3-3	M3-4	M4-1	M4-2	M4-3	M4-4
M1-1	2216	14	13	461	462	15	14	160	157	21	17	39	70	36	25	71
M1-2	14	2216	461	13	15	462	160	14	21	157	71	26	36	70	39	17
M1-3	13	461	2215	14	14	160	462	15	17	71	157	36	25	39	70	21
M1-4	461	13	14	2216	160	14	15	462	71	17	21	70	39	26	36	157
M2-1	462	15	14	160	2166	19	13	73	451	31	14	27	158	62	21	41
M2-2	15	462	160	14	19	2166	73	13	31	451	41	21	62	158	27	14
M2-3	14	160	462	15	13	73	2166	19	14	41	451	62	21	27	158	31
M2-4	160	14	15	462	73	13	19	2166	41	14	31	158	27	21	62	451
M3-1	157	21	17	71	451	31	14	41	2079	60	11	18	462	140	16	28
M3-2	21	157	71	17	31	451	41	14	60	2079	28	16	140	463	18	11
M3-3	17	71	157	21	14	41	451	31	11	28	2079	140	16	18	462	60
M3-4	39	26	36	70	27	21	62	158	18	16	140	1986	14	15	399	462
M4-1	70	36	25	39	158	62	21	27	462	140	16	14	1985	399	15	18
M4-2	36	70	39	26	62	158	27	21	140	463	18	15	399	1988	14	16
M4-3	25	39	70	36	21	27	158	62	16	18	462	399	15	14	1983	140
M4-4	71	17	21	157	41	14	31	451	28	11	60	462	18	16	140	2080

Each coil is composed of one turn. Unit of inductance is nH

Table 9-2　　　　Inductance matrix of modular coil and other coils

	Modular Coil				PFC		TFC		
	M1	M2	M3	M4	IV	OV	TC1	TC2	TC3
M1	56.1	13.5	5.0	4.0	0.06	0.81	-0.82	-0.21	
M2	13.5	47.1	9.7	6.9	0.25	0.20	-1.75	-0.34	
M3	5.0	9.7	45.5	14.1	-0.33	-0.50	-0.69	-1.07	
M4	4.0	6.9	14.1	47.9	-0.49	-0.58	-0.47	-1.41	
IV	0.06	0.25	-0.33	-0.49	4.08	0.68	0.00	0.00	
OV	0.81	0.20	-0.50	-0.58	0.68	17.27	0.00	0.00	
TC1	-0.82	-1.75	-0.69	-0.47	0.00	0.00	0.0029	0.0001	
TC2	-0.21	-0.34	-1.07	-1.41	0.00	0.00	0.0001	0.0025	
TC3									

Four coils in each modular coil, two coils in each PFC and four coils in each TFC are connected in series. One modular coil, one PFC and one TFC are composed of 72 turns, 32 turns and 8 turns respectively. Unit of inductance is mH.

Table 9-3 and Table 9-4 were obtained by Keye Co. at August 2018. Later, the design of the modular coil was changed, so it is slightly different from the latest value. But it is not so much.

Table 9-3   Inductance matrix of modular coil (Old)

name	M1-1	M1-2	M1-3	M1-4	M2-1	M2-2	M2-3	M2-4	M3-1	M3-2	M3-3	M3-4	M4-1	M4-2	M4-3	M4-4
M1-1	2368	14	13	451	450	15	14	156	151	21	17	69	69	36	26	39
M1-2	14	2368	451	13	15	450	156	14	21	151	69	17	36	69	39	26
M1-3	13	451	2368	14	14	156	450	15	17	69	151	21	26	39	69	36
M1-4	451	13	14	2369	156	14	15	450	69	17	21	151	39	26	36	69
M2-1	450	15	14	156	2314	19	13	72	436	31	14	41	154	62	21	27
M2-2	15	450	156	14	19	2314	72	13	31	436	41	14	62	154	27	21
M2-3	14	156	450	15	13	72	2313	19	14	41	436	31	21	27	154	62
M2-4	156	14	15	450	72	13	19	2314	41	14	31	436	27	21	62	154
M3-1	151	21	17	69	436	31	14	41	2212	59	12	27	456	138	16	19
M3-2	21	151	69	17	31	436	41	14	59	2213	27	12	138	456	19	16
M3-3	17	69	151	21	14	41	436	31	12	27	2212	59	16	19	456	138
M3-4	69	17	21	151	41	14	31	436	27	12	59	2212	19	16	138	456
M4-1	69	36	26	39	154	62	21	27	456	138	16	19	2146	399	16	15
M4-2	36	69	39	26	62	154	27	21	138	456	19	16	399	2146	15	16
M4-3	26	39	69	36	21	27	154	62	16	19	456	138	16	15	2147	399
M4-4	39	26	36	69	27	21	62	154	19	16	138	456	15	16	399	2146
sum	3907	3908	3907	3908	3838	3838	3837	3838	3719	3720	3720	3719	3638	3637	3638	3637

Table 9-4   Inductance matrix of modular coil group (old)

Name	M1	M2	M3	M4
M1	59	13	5	4
M2	13	50	11	5
M3	5	11	48	13
M4	4	5	13	53
sum	81	80	77	75

Four coils in each group are connected in series
Each coil is composed of 72 turns
Unit of inductance is mH

- Rough estimation of inductance

The inductance can be analytically estimated by the solenoid formula with the Nagaoka coefficient (https://keisan.casio.jp/exec/user/1488083605)

$$.L = K \times 4\pi \times 10^{-7} \times \mu_r \times N^2 \times S/Leng$$

where K is a Nagaoka coefficient, μ_r is a relative permeability, N is a number of turns, S is a cross section of inside area of coil and L_{eng} is a coil width.

M1 coil

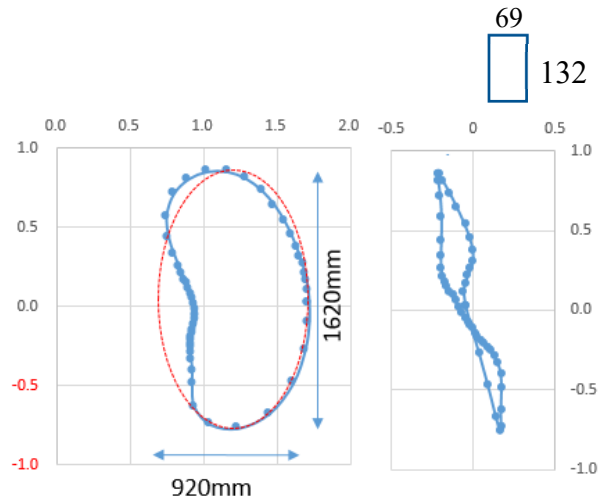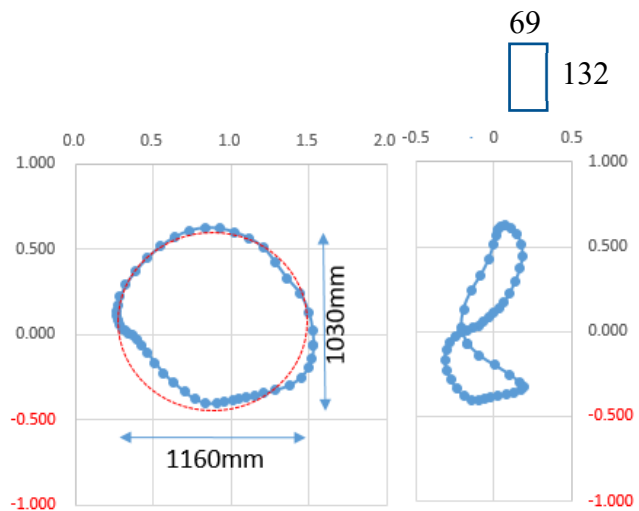S= π x0.92x1.62/4 = 1.17
L_{eng} = 0.069
$D/L_{eng} \sim 0.61/0.07 = 9$
K~0.2

$$L = \frac{0.2 \times 4\pi \times 10^{-7} \times 72^2 \times 1.17}{0.07} = 0.021 \text{ mH}$$

By the formula

$$L = 2213 \times 10^{-9} \times 72^2 = 0.0115 \text{ mH}$$

Obtained by the Maxwell

M4 coil

S= π x1.03x1.16/4 = 0.94
L_{eng} = 0.069
$D/L_{eng} \sim 0.55/0.07 = 7.9$
K~0.2

$$L = \frac{0.2 \times 4\pi \times 10^{-7} \times 72^2 \times 0.94}{0.07} = 0.017 \text{ mH}$$

By the formula

$$L = 2012 \times 10^{-9} \times 72^2 = 0.0104 \text{ mH}$$

Obtained by the Maxwell

[10]   RESISTANCE OF MODULAR COIL AND FORMULA FOR CFQS

Table 10-1   Resistance of modular coil

Name	S_{cu} (mm^2)	Total length (m) for four coils	R (mΩ)	
			Formula	Maxwell (*)
M1		1263	404	415.0
M2	58.825	1248	400	409.0
M3		1209	388	395.8
M4		1155	368	382.1

$$R = \rho_e L_{eng}/S_{CU}$$

where

Resistivity; $\rho_e = 1.895 \times 10^{-8}$ [Ωm   Cu at 75°C]
Length of conductor; L_{eng} [m]
Cross Section of a condcutor; $S_{cu} = 58.825 \times 10^{-6}$ [m^2]

(*) The resistances were obtained by ANSYS/Maxwell with the condition of the resistivity = 1.724 x 10^{-8} that was a value at room temperature and the cross section of a conductor = 126.5x10^{-6} that was an average value including isolator and cooling hole. Since there are large differences of the condition between the formula and the Maxwell, results of the Maxwell are multiplied by 2.4.

[11]   PRESSURE DROP AND AVERAGE TEMPERATURE RISE OF COOLING WATER FOR
        MODULAR COIL OF CFQS

11.1.   Calculation condition

Coil conductor length for one water circuit   L = 100 m
Size of water cooling hole in a conductor   D = 4 mmΦ
Flow velocity in a conductor $u = 1.2\,m/s$
Number of parallel circuit for a coil   n = 3
Number of coils   m = 16
Inner diameter of water cooling main pipe D_0 = 52.9 mmΦ (50A Sch10)
Series resistance of all coils   R = 2Ω (including margin)
Current   I = 4.34 kA
Pulse length   Δt = 2s
Discharge period   ΔT = 300s
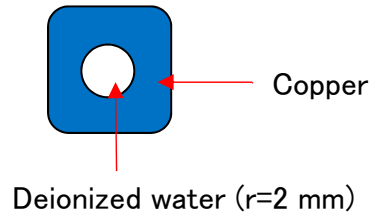
Fig. 11-1   Cross section of a conductor

11.2.   Pressure drop in a coil conductor

Flow rate in a conductor

$$Q = Au = \pi D^2/4 \times u = 12.566 \times 10^{-6} \times 1.2 = 1.51 \times 10^{-5}\ [m^3/s]$$
$$= 9.06 \times 10^{-4}\ [m^3/min] \cong 0.9\ [l/min]$$

Reynolds number

$$R_e = vD/v = \frac{1.2 \times 0.004}{0.803 \times 10^{-6}} = 5976$$

where v is a Kinematic viscosity

Tube friction coefficient obtained by the Bradius formula

$$\lambda = 0.3164 R_e^{-0.25} = 0.0360$$

Pressure drop obtained by the Fanning formula

$$\Delta P = \lambda \frac{L}{D} \frac{\rho u^2}{2} = 0.0360 \frac{100 \times 996 \times 1.2^2}{0.004 \times 2} = 6.45 \times 10^5\ [Pa] = 6.6\ [kgf/cm^2]$$

where $\rho = 996$ kg/m³ is a density of water.

11.3.   Average temperature rise

Flow rate in a main pipe

$$Q_0 = n \times m \times Q = 3{\times}16{\times}1.51 \times 10^{-5} \ [m^3/s] = 2.6 \ [m^3/hr]$$

Flow velocity in a main pipe

$$v_0 = Q_0/\left(\pi {D_0}^2/4 \right) = 7.248 \times 10^{-4} \ / \ 1.675 \times 10^{-3} = 0.43 \ [m/s]$$

Heat generation in one pulse

$$\Delta W = R I^2 \times \Delta t = 2 \times (4.34 \times 10^3)^2 \times 2 = 7.53 \times 10^7 \ [J]$$

Average temperature rise of cooling water

$$\Delta T_{water} = \frac{\Delta W/\Delta T}{Q_0 \times \rho\, C} = \frac{7.53 \times 10^7/300}{7.2 \times 10^{-4} \times 996 \times 4186} = 83.6 \ [k]$$

where $\rho = 996$ kg/m³ is a density and C = 4186 J/(kg k) is a specific heat capacity.

[12]   MG SET FOR THE FUSION DEVICE AS A REFERENCE

Table 12-1   MG set for the Fusion device

No	Fusion device	Generator		Drive	
		Capacity	Spec	Capacity	Spec
1	TRIAM-1M Kyushu University	125 MVA 60MJ	3Φ ACG 6.6kV 11kA 67-59Hz 670-590 rpm	1.4MW	3Φ IM
2	Heliotron-J Kyoto University	330 MVA 300MJ	3Φ ACG 18kV 10.58kA 65-50Hz 650-500 rpm	3.2MW	3Φ IM
3	JT-60 HMG QST	400 MVA 2.5GJ	3Φ ACG 18kV 12.83kA 77.6-54.2Hz 582-406 rpm	15MW	3Φ IM
4	JT-60 PMG QST	500 MVA 1.3GJ	3Φ ACG 18kV 16kA 77.6-54.2Hz 582-406 rpm	7MW	3Φ IM
5	JT-60 TMG QST	215 MVA 4 GJ	3Φ ACG 18kV 6.9kA 80-56Hz 600-420 rpm	19MW	Thyristor drive
6	Gamma 10 Tsukuba University	250 MVA 800MJ	3Φ ACG 18kV 8kA 77.6-54.3Hz 582-407rpm	2.4MW	3Φ IM
7	LHD, CHS NIFS	250 MVA 1.4GJ	3Φ ACG 18kV 8kA 93-58Hz 701-435rmp	8.5MW	3Φ IM
8	HL-2A SWIP, Chengdu (CHS Nagoya University)	125 MVA 200MJ	3Φ ACG 3kV 24kA 120-96Hz 3600 rpm	2.5MW	3Φ IM
9	HL-2A SWIP, Chengdu	300 MVA 1.35GJ	6Φ ACG 3kV 29kA 100-67Hz 500-335 rpm	8.5MW	3Φ IM
10	HL-2A SWIP, Chengdu	90MVA 250MJ	3Φ ACG 1650-1488 rpm	2.5MW	3Φ IM
11	HSX University of Winsconsin	84 MVA 42MWp Over 20MJ	DCM 30 motors 1.68kV 50kA		DCM

$$MVA = kV \times kA \times \sqrt{3}$$

Capacity of the above equipment Table 12-1   MG setis excessive for the CFQS, that expects 60MVA and 40MJ.

[13] NBI SYSTEM FOR CHS

We plan to transfer NBI system from CHS in NIFS to CFQS. Cconfiguration of the NBI power supply for CHS is shown in

Fig. 13-1 to Fig. 13-4.

A power capacity for the NBI system is shown in Table 13-1, Table 13-3 and Table 13-4. It should be noted that the commercial voltage is different in Japan and China as shown in Table 13-2.

Table 13-1   Power capacity of NBI 2 for CHS

Name	Voltage	Output Current	Capacity of input transformer
Acceleration power supply	AC6.6kV/DC 40KV	65A	3.7 MVA
Arc power supply	AC6.6kV/DC 130V	1 kA	250 kVA
Filament power supply	AC6.6kV/DC 12V	1.32 kA	
Low voltage 1Φ	AC 100V	48 A	4.8 kVA
Low voltage 3Φ	AC 200V	770 A	153.6 kVA

.

Table 13-2   Difference of power environment

	Frequency	High voltage	Low voltage 1Φ	Low voltage 3Φ
NIFS	60 (West Japan)	6.6kV	100V	200V
China	50	10kV	220V	380V

Table 13-3   Load list of low voltage power board for CHS

Row 1

No	V	Sys	Use	Load
u1	200V	ECH	Charger	24
u2	200V			
u3	200V	NBI 1	GTO PS	8
u4	200V	NBI 2	GTO PS	8
u5	100V	ECH	1Φ SWB	12
L1	100V	NBI 1	V CB	1.6
R1	100V	NBI 2	AVP CB	1.6
L2	100V	NBI 1	B CB	1.6
R2	100V	NBI 2	BLA CB	1.6
L3	100V			
R3	100V	NBI 2	TCB	1.6
L4	100V	NBI 1	CryoP CB	1.6
R4	100V	NBI 1	BL CB	1.6
L5	100V			
R5	100V	NBI 1	Gas	1.6
L6	100V			
R6	100V			
L7	100V			
R7	100V			
L8	100V			
R8	100V			
L9	100V	ECH	Ctrl room	1.6
R9	100V	ECH	LN2	0.8
L10	100V			
R10	100V			

Row2

No	V	Sys	Use	Load
L1	200V	NBI 1	DclPS	16
R1	200V	NBI 2	DclPS	16
L2	200V	NBI 1	GTO LV	16
R2	200V	NBI 2	GTO LV	16
L3	200V	NBI 1	Bmag PS	16
R3	200V	NBI 2	Bmag PS	16
L4	200V	NBI 1	VP	4.8
R4	200V	NBI 2	AVP	4.8
L5	200V	NBI 1	SCR CB	4.8
R5	200V	NBI 2	SCR CB	4.8

Row 3

No	V	Sys	Use	Load
L1	200V	NBI 1	Ref Cryo	8
R1	200V	NBI 1	Ref Cryo	8
L2	200V	NBI 1	Ref Cryo	8
R2	200V	NBI 1	Ref Cryo	8
L3	200V	NBI 1	Ref Cryo	8
R3	200V	NBI 1	Ref Cryo	8
L4	200V	NBI 1	Ref Cryo	8
R4	200V	NBI 1	Ref Cryo	8
L5	200V	NBI 1	Ref Cryo	8
R5	200V	NBI 1	DclCB	8
L6	200V	NBI 2	DclCB	8
R6	200V	NBI 1	Arc PS	8

Row 4

No	V	Sys	Use	Load
L1	200V	NBI 2	SB Gas	8
R1	200V	NBI 2	Ref Cryo	8
L2	200V	NBI 2	Ref Cryo	8
R2	200V	NBI 2	Ref Cryo	8
L3	200V	NBI 2	Ref Cryo	8
R3	200V	NBI 2	Ref Cryo	8
L4	200V	NBI 2	Ref Cryo	8
R4	200V	NBI 2	Ref Cryo	8
L5	200V	NBI 2	Ref Cryo	8
R5	200V	NBI 2	AVP	8
L6	200V			
R6	200V			

Row 5

No	V	Sys	Use	Load
L1	200V			
R1	200V			
L2	200V			
R2	200V			
L3	200V			
R3	200V			
L4	200V			
R4	200V	CHS	CryoP CB	8
L5	200V	ECH	Cool oil	5.28
R5	200V			
b1	200V	ECH	3Φ SWB	35.2
b2	200V			

Board name; KIT-1A-13. The unit of load is kVA.
A capacity for NBI2 system will be minimally required in CFQS torus hall
A capacity for ECH system will be also required in CFQS torus hall

Table 13-4   Abbreviation description

A/F PS	Arc/Filament power Supply	GS	Grounding switch
ACC	Acceleration	GTO	Gate turnoff Thyristor
AclPs	Accelerate power supply	IS	Ion source
ACSW	ACC SCR switch	ISOTB	Isolation table
AVP	Auxiliary vacuum pump	LV	Low voltage
B	Beam	PS	Power supply
BLA	Beam line auxiliary control board	Ref Cryo	Refrigerator for cryogenic pump
Bmag	Bending magnet	SB	Surge blocker
BndMag	Bending magnet	SCR	Thyristor
CB	Control board	SW	Switch
Cool oil	Cooling oil equipment	SWB	Switch board (or power board)
CP	Control Panel	TCB	Temperature converter board
CryoP	Cryogenic pump	TRF	Transformer
DCC	DC capacitor	V	Vacuum
DCL	DC reactor (or inductor)	VCB	Vacuum circuit breaker
DclCB	Deceleration control board	VD	Voltage divider
DclPs	Power supply for deceleration	VP	Vacuum pump
EQ	Equipment	VPS	Vacuum pumping system
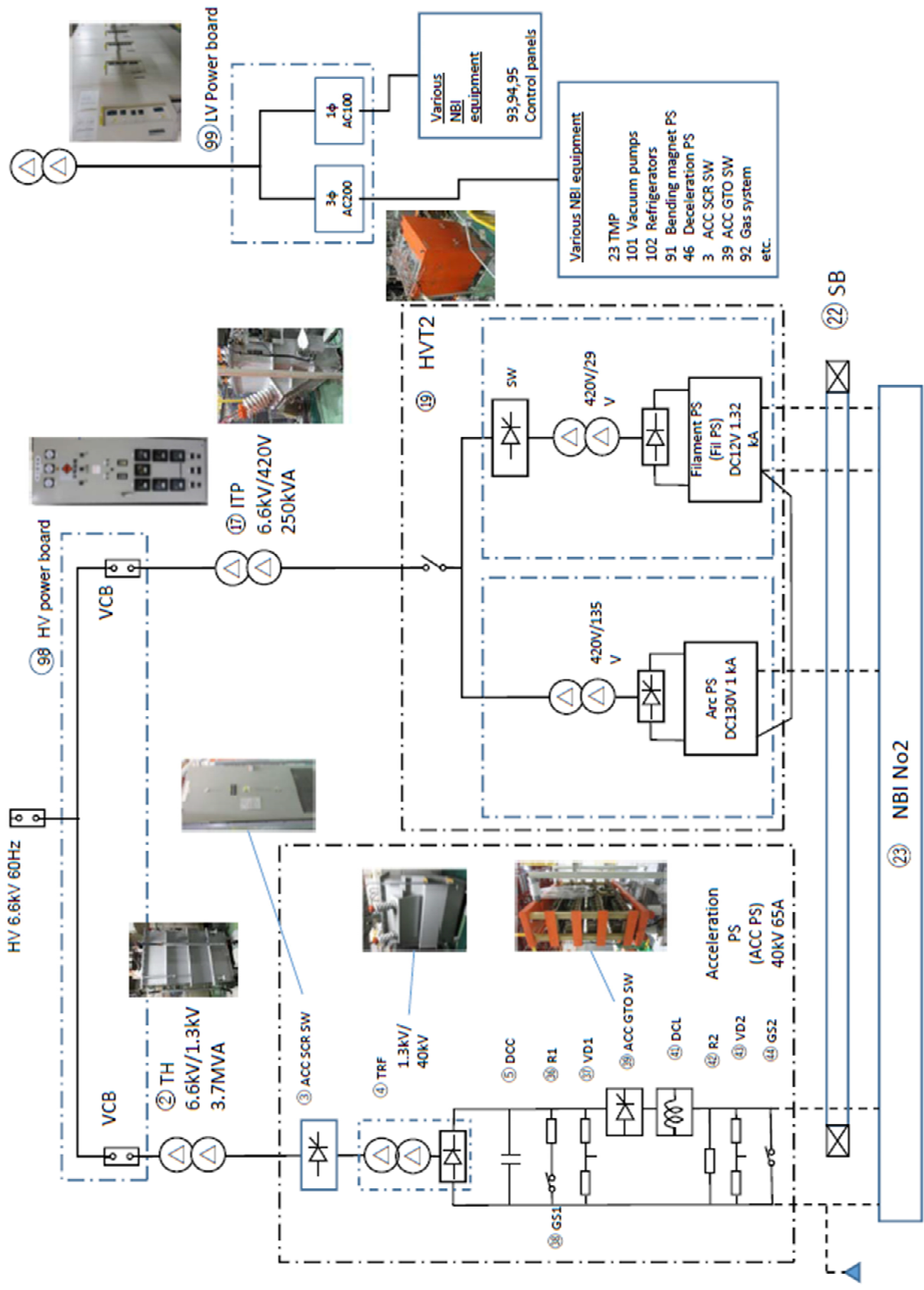
Fig. 13-1   One-line diagram of NBI 2 system
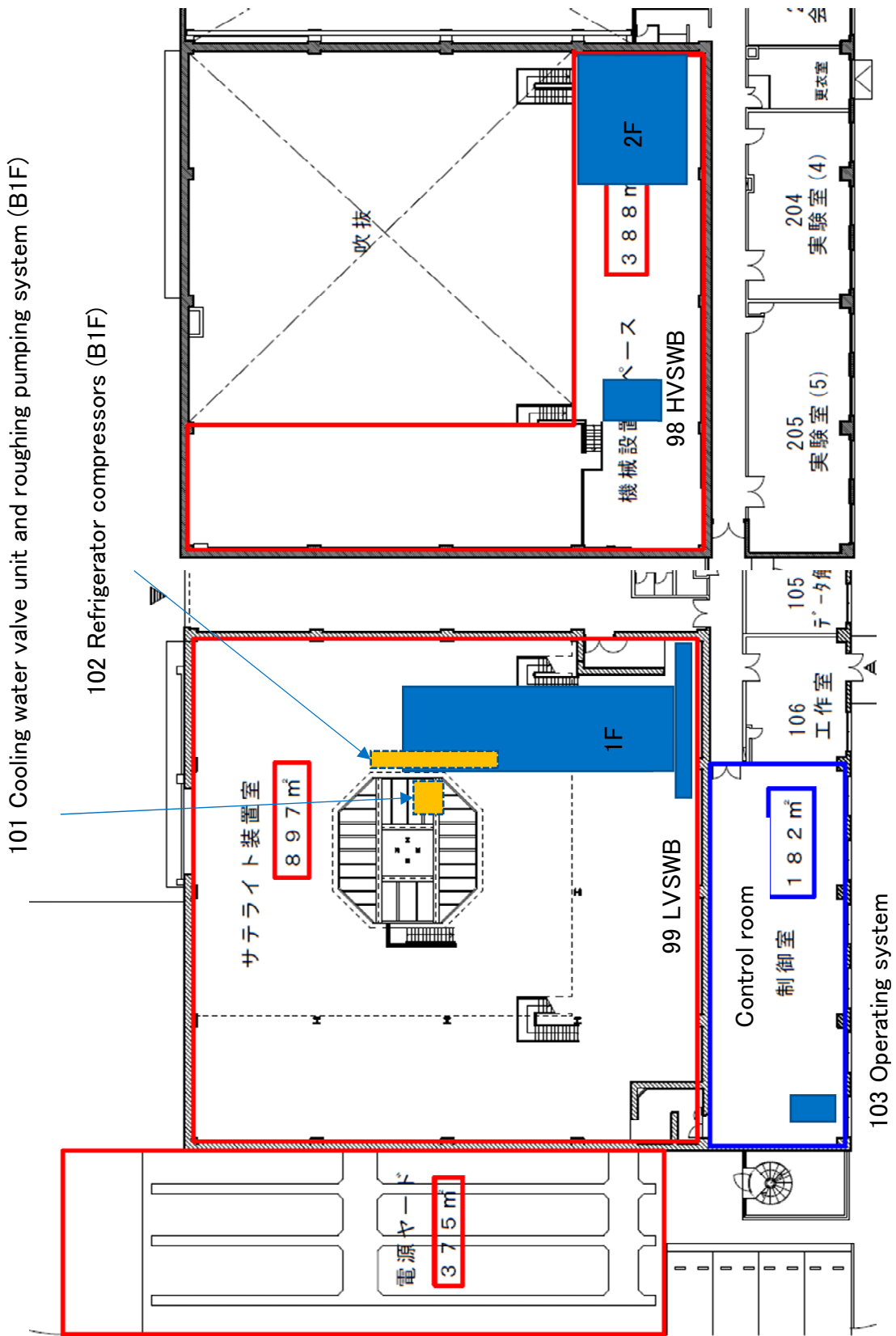
Fig. 13-2　　　Location of NBI 2 system at CHS
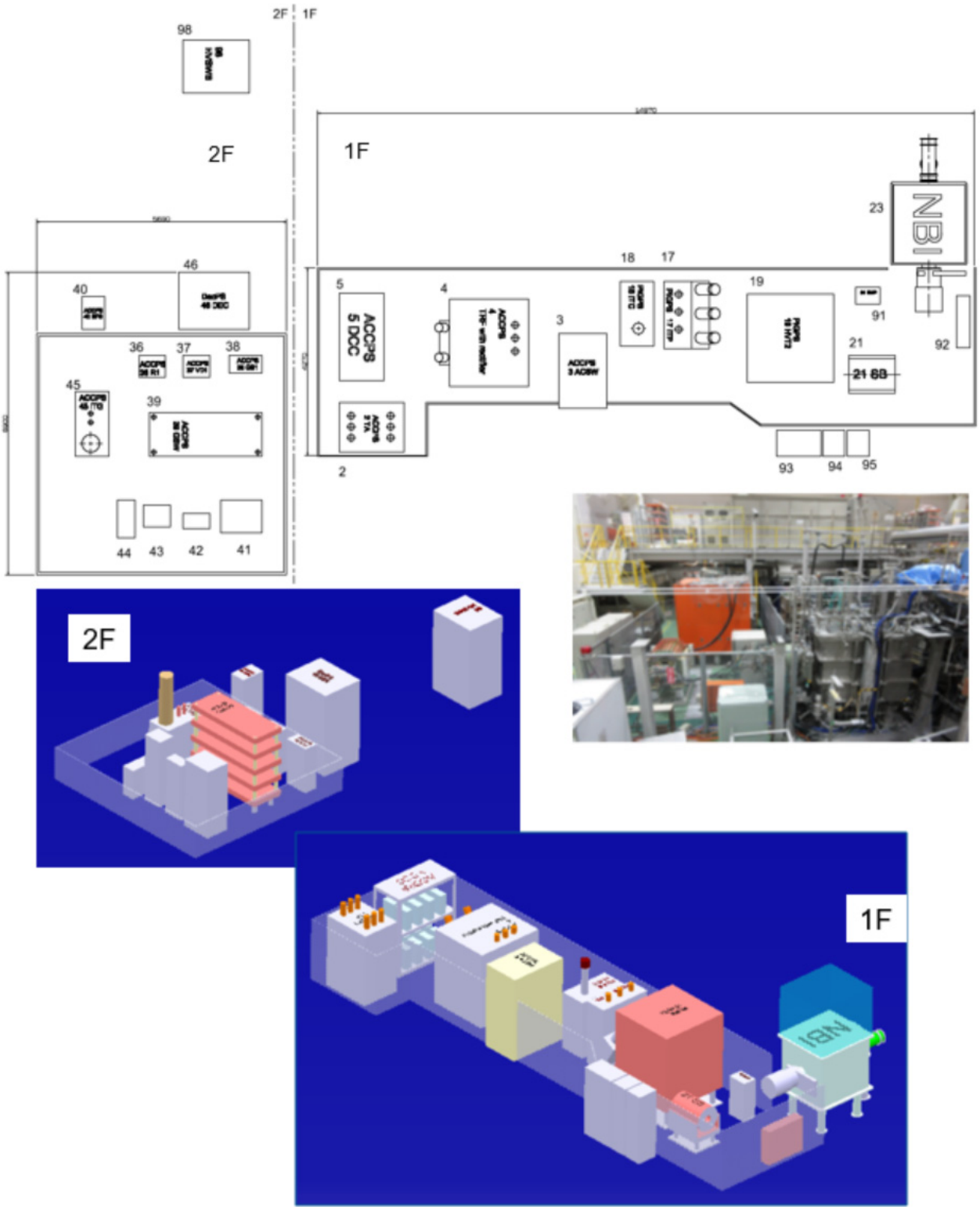
Fig. 13-3   Layout of NBI 2 system at CHS
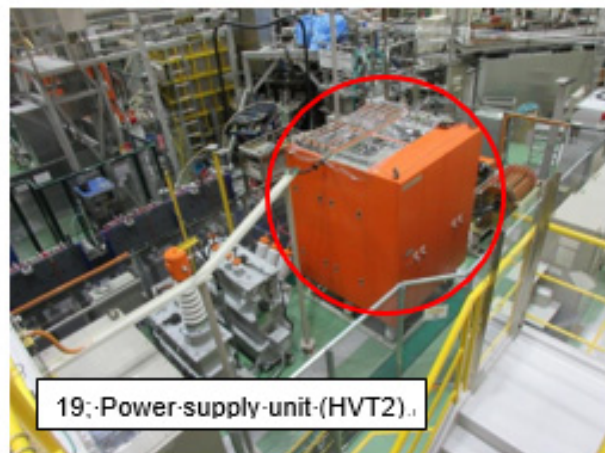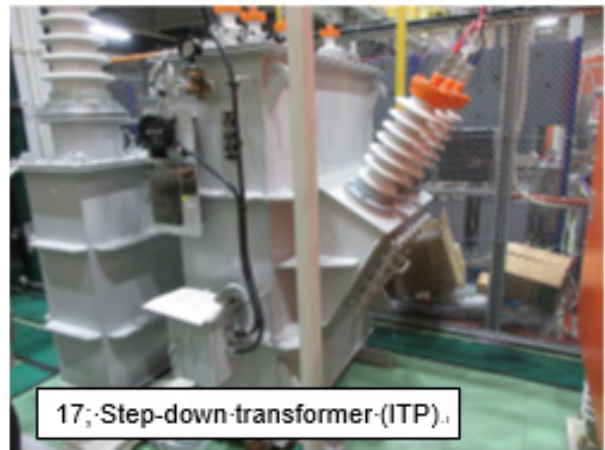
Fig. 13-4   Picture of main components for CHS NBI 2 system

Fig. 14-1   One line diagram of the CHS power supply system
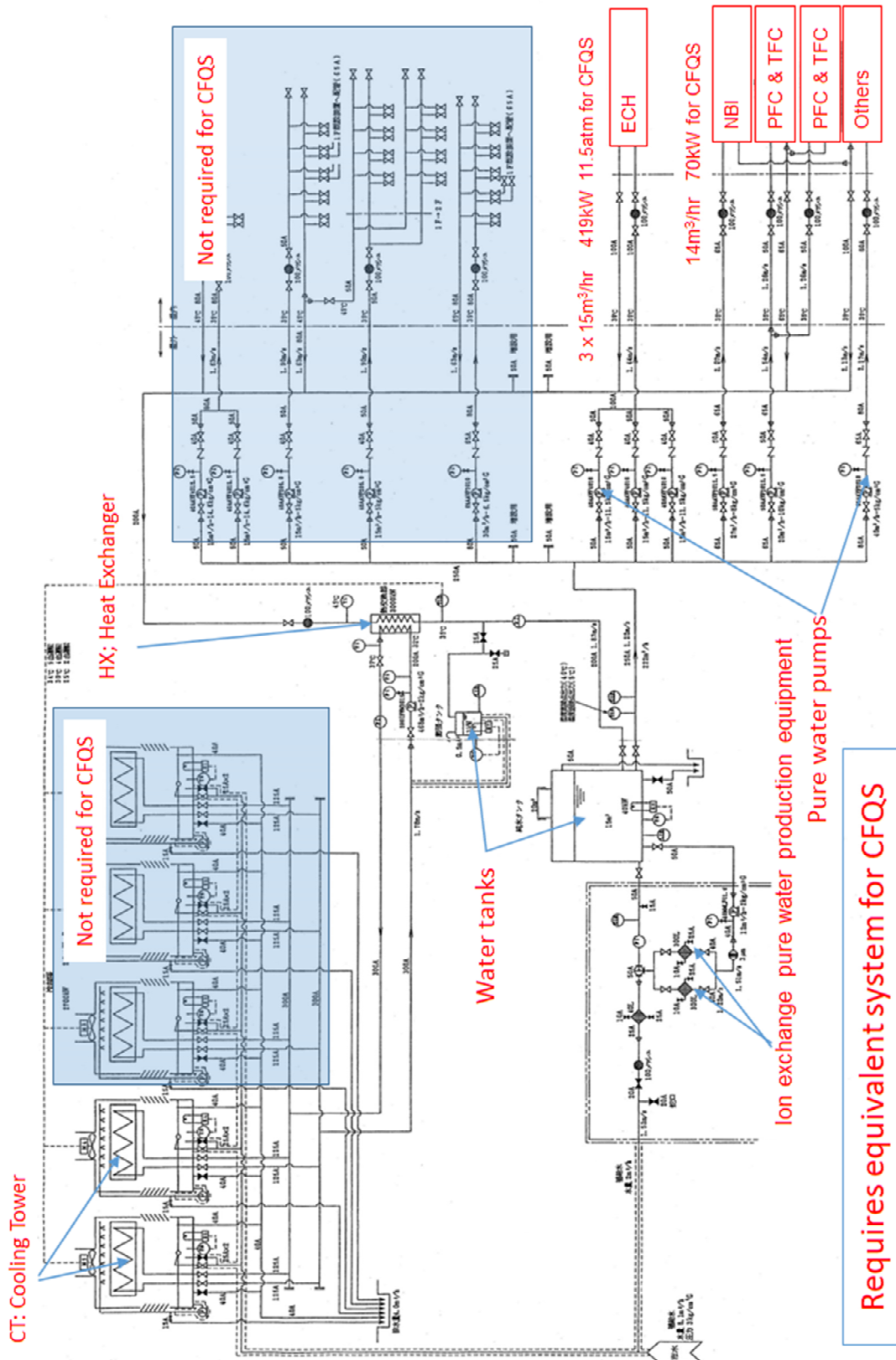
Fig. 15-1   Cooling water system diagram of CHS

[16]   MODELS DEVELOPED BY 3D PRINTER

Various reduced models were developed on the 3D printer in order to validate the device fabrication and assembly procedures.
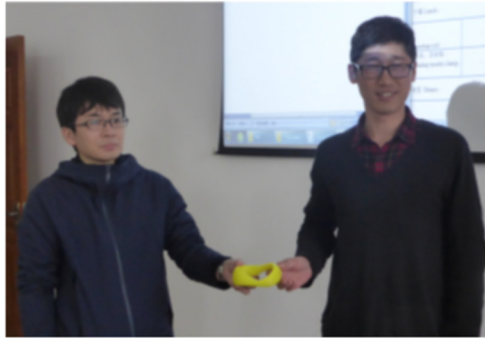
Fig. 16-1   Outermost magnetic surface of plasma
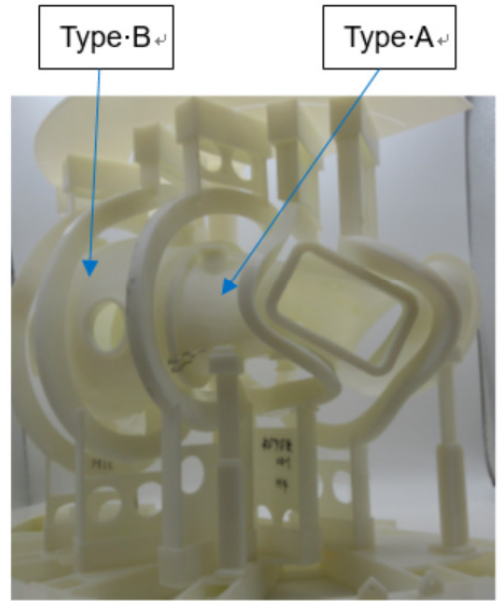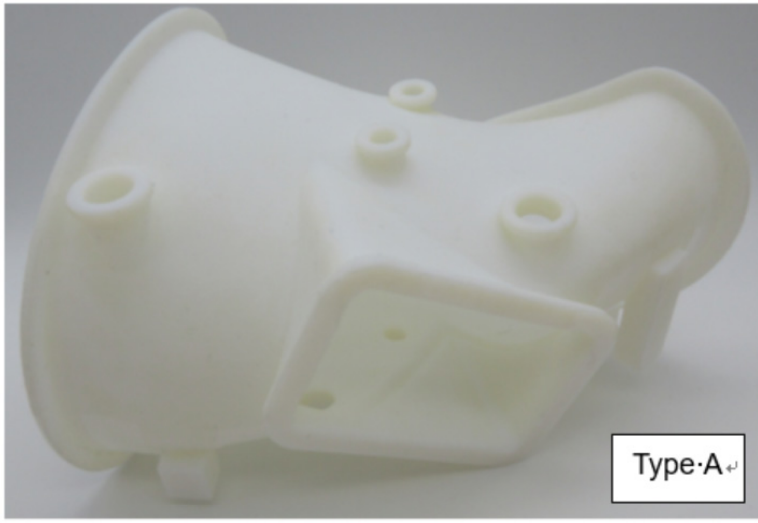
Fig. 16-2   Vacuum main vessel
(Preliminary; port size and position will be changed)
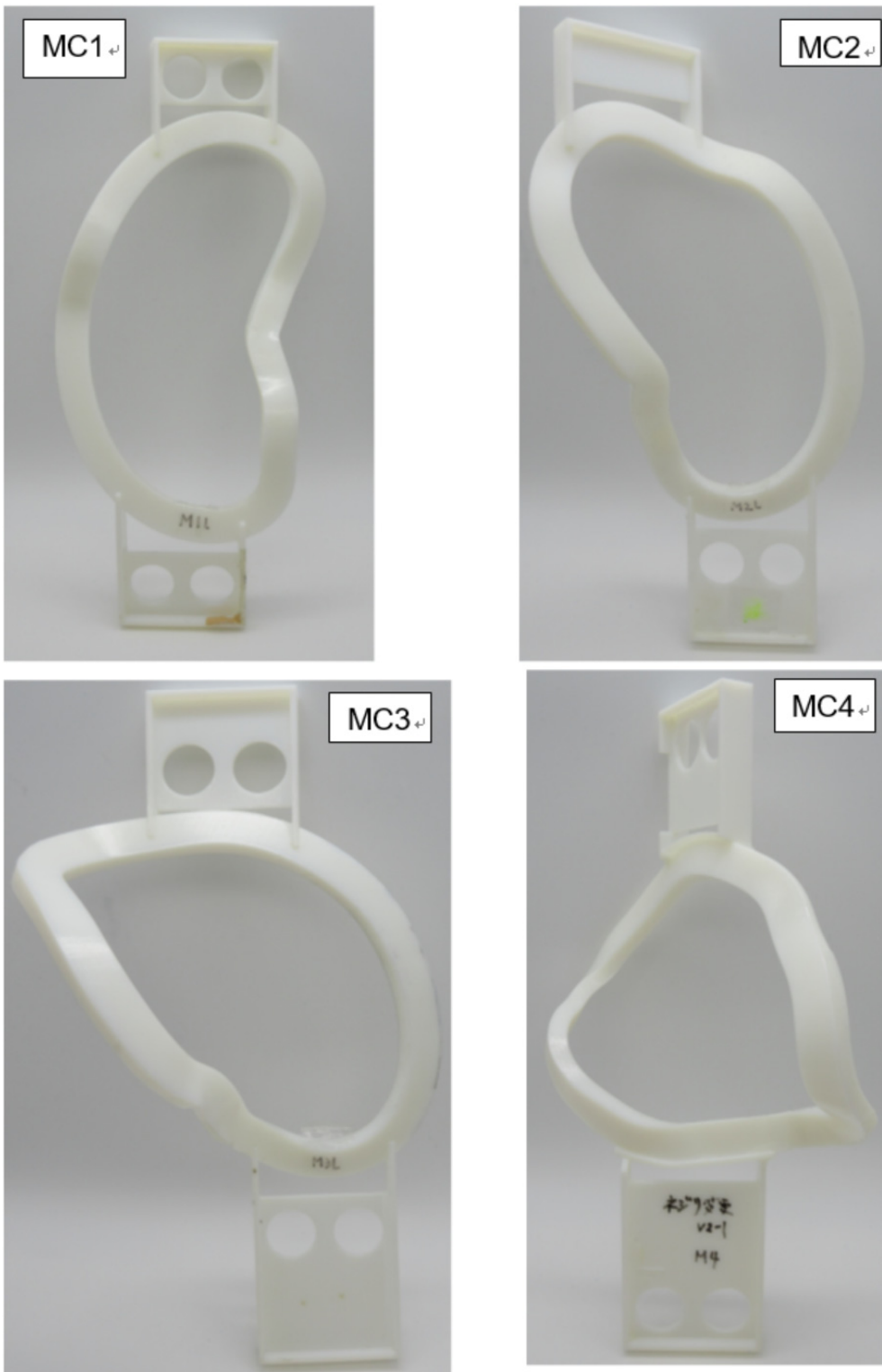
Fig. 16-3   Modular coil without case
(Preliminary; Coil case and leg will be modified)
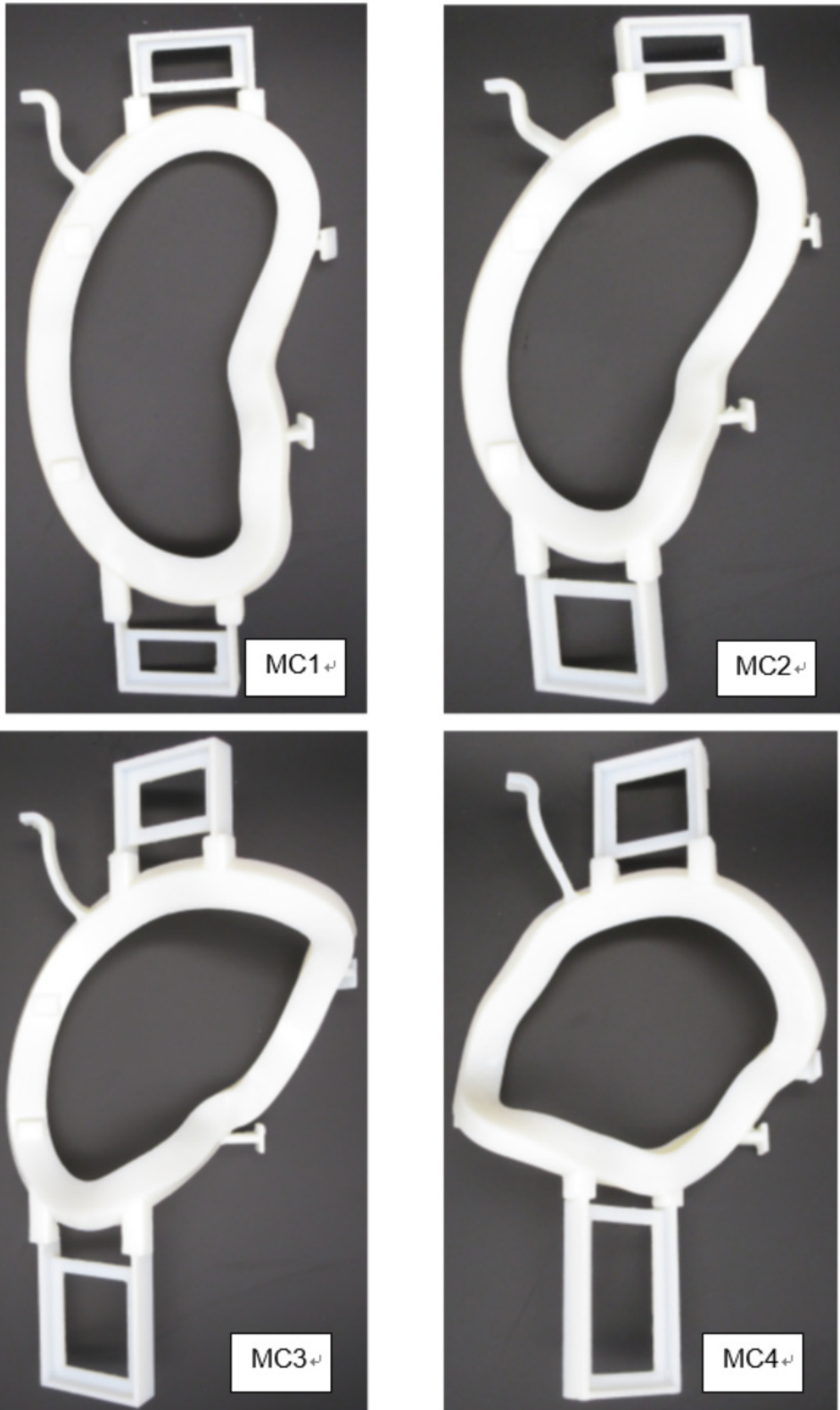
Fig. 16-4   Modular coil with case and support
（Latest at 2019/05/15）
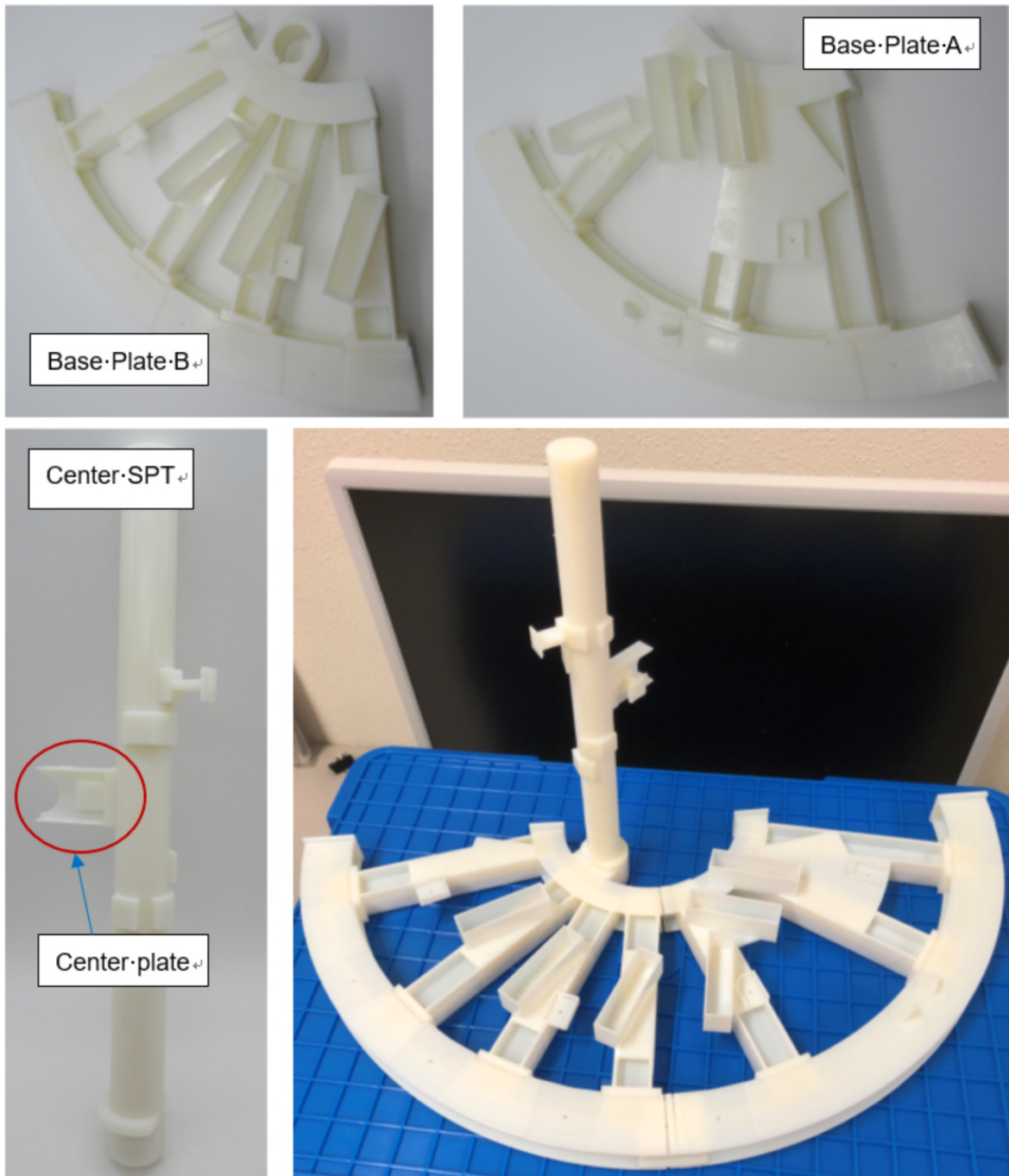
Fig. 16-5　　　　Coil supports
(Preliminary; Center plate will be modified)
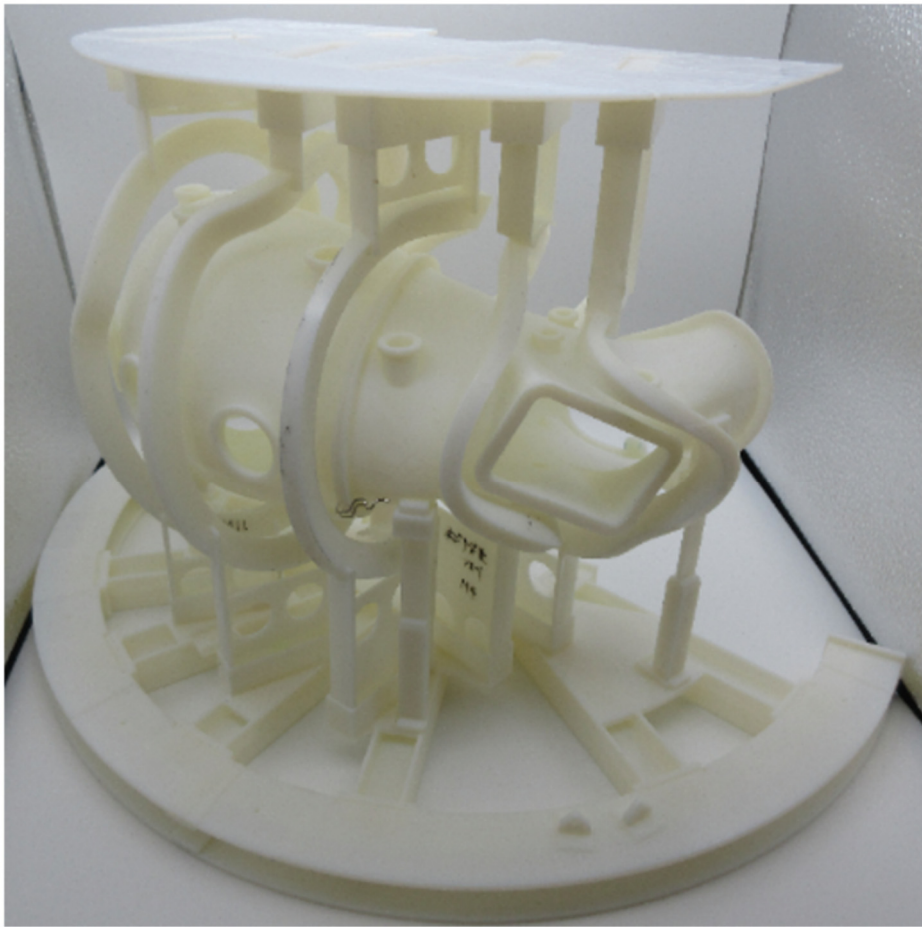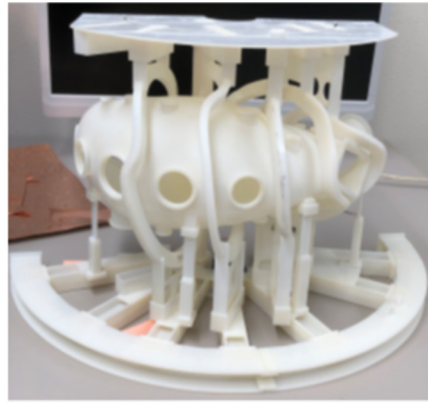
Fig. 16-6   Modular coils, vacuum vessel and coil supports
(Preliminary)
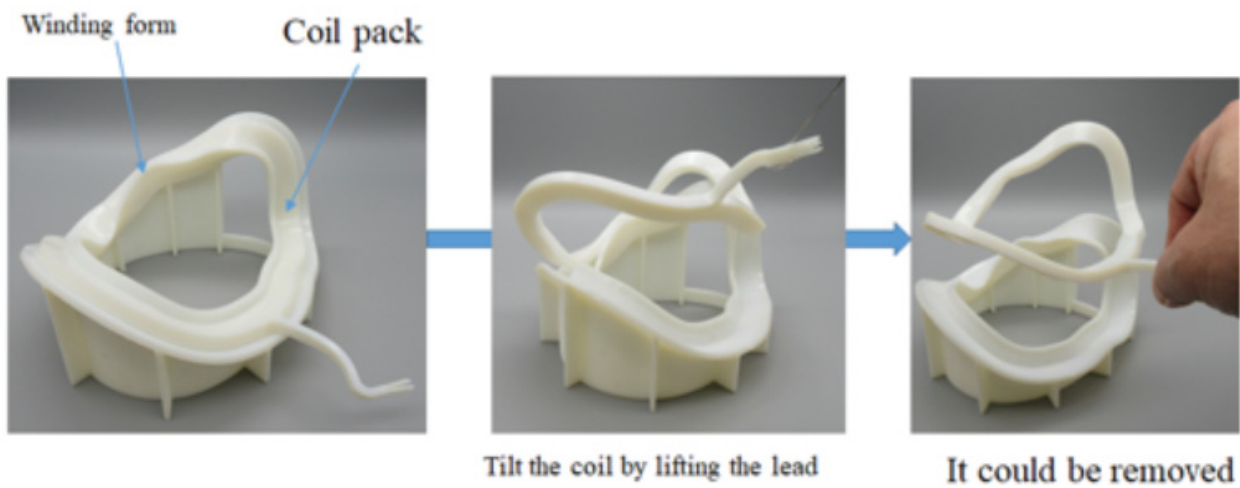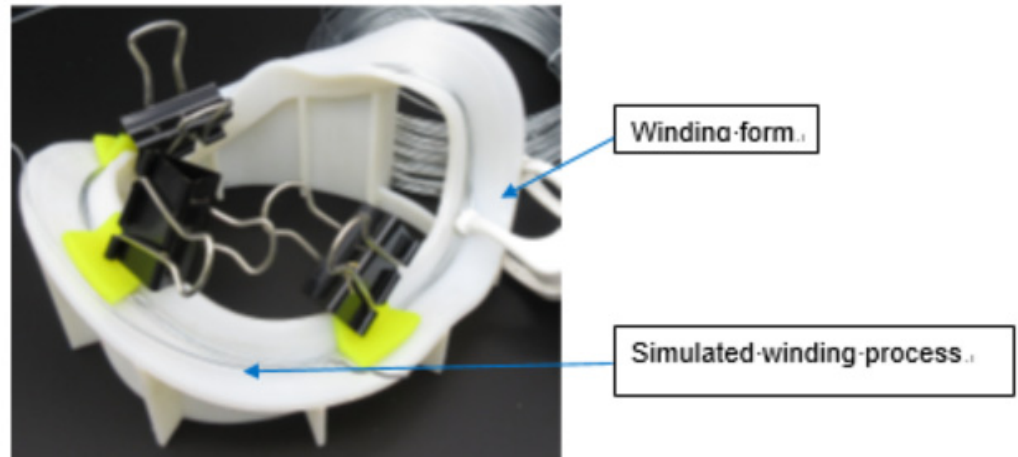
Fig. 16-7   Simulation of removing coil pack from winding frame for modular coil

[17]   CROSS SECTION OF VACUUM MAIN VESSEL FOR CFQS

The shape of inner surface is shown at different toroidal angle in this chapter. Fig. 17-1 shows how to define the shape and others show cross sectional shape at different angles.
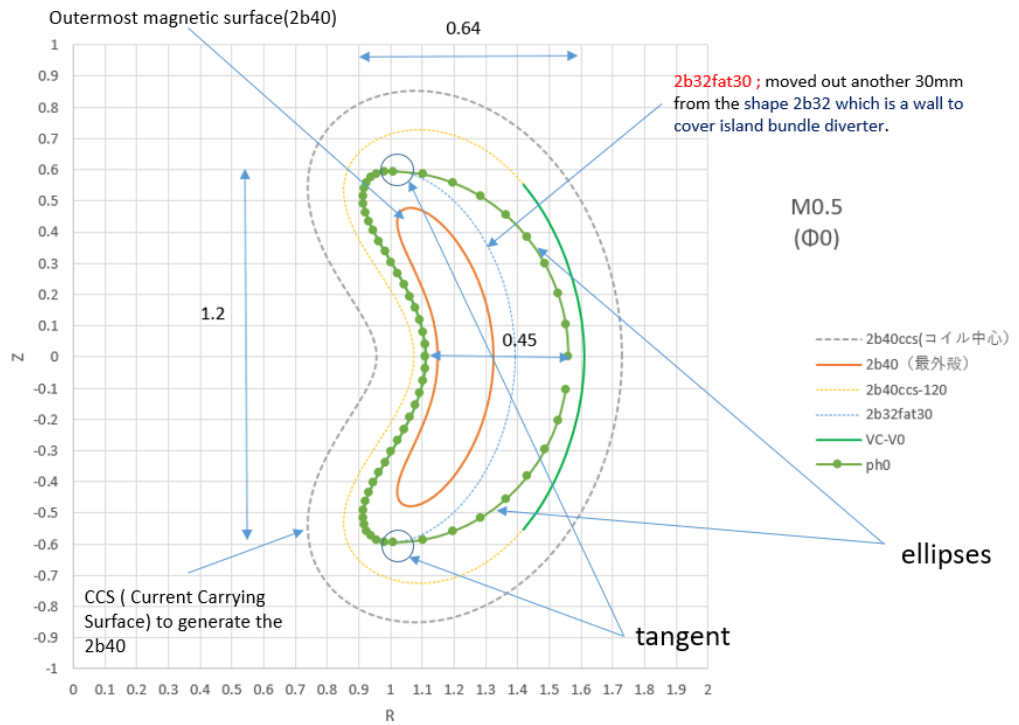
Fig. 17-1   Drawing with showing how to define inner shape of main vessel
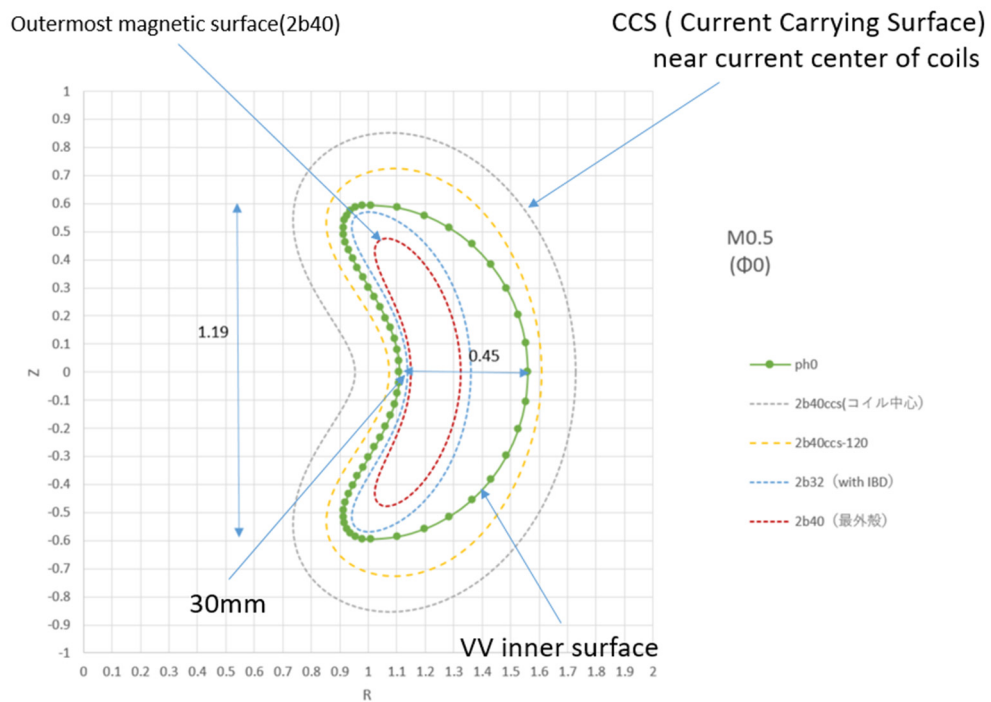
Fig. 17-2　　　　　Shape of main vessel at Φ＝0 degrees
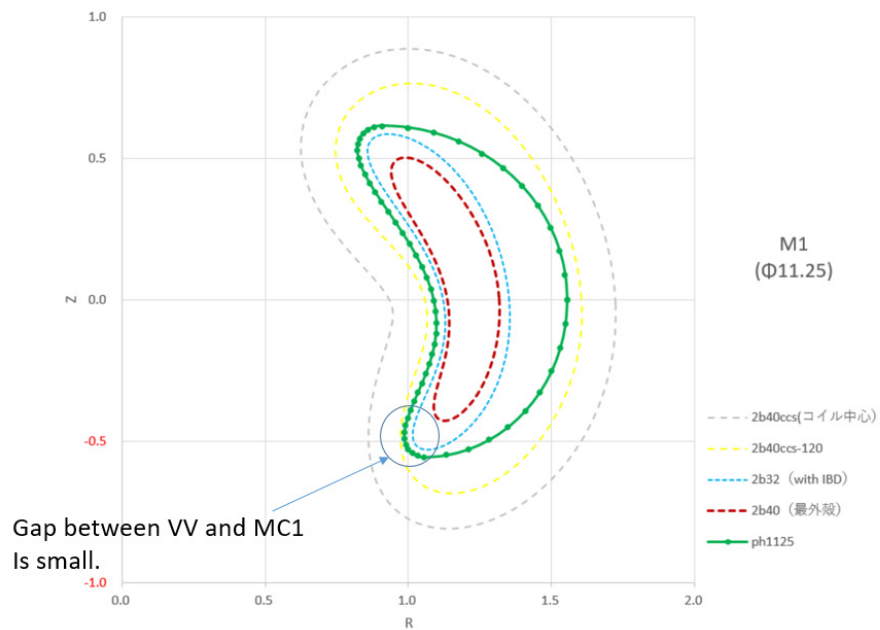
Fig. 17-3　　　　　Shape of main vessel at Φ＝11.25（1/8 x 90）degrees
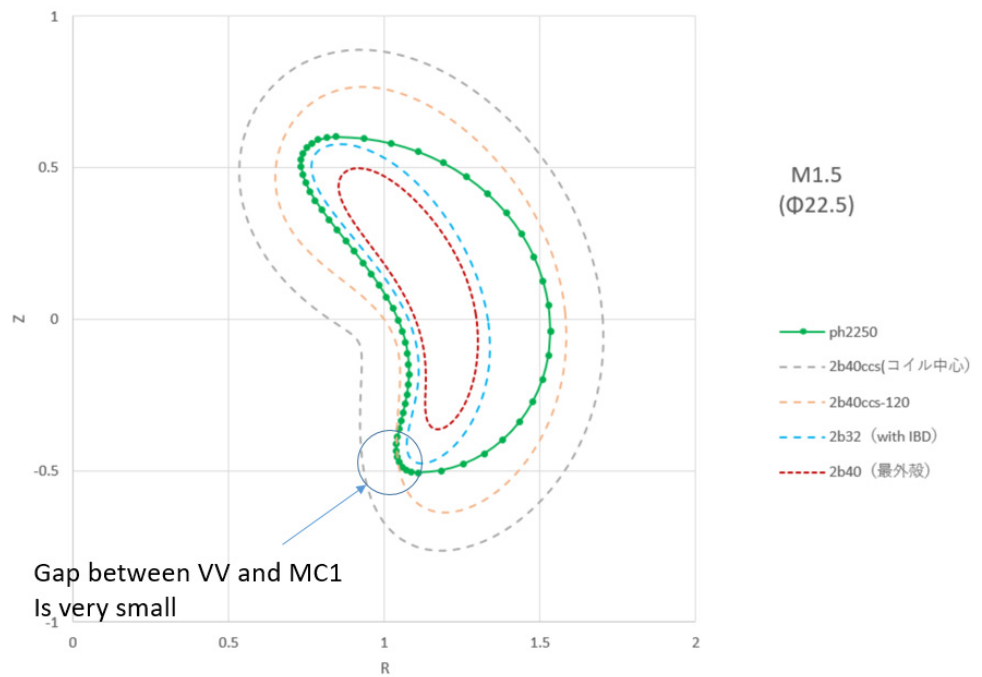
Fig. 17-4   Shape of main vessel at Φ＝22.5 (2/8 x 90) degrees
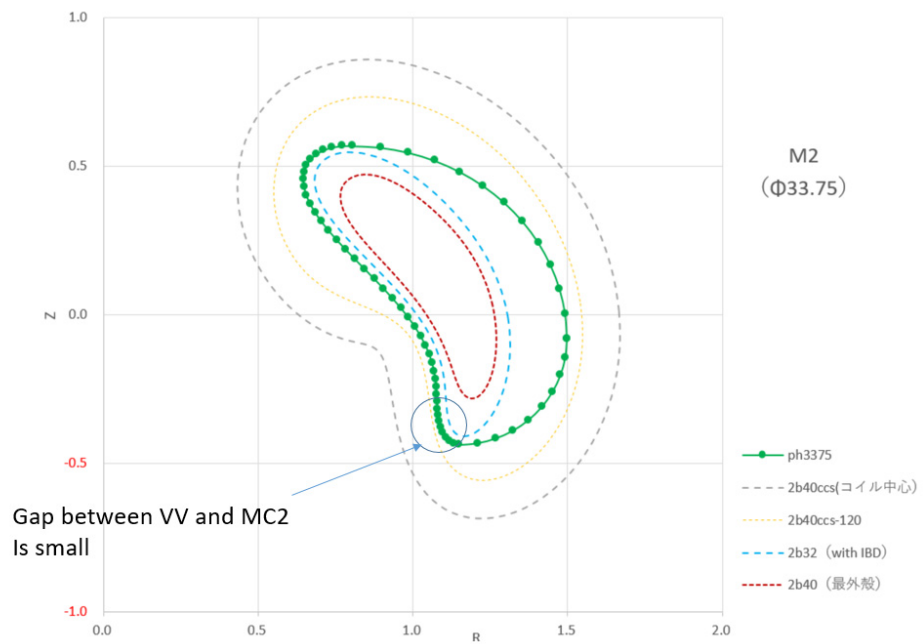
Fig. 17-5   Shape of main vessel at Φ＝33.75 (3/8 x 90) degrees
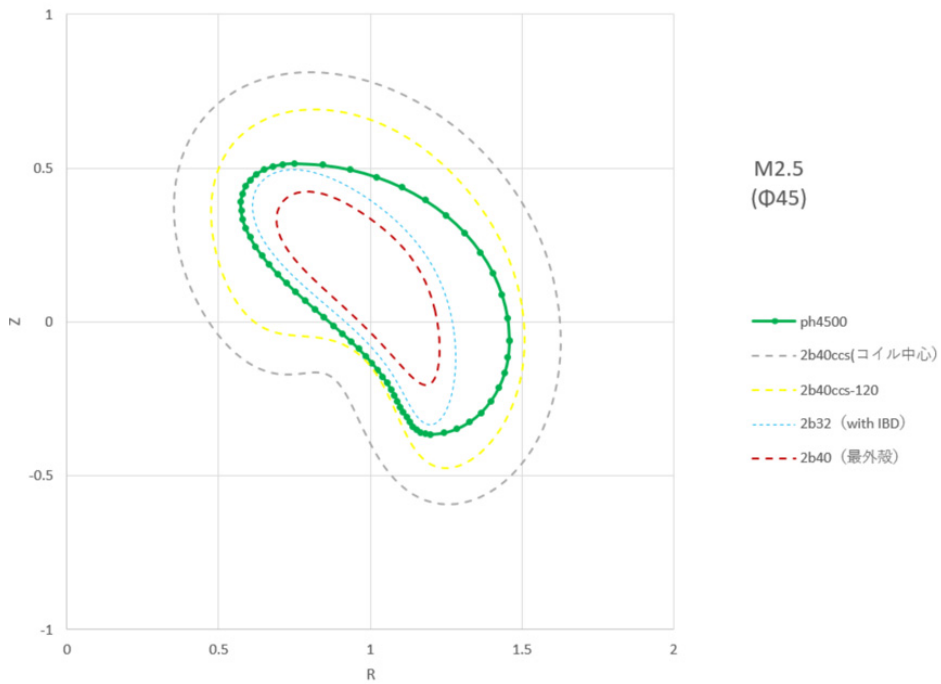
Fig. 17-6   Shape of main vessel at $\Phi = 45$ (4/8 x 90) degrees
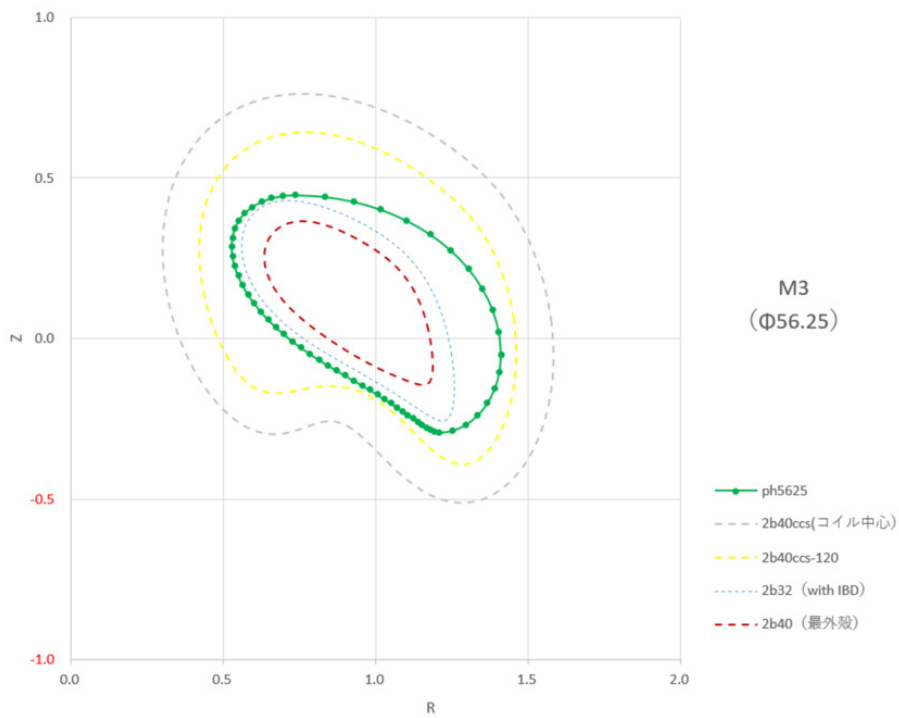
Fig. 17-7   Shape of main vessel at $\Phi = 56.25$ (5/8 x 90) degrees
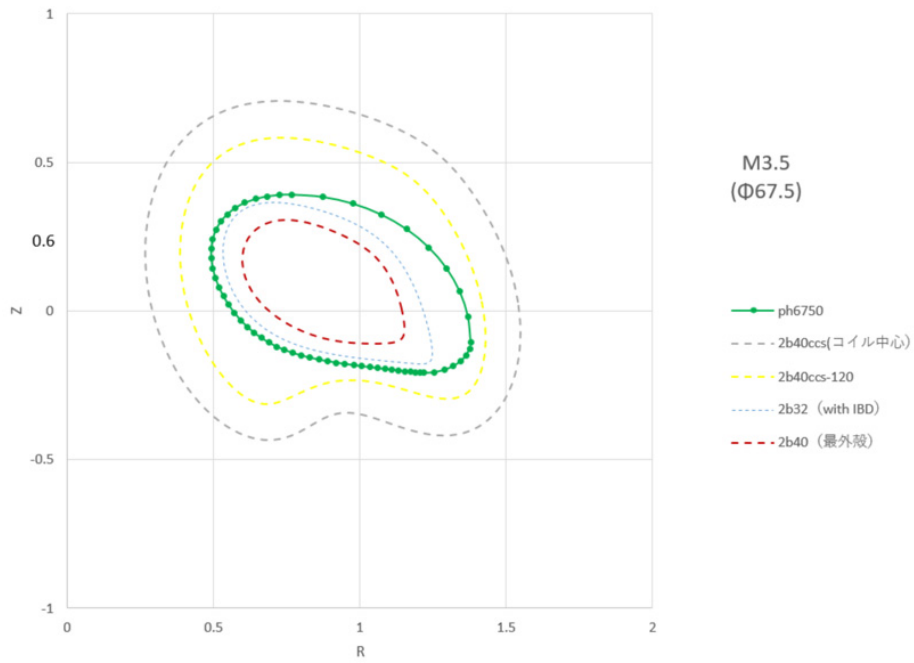
Fig. 17-8　　　　　Shape of main vessel at Φ＝67.5（6/8 x 90）degrees
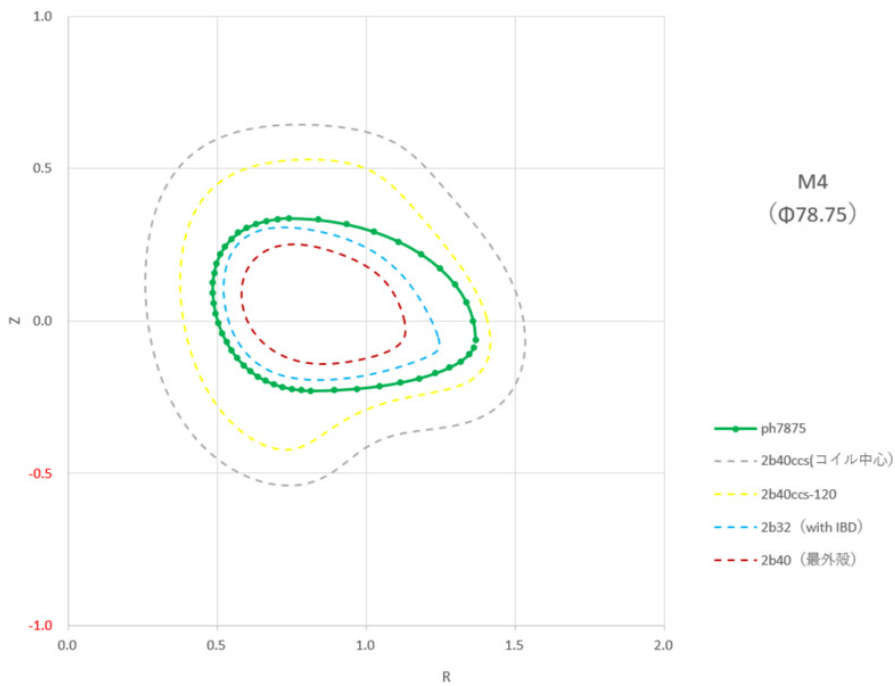
Fig. 17-9　　　　　Shape of main vessel at Φ＝78.75（7/8 x 90）degrees
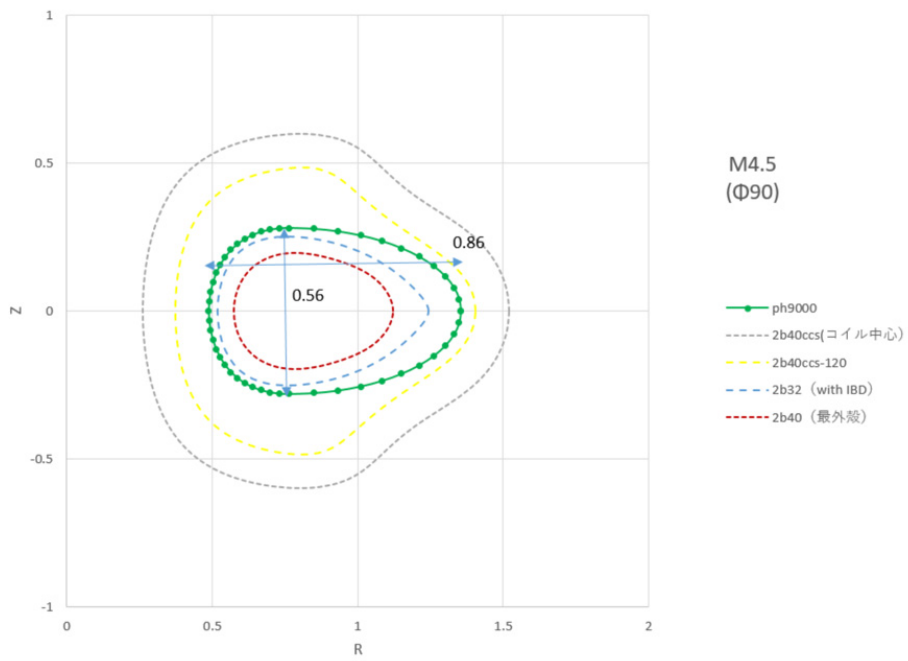
Fig. 17-10　　　　　Shape of main vessel at Φ＝90 degrees

[18]   LAYOUT OF PORT AND LEAF SPRING TYPE LEG FOR VACUUM VESSEL IN CFQS

This chapter includes a port list and some drawings to show the position of ports and leaf spring type legs.

18.1.   Position and size of ports

The design goal or policy to define ports as follows.

- Make it possible to divert as many CHS assets as possible.
- Allow one worker to enter the vacuum vessel and work inside to weld together split places of the vacuum vessel, to install measurement equipment like magnetic probes and some plates to protect vacuum vessel from heat input like beam dump for NBI.
- Establish as many and large ports as possible to make the experiment more flexible.

In order to achieve this purpose, we examined the location and size of the ports, and decided the draft in Table 18-1   Port list of CFQS, Fig. 18-1 and Fig. 18-4. However, small ports with a diameter of 70 or less may not be considered, and may be increased further. Fig. 18-5 shows sample of the tangential port for the NBI.

18.2.   Position and size of leaf spring type legs

Fig. 18-6 shows the position and size of leaf spring type leg. The size of leaf spring is 20 mm in thickness, 100mm in width, and 400mm in length. The buckling load of this spring is about 3 MN per one leg according to the buckling formula. Assuming that the load of the vacuum vessel is 4000 kg including the contents, the load per leg is about 5000N. The buckling safety factor is about 600 and is safe enough with sufficient margin.

Table 18-1 Port list of CFQS

No	Sector	Place	Name	Position		Size		Use	Comments
				V,R,P	Φ	Flange	Extension		
1	5	IN	I5	V0	90	Φ114	Φ63.5	Interferometer	Through with O-P
2	13	IN	I13	V0	270	Φ114	Φ63.5	Thomson	Through with O-P
3	1	OUT	O1U	P55	0	Φ203	Φ153		
4	1	OUT	O1	V0	0	Φ406	Φ350		
5	1	OUT	O1L	P55	0	Φ203	Φ153		
4	2	OUT	O2	V0	22.5	Φ356	Φ295		
5	3	OUT	O3	V0	45	Φ305	Φ250	Vacuum Pump	
6	5	OUT	O5	V0	90	440x680	380x620	NBI Interferometer	Through with I-P, Entrance
7	7	OUT	O7	V0	135	Φ305	Φ250		
8	8	OUT	O8	V0	157.5	Φ356	Φ295		
3	9	OUT	O9U	P55	180	Φ203	Φ153		
9	9	OUT	O9	V0	180	Φ406	Φ350	ECH	
5	9	OUT	O9L	P55	180	Φ203	Φ153		
10	10	OUT	O10	V0	202.5	Φ356	Φ295		
11	11	OUT	O11	V0	225	Φ305	Φ250	HIBP	
12	13	OUT	O13	V0	270	440x680	380x620	Thomson	Through with I-P
13	15	OUT	O15	V0	315	Φ305	Φ250		
14	16	OUT	O16	V0	337.5	Φ356	Φ295		
15	1.5	UP	U1.5	R1180	18	Φ253	Φ203		
16	3	UP	U3	R1000	45	Φ203	Φ153	CXRS & MSE	
17	4	UP	U4	R1000	63	Φ152	Φ101.6		
18	5	UP	U5	R1000	90	Φ152	Φ101.6		Through with L-P
19	5.5	UP	U5.5	R1250	102	Φ152	Φ101.6		
20	5.5	UP	U5.5a	R750	102	Φ152	Φ101.6		
21	6.5	UP	U6.5	R1200	130	Φ152	Φ101.6		
22	9.5	UP	U9.5	R1180	198	Φ253	Φ203		
23	11	UP	U11	R1000	225	Φ203	Φ153	HIBP	
24	12	UP	U12	R1000	243	Φ152	Φ101.6		
25	13	UP	U13	R1000	270	Φ152	Φ101.6	FIR	Through with L-P
26	13.5	UP	U13.5	R1250	282	Φ152	Φ101.6		
27	13.5	UP	U13.5a	R750	282	Φ152	Φ101.6		
28	15	UP	U15	R1200	310	Φ152	Φ101.6		
29	3.5	LW	L3.5	R1200	51	Φ152	Φ101.6		
30	4.5	LW	L4.5	R1250	78	Φ152	Φ101.6		
31	4.5	LW	L4.5a	R750	78	Φ152	Φ101.6		
32	5	LW	L5	R1000	90	Φ152	Φ101.6		Through with U-P
33	6	LW	L6	R1000	117	Φ152	Φ101.6		
34	7	LW	L7	R1000	135	Φ203	Φ153	CXRS(ref)	
35	8	LW	L8	R1180	162	Φ253	Φ203		
36	11.5	LW	L11.5	R1200	231	Φ152	Φ101.6		
37	12.5	LW	L12.5	R1250	258	Φ152	Φ101.6		
38	12.5	LW	L12.5a	R750	258	Φ152	Φ101.6		
39	13	LW	L13	R1000	270	Φ152	Φ101.6	FIR	Through with U-P
40	14	LW	L14	R1000	297	Φ152	Φ101.6		
41	15	LW	L15	R1000	315	Φ203	Φ153		
42	16	LW	L16	R1180	342	Φ253	Φ203		

V; Vertical position, R; Major Radius P; Poloidal angle
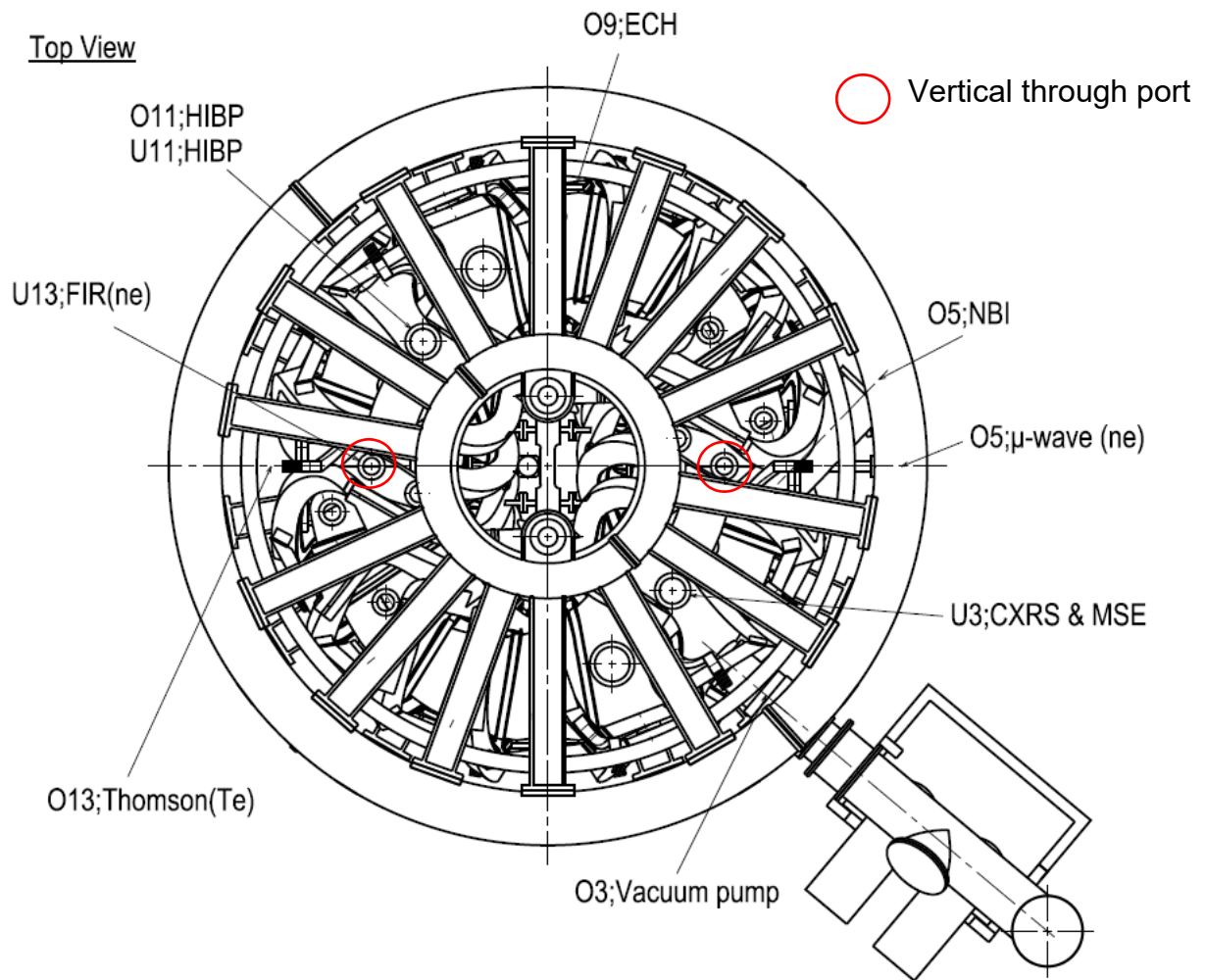IN; Inside port, OUT; Outside port, UP; Upper port, LW; Lower port
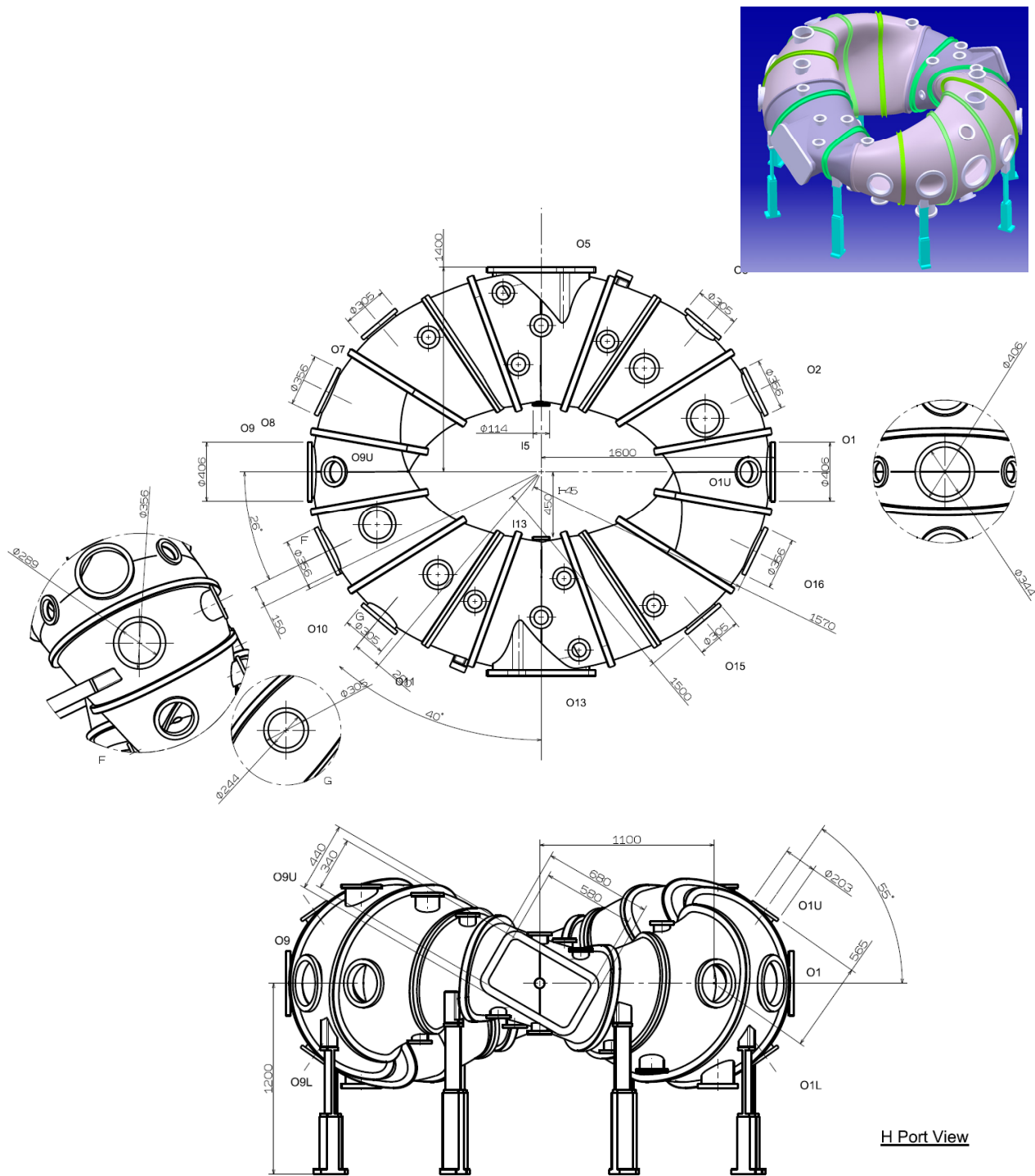
Fig. 18-1   Classification by use

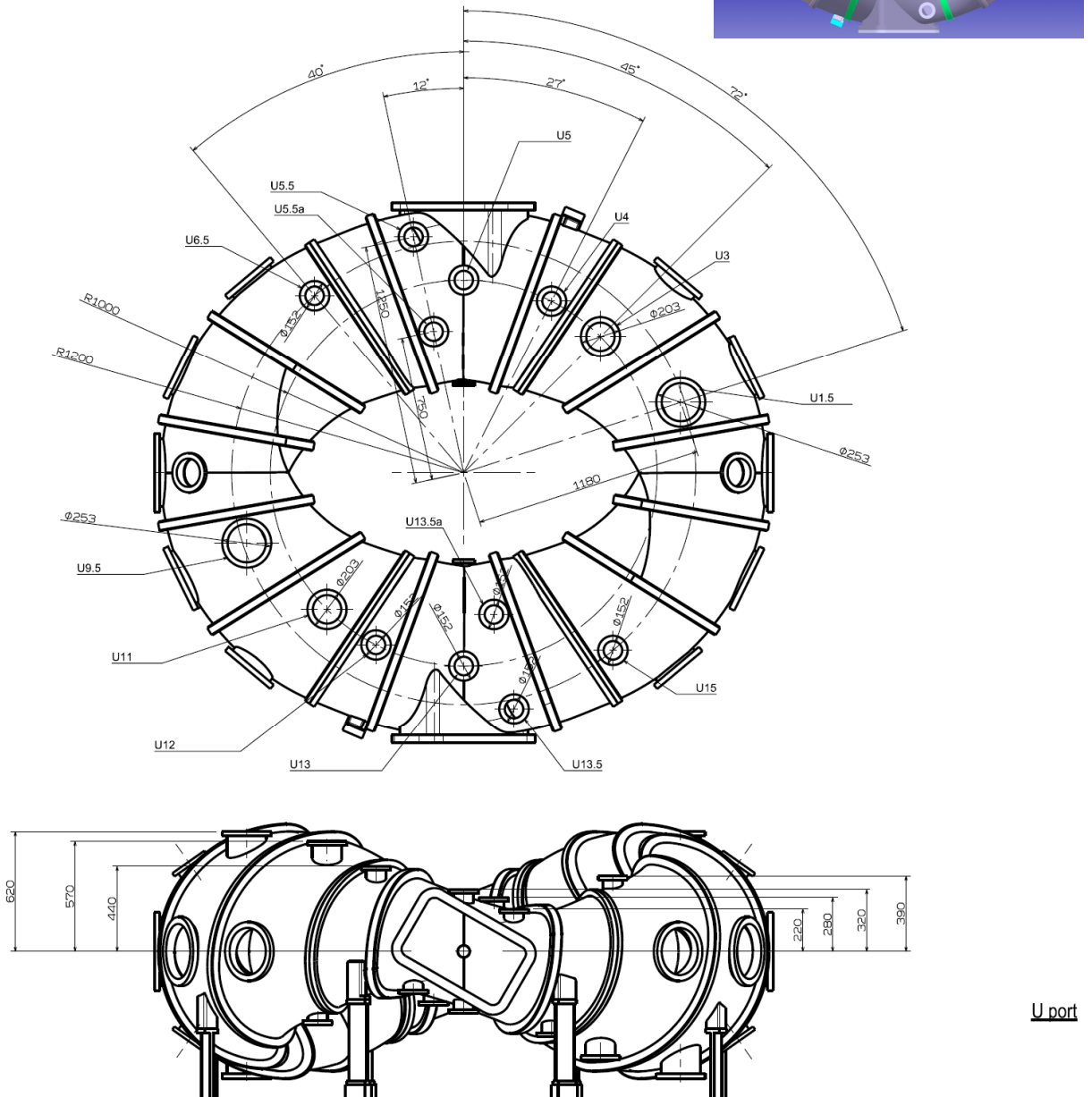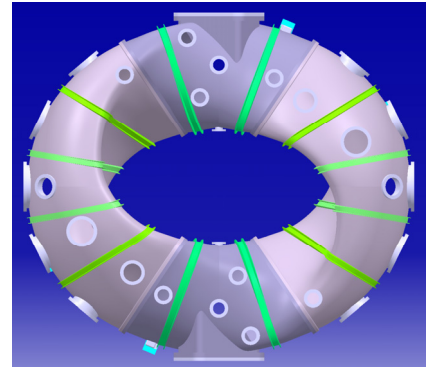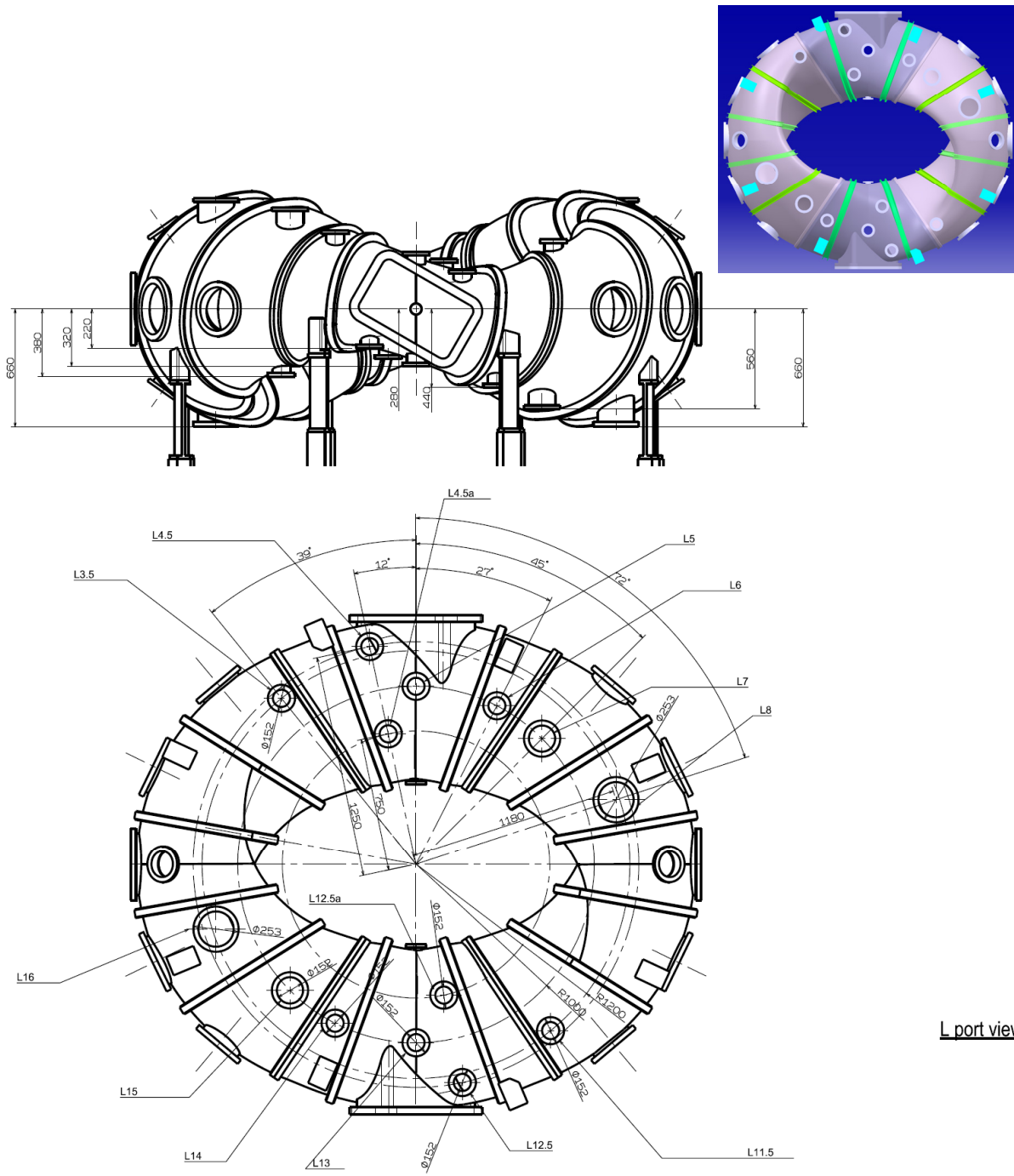Fig. 18-2   Position and size of horizontal ports

Fig. 18-3   Position and size of upper vertical ports

Fig. 18-4   Position and size of lower vertical ports
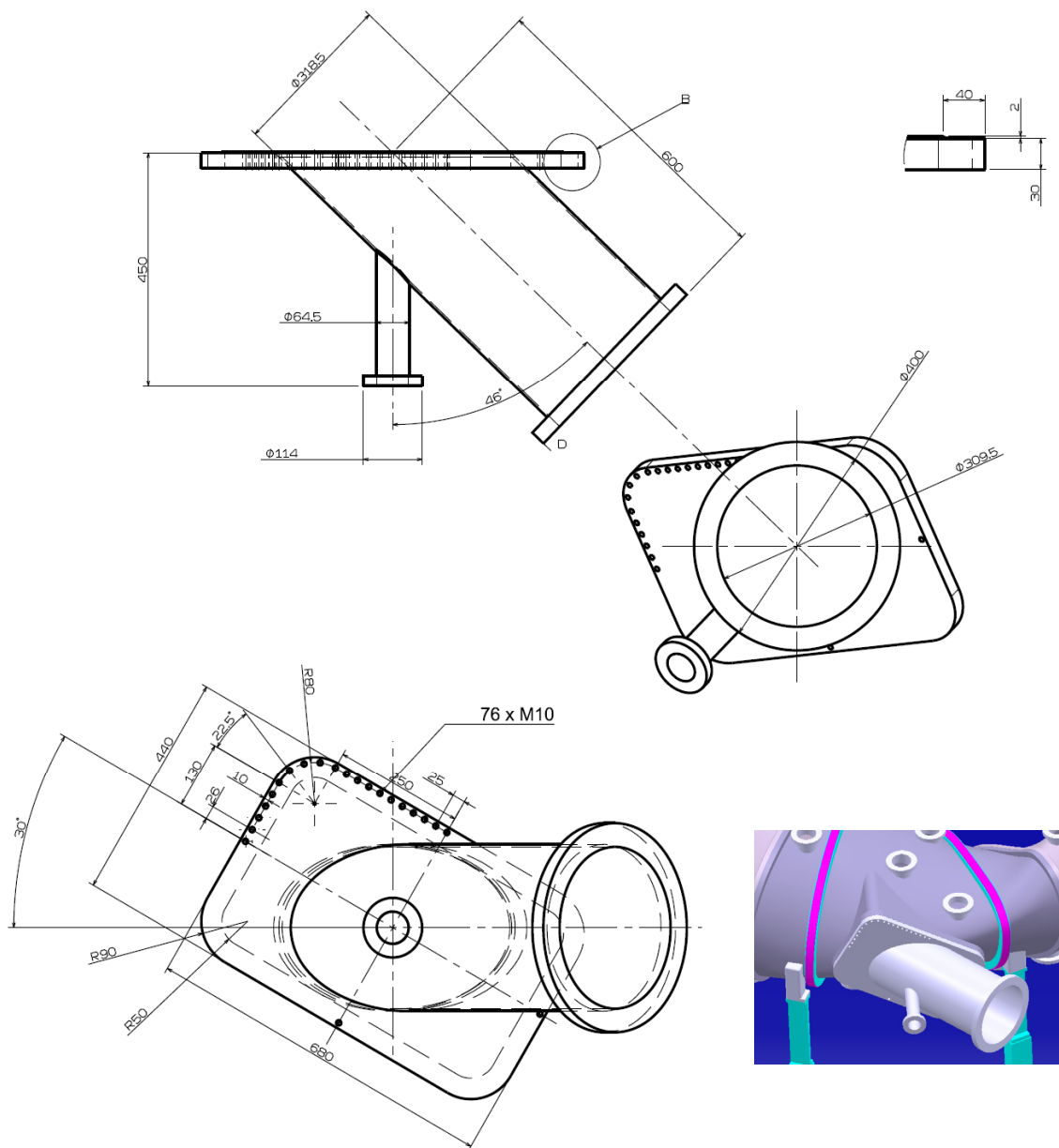
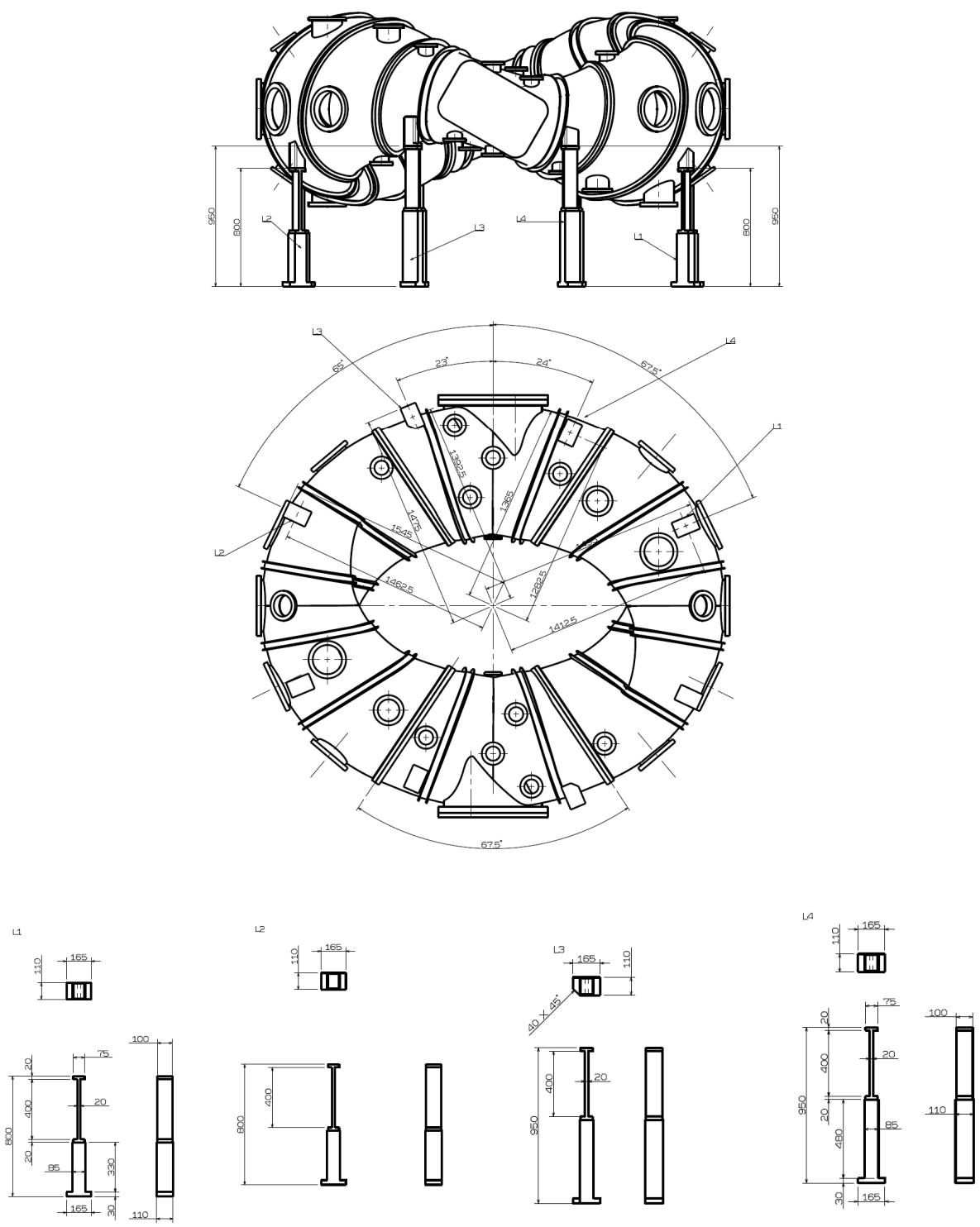Fig. 18-5   Tangential port for NBI

Fig. 18-6   Position and height of leaf-spring type leg for main vacuum vessel

[19]   MAIN DIMENSION DRAWING

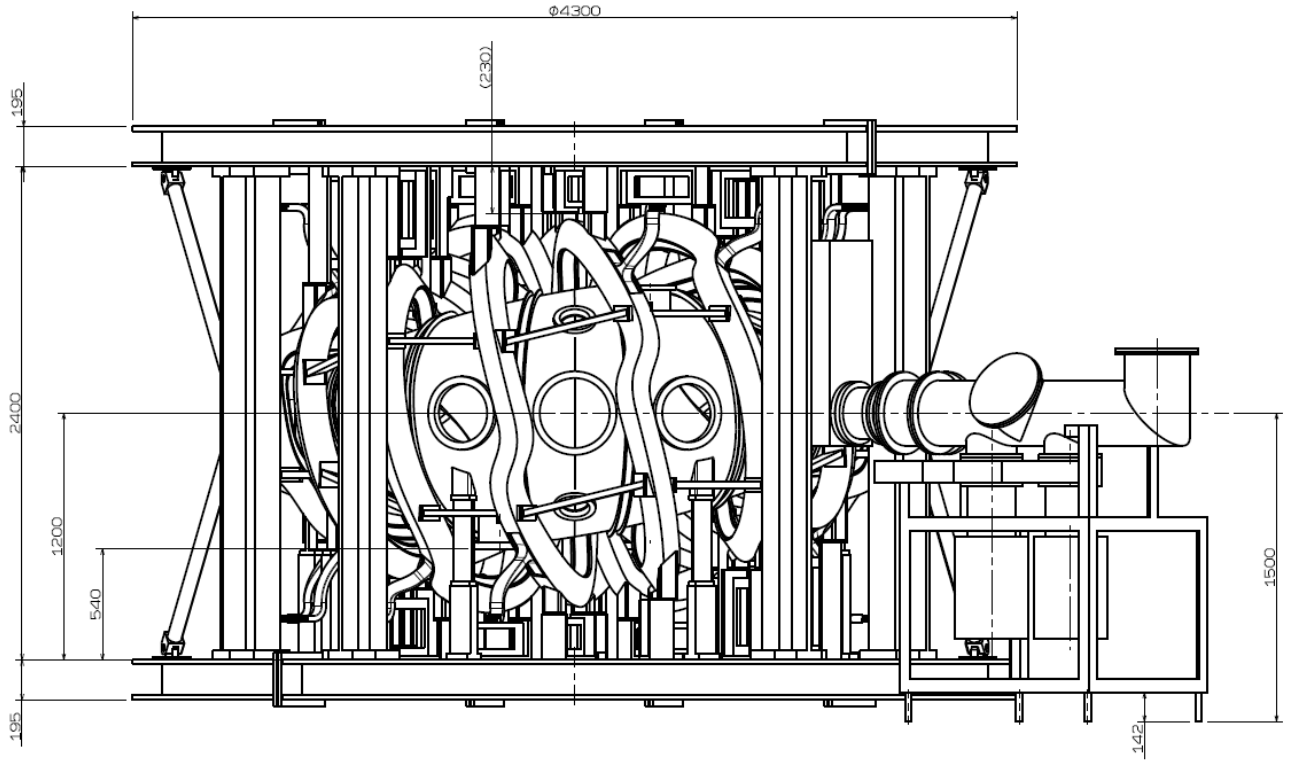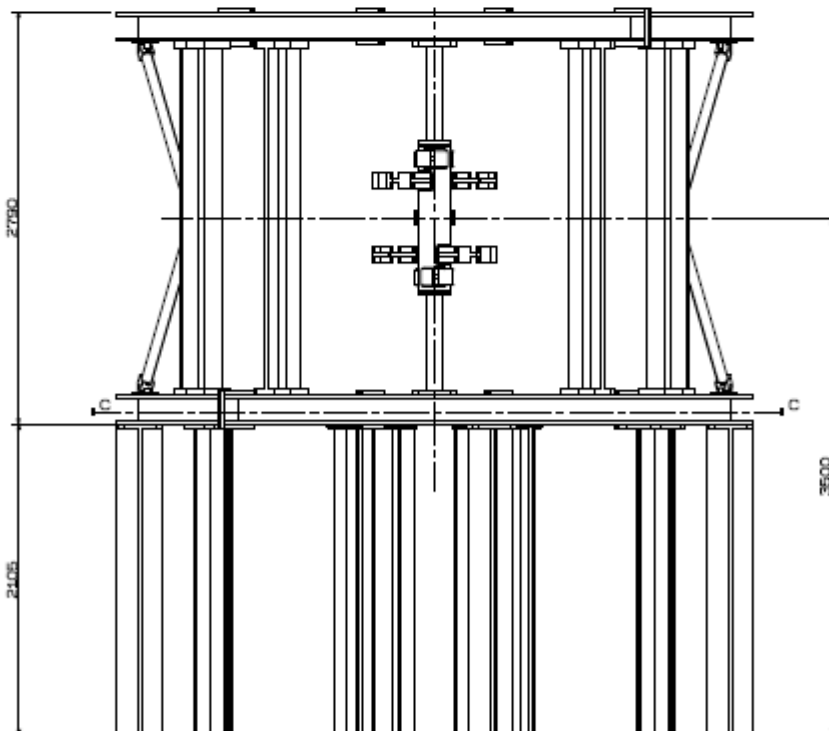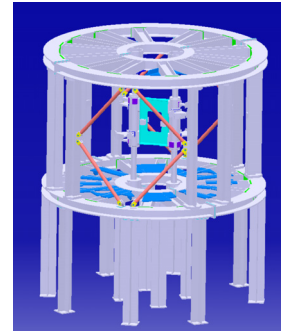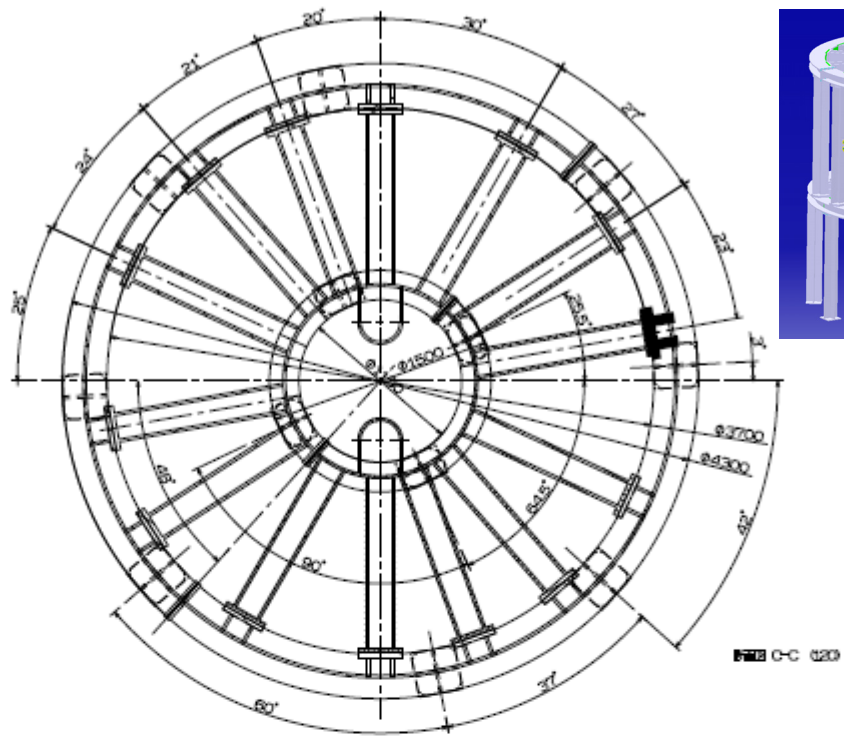This chapter includes some drawings to show the size of devices.

Fig. 19-1   Main dimension of the CFQS

Fig. 19-2   The cage type support structure
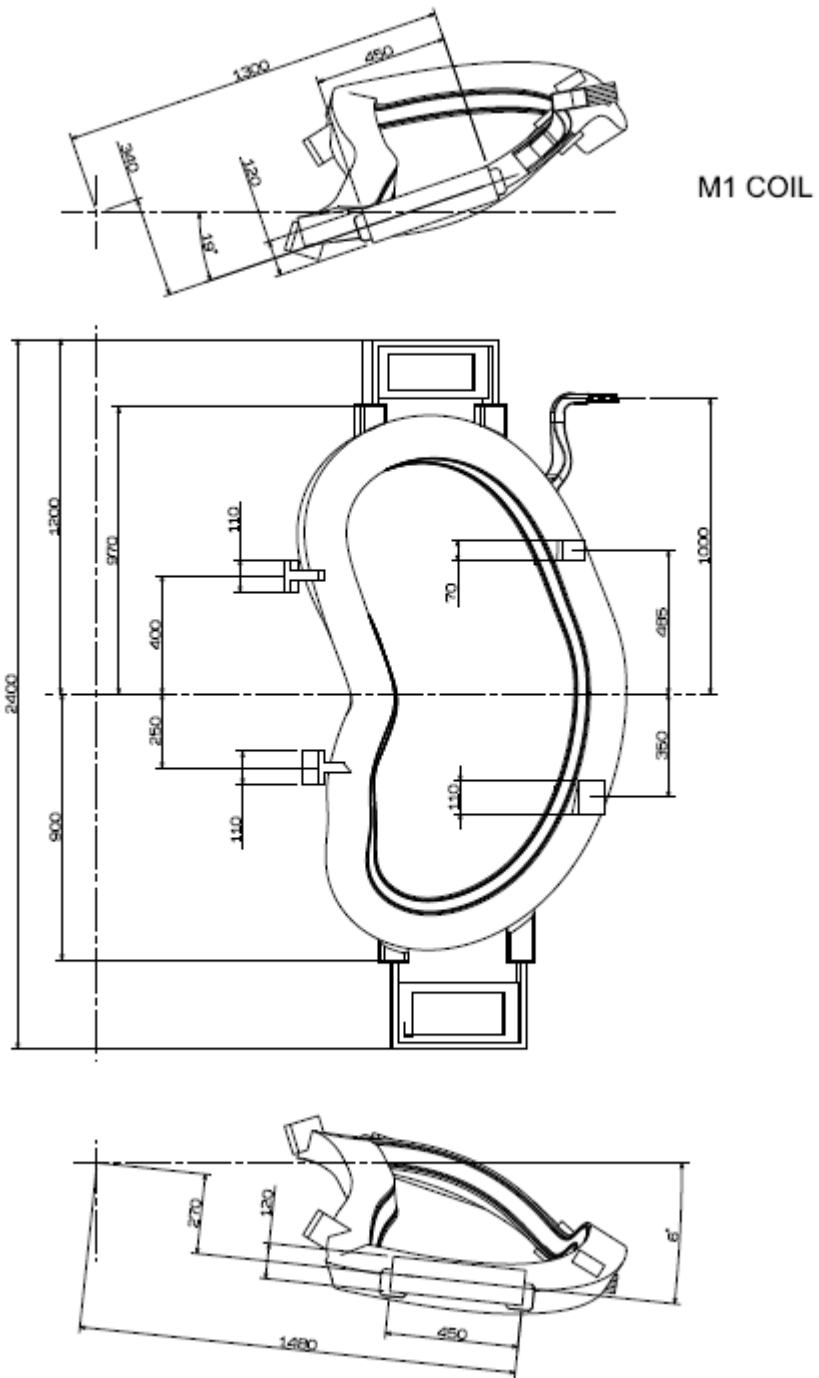
Fig. 19-3   Modular coil case for the M1 COIL
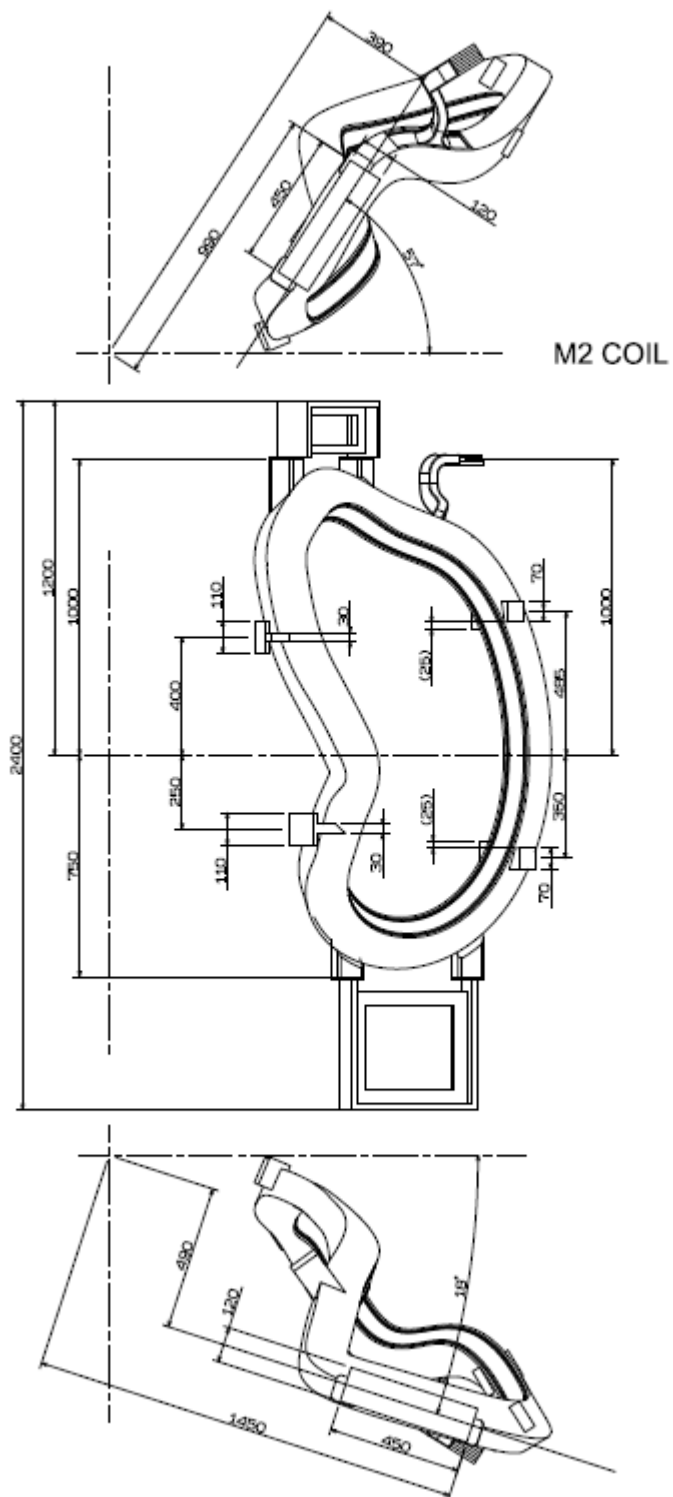
Fig. 19-4   Modular coil case for the M2 COIL
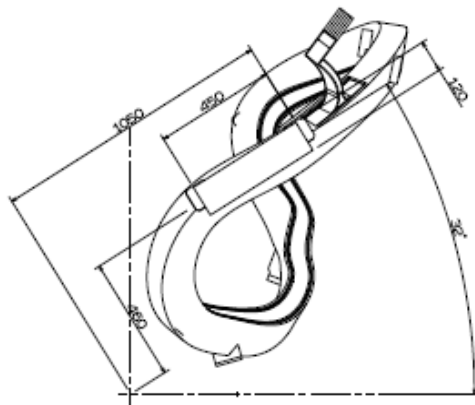
M3 COIL
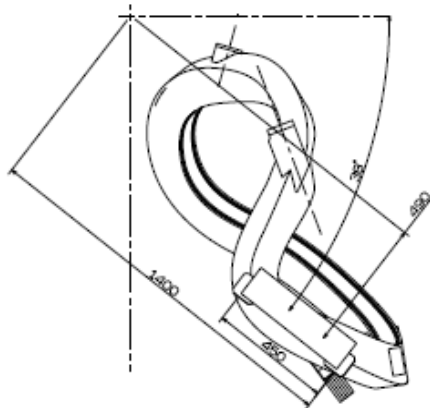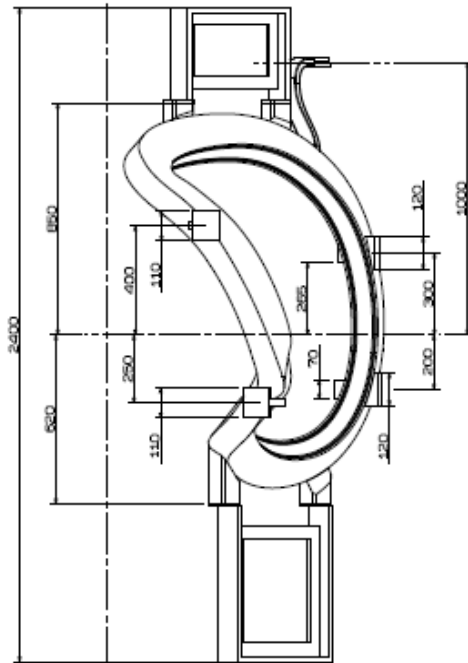
Fig. 19-5   Modular coil case for the M3 COIL
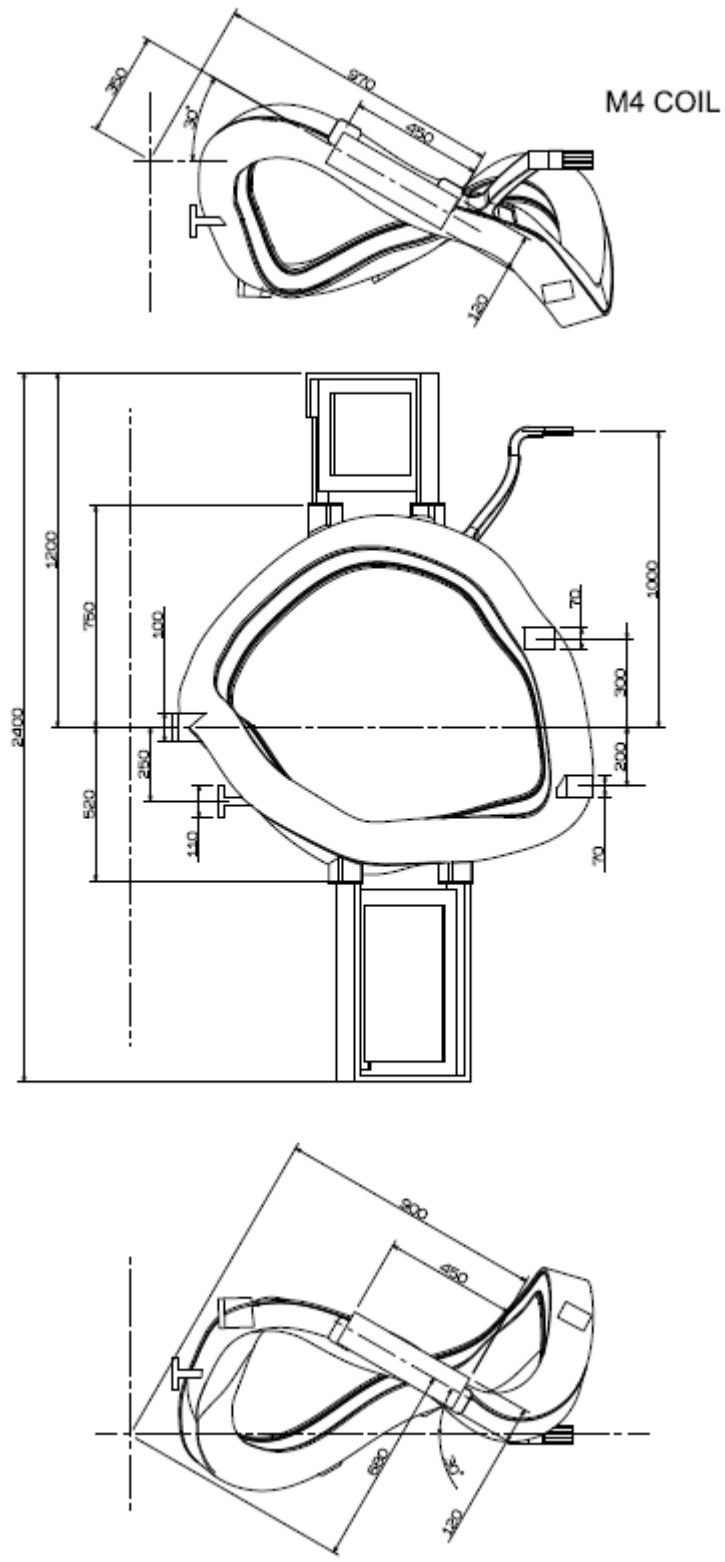
M4 COIL

Fig. 19-6   Modular coil case for the M4 COIL
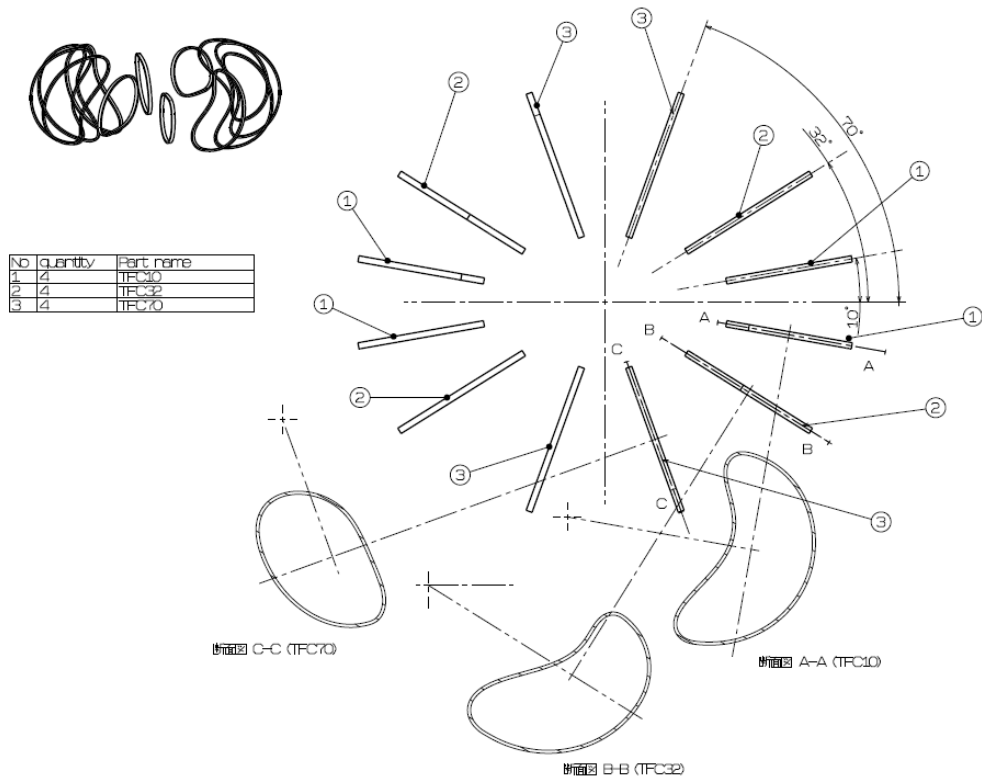
Fig. 19-7   Layout of the TFC
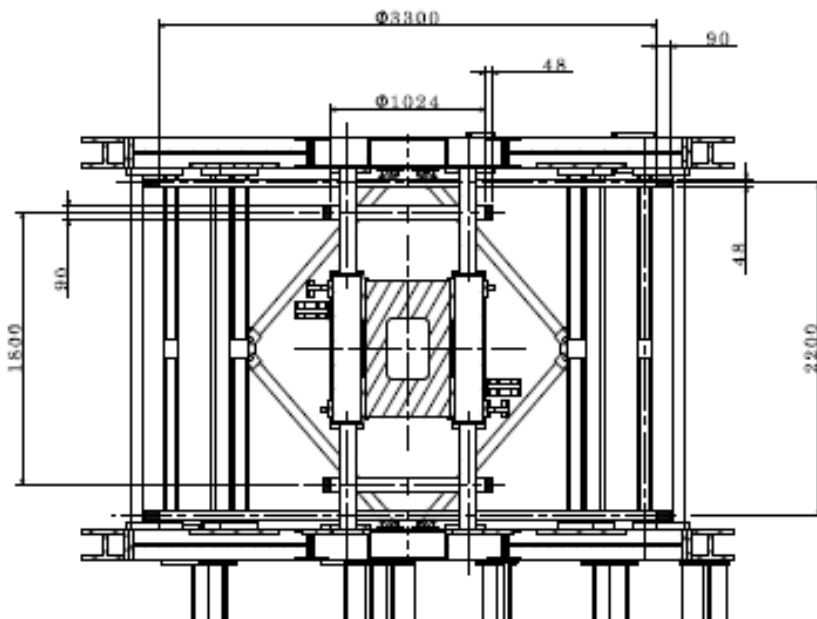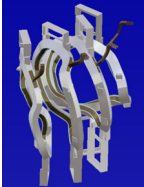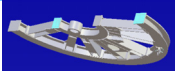

Fig. 19-8   Layout of the PFC

[20]   MASS LIST OF THE CFQS MAIN PARTS

The mass list is shown in the table below to study transportation and crane work.

Table 20-1   Mass list of the CFQS

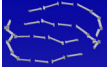| No	Part	Mass (kg)	Quantity	Total (kg)	Remarks	Picture
1	Vacuum vessel	2,568	1	2,568	Including TFC's and legs	
2	Modular coil	570	4	2,280	M1	
		572	4	2,288	M2	
		575	4	2,300	M3	
		568	4	2,272	M4	
3	Upper and lower frame	2,116	2	4,232	Top	
		2,162	2	4,324	Bottom	
4	Outer pillar	291	4	1,164	With a rod fixed seat	
		286	4	1,144		
5	Rod	48	8	384		
6	Lower pillar	217	8	1,736	Outer	
		175	4	700	Inner	
7	Center support	603	1	603		
8	Beam between the M-coils		28	280	A total of eight different shapes	
9	PFC	368	2	736	OV	
		116	2	232	IV	
10	Others (extra)			2,757		
	Sum total			30,000		

[21] DESIGN OF LEAF-SPRING TYPE LEG

In order to absorb the heat expansion deformation by the baking, the vacuum vessel is supported by eight leaf spring type legs. Since the leaf spring type leg will receive a compressive load, it is necessary to evaluate its buckling and bending stress. This chapter introduces the results of analysis and evaluation by hand calculation.

21.1. Design values

Design values of the leaf spring are as follows.

▸ Beam thickness;   H=20 mm

▸ Beam width;   B=100 mm

▸ Beam length   L=400 mm

▸ Number of legs   8

▸ Material;   SUS316L

> Design temperature; 150 degrees C
> Young's modulus E = 193 GPa
> Design allowable stress; S_m = 115 MPa
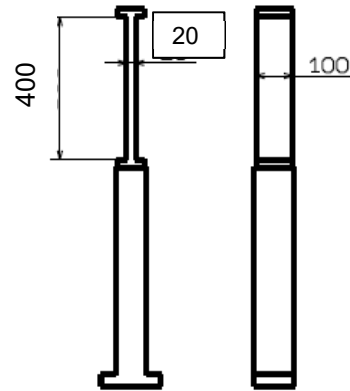> Yield stress; $\sigma_y = 173\ MPa$

Fig. 21-1   Design dimension of the leg

▸ Support load   500 kg

> The weight of the vacuum vessel is about 4000 kg with extra 1400 kg of additional devices, so one leg shares 500kg.

▸ Forced displacement by the baking δ =2 mm

> The thermal expansion of the stainless steel is 1.73x10-5/degree. The major radius increases by an average of 0.17% (=1.73x10^{-5} x 100) when the temperature of the vacuum vessel rises 100 degrees during baking. Since the major radius of the CFQS is 1 m, the amount of forced displacement is assumed to be 2 mm.

21.2. Buckling load and safety factor

The buckling load is calculated as follows by the formula of the beam fixed at two ends.

$$P_{cr} = \pi^2 EI/(KL)^2$$

$$\sigma_{cr} = \frac{P_{cr}}{A} = \pi^2 E/(KL/r)^2 < \sigma_y$$

where

  P_{cr} = Euler's critical load (longitudinal compression load on column)

  E= modulus of elasticity of column material (Young's modulus)

  I = minimum area moment of inertia of the cross section of the column

  L= unsupported length of column

  K=column effective length factor

K=0.5 for the beam fixed at two ends. The value of K may change in the range of 0.5 to 2 at fixed conditions at both ends. In the worst case, the critical load will be 1/16 times, so it is necessary for the design to have a sufficient margin.

σ_{cr} = Critical buckling stress

A = Area cross section

r= Radius of gyration, $r = \sqrt{I/A}$

Substituting the design values,

Moment of inertia, I =BH^3/12= (20^3 x100) x10^{-12} = 6.67 x 10^{-8} m^4

Radius of gyration, r = $\sqrt{6.67 \text{ x } 10^{-8}/(0.02*0.1)} = 0.00577\ m$

Slenderness ratio, KL/r = (0.5 x 0.4)/0.0577 = 34.7

Critical buckling stress, $\sigma_{cr} = \pi^2$ x 193 x 10^9 / 34.7^2 = 1.58 GPa

Buckling load, P_{cr} = 3.16 MN = 322 tons

The safety factor for buckling is about 644 (= 322000/500), which is considered to be sufficient.

21.3.   Bending stress with the forced displacement

The bending stress of beam fixed at two end can be obtained by expanding the model fixed at one end as shown in Fig. 21-2.

The deflection at the unsupported end of the model (b) is calculated as follows.

$$y = \frac{WX^3}{3EI}$$
$$\sigma_b = \frac{M}{Z}$$
$$M = WX$$

(a)   (b)
a beam (a) fixed at two ends and (b) fixed at one end and other free

Fig. 21-2   Bended shape of the beam.

Where

σ_b = bending stress at the fixed end of the model (b)
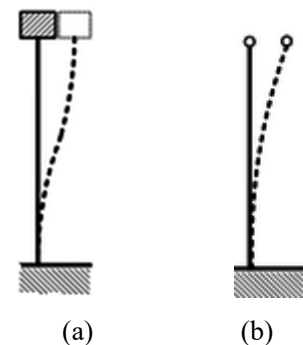
W = load at unsupported end of the model (b)

X = beam length of the model (b)

E = Young's modulus

I = moment of inertia

M= bending moment at the fixed end of the model (b)

Z = section modulus of the beam = I/(H/2). H is a thickness of the beam.

The bending stress of the model (a) is equal to a result with y = 0.5 x the deflection of the model (a) and X = 0.5 x the beam length of the model (a). Substituting the design values,

$$W = \frac{3EI(\delta/2)}{(L/2)^3} = 3 \times 193 \times 10^9 \times 6.67 \times 10^{-8} \times \frac{0.001}{0.2^3} = 4825 \, N$$

$$\sigma_b = \frac{4825 \times 0.2}{6.67 \times 10^{-8}/0.01} = 145 \, MPa$$

The compressive stress is easily obtained by

$$\sigma_m = \frac{500 \times 9.8}{0.02 \times 0.1} = 2.45 \, MPa$$

The membrane plus bending stress is

$$\sigma_m + \sigma_b = 147 \, MPa < \sigma_y = 1.5 \times S_m = 173 \, MPa$$

It satisfies the design guideline as shown in the chapter [1] and [2] Allowable limit value of stress and strain for CFQS.

Publication List of NIFS-PROC. Series

NIFS-PROC-100　Edited by Yeong-Kook OH, Shigeru MORITA and Liqun HU
Proceeding of A3 Foresight Program Seminar on Critical Physics Issues Specific to Steady State Sustainment of High-Performance Plasmas 19-22 May, 2015, Chuncheon, Korea
Jul. 25. 2016

NIFS-PROC-101　Edited by Shigeru MORITA, Liqun HU and Yeong-Kook OH
Proceeding of A3 Foresight Program Seminar on Critical Physics Issues Specific to Steady State Sustainment of High-Performance Plasmas 1-4 December, 2015, Gotemba, Japan
Sep. 09. 2016

NIFS-PROC-102　Edited by Liqun HU, Shigeru MORITA and Yeong-Kook OH
Proceeding of A3 Foresight Program Seminar on Critical Physics Issues Specific to Steady State Sustainment of High-Performance Plasmas May 17-20, 2016, Yinchuan, China
Jan. 23. 2017

NIFS-PROC-103　Edited by Daiji Kato, Zhengying Cui and Chenzhong Dong
JSPS-NRF-NSFC A3 Foresight Program Seminar Proceedings of Japan-China-Korea Joint Seminar on Atomic and Molecular Processes in Plasma Jul. 26 - 28, 2016, Chengdu, China
Mar. 17, 2017

NIFS-PROC-104　Atsuo Iiyoshi
Fusion for Sustainable World Development
Mar. 27, 2017

NIFS-PROC-105　Edited by Weihua Jiang
Frontiers of Applied Pulse Power Technology
Aug. 28. 2017

NIFS-PROC-106　Edited by Keiichi Kamada and Tetsuo Ozaki
Evolution of Pulse Power and its Peripheral Technology
Nov. 01, 2017

NIFS-PROC-107　Edited by Hiroaki Ito and Tetsuo Ozaki
Recent Progress of Pulsed Power Technology and its Application to High Energy Density Plasma
Nov. 27, 2017

NIFS-PROC-108　Edited by Yeong-Kook OH, Shigeru MORITA and Liqun HU
Proceeding of A3 Foresight Program Seminar on Critical Physics Issues Specific to Steady State Sustainment of High-Performance Plasmas November 22-25, 2016, Jeju, Korea
Jan. 11,. 2018

NIFS-PROC-109　Edited by Shigeru MORITA, Liqun HU and Yeong-Kook OH
Proceeding of A3 Foresight Program Seminar on Critical Physics Issues Specific to Steady State Sustainment of High-Performance Plasmas 11-14 July, 2017, Sapporo, Japan
Jan. 12, 2018

NIFS-PROC-110　Edited by Jun Hasegawa and Tetsuo Ozaki
Resent Developments of Pulsed Power Technology and Plasma Application Research
Jan. 12, 2018

NIFS-PROC-111　Edited by Liqun HU, Shigeru MORITA and Yeong-Kook OH
Proceeding of A3 Foresight Program Seminar on Critical Physics Issues Specific to Steady State Sustainment of High-Performance Plasmas 12 - 15 December, 2017, Chongqing, China
Jun. 11, 2018

NIFS-PROC-112　Edited by E. Kikutani (KEK) and S. Kubo (NIFS)
Proceedings of the meeting on Archives in Fields of Natural Sciences in FY 2017
Oct. 18, 2018

NIFS-PROC-113　Pulsed Power and High-Density Plasma and its Applications
Edited by Koichi Takaki and Tetsuo Ozaki
Feb. 6, 2019

NIFS-PROC-114　The 7th Japan-China-Korea Joint Seminar on Atomic and Molecular Processes in Plasma (AMPP2018)
Edited by Daiji Kato, Ling Zhang, and Xiaobin Ding
May 10, 2019

NIFS-PROC-115　CFQS TEAM
NIFS-SWJTU JOINT PROJECT FOR CFQS -PHYSICS AND ENGINEERING DESIGN-
VER. 2.1 2019. SEP.
Nov. 8, 2019